Paris VI University - Pierre et Marie Curie, France

Jagiellonian University in Cracow, Poland

Thesis submitted to obtain the PhD degree in Physics

Theoretical predictions for the Drell-Yan process through a Monte Carlo event generator

presented by

Andrzej Siódmok

written under the supervision of

Prof. Wiesław Płaczek (Jagiellonian University)
Prof. Mieczysław W. Krasny (Paris VI University)

To my family.

Contents

Preface

The Drell-Yan process has been widely studied in many past [1] and present [2] hadron collider experiments and played a significant role in the development of our understanding of quantum chromodynamics (QCD) and electroweak (EW) interactions, both from the experimental and theoretical point of view. Certainly this will also be the case for the LHC experiments, especially because it will soon become the unique W and Z boson production factory which is expected to collect 300 million W and 20 million Z events per year of its operation at energies $\sqrt{s} = 14$ TeV and the luminosity of $10^{33}\ cm^{-2}s^{-1}$. High-precision studies of electroweak bosons properties, their propagation in vacuum and in hadronic matter, their interactions with matter and with the radiation quanta are expected to provide the decisive experimental insight into the mechanism governing the electroweak symmetry breaking. In order to achieve these aims and make the LHC successful it is essential that we simultaneously improve our theoretical predictions and phenomenological tools, such as Monte Carlo event generators, and, on the other hand, design novel measurement strategies which are both robust and assure the highest-achievable precision in controlling the detection and reconstruction systematic biases. In the presented thesis these very important aspects for the LHC are of great concern.

In the first part of this thesis we present a new member of the Krakow YFS Monte Carlo event generator family – ZINHAC, which is a dedicated Monte Carlo event generator, written in C++, for the single Z-boson[1] production in hadronic collisions with YFS multiphoton radiation effects in leptonic decays.

The Drell–Yan-like production of the single Z-boson, with the weak boson decaying into a lepton pair, is a clean process with a large cross section at hadron colliders. It is well suited for a number of precision measurements, both at the proton–antiproton ($p\,\bar{p}$) Fermilab Tevatron collider and at the proton–

[1] All our calculations include virtual photon γ^* and the full interference between γ^* and Z in the Drell–Yan-like process, but for the convenience we will refer in the following to this process as to Z-boson production.

proton (p p) CERN Large Hadron Collider (LHC) [3, 4]. Just to give one example here, as we will see in Chapter 3 that the precise description of the neutral–curent Drell–Yan-like process is very important for the W-boson mass and width measurements, both for the novel [5] and "standard" [6] methods. For this reason, it is of utmost importance to predict the Z observables with as-high-as-possible theoretical precision. Among radiative corrections that affect the Z-boson observables considerably is the photon radiation in leptonic Z decays. It distorts Z-invariant-mass distributions reconstructed from Z-decay products as well as affects lepton pseudorapidity and transverse momentum distributions. These distortions are strongly acceptance-dependent. Therefore, in view of the expected precision at the LHC, it will be necessary to eliminate (or largely reduce) this source of theoretical uncertainty in the experimental analysis by including multiple photon corrections to the process of the single Z production. In order to be fully applicable in a realistic experimental situation, such predictions have to be provided in terms of a Monte Carlo event generator, which is central to any high-energy physics experiment. The above requirements are fulfilled by the ZINHAC Monte Carlo event generator.

In the second part of the thesis we will concentrate on the QCD corrections, more specifically on the improvement of theoretical predictions for the transverse momentum spectrum of vector bosons in the Drell–Yan processes, which is one of the most useful and important Z and W observables for the experimental program at the LHC. For this reason, it is of utmost importance to predict the W and Z observables with as-high-as possible theoretical precision. The sources of uncertainty in the QCD theoretical predictions of W and Z observables, such as the transverse momentum of electroweak bosons are of perturbative and non-perturbative origin. In Chapter 2 we will concentate on the modelling of the latter in the framework of a backward evolution parton shower approach [7] which is widely used in general-purpose Monte Carlo generators, such as Herwig [8] or Pythia [9], and has become a key component of a wide range of comparisons between theory and experiment. Clearly, it will also be the case with the new generation of event generators, such as HERWIG++ [10], the object oriented version of Pythia [11] or Sherpa [12]. Therefore, parton-shower algorithms are important and challenging topics which still seek great improvement. In Chapter 2 we present an example of such improvement which is a new model of non-perturbative gluon emission in an initial-state parton shower. This model gives a good description of transverse-momentum spec-

trum of vector bosons for the data taken in previous experiments over a wide range of CM energy. At the end of the chapter the model's prediction for the transverse momentum distribution of the Z bosons for the LHC is presented and used for a comparison with other approaches. This quantity is very important for the experimental program at the LHC, for example in the case of W-boson production – the uncertainty in the shape of the transverse momentum spectrum directly affects the measurement of the W mass [6] and its mass charge asymmetry $M_{W^+} - M_{W^-}$ [13].

Last but not least, in Chapter 3 we present a new strategy for the W-boson mass measurement at the LHC. First, we show how to significantly reduce the impact on the precision of the effects which are the strongest and, as a consequence, the most important for the W-mass measurement at the Tevatron. In the proposed strategy the impact on the precision of the measured parameters is reduced by using dedicated observables and dedicated measurement procedures which exploit flexibilities of the collider and detector running modes. This method features its robustness with respect to the systematic measurement and modeling error sources and optimises the use of the Z-boson production process as *"the standard reference candle"* for the W-mass measurement at the LHC. The presented strategy allows to factorize and to directly measure those of the QCD effects which are not under good theoretical control and which affect differently the W and Z production processes. In the contrary to the QCD effects, the electroweak corrections in the neutral and charged Drell–Yan processes can be controlled very precisely via dedicated Monte Carlo generators, such as WINHAC and presented in the first part of the thesis ZINHAC. In the second part of this chapter we demonstrate "new" error sources which are not important for the Tevatron $p\bar{p}$ collisions but will play an important role in the pp collisions at the LHC. We argue that in order to reach the $\mathcal{O}(10)$ MeV precision target, claimed by both the ATLAS [6] and CMS [14] Collaborations, some novel LHC-specific measurement strategies must be developed. At the end of this chapter two examples of such strategies are proposed. In the first one we circumvent the LHC specific precision 'brick-walls' by proposing the dedicated LHC runs with deuterium or helium ion beams. The second, alternative strategy includes a dedicated fixed-target "LHC-support" experiment with a high-intensity muon beam.

Chapter 1

The Monte Carlo event generator ZINHAC

Abstract

In this chapter we present the calculation of multiphoton radiation effects in leptonic Z-boson decays in the framework of the Yennie-Frautschi-Suura exclusive exponentiation. This calculation is implemented in the dedicated Monte Carlo event generator for precision description of the neutral-current Drell–Yan process, i.e. Z/γ^* production with leptonic decays in hadronic collisions. Some numerical results obtained with the help of this program and comparisons with SANC program are also presented.

This chapter is based on the following materials: [15], [16], [17] and [18].

1.1 Introduction

The infrared (IR) divergences may emerge if considered theory includes a massless field like the photon in quantum electrodynamics (QED). This type of divergences comes from the region of real and virtual soft gauge bosons. The divergences appear in every higher order of perturbative expantion to any elastic scattering amplitude when a charged particle in QED (or a colour-charged particle in QCD) changes the direction of its motion. In QED the resolution of this problem is well known and the physical picture behind it is well understood. When the infrared divergences in all loops are summed up, the elastic amplitude vanishes. This is very natural and can already be explained at the classical level: scattering of charged particles is always accompanied by the bremsstrahlung of soft photons and the probability not to emit such a photon is zero. But a pure elastic scattering is not a physical process. The detector always has a finite energy resolution $\Delta\epsilon$. We never know whether soft photons with energy $\Delta\epsilon$ were emitted or not and we have to sum over the probabilities of all these processes. Such a sum is called a physical cross section. These physical cross sections are always finite: infrared divergences which show up in the probabilities of individual processes cancel out of the sum.

At the first order of perturbative expantion, the mechanism of this cancellation in QED was understood by Bloch and Nordsieck [19] back in 1937 and is explained in the textbooks [20, 21, 22]. It was generalized to higher orders by Yennie, Frautchi and Suura (YFS) [23][1]. The YFS approach is based on the concept of resumming the infrared contributions to all orders. The big advantage of the YFS formalism is that, in addition, it allows for a systematic improvement of this eikonal approximation, order-by-order in the QED coupling constant. This is the reason why the most precise tools for the simulation of QED radiation are based on this algorithm. Some examples of these programs will be mentioned later in this section. In their pioneering paper Yennie, Frautchi and Suura presented the exact result for the processes:

$$f_1(p_1) + f_2(p_2) \to f_3(p_3) + f_4(p_4) + n(\gamma), \tag{1.1}$$

accompanied by the original applications of their results at the precision of the leading term. For example, for initial state radiation (ISR) in e^+e^- annihilation

[1] Their proof was polished and presented in a nice transparent form by Weinberg [24].

the result[2] is as follows:

$$d\sigma_{exp} \cong \gamma F_{YFS}(\gamma)(1-z)^{\gamma-1}\sigma_B dz \tag{1.2}$$

where we have defined:

$$z = s'/s,\ \gamma = \frac{2\alpha}{\pi}\left(\ln\frac{s}{m^2} - 1\right),\ s = (p_1+p_2)^2,\ s' = (p_3+p_4)^2 \tag{1.3}$$

and

$$F_{YFS}(\gamma) = \frac{e^{-C\gamma}}{\Gamma(1+\gamma)}, \tag{1.4}$$

here $C \cong 0.5772$ denotes the Euler's constant and σ_B is the respective Born-level cross section. These first early applications were (semi-)analytical and their accuracy was around $\lesssim 10\%$, which was quite adequate for applications of that time experiments in which errors on σ_B were much larger.

This situation changed during LEP1/SLC and LEP2 era where the precision of the electroweak measurements improved drastically and, as a consequence, there was a great need to improve precision of theoretical predictions. It turned out that this was possible with the application of [23] to precision predictions from quantum field theory via Monte Carlo (MC) methods. The pioneering solution to this problem was given by S. Jadach in Ref. [25] which opened the way to use the exact result of [23] via Monte Carlo methods, so that very high precision predictions could be obtained on an event-by-event basis. The first realistic MC for precision SLC/LEP1 physics – YFS1 with an exact $\mathcal{O}(\alpha)$, YFS-exponentiated multiple-photon MC for $e^+e^- \to f\bar{f} + n(\gamma),\ \ f \neq e$, was published by S. Jadach and B.F.L. Ward in Ref. [26]. The precision reached by the program in Z physics was $\lesssim 1\%$. Shortly after that the same authors published in Ref. [27] the first realistic exact $\mathcal{O}(\alpha)$, YFS-exponentiated multiple-photon MC for $e^+e^- \to e^+e^- + n(\gamma)$ at low angles, BHLUMI 1.0, for LEP/SLC physics, where the primary applications were precision luminosity predictions. Again, the precision tag was $\lesssim 1\%$.

The large number of Z's at LEP1 (2×10^7 were detected) necessitated the per-mille-level theory precision in order that the theoretical error would not compromise the outstanding experimental error in the attendant tests of the electroweak (EW) and QCD theories. It was achieved by the YFS2 and YFS3 MC realizations of the YFS approach in Refs. [28, 29], wherein the precision

[2] Only the leading terms in γ are then retained in this $\bar{\beta}_0$-level approximation, see Ref [23] for details.

tags were 0.1% for initial state radiation and for the combination of initial state and final state radiation, respectively.

The whole family of YFS Monte Carlo event generators was developed: KORALZ 3.8, 4.04 [30,31,32] with the 0.1% precision tag on $2f$ production at the Z regime at LEP1/SLC, BHLUMI 2.01, 2.30, 4.04 [33,34] for the LEP1/SLC luminosity-process small-angle Bhabha scattering and BHWIDE [35] for the large-angle Bhabha scattering with the precision tag at 0.2% at the Z regime at LEP1/SLC.

For LEP2 experiments there was a need for novel precise tools, therefore new series of MC event generators appeared, KKMC [36], which gives 0.2% precision on radiative return $2f$ production at LEP2 energies, YFSWW3 [37] with the 0.4% precision on WW production, KoralW 1.02, 1.42 [38,39] with the 1.0% precision on the $4f$ background processes, KoralW 1.51 [40], the concurrent KoralW&YFSWW3 MC, with the 0.4% precison on the $4f$ production near the WW regime, and YFSZZ [41] with the 2% precision for ZZ production. The precisions of BHWIDE and BHLUMI at LEP2 was 0.4% and 0.122%, respectively. All these programs, which are based on the rigorous MC realization of the YFS approach on the event-by-event basis, played an important role for the precise description of leptonic collisions. More details and examples of the YFS MC event generators can be found in Ref. [42].

The situation becomes even more complicated in the case of hadron colliders due to additional quantum chromodynamics (QCD) effects which have to be taken in to account. One of many QCD complications will be discussed in Chapter 2, nevertheless, as we will see in in Chapter 3, the electroweak corrections still play an important role in the experimental analysis and it is of utmost importance to predict them with as-high-as-possible theoretical precision. To evaluate, for example, the impact of electroweak corrections in the case of the CDF and DØ, both collaborations at the Tevatron Run I made use of the fixed-order calculations of Refs. [43,44] for the single W production and for the single Z process. However, the anticipated precision for the Drell–Yan process at the LHC, requires that leading contributions from radiation of multiple photons are included [45, 46]. A first attempt towards the inclusion of higher-order QED corrections was the calculation of the W and Z production with radiation of two additional photons in Ref. [47]. For the very first time the higher-order corrections due to multi-photon (real and virtual) radiation in W decays at hadron colliders have been computed in Ref. [48] and the new member

of Krakow Monte Carlo generators family – the first Monte Carlo event generator for hadronic collisions which included calculation of multiphoton radiation effects in leptonic decays in the framework of the Yennie-Frautschi-Suura exclusive exponentiation – called WINHAC was constructed. Independently C. Carloni Calame, G. Montagna, O. Nicrosini and M. Treccani constructed HORACE [49] – the Monte Carlo generator for a Drell–Yan-like processes in which the corrections due to multiphoton radiation are computed using QED structure function approach. The corrections are calculated by solving numerically the DGLAP evolution equation for the QED structure function by means of the parton shower algorithm described in detail in Ref. [50]. Those two different approaches were compared in the case of single W-boson production in hadronic collisions with multiphoton effects in leptonic W decays [51]. These comparisons were performed first at the parton level with fixed quark-beams energy, and then at the hadron level for proton–proton collisions at the LHC. In general, a very good agreement – ar the per-mille level between – HORACE and WINHAC has been found. WINHAC was also compared with the SANC MC integrator [52]. The main and very important conclusion of this comparison was that both programs have reached the agreement for the $\mathcal{O}(\alpha)$ EW corrections to the charged-current Drell-Yan process at the sub-per-mill level, both for the inclusive cross section and for the main distributions.

In this chapter we will present a new member of the Cracow YFS Monte Carlo event generator family – ZINHAC, which is a dedicated Monte Carlo event generator for the single Z-boson[3] production in hadronic collisions with YFS multiphoton radiation effects in leptonic decays.

The Drell–Yan-like production of single Z boson, with the weak boson decaying into a lepton pair, is a clean process with a large cross section at hadron colliders. Therefore, it is ideal for a number of precision measurements, both at the proton–antiproton ($p\bar{p}$) Fermilab Tevatron collider and at the proton–proton (pp) CERN Large Hadron Collider (LHC) [3, 4]. As we will see in Chapter 3, the precise description of the neutral–curent Drell–Yan-like process is very important for the W-boson mass and width measurement, both for the novel [5] and "standard" [6] methods. The forward–backward asymmetry in the neutral–current channel can be used to measure the weak mixing

[3]All our calculations include virtual photon γ^* and the full interference between γ^* and Z in the Drell–Yan-like process, but for the convenience we continue to refer in this chapter to this process as Z-boson production.

angle. The Z-boson data is also well suited for the so called "standard candles", i.e. as means to understand the detector performances and to accurately calibrate its parameters, such as the energy scale and resolution of the electromagnetic calorimeter, as well as to monitor the collider luminosity with a per-cent precision and constrain the parton distribution functions (PDFs), by using observables such as the W/Z rapidity and lepton pseudorapidity. It is important also as the Standard Model (SM) backgrounds to new physics searches, such as the search for heavy Z' gauge bosons predicted by various extensions of the SM. In this case, the relevant experimental observables are, for example, the invariant mass of the final state leptons in the high tail, i.e. in the few-TeV region at the LHC. For the above reasons, it is of utmost importance to predict the Z observables with as-high-as-possible theoretical precision. Among radiative corrections that affect the mentioned above Z-boson observables considerably is the photon radiation in leptonic Z decays. It distorts Z-invariant-mass distributions reconstructed from Z-decay products as well as affects lepton pseudorapidity distributions. These distortions are strongly acceptance-dependent.

Therefore, in view of the expected precision at the LHC, it will be necessary to eliminate (or largely reduce) this source of theoretical uncertainty in the experimental analysis by including multiple photon corrections to the process of the single Z production. In order to be fully applicable in a realistic experimental situation, such predictions have to be provided in terms of a Monte Carlo event generator, which is central to any high-energy physics experiment. They are used by almost all experimental collaborations to plan their experiments and analyze their data. The above requirements are fulfilled by ZINHAC Monte Carlo event generator. As conclusion, in Table 1.1 we stress the place of ZINHAC with respect to multi-purpose and a few specialised Monte Carlo programs that can produce W or Z in the Drell–Yan process. In this table MC event generators (MCEG) are distinguished from the ones using Monte Carlo methods only as a mean for integration (MCI). As can be seen, there is up to date (2009) no Monte Carlo program that includes the QCD and EW corrections at the same level of detail.

The chapter is organized as follows. In Section 1.2 we discuss the YFS exponentiation in leptonic Z-boson decays, together with spin amplitudes for the

[4]Currently this is possible by interfacing ZINHAC with a general purpose Monte Carlo event generators such as Pythia 8 or Herwig++ via the Les Houches event files [75].

Monte Carlo	Ref.	Process	QCD	EW	Type
ZINHAC	[18]	Z	PDF(x), impr.[4] LO	QED YFS$\otimes\mathcal{O}(\alpha)$	MCEG
WINHAC	[48,53,54]	W	PDF(x), impr. LO	QED YFS$\otimes\mathcal{O}(\alpha)$	MCEG
HORACE	[49,55]	W, Z	PDF(x), impr. LO	QED PS$\otimes\mathcal{O}(\alpha)$	MCEG
Pythia	[9,56]	W, Z	PDF(x), impr. LO	LO	MCEG
HERWIG	[8,57]	W, Z	PDF(x, p_T), impr. LO	LO	MCEG
Herwig++	[10,58]	W, Z	PDF(x, p_T), NLO	LO	MCEG
Sherpa	[59,60]	W, Z	PDF(x, p_T), impr. LO	LO	MCEG
MC@NLO	[61,62]	W, Z	parton shower, NLO	LO	MCEG
AcerMC	[63,64]	W, Z	PDF(x), LO	LO	MCEG
ResBos-A	[65,66]	W, Z	PDF(x, p_T), NLO	FS $\mathcal{O}(\alpha)$	MCI
ResBos	[67,68]	W, Z	PDF(x, p_T), NLO	LO	MCI
WGRAD	[44,69]	W	PDF(x), LO	$\mathcal{O}(\alpha)$	MCI
ZGRAD2	[70,71]	Z	PDF(x), LO	$\mathcal{O}(\alpha)$	MCI
SANC	[72,73,74]	W, Z	PDF(x), LO	$\mathcal{O}(\alpha)$	MCI

Table 1.1: The overview of some Monte Carlo programs capable of simulating the single W or Z production in hadronic colliders. The quoted references corresponds to the main reference and the software homepage for further references and details on the Monte Carlo program, respectively.

Born-level process and for the process with single-photon radiation in Z decays. In Section 1.4 we describe the Monte Carlo algorithm. Numerical results and comparison with SANC are presented in Section 1.7. Section 1.8 summarizes the chapter and gives some outlook. Finally, the appendices contain supplementary formulae.

1.2 The YFS exponentiation in leptonic Z decays

As was mentioned in the Introduction, the main purpose of this work is to provide a theoretical prediction for the multiphoton radiation in leptonic Z-boson decays within the YFS exclusive exponentiation scheme. We restrict ourselves to consider final-state QED corrections only (as is shown in the Fig. 1.1), because it is known from previous investigations that the electroweak corrections to Drell–Yan-like processes are largely dominated by photon radiation from the final-state charged leptons [43, 44, 76].

The total cross-section for the neutral–current Drell–Yan-like process in hadron collisions accompanied by emission of an arbitrary number of photons in the

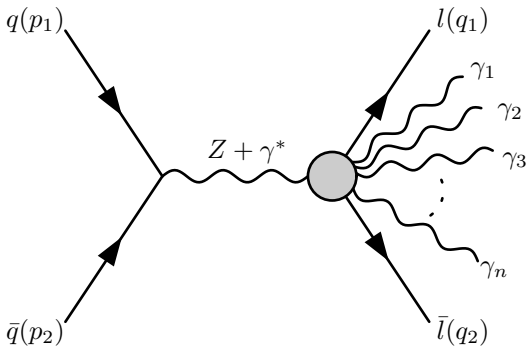

Figure 1.1: The production of a single $Z+\gamma^*$ in quark–antiquark collisions with multiphoton radiation in the final state.

final state:

$$h_1 + h_2 \longrightarrow Z + \gamma^* \longrightarrow l + \bar{l} + n(\gamma),\ (n = 0, 1, ...), \tag{1.5}$$

where $l = e, \mu$ and $h_1,\ h_2 \in \{p,\ \bar{p}, N\}$ can be written using factorization formula and the YFS formalism as follows:

$$\sigma = \sum_q \int_0^1 dx_1 dx_2 \Big[f_{q/h_1}(x_1, P^2) f_{\bar{q}/h_2}(x_2, P^2) + (q \leftrightarrow \bar{q}) \Big] \sigma^{YFS}_{q\bar{q}\longrightarrow l+\bar{l}+n(\gamma),} \tag{1.6}$$

here q stands for a parton $\in \{g, d, u, s, c, b\}$, $f_{(q,\bar{q})/h}(x, P^2)$ are the parton distribution functions (PDF) of a parton q (or $\bar{q}$) in a hadron h for the Bjorken variable x and hard-process scale P^2, $\sigma^{YFS}_{q\bar{q}\longrightarrow l+\bar{l}+n(\gamma)}$ denotes the QED YFS-exponentiated total cross section for the process

$$q_1(p_1) + \bar{q}_2(p_2) \longrightarrow Z/\gamma(P) \longrightarrow l(q_1) + \bar{l}(q_2) + \gamma(k_1) + \ldots + \gamma(k_n),\ (n = 0, 1, \ldots), \tag{1.7}$$

which is also depicted diagrammatically in Fig. 1.1.
The $\mathcal{O}(\alpha)$ QED YFS-exponentiated total cross section reads

$$\sigma^{YFS}_{q\bar{q}\longrightarrow l+\bar{l}+n(\gamma)} = \sum_{n=0}^{\infty} \frac{1}{n!} \int d\tau_{n+2}(p_1 + p_2; k_1, ..., k_n)\ \rho_n^{(1)}, \tag{1.8}$$

where

$$d\tau_n(P; p_1, p_2, ..., p_n) = \prod_{j=1}^{n} \frac{d^3 p_j}{2p_j^0}\ \delta^{(4)}\left(P - \sum_{j=1}^{n} p_j \right), \tag{1.9}$$

denotes the Lorentz-invariant phase space. The total cross-section is expressed in terms of the final-state differential multiphoton distribution

$$\begin{aligned}\rho_n^{(1)}(p_1,p_2,q_1,q_2,k_1,...,k_n) = e^{Q_f^2 Y_{\Omega_F}(q_1,q_2)} \prod_{l=1}^{n} \tilde{S}_F(k_l)\, \bar{\Theta}(\Omega_F;k_l) \\ \times \left[\bar{\beta}_0^{(1)}(p_1,p_2,q_1,q_2) + \sum_{i=1}^{n} \frac{\bar{\beta}_1^{(1)}(p_1,p_2,q_1,q_2,k_i)}{\tilde{S}_F(k_i)}\right],\end{aligned} \tag{1.10}$$

where for the final-state charged leptons $Q_f^2 = 1$. The YFS soft (eikonal) factors for real photons emitted from the final-state fermions read

$$\tilde{S}_F(k_l) = -\frac{\alpha}{4\pi^2}\left(\frac{q_1}{k_l q_1} - \frac{q_2}{k_l q_2}\right)^2. \tag{1.11}$$

The YFS form factor is defined as follows

$$Y_\Omega(p_1,p_2) \equiv 2\alpha \tilde{B}(\Omega,p_1,p_2) + 2\alpha \Re B(p_1,p_2) \tag{1.12}$$

where B and $\tilde{B}$ are the virtual and real-photon infrared YFS functions, given explicitly in the next section for arbitrary four-momenta and masses of charged particles.

In Eq. (1.10), $\bar{\beta}_0^{(1)}$ and $\bar{\beta}_1^{(1)}$ are the YFS IR-finite functions, which can be calculated perturbatively from the Feynman diagrams. We present them below in the centre-of-mass (CM) frame of the incoming quarks, i.e. the rest frame of the intermediate boson, with the $+z$ axis pointing in the quark q direction.

The function $\bar{\beta}_0^{(1)}$ is given by

$$\bar{\beta}_0^{(1)}(p_1,p_2,q_1,q_2) = \bar{\beta}_0^{(0)}(p_1,p_2,q_1,q_2)\left[1 + \delta^F(q_1,q_2)\right], \tag{1.13}$$

where $\bar{\beta}_0^{(0)}$ is related to the Born-level cross section through

$$\frac{1}{2}\bar{\beta}_0^{(0)} = \frac{1}{\sqrt{\lambda(1,m_l/M,m_{\bar{l}}/M)}}\frac{d\sigma_0}{d\Omega_l} = \frac{1}{16 s_P (2\pi)^2}\frac{1}{12}\sum \left|\mathcal{M}^{(0)}\right|^2, \tag{1.14}$$

with $s_P = (p_1+p_2)^2$, $\lambda(x,y,z) = x^2+y^2+z^2-2xy-2xz-2yz$ and M is the invariant mass of the intermediate boson ($M^2 = P^2$). The factor $\frac{1}{12} = \frac{1}{4}\cdot\frac{1}{3}$ corresponds to averaging over the initial-state quark spins and colours (the colour contents has been extracted explicitly), and the sum $\sum$ runs over all the initial- and final-state spin indices. In Eq. (1.127), the correction

$$\delta^F(q_1,q_2) = \delta^F_{\rm EW}(q_1,q_2;m_\gamma) - 2\alpha \Re B(q_1,q_2;m_\gamma) \tag{1.15}$$

is the 1st order non-IR correction to the $\bar{\beta}_0$ function, where $\delta^v_{\rm EW}$ is the $\mathcal{O}(\alpha)$ EW virtual correction. In ZINHAC the EW corrections are incorporated from the SANC system. The expression for the pure QED corrections is much simpler:

$$\delta^F_{\rm QED}(q_1,q_2) = \frac{\alpha}{\pi}\left(\ln\frac{2q_1q_2}{m_l^2} - 1\right), \tag{1.16}$$

therefore they are directly implemented in ZINHAC. These corrections are also available in SANC framework, which is useful for tests of the ZINHAC to SANC interface. The function $\bar{\beta}_1^{(1)}$ is the YFS non-IR function corresponding to the single-real-hard photon radiation. It is related to differential cross sections through

$$\frac{1}{2}\bar{\beta}_1^{(1)}(p_1,p_2,q_1,q_2,k) = \frac{1}{\sqrt{\Lambda(k)}}\frac{d\sigma_1}{d\Omega_l k^0 dk^0 d\Omega_k} - \tilde{S}_F(k)\frac{1}{\sqrt{\lambda}}\frac{d\sigma_0}{d\Omega_l}, \tag{1.17}$$

where

$$\frac{d\sigma_1}{d\Omega_l k^0 dk^0 d\Omega_k} = \frac{\sqrt{\Lambda(k)}}{32 s_P\,(2\pi)^5}\frac{1}{12}\sum\left|\mathcal{M}^{(1)}_{FSR}\right|^2, \tag{1.18}$$

with

$$\sqrt{\Lambda(k)} = \frac{2\,|\vec{q}_1|^2}{|\vec{q}_1|(M-k^0) + q_1^0|\vec{k}|\cos\theta_{1k}} \tag{1.19}$$

being the phase-space factor (coming from the phase-space integration eliminating the energy-momentum conservation $\delta^{(4)}$-function for single-photon radiation), where $\theta_{1k} = \angle(\vec{q}_1,\vec{k})$; in the soft-photon limit $\Lambda(k\to 0)\to\lambda$. The sum $\sum$ in Eq. (1.18) again runs over the initial- and final-state spin indices, this time including also those of the radiative photon. Thus, we finally have

$$\bar{\beta}_1^{(1)}(p_1,p_2,q_1,q_2,k) = \frac{1}{16 s\,(2\pi)^5}\frac{1}{12}\sum\left|\mathcal{M}^{(1)}_{FSR}\right|^2 - \tilde{S}_F(k)\bar{\beta}_0^{(0)}(p_1,p_2,q_1,q_2). \tag{1.20}$$

The calculation of the matrix elements $\mathcal{M}$ will be presented in Section 1.4 and, as we will see, the spin amplitudes formalism is applied for this purpose.

This completes our description of the cross section for the process (1.7) with the $\mathcal{O}(\alpha)$ QED YFS exponentiation for the FSR. In order to compute this cross section and generate events, we have developed an appropriate MC algorithm which will be described in detail Section 1.5, but first we will present some analytical representations of the YFS infrared functions corresponding to emission of virtual and real photons, and then show the calculations of the matrix elements needed for the IR finite functions $\bar{\beta}_0^{(1)}$ and $\bar{\beta}_1^{(1)}$.

1.3 YFS infrared functions

The IR functions defined in the previous section

$$\begin{aligned} Y_\Omega(q_1,q_2) &\equiv 2\alpha\tilde{B}(\Omega,q_1,q_2)+2\alpha\Re B(q_1,q_2) \\ &\equiv -2\alpha\,\frac{1}{8\pi^2}\int\frac{d^3k}{k^0}\Theta(\Omega;k)\left(\frac{q_1}{kq_1}-\frac{q_2}{kq_2}\right)^2 \\ &\quad +2\alpha\Re\int\frac{d^4k}{k^2}\frac{i}{(2\pi)^3}\left(\frac{2q_1+k}{2kq_1+k^2}-\frac{2q_2-k}{2kq_2-k^2}\right)^2 \end{aligned} \tag{1.21}$$

have to be regularized for example by the dummy photon mass m_γ, which cancels out in their sum. The real-photon function $\tilde{B}$ depends also on the soft-photon energy cut-off. We define the IR domain Ω_F with the condition $k^0 < E_{\min} \ll \sqrt{s}$ in the rest frame of $Q = q_1 + q_2$ referred to as QMS, which means that it was integrated analytically over the photons with energies $k^0 \leq E_{min}$. The photons with energies $k^0 > E_{min}$ are generated exclusively with the help of Monte Carlo techniques. The soft cut-off E_{min} is a dummy parameter, i.e. the resulting cross section does not depend on it, which can be checked both analytically and numerically (by evaluating the cross section for different values of E_{min}). One of the advantages of exponentiation is that E_{min} can be put arbitrarily low without causing any part of the cross section to become negative – in contrast to fixed-order calculations.

An important feature of the representations of the YFS IR functions presented in Ref. [77] is that they are stable and fast in numerical evaluation. Thus, they are particularly suited for Monte Carlo implementations such as ZINHAC.

Here we just present the YFS form factor for our choice of Ω in the approximation where $m_1, m_2 \ll \sqrt{s}$:

$$\begin{aligned} Y_f(\Omega_F;q_1,q_2) &= \gamma_f \ln\frac{2E_{min}}{\sqrt{(q_1+q_2)^2}}+\frac{1}{4}\gamma_f+Q_f^2\frac{\alpha}{\pi}\left(-\frac{1}{2}+\frac{\pi^2}{3}\right), \\ \gamma_f &= 2Q_f^2\frac{\alpha}{\pi}\left(\ln\frac{2q_1q_2}{m_f^2}-1\right). \end{aligned} \tag{1.22}$$

This result, because of its simplicity, is very useful for the testing purposes as well as for definition of the so-called simplified cross-section defined in Section 1.5.2. However, in our Monte Carlo generator we used general formulation of the YFS form factor, without any approximation which has much more complicated structure, therefore presented in Appendix A.1.

1.4 Matrix elements

In this subsection we will present the calculations of tree-level matrix elements needed by IR finite functions $\bar{\beta}_0^{(1)}$ and $\bar{\beta}_1^{(1)}$, i.e the matrix elements at the Born level and $\mathcal{O}(\alpha)$ in the convention of Ref. [78]. There are several advantages of using spin amplitudes for calculation of matrix elements. Firstly, the spin amplitudes can be seen as a kind of "Lego" toy in the sense that like in this famous children game we can use some basic bricks (spinorial string functions) to build more complicated objects (tree level amplitudes). The bricks can be assembled and connected in many ways, to construct complicated tree amplitudes, moreover we can reuse those complicated structures to build even more complicated objects[6]. Secondly, the spin amplitudes are derived without the assumption of the energy-momentum conservation. Therefore, they can be used directly in evaluations of the above YFS $\bar{\beta}$-functions over the multiphoton phase space, without the need to resort to any "reduction procedure", which reduces the multiphoton phase space to the 0-photon phase space for $\bar{\beta}_0$ and the 1-photon phase space for $\bar{\beta}_1$, see e.g. [23]. On top of that, since the spin amplitudes are obtained for massive fermions, there is no need to use any phase-space slicing or subtraction methods in order to separate the mass singularities [79]. Using spin amplitudes instead of explicit analytical formulae for the squared matrix elements may also be useful for some dedicated studies, such as investigation of various Z-polarization contributions, "new physics" searches (spin amplitudes can be easily modified to include some "new physics" components like Z'), etc. And, which is important in practice, the numerical evaluation of the matrix elements based on the above spin amplitudes is fast in terms of CPU time.

The section is organized as follows. First we introduce the basic blocks of the spin amplitudes in the framework of Ref. [78], i.e. the spinorial string function $S(p_i, a_1, \ldots, a_n, p_j)^{\alpha}_{\lambda_i,\lambda_j}$, then we use them to construct the amplitude for the Drell–Yan process at the Born and $\mathcal{O}(\alpha)$ QED level. For calculation of the latter we will reuse the result of the structure constructed for the spin amplitudes at the Born level.

[6] We will see later in this section how we will reuse the Born–level building blocks to construct the $\mathcal{O}(\alpha)$ matrix elements.

1.4.1 Basic blocks – spinorial string functions

In the approach of Hagiwara–Zeppenfeld [78], a generic four-spinor ψ_i for a fermion or anti-fermion with momentum p and helicity λ,

$$\psi_i = u(p_i, \lambda_i) \text{ or } \psi_i = v(p_i, \lambda_i)^{7} \tag{1.23}$$

is expressed in terms of the 2-component Weyl spinors, $(\psi_i)_\pm$:

$$\psi_i = \begin{bmatrix} (\psi_i)_- \\ (\psi_i)_+ \end{bmatrix}, \qquad \bar{\psi}_i = \left[(\psi_i)_+^\dagger, (\psi_i)_-^\dagger \right] . \tag{1.24}$$

As a basis for free spinors the helicity eigenstates $\chi_\pm(p)$ are used:

$$\frac{\vec{\sigma}\cdot\vec{p}}{|\vec{p}|}\chi_\lambda(p) = \lambda\chi_\lambda(p), \tag{1.25}$$

where $\vec{\sigma}$ is the "vector" of Pauli matrices in the standard basis (see Appendix A.2). The free spinors in this basis read,

$$u(p,\lambda)_\pm = \omega_{\pm\lambda}(p)\chi_\lambda(p), \qquad v(p,\lambda)_\pm = \pm\lambda\omega_{\mp\lambda}(p)\chi_{-\lambda}(p), \tag{1.26}$$

where

$$\omega_\pm(p) = (E \pm |\vec{p}|)^{1/2}. \tag{1.27}$$

For an arbitrary momentum $p^\mu = (E, \vec{p}) = (E, p_x, p_y, p_z)$ with $|\vec{p}| + p_z \neq 0$ we have:

$$\chi_+(p) = \left[2\ |\vec{p}|(|\vec{p}| + p_z)\right]^{-\frac{1}{2}} \begin{pmatrix} |\vec{p}| + p_z \\ p_x + ip_y \end{pmatrix}, \tag{1.28}$$

$$\chi_-(p) = \left[2\ |\vec{p}|(|\vec{p}| + p_z)\right]^{-\frac{1}{2}} \begin{pmatrix} -p_x + ip_y \\ |\vec{p}| + p_z \end{pmatrix}. \tag{1.29}$$

In the case when $|\vec{p}| = p_z$ we use the convention:

$$\chi_+ = \begin{pmatrix} 0 \\ 1 \end{pmatrix}, \qquad \chi_- = \begin{pmatrix} -1 \\ 0 \end{pmatrix}. \tag{1.30}$$

The free spinors satisfy the Dirac equation of motion ($p^2 = m^2$):

$$\not{p}_\pm u(p,\lambda)_\pm = mu(p,\lambda)_\mp, \qquad \not{p}_\pm v(p,\lambda)_\pm = -mv(p,\lambda)_\mp, \tag{1.31}$$

[7] See Appendix A.3 for details on our convention.

and are normalised as:

$$\bar{u}(p,\lambda)u(p,\lambda) = 2m, \qquad \bar{v}(p,\lambda)v(p,\lambda) = -2m, \tag{1.32}$$

which fixes our convention for the spinors.

In general, an arbitrary tree amplitude with external fermions can be expressed as a "fermion spinorial string":

$$\bar{\psi}_1 P_{-\alpha} \not{a}_1 \not{a}_2 \dots \not{a}_n \psi_2 \tag{1.33}$$

where

$$P_\pm = \frac{1}{2}(1 \pm \gamma_5), \tag{1.34}$$

and

$$\not{a} = a_\mu \gamma^\mu = \begin{bmatrix} 0 & (\not{a})_+ \\ (\not{a})_- & 0 \end{bmatrix}. \tag{1.35}$$

Above we use the chiral (Weyl) representation of γ matrices (see Appendix A.2 for details) and $a^\mu = (a^0, a^1, a^2, a^3)$ denotes the four-vector in the Minkowski space. The $a_\pm$ are 2×2 c-number matrices

$$(\not{a})_\pm = a_\mu \sigma^\mu_\pm = \begin{bmatrix} a^0 \mp a^3 & \mp(a^1 - ia^2) \\ \mp(a^1 + ia^2) & a^0 \pm a^3 \end{bmatrix}. \tag{1.36}$$

The block structure of $\not{a}$ allows us to rewrite the "fermion spinorial string" eq. (1.33) in terms of the 2-dimentional Weyl spinors

$$\bar{\psi}_1 P_{-\alpha} \not{a}_1 \not{a}_2 \dots \not{a}_n \psi_2 = (\psi_1)^\dagger_\alpha [a_1, a_2, \dots, a_n]^\alpha (\psi_2)_{-\delta_n \alpha}. \tag{1.37}$$

The internal part of the above string function

$$[a_1, a_2, \dots, a_n]^\alpha = (\not{a}_1)_\alpha (\not{a}_2)_{-\alpha} \dots (\not{a}_n)_{(-1)^{n+1}\alpha}, \tag{1.38}$$

is the product of 2×2 c-number matrices. Now pluging (1.37) into (1.26) we get final expression for the "fermion spinorial string":

$$(\psi_i)^\dagger_\alpha [a_1, a_2, \dots, a_n]^\alpha (\psi_j)_\beta = C_i C_j \omega_{\alpha\lambda_i}(p_i) \omega_{\beta\lambda_j}(p_j) S(p_i, a_1, \dots, a_n, p_j)^\alpha_{\lambda_i,\lambda_j}, \tag{1.39}$$

where the constants C_i and C_j are determined by (1.26):

$$C_k = \begin{cases} 1 & \text{for } (\psi_i)_\alpha = u(p_k, \lambda_k)_\alpha, \\ -\lambda_k \alpha & \text{for } (\psi_i)_\alpha = v(p_k, -\lambda_k)_\alpha. \end{cases} \tag{1.40}$$

Finally, the basic brick of the method – the spinorial string function reads

$$S(p_i, a_1, \ldots, a_n, p_j)^{\alpha}_{\lambda_i,\lambda_j} = \chi^{\dagger}_{\lambda_i}(p_i)[a_1, \ldots, a_n]^{\alpha}\chi_{\lambda_j}(p_j). \tag{1.41}$$

As was advertised, the spinorial function S can be easily evaluated numerically for arbitrary n. One can for example compute a product of internal 2×2 matrices $(\not{a}_i)_\alpha$, and then multiply the resulting matrix by the external 2-dimensional c-number vectors χ. However, a better and more efficient metod is, instead of matrix-by-matrix multiplication, to perform recursively matrix-by-vector multiplication. In our computation of the function S, we start from multiplying the left-hand-side vector $\chi^{\dagger}$ by the matrix $(\not{a}_1)_\alpha$, and continue by multiplying the resulting vectors by the consecutive matrices $(\not{a}_i)_\alpha$ until we reach the last matrix, $(\not{a}_n)_\alpha$. The computation is completed by performing the scalar product of the final vector of the above multiplication with the right-hand-side vector χ.

Three polarization vectors of a massive vector-boson with four-momentum $k = (k^0, \vec{k}) = (k^0, k^1, k^2, k^3)$ and the mass m are, in the Cartesian basis, given by

$$\begin{aligned}
\epsilon^{\mu}(k, \lambda = 1) &= \frac{1}{|\vec{k}|k_T}\left(0, k^1k^3, k^2k^3, -k_T^2\right), \\
\epsilon^{\mu}(k, \lambda = 2) &= \frac{1}{k_T}\left(0, -k^2, k^1, 0\right), \\
\epsilon^{\mu}(k, \lambda = 3) &= \frac{k^0}{m|\vec{k}|}\left(\frac{|\vec{k}|^2}{k^0}, k^1, k^2, k^3\right),
\end{aligned} \tag{1.42}$$

where $k_T = \sqrt{(k^1)^2 + (k^2)^2}$ is the transverse momentum. For massless vector bosons, such as photons, $\epsilon^{\mu}(\lambda = 3) = 0$, i.e. there are only two non-zero polarizations $\epsilon^{\mu}(\lambda = 1)$ and $\epsilon^{\mu}(\lambda = 2)$. Helicity eigenstates can be obtained from the above polarization vectors through

$$\begin{aligned}
\epsilon_{hel}(k, \lambda = \pm) &= \frac{1}{\sqrt{2}}\left[\mp\epsilon(k, \lambda = 1) - i\epsilon(k, \lambda = 2)\right], \\
\epsilon_{hel}(k, \lambda = 0) &= \epsilon(k, \lambda = 3),
\end{aligned} \tag{1.43}$$

which ends this subsection and we can move to the calculation of matrix elements.

1.4.2 Born level

As is shown in the Fig. 1.2 the Born-level matrix element for the Z or γ^* boson[8] in the Drell–Yan process is given by the coherent sum of the single Z or γ^*

[8] In this section we will always use B to denote Z or γ^* boson.

production and decay spin amplitudes over the boson polarizations multiplied its propagator. In general for a given boson B, where $B = \gamma^*, Z$ the Born-level

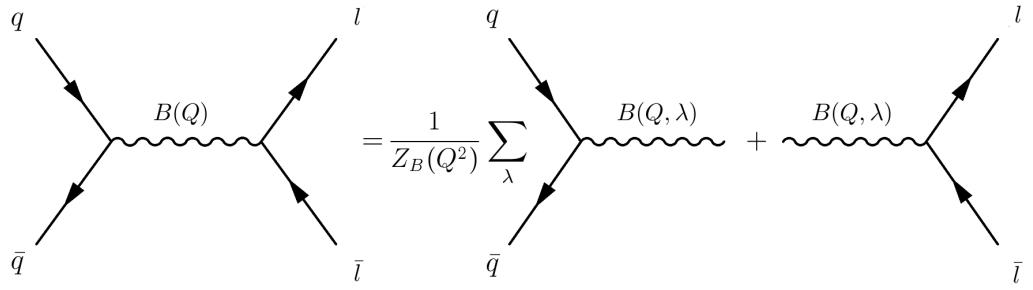

Figure 1.2: Born level feynman diagram for Z or γ^*, denoted by B, as the intermediate boson in the Drell–Yan process.

matrix element reads:

$$\mathcal{M}^{(0)B}(\sigma_1, \sigma_2; \tau_1, \tau_2) = \frac{1}{Z_B(Q^2)} \sum_{\lambda} \mathcal{M}_P^{(0)B}(\tau_1, \tau_2; \lambda) \mathcal{M}_D^{(0)B}(\lambda; \sigma_1, \sigma_2). \quad (1.44)$$

where the inverse of the boson propagator $Z_B(Q^2)$ in case of photon is equal to

$$Z_\gamma(Q^2) = Q^2, \quad (1.45)$$

while in the case of Z boson the Breit–Wigner function corresponds to the Z propagator, therefore

$$Z_Z(Q^2) = Q^2 - M_Z^2 + i\gamma_Z(Q^2) \quad (1.46)$$

and

$$\gamma_Z(Q^2) = \begin{cases} M_Z\Gamma_Z : & \text{in the fixed-width scheme,} \\ Q^2\Gamma_Z/M_Z : & \text{in the running-width scheme.} \end{cases} \quad (1.47)$$

here M_Z and Γ_Z are the mass and width of the Z boson.

It is worth to mention that in the analogical way one can construct the tree-level spin amplitude for an arbitrary complicated process with external fermions and vector bosons, for example for the process

$$e^+ + e^- \longrightarrow l^+ + l^- \longrightarrow (\nu_L f_1 \bar{f}_2)(\bar{\nu_L} f_3 \bar{f}_4). \quad (1.48)$$

which is depicted in Fig. 1.3 where $k's$, $q's$, $p's$ and $\kappa's$, $\sigma's$ $\lambda's$ denote, respectively the four-momenta and helicities of the fermions. For a given heavy

lepton helicities σ_1 and σ_2, the amplitude of the full process can be written as a product of three amplitudes $\mathcal{M}_i$, $(i = 1, 2, 3)$, where $\mathcal{M}_1$ describes the production of the $l\bar{l}$–pair, while $\mathcal{M}_2$ and $\mathcal{M}_3$ are the decay amplitudes of $l\bar{l}$. We can hence write the amplitude of the full process as

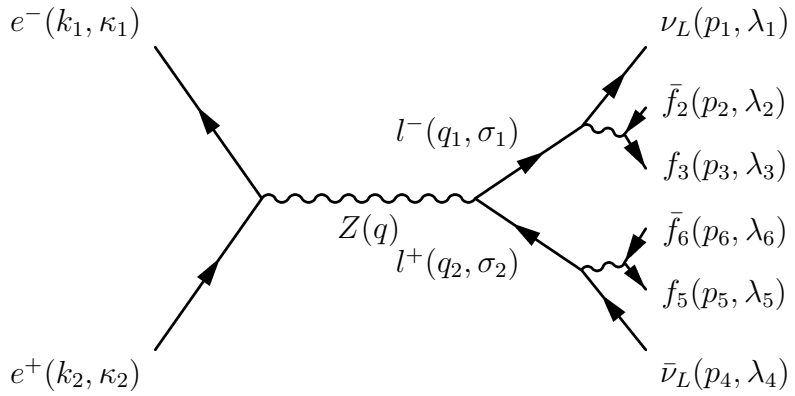

Figure 1.3: Example of the more complicated tree-level amplitude.

$$\mathcal{M}(\kappa_1, \kappa_2, \lambda_1, \lambda_2, \lambda_3, \lambda_4.\lambda_5\lambda_6) = \frac{1}{Z_l(q_1^2)} \frac{1}{Z_{\bar{l}}(q_2^2)} \times \sum_{\sigma_1, \sigma_2} \mathcal{M}_1(\kappa_1, \kappa_2, \sigma_1, \sigma_2) \mathcal{M}_2(\sigma_1, \lambda_1, \lambda_2, \lambda_3) \mathcal{M}_3(\sigma_2, \lambda_4, \lambda_5, \lambda_6). \tag{1.49}$$

The amplitudes $\mathcal{M}_i$, $i = 1, 2, 3$, have identical structure but different quantum numbers (which can be translated into "Lego" language as a three the same "Lego" blocks with different colours). Therefore, in order to calculate this spin amplitude it is enough to know the amplitude for much simpler process depicted on the left–hand side of Fig. 1.2.

(a) Born-level Z-boson decay

The Feynman diagram for the Born-level Z or γ^* (denoted by B) decay:

$$B(Q, \lambda) \longrightarrow l(q_1, \tau_1) + \bar{l}(q_2, \tau_2), \tag{1.50}$$

where (p_i, τ_i) are four-vector and helicity of the fermion/antifermion, (Q, λ) denotes the four-vector and polarisation of the boson B, is shown diagrammatically in Fig. 1.2 (the second diagram on the right–hand side of the equation in the figure). Using the Feynman rules from Appendix A.3, the matrix element for this process can be expressed as fallows

$$\mathcal{M}_D^{(0)B}(\lambda; \tau_1, \tau_2) = -ie\epsilon_\mu(Q, \lambda)\bar{u}(q_1, \tau_1)\gamma^\mu \left\{ c_L^{Bl\bar{l}} \frac{1 - \gamma_5}{2} + c_R^{Zl\bar{l}} \frac{1 + \gamma_5}{2} \right\} v(q_2, \tau_2). \tag{1.51}$$

Making use of definitions from Section 1.4.2 and information from Appendix A.15), we can evaluate this expression and write it in terms of the spinorial string functions:

$$\begin{aligned}\mathcal{M}_D^{(0)B}(\lambda;\tau_1,\tau_2) = ie\Big[&c_L^{Bl\bar{l}}\omega_{-\tau_1}(q_1)\tau_2\omega_{\tau_2}(q_2)S\big(q_1,\epsilon_B(Q,\lambda),q_2\big)^-_{\tau_1,-\tau_2} - \\ &- c_R^{Bl\bar{l}}\omega_{\tau_1}(q_1)\tau_2\omega_{-\tau_2}(q_2)S\big(q_1,\epsilon_B(Q,\lambda),q_2\big)^+_{\tau_1,-\tau_2}\Big],\end{aligned} \tag{1.52}$$

with $B=\gamma,Z$ which means that this expression is valid both for the Z-boson and the photon as a decaying particles.

(b) Born-level Z-boson production

The spin amplitude for single-Z or γ^* production in fermion–antifermion collisions

$$q(p_1,\sigma_1)+\bar{q}(p_2,\sigma_2)\longrightarrow B(Q,\lambda), \tag{1.53}$$

shown diagrammatically in Fig. 1.2 (the first diagram on the right–hand side of the equation in the figure), is given by

$$\begin{aligned}\mathcal{M}_P^{(0)B}(\sigma_1,\sigma_2;\lambda) = ie\times\Big[&c_L^{Bq\bar{q}}\omega_{-\sigma_1}(p_1)\sigma_2\omega_{\sigma_2}(p_2)S(p_2,\epsilon_B^*(Q,\lambda),p_1)^-_{-\sigma_2,\sigma_1} \\ &- c_R^{Bq\bar{q}}\omega_{\sigma_1}(p_1)\sigma_2\omega_{-\sigma_2}(p_2)S(p_1,\epsilon_B^*(Q,\lambda),p_2)^+_{-\sigma_2,\sigma_1}\Big].\end{aligned} \tag{1.54}$$

Details on the calculation of above spin amplitudes as well as the ones of the order $\mathcal{O}(\alpha)$ presented later in this section are demonstrated in the Appendix (A.4.1), here we just restrict ourself to the final results.

The above spin amplitudes can be easily translated from the vector-boson Cartesian basis into the helicity basis, using the following transformations:

$$\begin{aligned}\mathcal{M}_{hel}(\lambda=\pm) &= \frac{1}{\sqrt{2}}\left[\mp\mathcal{M}(\lambda=1)-i\mathcal{M}(\lambda=2)\right], \\ \mathcal{M}_{hel}(\lambda=0) &= \mathcal{M}(\lambda=3).\end{aligned} \tag{1.55}$$

for decay amplitudes. For production amplitudes one should replace in the first line of the above equation $i\to -i$ (due to ϵ_B^*).

Pluging Eq. (1.54) and Eq. (1.52) in to formulae (1.44) we can easily calculate the matrix element at the Born Level for the Drell–Yan process for a given intermediate bosons γ and Z. The full matrix element for the neutral current Drell–Yan proces at the Born level is a sum of those two matrix elements:

$$\mathcal{M}^{(0)\gamma+Z}(\sigma_1,\sigma_2;\tau_1,\tau_2) = \mathcal{M}^{(0)\gamma}(\sigma_1,\sigma_2;\tau_1,\tau_2)+\mathcal{M}^{(0)Z}(\sigma_1,\sigma_2;\tau_1,\tau_2) \tag{1.56}$$

1.4.3 Real hard-photon radiation

In this subsection we present the scattering amplitudes for single hard-photon radiation in leptonic B boson (Z or γ^*) decays

$$q(p_1,\sigma_1)+\bar{q}(p_2,\sigma_2)\longrightarrow B(Q,\lambda)\longrightarrow l(q_1,\tau_1)+\bar{l}(q_2,\tau_2)+\gamma(k,\kappa) \tag{1.57}$$

and productions

$$q(p_1,\sigma_1)+\bar{q}(p_2,\sigma_2)+\gamma(k,\kappa)\longrightarrow B(Q,\lambda)\longrightarrow l(q_1,\tau_1)+\bar{l}(q_2,\tau_2), \tag{1.58}$$

using the spin-amplitude formalism and the notation introduced in the previous subsections.

(a) Single hard-photon radiation in leptonic Z-boson decays

For calculations of the matrix element for the single hard-photon radiation in leptonic B boson decays (Eq. 1.57) we will take advantage of the "Lego" feature of spin amplitudes. Therefore, in order to obtain the spin amplitude for this process we will replace in Eq. (1.44) a "brick" $M_D^{(0)B}$ by the new one $M_D^{(1)B}$ which denotes the spin amplitude for the single hard-photon radiation in leptonic B (Z or γ) boson decays

$$B(Q,\lambda)\longrightarrow l(q_1,\tau_1)+\bar{l}(q_2,\tau_2)+\gamma(k,\kappa), \tag{1.59}$$

thus, we have

$$\mathcal{M}_{FSR}^{(1)B}(\sigma_1,\sigma_2;\tau_1,\tau_2,\kappa)=\frac{1}{Z_B(Q^2)}\sum_{\lambda}\mathcal{M}_P^{(0)B}(\sigma_1,\sigma_2;\lambda)\mathcal{M}_D^{(1)B}(\lambda;\tau_1,\tau_2,\kappa). \tag{1.60}$$

The missing element – the spin amplitude $M_D^{B(1)}$ can be obtained from the Feynman diagrams given in Fig. 1.4.

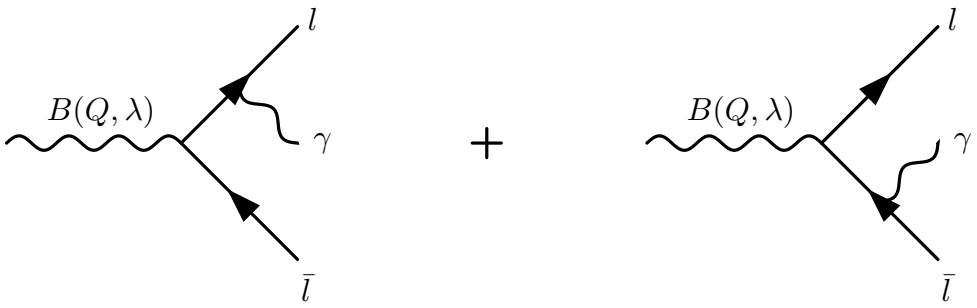

Figure 1.4: The Feynman diagrams for, denoted by B in this figure, Z-boson or γ^* decay including single real-photon radiation.

This spin amplitude reads

$$
\begin{aligned}
M_D^{B(1)}(\lambda;\tau_1,\tau_2,\kappa) = {} & \frac{-ie^2Q_l}{2} \\
& \Bigg[c_L^{Bl\bar{l}}\omega_{-\tau_1}(q_1)\tau_2\omega_{\tau_2}(q_2)\Bigg\{\left(\frac{2q_2\cdot\varepsilon^*}{q_2\cdot k}-\frac{2q_1\cdot\varepsilon^*}{q_1\cdot k}\right)S(q_1,\varepsilon_Z,q_2)^-_{\tau_1,-\tau_2}+ \\
& \quad +\frac{1}{q_2\cdot k}S(q_1,\varepsilon_Z,k,\varepsilon^*,q_2)^-_{\tau_1,-\tau_2}-\frac{1}{q_1\cdot k}S\big(q_1,\varepsilon^*,k,\varepsilon_Z,q_2\big)^-_{\tau_1,-\tau_2}\Bigg\}- \\
& - c_R^{Bl\bar{l}}\omega_{\tau_1}(q_1)\tau_2\omega_{-\tau_2}(q_2)\Bigg\{\left(\frac{2q_2\cdot\varepsilon^*}{q_2\cdot k}-\frac{2q_1\cdot\varepsilon^*}{q_1\cdot k}\right)S(q_1,\varepsilon_Z,q_2)^+_{\tau_1,-\tau_2} \\
& \quad +\frac{1}{q_2\cdot k}S(q_1,\varepsilon_Z,k,\varepsilon^*,q_2)^+_{\tau_1,-\tau_2}-\frac{1}{q_1\cdot k}S\big(q_1,\varepsilon^*,k,\varepsilon_Z,q_2\big)^+_{\tau_1,-\tau_2}\Bigg\}\Bigg].
\end{aligned}
\tag{1.61}
$$

See Appendix A.4.2 for details. The full matrix element for the neutral current Drell–Yan process with the final state single photon radiation is a sum of the matrix element for Z-boson and γ^* obtained from Eq. (1.60):

$$
\mathcal{M}_{FSR}^{(1)\gamma+Z}(\sigma_1,\sigma_2;\tau_1,\tau_2,\kappa) = \mathcal{M}_{FSR}^{(1)\gamma}(\sigma_1,\sigma_2;\tau_1,\tau_2,\kappa) + \mathcal{M}_{FSR}^{(1)Z}(\sigma_1,\sigma_2;\tau_1,\tau_2,\kappa)
\tag{1.62}
$$

(b) Single hard-photon radiation in quarkonic Z boson production

The spin amplitude for the process of single hard-photon radiation in Z-boson or γ^* production (see Eq. (1.58)) will be needed in order to introduce into our calculations the "initial-final" interference effects, therefore it will also be presented here. This calculation is very similar to the one performed in the previous subsection, but this time we will replace in Eq. (1.44) the "brick"

$M_P^{B(0)}$ by the $M_P^{B(1)}$ which denotes the spin amplitude for the single hard-photon radiation in leptonic Z boson production

$$q(p_1,\sigma_1)+\bar{q}(p_2,\sigma_2)+\gamma(k,\kappa)\longrightarrow B(Q,\lambda) \tag{1.63}$$

thus we have

$$\mathcal{M}_{ISR}^{(1)B}(\sigma_1,\sigma_2;\tau_1,\tau_2,\kappa)=\frac{1}{Z_B(Q^2)}\sum_{\lambda}\mathcal{M}_P^{(1)B}(\sigma_1,\sigma_2;\lambda,\kappa)\mathcal{M}_D^{(0)B}(\lambda;\tau_1,\tau_2). \tag{1.64}$$

The spin amplitude $M_D^{B(1)}$ can be obtained from the Feynman diagrams given in Fig. 1.5. This spin amplitude reads

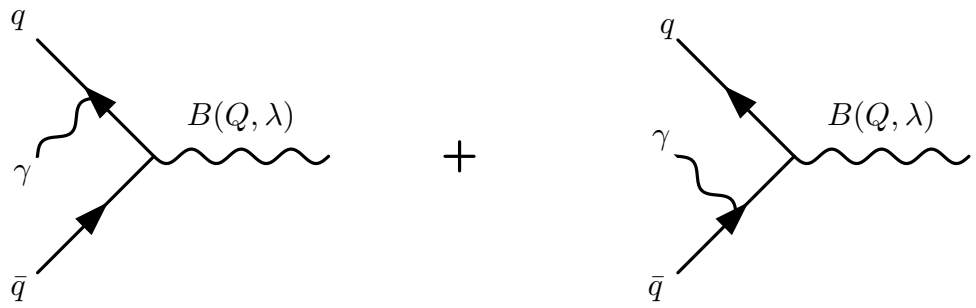

Figure 1.5: The Feynman diagrams for Z-boson or γ^* production including single real-photon radiation.

$$\begin{aligned}\mathcal{M}_P^{(1)B}=&\frac{-ie^2Q_q}{2}\\&\Bigg\{c_L^{Bq\bar{q}}\sigma_2\omega_{\sigma_2}(p_2)\omega_{-\sigma_1}(p_1)\Bigg[\left(\frac{2p_2\epsilon^*}{p_2\cdot k}-\frac{2p_1\epsilon^*}{p_1\cdot k}\right)S(p_2,\epsilon_Z^*,p_1)^-_{-\sigma_2,\sigma_1}-\\&-\frac{1}{p_2\cdot k}S(p_2,\epsilon^*,k,\epsilon_Z^*,p_1)^-_{-\sigma_2,\sigma_1}+\frac{1}{p_1\cdot k}S(p_2,\epsilon_Z^*,k,\epsilon^*,p_1)^-_{-\sigma_2,\sigma_1}\Bigg]-\\&-c_R^{Bq\bar{q}}(\sigma_2)\omega_{-\sigma_2}(p_2)]\omega_{\sigma_1}(p_1)\Bigg[\left(\frac{2p_2\epsilon^*}{p_2\cdot k}-\frac{2p_1\epsilon^*}{p_1\cdot k}\right)S(p_2,\epsilon_Z^*,p_1)^+_{-\sigma_2,\sigma_1}-\\&-S(p_2,\epsilon^*,k,\epsilon_Z^*,p_1)^+_{-\sigma_2,\sigma_1}+S(p_2,\epsilon_Z^*,k,\epsilon^*,p_1)^+_{-\sigma_2,\sigma_1}\Bigg]\Bigg\}.\end{aligned} \tag{1.65}$$

The full matrix element for the neutral current Drell–Yan process with the initial state single photon radiation is a sum of the matrix element for Z-boson and γ^* obtained from Eq. (1.64):

$$\mathcal{M}_{ISR}^{(1)\gamma+Z}(\sigma_1,\sigma_2;\tau_1,\tau_2,\kappa)=\mathcal{M}_{ISR}^{(1)\gamma}(\sigma_1,\sigma_2;\tau_1,\tau_2,\kappa)+\mathcal{M}_{ISR}^{(1)Z}(\sigma_1,\sigma_2;\tau_1,\tau_2,\kappa) \tag{1.66}$$

We have performed two tests on these calculations. First, we have checked analytically and numerically that these amplitudes are QED gauge invariant which means that

$$\mathcal{M}^{(1)B}(\varepsilon_\gamma \to k) = 0. \tag{1.67}$$

By substituding in Eq. (1.65) for the photon's four-momentum k the ε_γ we see that the expressions in round brackets becomes equal to 0 and what is left are terms which consist the spinoral string functions of the type $S(\ldots, k, k, \ldots)$. They are equal to zero, because from the spinoral string function definition Eq. (1.41) we have

$$\begin{aligned} S\big(q_1, \ldots, k, k, \ldots, q_2\big)^{\alpha}_{\tau_1,\tau_2} =& \chi(q_1,\tau_1)^\dagger [q_1, \ldots, k, k, \ldots, q_2]^\alpha \chi(q_2,\tau_2) = \\ =& \chi(q_1,\tau_1)^\dagger (\not{q}_1)_\alpha \ldots (\not{k})_\pm (\not{k})_\mp \ldots (\not{q}_2)_{-\delta_n\alpha} \chi(q_2,\tau_2) = 0, \end{aligned} \tag{1.68}$$

where in the last line we have used masslessnees of the photon, $k^2 = 0$, in the following way:

$$\mathbb{1}\cdot 0 = \mathbb{1}\cdot k^2 = \mathbb{1}\cdot \not{k}\not{k} = \begin{pmatrix} 0 & \not{k}_+ \\ \not{k}_- & 0 \end{pmatrix} \begin{pmatrix} 0 & \not{k}_+ \\ \not{k}_- & 0 \end{pmatrix} = \begin{pmatrix} \not{k}_+\not{k}_- & 0 \\ 0 & \not{k}_-\not{k}_+ \end{pmatrix}, \tag{1.69}$$

which means that $(\not{k})_\pm(\not{k})_\mp = 0$. This is also true for the matrix element for single hard-photon radiation in leptonic Z-boson decays Eq. (1.61). The numerical check has also shown that after the replacement $\varepsilon_\gamma \to k$, the values of the spin amplitudes are consistent with zero within the double-precision accuracy.

The second test is the so-called soft-photon limit, which means

$$\lim_{k\to 0} \mathcal{M}^{(1)B} \backsim \varepsilon^*_\mu \left(\frac{q_1^\mu}{q_1\cdot k} - \frac{q_2^\mu}{q_2\cdot k} \right) \mathcal{M}_D^{(0)B}. \tag{1.70}$$

By taking the soft-photon limit for the amplitude for single hard-photon radiation in leptonic Z-boson decays, Eq. (1.61), we see that all terms with the spinoral string function S containing photon's four-momenta disappear. This follows directly from the spinoral string function definition, see Eq. (1.41). What is left can be rewritten in the following way:

$$\lim_{k\to 0}\mathcal{M}_D^{(1)B} = ie^2\sum_{B=Z,\gamma}\left(\frac{q_1\cdot\varepsilon^*}{q_1\cdot k}-\frac{q_2\cdot\varepsilon^*}{q_2\cdot k}\right)$$
$$\times\left[c_L^B\omega_{-\tau_1}(q_1)\tau_2\omega_{\tau_2}(q_2)S(q_1,\varepsilon^*,q_2)^-_{\tau_1,-\tau_2}-c_R^B\omega_{\tau_1}(q_1)\tau_2\omega_{-\tau_2}(q_2)S(q_1,\varepsilon_Z,q_2)^+_{\tau_1,-\tau_2}\right]$$
$$=-ie^2\left(\frac{q_1\cdot\varepsilon^*}{q_1\cdot k}-\frac{q_2\cdot\varepsilon^*}{q_2\cdot k}\right)\mathcal{M}_D^{(0)B}$$
$$\sim\varepsilon^*_\mu\left(\frac{q_1^\mu}{q_1\cdot k}-\frac{q_2^\mu}{q_2\cdot k}\right)\mathcal{M}_D^{(0)B}, \tag{1.71}$$

which ends the proof. The soft-photon limit test has also been preformed, in a very similar way, in the case of the single hard-photon radiation in quarkonic Z-boson production. The numerical soft-photon limit tests have also given satisfactory results.

1.5 Monte Carlo algorithm

Having all ingredients in the place, we are now ready to construct a Monte Carlo algorithm for the generation of multiphoton radiation in the final state for the Drell–Yan process according to eq. (1.8). Our algorithm is constructed using elementary techniques of weighting, multibranching[9] and, wherever it is gainful, mapping (change of integration variables). More details about those methods can be found for example in Ref. [80]. The procedure of constructing our Monte Carlo algorithm has two stages. In the first stage, called *"phase-space reorganization"*, we will transform the original integrand of eq. (1.8) without any approximations to the form which is the most convenient for the MC generation. In the second stage, called *"simplification of the distribution"*, we simplify step-by-step this transformed but still very difficult integrand, such that at the end we obtain a simple distribution, which we can integrate analytically over certain integration variables and generate those variables easily with the help of the standard uniform random numbers[10]. For each such a simplification s, we introduce a correction weight w_s. Therefore the events generated with the simplified distribution have to be corrected by the total weight

$$w^{\text{tot}} = w_1 w_2 ... w_{n-1} w_n, \tag{1.72}$$

[9] We used the multibranching technique when it was unavoidable for example for the generation of the photons kinematics (i.e. $\cos\theta_j$, see Eq. (1.112)).

[10] The remaining small subset of variables for which we are not able to perform the manual/analytical integration/mapping is treated with the help of the self-adapting cellular Monte Carlo sampler Foam [81].

where n is the total number of modifications introduced in order to obtain the simplified distribution from the original one. The integrated original cross section can be numerically calculated using the average weights from the Monte Carlo run

$$\sigma^{\text{exact}} = \langle W^{\text{tot}} \rangle \, \sigma^{\text{simple}} \tag{1.73}$$

and may be obtained with an arbitrary precision, simply by increasing the number of generated events.

ZINHAC is in fact more than just the phase-space integrator, because we can require that events are generated with total weight equal to 1, which means that they can be directly used in a detector simulation programs such as [82,83, 84, 85] and compared with experimental data. It is quite a strong restriction on the MC algorithm and it means that our MC program is not merely a phase-space integrator, but the full-scale MC event generator (MCEG).

1.5.1 Phase-space reorganization

The total cross section at the parton level (see eq. (1.8)) in the PMS frame (the rest frame of $P = p_1 + p_2$) reads

$$\begin{aligned} \sigma^{YFS}_{q\bar{q}\to l+\bar{l}+n(\gamma)} = & \int d\tau_{n+2}(P; k_1, \ldots, k_n, q_1, q_2) e^{Q_f^2 Y_{\Omega_F}(q_1,q_2)} \\ & \prod_{l=1}^{n} \tilde{S}_F(k_l) \; \bar{\Theta}(\Omega_F; k_l) \bar{\beta}^{(1)}_{0+1}(p_1, p_2, q_1, q_2, k_l), \end{aligned} \tag{1.74}$$

where

$$\begin{aligned} \bar{\beta}^{(1)}_{0+1} &= \bar{\beta}^{(1)}_{0+1}(p_1, p_2, q_1, q_2, k_1, ..., k_l) \\ &\equiv \bar{\beta}^{(0)}_0(p_1, p_2, q_1, q_2) + \sum_{l=1}^{n} \frac{\bar{\beta}^{(1)}_1(p_1, p_2, q_1, q_2, k_l)}{\tilde{S}_F(k_l)}. \end{aligned} \tag{1.75}$$

Unfortunately, the straightforward Monte Carlo generation of photons momenta from this distribution is impossible. The reason for that is simply that we do not know the four-momenta of the final leptons q_1 and q_2 before photons momenta are generated and both q_1 and q_2 are inside of the integral in both $d\tau_{n+2}(P; k_1, \ldots, k_n, q_1, q_2)$ and $\tilde{S}_f(k_l)$ factors, therefore they are necessary in order to generate photons momenta. So it is a *"catch-22"* situation and we are stuck. Fortunately, the total cross-section from eq. (1.74) is Lorentz–invariant and, in principle, can be evaluated in any reference frame. Therefore we can

take advantage of the reference frame "attached" to the q_1 and q_2, i.e. "co-moving" with them, that is in the frame where $\overrightarrow{Q} = \overrightarrow{q_1}+\overrightarrow{q_2} = 0$[11] (QMS frame). In the QMS reference frame the integration over final leptons four-momenta vanishes and this is actually the reason why we will simulate emissions in the rest frame of the charged dipol. However, the problem is still there because we cannot make a transformation from PMS to QMS frame simply because, as before, we do not know $Q = P - \sum_i k_i$, and we have to know photons four–momenta k_i in the first place. So we have made a step forward but in some sense we have just moved the problem from one place to the another. The final solution to this problem is to reparametrize the integral with the help of the integration over the Lorentz group, like it was showed in detail in Refs. [86,87]. Here we just apply the result of this work and obtain the new formula:

$$\begin{aligned}\sigma^{YFS}_{q\bar{q}\to l+\bar{l}+n(\gamma)} = & \int d\psi d\cos\omega \sum_{n=0}^{\infty}\frac{1}{n!}\int ds_Q \prod_{l=1}^{n}\frac{d^3\tilde{k}_l}{2\tilde{k}_l^0}\,\frac{s_Q}{s_P}\,\frac{\beta_f}{2} \\ & \tilde{S}_f(\tilde{k}_l)\bar{\Theta}_f(\tilde{k}_l)\;\delta\left(s_P - \left[\tilde{Q}+\sum_{j=0}^{n}\tilde{k}_j\right]^2\right)\;\tilde{\beta}^{(1)}_{0+1}\;e^{Y_{\tilde{\Omega}_F}(\tilde{q}_1,\tilde{q}_2)},\end{aligned} \tag{1.76}$$

where

$$\tilde{Q}\equiv(\sqrt{s_Q},0,0,0),\quad \tilde{q}_1\equiv\frac{\sqrt{s_Q}}{2}(1,0,0,\beta_f),\quad \tilde{q}_2\equiv\frac{\sqrt{s_Q}}{2}(1,0,0,-\beta_f), \tag{1.77}$$

here $P = p_1+p_2$, $s_P = P^2$, $s_Q = (q_1+q_2)^2 = 2q_1q_2+2m_f^2$, $\beta_f = \sqrt{(1-4m_f^2/s_Q)}$. All variables with a tilde are defined in the QMS frame. The explicit transformation from QMS to PMS defines the meaning of the new ψ, ω integration variables:

$$q_i = L_A\tilde{q}_i, \tag{1.78}$$

where $L_A = R_3(\psi)R_2(\omega)B^{-1}_{\tilde{P}}$ is the Lorentz transformation consisting of the z and y rotations $R_3(\psi)R_2(\omega)$ and the parallel boost along $\tilde{P}$ denoted by $B^{-1}_{\tilde{P}}$,where $\tilde{P}$ is defined in the rest frame of the outgoing fermions. The corresponding transformation matrix is

$$B_{\tilde{P}} = \begin{bmatrix} \frac{\tilde{P}^0}{M_{\tilde{P}}}, & \frac{\vec{\tilde{P}}^T}{M_{\tilde{P}}} \\ \\ \frac{\vec{\tilde{P}}}{M_{\tilde{P}}}, & I+\frac{\vec{\tilde{P}}\otimes\vec{\tilde{P}}}{M_{\tilde{P}}(M_{\tilde{P}}+\tilde{P}^0)} \end{bmatrix},\ \tilde{P}^2 = M^2_{\tilde{P}}, \tag{1.79}$$

[11] here $q_1 = (q_1^0, 0, 0, |q_0^3|)$

where T marks the matrix transposition and $\otimes$ marks the tensor product. The Jacobian due to the reparametrization of the integral is equal to $\frac{s_P}{s_Q}\ \frac{2}{\beta_f}$. Let us work a little bit more on the eq. (1.76). Firstly, we express the photon momenta as a fraction of $\frac{1}{2}\sqrt{s_Q}$ and in the polar coordinate system:

$$\tilde{k}_j \equiv \frac{\sqrt{s_Q}}{2}\ \bar{k}_j \equiv \frac{\sqrt{s_Q}}{2}\ x_j\ (1, \sin\theta_j \cos\phi_j, \sin\theta_j \sin\phi_j, \cos\theta_j), \tag{1.80}$$

and denote the sum of photons momenta as

$$\tilde{K} = \sum_{l=0}^{n} \tilde{k}_l \equiv \frac{\sqrt{s_Q}}{2}\ \bar{K}. \tag{1.81}$$

This allows us to use the δ-function:

$$\begin{aligned}\int\limits_{4m_f^2}^{s_P} ds_Q\ \delta\left(s_P - \left(\tilde{Q} + \sum_{l=0}^{n} \tilde{k}_l\right)^2\right) &= \int\limits_{4m_f^2}^{s_P} ds_Q\ \delta\left(s_P - s_Q\left(1 + \bar{K}^0 + \frac{1}{4}\bar{K}^2\right)\right) \\ &= \frac{\Theta\big(s_Q(\bar{k}_1, ..., \bar{k}_n) - 4m_f^2\big)}{1 + \bar{K}^0 + \frac{1}{4}\bar{K}^2},\end{aligned} \tag{1.82}$$

and write s_Q in the following maner

$$s_Q = s_Q(\bar{k}_1, ..., \bar{k}_n) \equiv \frac{s_P}{1 + \bar{K}^0 + \frac{1}{4}\bar{K}^2}. \tag{1.83}$$

The single-photon distribution also gets transformed:

$$\begin{aligned}&\frac{d^3\tilde{k}_j}{\tilde{k}_j^0}\ \tilde{S}_f(\tilde{k}_j) = \frac{dx_j}{x_j}\ \frac{d\phi_j}{2\pi}\ d\cos\theta_j\ \frac{\alpha}{\pi}\ \tilde{s}_f\left(\theta_j, \frac{m_f^2}{s_Q}\right), \\ &\tilde{s}_f\left(\theta_j, \frac{m_f^2}{s_Q}\right) = \frac{1 + \beta_f^2}{\delta_{1j}\delta_{2j}} - \frac{\mu_f^2}{2}\ \frac{1}{\delta_{1j}^2} - \frac{\mu_f^2}{2}\ \frac{1}{\delta_{2j}^2}, \\ &\delta_{1j} = 1 - \beta_f \cos\theta_j, \quad \delta_{2j} = 1 + \beta_f \cos\theta_j,\end{aligned} \tag{1.84}$$

and the whole integral is transformed into the semi-factorised form:

$$\begin{aligned}\sigma^{YFS}_{q\bar{q}\to l+\bar{l}+n(\gamma)} = \int d\psi d\cos\omega \sum_{n=0}^{\infty} \frac{1}{n!} \prod_{j=1}^{n} \int\limits_{\varepsilon_f}^{\infty} \frac{dx_j}{x_j} \int\limits_{0}^{2\pi} \frac{d\phi_j}{2\pi} \int\limits_{-1}^{1} d\cos\theta_j\ \tilde{\beta}^{(1)}_{0+1} \\ \frac{s_Q}{s_P}\ \frac{\beta_f}{2}\ \frac{\alpha}{\pi}\ \tilde{s}_f\left(\theta_j, \frac{m_f^2}{s_Q}\right)\ \frac{\Theta(s_Q - 4m_f^2)}{1 + \bar{K}^0 + \frac{1}{4}\bar{K}^2}\ e^{Y_{\tilde{\Omega}_F}(q_1,q_2)}.\end{aligned} \tag{1.85}$$

We have called the above formulae "*semi-factorised*" because it does not factorise yet into a product of independent integrals, one per photon, which would

allow us to perform generation of photons momenta. The reason for this is that all photon momenta $\bar{k}_j$ are connected through the variable s_Q, see eq. (1.80). The second problem caused by the use of $\frac{1}{2}\sqrt{s_Q}$ as an energy scale is that, in the case of the hard photon emission, the upper limit of x_j extends to large values, not really to infinity because of the $\Theta(s_Q - 4m_f^2)$ condition which is not very good for the MC integration. This problem can be solved by a simple change of variables:

$$\begin{aligned} y_i &= \frac{x_i}{1+\sum x_j}, \quad x_i = \frac{y_i}{1-\sum y_j}, \\ 1+\sum_j x_j &= \frac{1}{1-\sum_j y_j} = 1+\bar{K}^0 = 1+\frac{2K\cdot Q}{s_Q} = \frac{s_P}{s_Q}\left(1-\frac{K^2}{s_P}\right), \end{aligned} \tag{1.86}$$

which leads us to the final form for the total cross-section at the parton level

$$\begin{aligned} \sigma^{YFS}_{q\bar{q}\to l+\bar{l}+n(\gamma)} = & \int d\psi d\cos\omega \sum_{n=0}^{\infty}\frac{1}{n!}\prod_{j=1}^{n}\int\limits_{\varepsilon_f/(1+\bar{K}^0)}^{1}\frac{dy_j}{y_j}\int\limits_0^{2\pi}\frac{d\phi_j}{2\pi}\int\limits_{-1}^{1}d\cos\theta_j\,\frac{s_Q}{s_P}\,\frac{\beta_f}{2} \\ & \frac{\alpha}{\pi}\,\tilde{s}_f\left(\theta_j,\frac{m_f^2}{s_Q}\right)\frac{1+\bar{K}^0}{1+\bar{K}^0+\frac{1}{4}\bar{K}^2}\,\Theta(s_Q-4m_f^2)\,e^{Y_{\tilde{\Omega}_F}(q_1,q_2)}\,\tilde{\beta}^{(1)}_{0+1}. \end{aligned} \tag{1.87}$$

With the new variables the condition $s_Q > 4m_f^2$ (easily implementable in the MC) translates approximately into $\sum_j y_j < 1$. Furthermore, we have

$$\frac{1+\bar{K}^0}{1+\bar{K}^0+\frac{1}{4}\bar{K}^2} \leq 1, \tag{1.88}$$

which is ideal for the MC. The new IR limit $y_j > \varepsilon_f/(1+\bar{K}^0)$ is however inconvenient for the MC. The solution is to substitute

$$\varepsilon_f = \delta_f\,(1+\bar{K}^0) \tag{1.89}$$

where $\delta_f \ll 1$ is from now on the new IR regulator for FSR real photons. Note that this sets

$$E'_{\min} = \delta_f\frac{1}{2}\sqrt{s_Q}(1+\bar{K}^0) = \delta_f\frac{1}{2}\sqrt{s_Q}\left(1+\frac{2K\cdot\tilde{Q}}{s_Q}\right) \tag{1.90}$$

as a lower limit for the photon energy in the QMS, which is *higher* than the previous one $E_{\min} = \frac{1}{2}\sqrt{s_Q}\delta_f$ (for $\varepsilon = \delta_f$). Consequently, we have to keep the value of δ_f very low, in fact we need $\delta_f \ll m_f^2/s_P$.

There is a one-to-one correspondence between the points in the Lorentz-invariant phase space from the original of integral Eq. (1.74) and the points in space of our new variables:

$$\{n, (\tilde{k}_1, \ldots, \tilde{k}_n)\} \leftrightarrow \{n, (y_j, \theta_j, \phi_j), j = 1, \ldots, n\}, \tag{1.91}$$

moreover, as has been advertised before all transformations which were introduced in this subsection were performed without any approximations. The first simplification to the eq. (1.74) will be introduced in the next subsection.

1.5.2 Simplification of the distribution

This is the point from which we are ready to step by step simplify the very difficult formulae for the total cross-section from Eq. (1.87) and its phase space limits, such that at the end we obtain a simple distribution, which we can integrate analytically over certain integration variables. For each such a modification, we introduce a correction weight for the events generated with the simplified distribution, so that at the end the events will be generated according to the original distribution of eq. (1.8). The simplifications consist of four steps:

Step 1. Simplification of non-IR YFS $\bar{\beta}$-functions:

$$\tilde{\beta}_{0+1}^{(1)} \to \tilde{\beta}_{cru} = \frac{s_P}{s_Q} \frac{2}{\beta_f} \rho_0(\hat{s}, \phi, \cos\theta) \tag{1.92}$$

where $\rho_0(\hat{s}, \phi, \cos\theta)$ is the Born-level differential cross section presented in Appendix A.5. This simplification is corrected by so-called model weight:

$$w_{mod}(p_1, p_2, q_1, q_2, k_1, ..., k_n) = \frac{\tilde{\beta}_{0+1}^{(1)}(p_1, p_2, q_1, q_2, k_1, ..., k_n)}{\tilde{\beta}_{cru}(p_1, p_2, q_1, q_2, k_1, ..., k_n)}. \tag{1.93}$$

The numerator in the above equation is a model distribution which can have several variants (for example different perturbative orders, other variants of corrections, the BSM contributions, ect.). In our case the best model distributions is from eq. (1.75) but in the section with numerical results we will consider also other model distributions.

Step 2. Simplification of the eikonal factors:

$$\tilde{s}_f\left(\theta_j, \frac{m_f^2}{s_Q}\right) \to \bar{s}_f\left(\theta_j, \frac{m_f^2}{s_P}\right) = \frac{1 + \bar{\beta}_f^2}{\bar{\beta}_f} \frac{1}{1 - \bar{\beta}_f^2 \cos^2\theta_j}, \tag{1.94}$$

compensated by weight

$$w_j^s = \frac{\tilde{s}_f\left(\theta_j, \frac{m_f^2}{s_Q}\right)}{\bar{s}_f\left(\theta_j, \frac{m_f^2}{s_P}\right)}. \tag{1.95}$$

Step 3. Substitution:

$$\frac{1+\bar{K}^0}{1+\bar{K}^0+\frac{1}{4}\bar{K}^2}\,\Theta(s_Q - 4m_f^2) \;\to 1, \tag{1.96}$$

which is corrected by

$$w^{\bar{K}} = \frac{1+\bar{K}^0}{1+\bar{K}^0+\frac{1}{4}\bar{K}^2}\,\Theta(s_Q - 4m_f^2). \tag{1.97}$$

Removing $\Theta(s_Q - 4m_f^2)$ in the simple distribution means that we cannot map every event generated according to the simple distribution into a Lorentz-invariant phase-space point of the original distribution $d\sigma^{YFS}_{q\bar{q}\longrightarrow l+\bar{l}+n(\gamma)}$. This problem is simply cured by seting $w^{\bar{K}} = 0$ for events which do not fulfil $\Theta(s_Q - 4m_f^2)$ requirement.

Step 4. Simplification of the YFS form-factor

$$e^{Y_{\tilde{\Omega}_F}(q_1,q_2)} \to e^{\bar{\gamma}_f \ln(\delta_f)}, \tag{1.98}$$

where $\bar{\gamma}_f = Q_f^2\,\frac{\alpha}{\pi}\,\frac{1+\bar{\beta}_f^2}{\bar{\beta}_f}\,\ln\frac{1+\bar{\beta}_f}{1-\bar{\beta}_f}$, $\quad \bar{\beta}_f = \sqrt{1-(4m_f^2/s_P)}$.
This modification is compensated by a weight

$$w^{\gamma_f} = e^{Y_{\tilde{\Omega}_F}(q_1,q_2) - \bar{\gamma}_f \ln(\delta_f)}. \tag{1.99}$$

The remaining dependence on the momenta of all photons through s_Q is removed by simple replacing s_Q by s_P.
The resulting *simple* differential distribution is:

$$\begin{aligned}\sigma^{Simple}_{q\bar{q}\to l+\bar{l}+n(\gamma)} = & \int d\psi d\cos\omega \sum_{n=0}^{\infty}\frac{1}{n!}\prod_{j=1}^{n} \\ & \int dy_j\; d\cos\theta_j\; d\phi_j \rho^{Simple}(y_j,\theta_j)\rho_0(s_P,\phi,\cos\theta)\end{aligned} \tag{1.100}$$

where

$$\rho^{Simple}(y_j,\theta_j) = e^{\bar{\gamma}_f \ln(\delta_f)}\left(\frac{\alpha}{2\pi^2}\right)^n \prod_{j=1}^{n}\frac{\Theta(y_j-\delta_f)}{y_j}\bar{s}_f\left(\theta_j,\frac{m_f^2}{s_P}\right). \tag{1.101}$$

By convoluting the parton level result with the PDFs we obtain the total crude cross section in hadron collisions

$$\begin{aligned}\sigma_{cru} =& \sum_q \int_0^1 dx_1 dx_2 \Big[f_{q/h_1}(x_1,Q^2) f_{\bar{q}/h_2}(x_2,Q^2) + (q \leftrightarrow \bar{q}) \Big] \\ & \sigma^{Simple}_{q\bar{q}\longrightarrow l+\bar{l}+n(\gamma)}(s_P)\delta(s_P - x_1 x_2 S) \\ =& \sum_q \int_0^1 dx_1 dx_2 \int d\psi d\cos\omega \\ & \Big[f_{q/h_1}(x_1,Q^2) f_{\bar{q}/h_2}(x_2,Q^2) + (q \leftrightarrow \bar{q}) \Big] \rho_0(s_P,\phi,\cos\theta)\delta(s_P - x_1 x_2 S) \\ & \sum_{n=0}^{\infty} \frac{1}{n!} \prod_{j=1}^{n} \int dy_j \; d\cos\theta_j \; d\phi_j \rho^{Simple}(y_j,\theta_j),\end{aligned} \tag{1.102}$$

The total crude cross-section clearly factorizes into two independent parts, the "hadronic" part with parton distribution functions and the differential Born level partonic cross-section with the principal integration variables x_1, x_2, ψ and $\cos\omega$

$$\begin{aligned}J^{had} =& \sum_q \int_0^1 dx_1 dx_2 \int d\psi d\cos\omega \\ & \Big[f_{q/h_1}(x_1,Q^2) f_{\bar{q}/h_2}(x_2,Q^2) + (q \leftrightarrow \bar{q}) \Big] \rho_0(s_P,\phi,\cos\theta)\delta(s_P - x_1 x_2 S),\end{aligned} \tag{1.103}$$

and photon radiation part from which we will generate photons momenta

$$J^{YFS} = \sum_{n=0} J^{YFS}_n = \sum_{n=0}^{\infty} \frac{1}{n!} \prod_{j=1}^{n} \int dy_j \; d\cos\theta_j \; d\phi_j \rho^{Simple}(y_j,\theta_j), \tag{1.104}$$

In the next section we will show how to generate variables from the both distributions.

1.5.3 Generation of variables

Now we introduce variables that are generated at the lowest level of the MC algorithm according to the photonic and hadronic distribution.

(a) "Hadronic" part

The total integral of the "hadronic" part J^{had} plays in our algorithm a role of σ^{simple}[12]from eq. (1.73) and is performed using the general-purpose, self-adapting cellular Monte Carlo (MC) program Foam. Foam also provide us

[12]As we will see the total integral of the "partonic" part is equal to 1.

the Bjorken x's of quark and antiquark from which we are able to reconstruct the kinematics of both partons in the PMS frame. The angles θ, ϕ can be respectively assosieted with ω and ψ. Then ϕ is trivial to generate:

$$\phi = 2\pi r, \tag{1.105}$$

where r is the standard uniform random number $0 < r < 1$. The distribution of $\cos\theta$ requires applying the branching method or can be also generated by Foam. The total weight for this part of generation is simply equal to the weight provided by Foam

$$w^{had} = w^{Foam}. \tag{1.106}$$

For the given Bjorken variables x_1 and x_2 we can generate partons flavour q_f according to a probability

$$P_{q_f} = \frac{\Big[f_{q_f/h_1}(x_1,Q^2) f_{\bar{q}_f/h_2}(x_2,Q^2) + (q_f \leftrightarrow \bar{q}_f)\Big]\rho_0(s_P,\phi,\cos\theta)}{\sum_{q_f=u,d,c,s,b}\Big[f_{q_f/h_1}(x_1,Q^2) f_{\bar{q}_f/h_2}(x_2,Q^2) + (q_f \leftrightarrow \bar{q}_f)\Big]\rho_0(s_P,\phi,\cos\theta)} \tag{1.107}$$

Having reconstructed kinematics we can calculate s_P and move forward to the generation of photons kinematics.

(b) "Photonic" part

As was mentioned before the J_n^{YFS} integral can be calculated analytically:

$$\begin{aligned} J_n^{YFS} &= \sum_{n=0}^{\infty}\frac{1}{n!}\prod_{j=1}^{n}\int_{\delta_f}^{1}\frac{dy_j}{y_j}\int_0^{2\pi}\frac{d\phi_j}{2\pi}\int_{-1}^{1} d\cos\theta_j\,\frac{\alpha}{\pi}\,\bar{s}\left(\theta_j,\frac{m_f^2}{s_P}\right) e^{\bar{\gamma}_f \ln(\delta_f)} \\ &= \sum_{n=0}^{\infty} e^{-\bar{\gamma}_f \ln\frac{1}{\delta_f}}\frac{1}{n!}\left(\bar{\gamma}_f \ln\frac{1}{\delta_f}\right)^n = \sum_{n=0}^{\infty} e^{-\langle n\rangle}\,\frac{\langle n\rangle^n}{n!} = 1. \end{aligned} \tag{1.108}$$

From eq. (1.108) we see that the photon multiplicity for the simple distribution is the standard Poisson distribution, with the average given by

$$\langle n\rangle = \bar{\gamma}_f \ln\frac{1}{\delta_f}, \tag{1.109}$$

and the overall normalization equal to 1. Therefore the photon multiplicity can be easily generated using standard uniform random numbers. Having generated number of photons n, next we generate other variables according to the differential distribution

$$\frac{dJ_n^{YFS}}{\prod_{j=1}^{n} dy_j\, d\phi_j\, d\cos\theta_j}. \tag{1.110}$$

It is rather not complicated because this distribution is fully factorized and the variables $\cos\theta_j$, ϕ_j and y_j can be generated independently. The distribution of ϕ_j is just flat and the distribution of y_j is trivial to generate:

$$\phi_j = 2\pi r_{1j}, \quad y_j = \delta_f^{r_{2j}}, \tag{1.111}$$

where r_{ij} are the standard uniform random numbers $0 < r_{ij} < 1$. The distribution of $\cos\theta_j$ requires applying the branching method: it is split into two components

$$\frac{2}{1-\bar{\beta}_f\cos^2\theta_j} = \frac{1}{1-\bar{\beta}_f\cos\theta_j} + \frac{1}{1+\bar{\beta}_f\cos\theta_j}, \tag{1.112}$$

and $\cos\theta_j$ is generated according to one component, chosen with the equal probability between the two. For example, if the first component $1/(1-\bar{\beta}_f\cos\theta_j)$ is chosen then

$$\cos\theta_j = \frac{1}{\bar{\beta}_f}\left\{(1-(1+\bar{\beta}_f)\left(\frac{1-\bar{\beta}_f}{1+\bar{\beta}_f}\right)^{r_{3j}}\right\}, \tag{1.113}$$

where r_{3j} is another uniform random number.

1.5.4 Kinematics

Having shown how all the variables are generated, we are now ready to trace how from these variables the kinematics of all the particles in the event is constructed. The construction of the kinematics consist of four steps:

Step 1. The four-momenta of the initial state partons in the PMS frame.
The Bjorken variable x_i $(i = 1, 2)$ is treated as a fraction of hadron's h_i light-cone momentum in the beams center-of-mass (CM) frame. In terms of the light-cone variables a given four-vector $V^\mu = (V^0, V^1, V^2, V^3)$ can be expressed as follows:

$$V^\mu = \left(\frac{V^+ + V^-}{2}, V^1, V^2, \frac{V^+ - V^-}{2}\right) \tag{1.114}$$

where $V^\pm = V^0 \pm V^3$. The four-momenta of quarks in the laboratory frame (the beams CMS frame), with the $+z$ axis pointing in the h_1 direction, read:

$$p_1^{\mu(lab)} = \left(\frac{p_1^+}{2} + \frac{m_1^2}{2p_1^+}, 0, 0, \frac{p_1^+}{2} - \frac{m_1^2}{2p_1^+},\right), \tag{1.115}$$

$$p_2^{\mu(lab)} = \left(\frac{p_2^-}{2} + \frac{m_2^2}{2p_2^-}, 0, 0, -\frac{p_2^-}{2} + \frac{m_2^2}{2p_2^-} \right), \tag{1.116}$$

where $p_i^{\pm} = x_i P_{h_i}^{\pm}$ and $P_{h_i}^{\pm}$ is a light-cone momentum variable of the hadron h_i. Therefore, the four-momenta of the partons in the PMS frame are:

$$\begin{aligned} p_1^{\mu} &= (E, 0, 0, p_z), \\ p_2^{\mu} &= (\sqrt{s_P} - E, 0, 0, -p_z), \end{aligned} \tag{1.117}$$

where $s_P = p_1^{\mu} p_{2\mu}$, $E = \frac{s_P + m_1^2 - m_2^2}{2\sqrt{s_P}}$ and $p_z = \sqrt{E^2 - m_1^2}$.

Step 2. The four-momenta of the final state photons in the QMS frame.
Having calculated s_P, we are able to move forward and construct the photons kinematics $\{\bar{k}_j,\ j-1, ..., n\}$ in the QMS frame[13]. It is achieved by pluging the variables $x_j(y_1, ...y_n)$, $\cos\theta_j$ and ϕ_j, $j = 1, ..., n$; into Eq. (1.80).

Step 3. The four-momenta of the final-state leptons in the QMS frame.
From the photons kinematics we are able to calculate $\tilde{Q}$, which then can be used to obtain the final-state leptons kinematics in the QMS frame according to Eq. (1.77).

Step 4. Transformation to the *laboratory* frame.
First, the momenta of all the photons and final-state leptons are transformed from the QMS frame to the PMS frame using transformation described by Eq. (1.78). In this transformation the angles ψ and ω of the rotations $R_3(\psi)R_2(\omega)$ are assigned respectively to generated variables ϕ and θ. This ensures that at the Born level in the PMS frame the azimuthal and the polar angles between momentum of the quark q and the lepton l^- are equal to the ϕ and θ, respectively. Then the four-momenta of all the particles are transformed from the PMS frame to the laboratory frame according to the transformation $B_{P^{(lab)}}$, where $P^{(lab)} = p_1^{(lab)} + p_2^{(lab)}$, and the transformation itself is defined by Eq. (1.79).

The list of all the particles with their PDG codes and four-momenta in both the *lab* and the PMS frames creates the *event record*, see Subsection 1.5.6.

[13] In the case of $n = 0$, $s_P = s_Q$ and we are able to directly reconstruct the kinematics of the leptons.

1.5.5 Total compensating weight and unweighted events

The total compensating weight which corrects all approximations to the original cross-section introduced in this subsection is

$$w_{\rm simple} = w_{\rm mod} w^{\bar{K}} w^{\gamma_f} \prod_{j=1}^{n} w_j^s. \tag{1.118}$$

In other words, one can write the original YFS parton-level cross-section of Eq. (1.87) in terms of the *simple* distribution ρ^{simple} in the following maner

$$\sigma^{YFS}_{q\bar{q}\to l+\bar{l}+n(\gamma)} = \int d\psi d\cos\omega \int \prod_{j=1}^{n} dy_j \; d\cos\theta_j \; d\phi_j \rho^{Simple} w_{\rm simple} \tag{1.119}$$

The total weight is then equal:

$$w_{\rm tot} = w_{\rm simple} w^{had}. \tag{1.120}$$

The consistent and unbiased Monte Carlo estimator of the total cross-section reads

$$\hat{\sigma}^{YFS}_{q\bar{q}\to l+\bar{l}+n(\gamma)} = \sigma_{cru} \left\langle w_{\rm tot} \right\rangle = \sigma_{cru} \frac{1}{N} \sum_{i=1}^{N} w_{\rm tot}^{(i)} \tag{1.121}$$

when i runs over the sample of N Monte Carlo events, and the consistent and unbiased Monte Carlo estimator of its standard deviation is

$$\hat{\delta} = \frac{\sigma_{\rm cru}}{\sqrt{N(N-1)}} \sqrt{\sum_{i=1}^{N} \left[w_{\rm tot}^{(i)} \right]^2 - \frac{1}{N} \left[\sum_{i=1}^{N} w_{\rm tot}^{(i)} \right]^2}. \tag{1.122}$$

Therefore, in principle the final MC result may be obtained with an arbitrary precision, simply by increasing the number of generated events N. The result of the computation of eq.(1.121) depends on the sequence of the random numbers used in the Monte Carlo generation and its distribution is interpreted in the sense of the Central Limit Theorem, see e.g. Ref. [88].

Unweighted event generation can be switched on in ZINHAC and is obtained using the standard Monte Carlo hit-and-miss method. For each generated event after calculating the total weight w^{tot} we accept event if

$$\frac{w^{tot}}{w^{max}} > r, \tag{1.123}$$

where r is a uniform random number from the range $(0, 1)$ and w^{max} is a maximum weight for the process estimated for example by sampling the total

cross-section many times. If the inequality (1.123) is not fulfilled the event is rejected. This ensures that the accepted events are distributed according to the distribution provided by the original cross-section, and so all have the unit weight, see for example Ref. [80] for details.

It is worth mentioning that in the case of weighted event generation in a single Monte Carlo run (generation of N events) we can analyse not just one model but we are able to construct a vector of m model weights $w_{\mathrm{mod}}^{(k)}$ where $k = 1, 2, ..., m$ which allows us to investigate results of many models at the same time.

1.5.6 Event record structure

Each *event* is made up of individual *steps* that reflect the treatment of the event as it passes through the various stages of the generator (detailed description of the structure of the program and the *steps* as is presented in Section 1.6). The example of the *step* structure is presented in Fig. 1.6, every *particle* in a single step has an entry like

```
ID  PDG  Parents   Children  (Px, Py, Pz; E)                Mass
5   23   [3,4]     (6,7,8)   (0.0,0.0,985.577;990.1801)   19.21
```

Jt contains `5` – the particle's label (ID) in this event; `23` – the PDG code; `[3,4]` – the label(s) of parent particle(s), the particle without parents (*beam particle*) is denoted by `[b]` ; `(6,7,8)` the label(s) of child particle(s), by `(f)` the final-state particle is denoted; the four-momentum of the particle $(p_x, p_y, p_z; E)$ and $\pm\sqrt{|E^2 - \vec{p}^2|}$ called mass. Each step contains the information about particle's four-momentum in both the PMS and *lab* frames; in the Fig. 1.6 we present the print-out of the four-momenta in the *lab* frame.

From this exemplary event record we can read that this event was produced in the proton-proton collision at the nominal LHC energy of 14 GeV. The children of the proton–proton system were two so-called protons remnants, both with the ID = 82, and a quark–antiquark pair $u\bar{u}$. From the quark–antiquark pair the Z boson was produced. Then the Z boson decayed into the electron–positron pair from which one photon was radiated. The electron, the positron and the photon are the final-state particles which can be detected by experimental aparatus.

```
Step 3: ModelHandler frame (lab)
1  2212 [b]   (3,5)    ( 0.0, 0.0, 6999.9999; 7000.0)  0.93827
2  2212 [b]   (4,6)    ( 0.0, 0.0,-6999.9999; 7000.0)  0.93827
3  82   [1]   ()       ( 0.0, 0.0, 6012.1332; 6012.1)  9.61941
4  82   [2]   ()       ( 0.0, 0.0,-6997.7103; 6997.6) -330.151
5  2    [1]   (7)      ( 0.0, 0.0, 987.8667; 987.866)  0.33
6 -2    [2]   (7)      ( 0.0, 0.0,-2.28961; 2.313271)  0.33
7  23   [5,6] (8,9,10)( 0.0, 0.0, 985.577; 990.1801)  95.363988
8  11   [7]   (f)      ( 4.115, 22.053, 42.05; 47.66)  0.0005109
9 -11   [7]   (f)      (-4.146,-19.653,-36.75; 41.88)  0.0005109
10 22   [7]   (f)      ( 0.0307,-2.399,-5.301; 5.818) -6.098e-08

Four-momentum conservation check (sum of the final momenta):
         (-2.9143354e-16,8.8817842e-16,1.7763568e-15;95.363988)
```

Figure 1.6: The example of the *step* structure.

In the case of weighted events the *event record*, in addition to the list of the particles with their four-momenta, includes also the best event weight, the vector of model weights and the crude weight.

1.5.7 Including interference effects and weak corrections

If we were only interested in the pure final-state photon radiation we could stop here. But since we also want to include into our calculations interference between the initial and final-state radiation (the pure initial-state radiation in hadronic collisions can be left for a parton-shower Monte Carlo generator), we need to add interferences effects in our Monte Carlo algorithm: in the YFS form factor, in the IR $\tilde{S}$-factor and in the non-IR $\bar{\beta}$-functions. Moreover, we would like to include also the pure weak $\mathcal{O}(\alpha)$ corrections.

Let us start from the non-IR $\bar{\beta}$-functions. In the $\bar{\beta}_0^{(1)}$-function we need to include the interference virtual correction. Therefore, the new virtual correction which includes interferences takes the form

$$\delta_{\rm EW} = \delta^{\rm F} + \delta^{\rm int} + \delta^{\rm weak}, \tag{1.124}$$

where the weak corrections $\delta^{\rm weak}$ are calculated using the SANC [74,73] library,

$\delta^{\rm F}$ was defined before, see Eq. (1.15), and interference part reads

$$\delta^{\rm int} = \delta^{\rm int}_{\rm QED} - Y^{\rm int}_{\Omega}. \tag{1.125}$$

The interference form factor $Y^{\rm int}_{\Omega}$ from the equation above can be expressed in therms of '*dipole*' form factors $Y_{\Omega}(p_1, p_2)$, defined in Appendix A.1, in the following maner

$$Y^{\rm int}_{\Omega}(p_1, p_2, q_1, q_2) = |Q_q|\{Y_{\Omega}(p_1, q_1) + Y_{\Omega}(p_2, q_2) - Y_{\Omega}(p_1, q_2) - Y_{\Omega}(p_2, q_1)\}, \tag{1.126}$$

where Q_q is the value of the quark charge in the units of the positron charge. The $\delta^{\rm int}_{\rm QED}$ part is calculated using the SANC [73, 74] library. The function $\bar{\beta}^{(1)}_0$ is now given by

$$\bar{\beta}^{(1)}_0(p_1, p_2, q_1, q_2) = \bar{\beta}^{(0)}_0(p_1, p_2, q_1, q_2)\,[\,1 + \delta_{\rm EW}(p_1, p_2, q_1, q_2)\,]\,, \tag{1.127}$$

In $\bar{\beta}^{(1)}_1$ we need to add the interference matrix element for the real-photon radiation. This interference matrix element is obtained from calculated in previous section spin amplitudes for boson production and decay with the single-photon radiation

$$\left|\mathcal{M}^{(1)}_{int}\right|^2 = 2{\rm Re}\left(\mathcal{M}^{(1)}_{ISR}\mathcal{M}^{(1)*}_{FSR}\right), \tag{1.128}$$

where $\mathcal{M}^{(1)}_{ISR}$ is given by Eq. (1.66). The $\bar{\beta}^{(1)}_1$-function now reads

$$\bar{\beta}_1 = \frac{1}{16s\,(2\pi)^5}\,\frac{1}{12}\sum\left[\left|\mathcal{M}^{(1)}_{FSR}\right|^2 + \left|\mathcal{M}^{(1)}_{int}\right|^2\right] - \left[\tilde{S}_F(k) - \tilde{S}_{int}(k)\right]\bar{\beta}^{(0)}_0, \tag{1.129}$$

where

$$\tilde{S}_{int}(k) = |Q_q|\left\{\tilde{S}(p_1, q_1, k) + \tilde{S}(p_2, q_2, k) - \tilde{S}(p_1, q_2, k) - \tilde{S}(p_2, q_1, k)\right\} \tag{1.130}$$

is expressed in terms of the eikonal factor

$$\tilde{S}(q_1, q_2, k) = -\frac{\alpha}{4\pi^2}\left(\frac{q_1}{kq_1} - \frac{q_2}{kq_2}\right)^2. \tag{1.131}$$

Including the interferences in to the IR $\tilde{S}$-factor creates an additional weight:

$$w^{int}_{\tilde{S}} = \prod_{l=1}^{n}\frac{\tilde{S}_{int}(k_l) + \tilde{S}_F(k_l)}{\tilde{S}_F(k_l)}. \tag{1.132}$$

The implementation of the interferences into YFS form factor corresponds to including a new correction weight

$$w_Y^{int} = e^{Y_\Omega^{\rm int}}. \tag{1.133}$$

All the above interferences effects cannot, however, be implemented directly in the MC algorithm described so far. In order to do this we need to set a common framework for the ISR and the FSR. In the contrary to the FSR, where the most convenient reference frame for photons generation is the QMS frame in the case of the ISR the most natural frame is the PMS frame. As a consequence we have two different IR domains: one for ISR with Ω_I defined in the PMS frame and one for FSR with Ω_F defined in the QMS frame. Because we have an analytical representation of the IR function $\tilde{B}(\Omega, q_1, q_2)$ for spherical Ω, the obvious choice for both Ω_I and Ω_F in their reference frames are spheres. Therefore, we define Ω_I by: $k_j^0 < \varepsilon_e \frac{1}{2}\sqrt{s}$ in the PMS frame and for FSR Ω_F was already defined by $k_j^0 < \delta_f((s_Q + 2KQ)/s_Q)\frac{1}{2}\sqrt{s_Q}$ in the QMS. It is clear that the two soft-photons regions, Ω_I and Ω_F partly overlap but they cannot be the same because of the Lorentz transformation which connects both frames. For example Ω_F when transformed to the PMS frame loses its spherical shape and becomes elliptical. We need to find a way how to introduce a common soft-photon region Ω for both the ISR and the FSR. The simplest solution is a rather crude method in which we generate photons using small $\Omega_F \subset \Omega_I$ (i.e. by setting δ_f very small) and assign the zero weight to all events where at least one photon falls into Ω_I. This method although perfectly fine is however, very inefficient – many events are generated with the zero weight. The second solution has exactly the same orgin, but instead of removing the whole event, we just remove photons when $k_i \in \delta\Omega = \Omega_I \setminus \Omega_F$. This method by construction is of course much more efficient then the previous one. As a short algebraic calculation shows [36], this treatment has to be corrected by the additional weight

$$\begin{aligned} w_{\rm hide} = \exp\Big\{ &- 2\alpha|{\rm Q_f}|\Big[\tilde{B}(\Omega_I; q_1^*, q_2^*) - \tilde{B}(\Omega_F; q_1^*, q_2^*) \\ &- \tilde{B}(\Omega_I; q_1, q_2) + \tilde{B}(\Omega_F; q_1, q_2)\Big]\Big\} \end{aligned} \tag{1.134}$$

where $q_i^*, i = 1, 2$, are defined such that $(q_i^*)^2 = m_f^2(s_Q/s_P)$. Moreover, in the QMS they have the same directions as the original $\vec{q}_i$ and the same total energy, $q_1^{*0} + q_2^{*0} = \sqrt{s_Q}$.

This method is very useful for the inclusion of the interference effects, which will be implemented in the ZINHAC program in the future, but can be conveniently used for the pure FSR as well, which is the case of the current version of the ZINHAC program.

1.6 Implementation of ZINHAC Monte Carlo generator

This section is designed to give basic information about the structure of the ZINHAC program and to supplement the ZINHAC Doxygen[14] documentation. The Doxygen documentation is written within code, and is thus quite easy to keep up to date. Doxygen can cross reference documentation and code, so that the reader of a document can easily refer to the actual code. The ZINHAC Doxygen documentation of the source code in the html format will be available at dedicated ZINHAC Trac website:

`http://th-www.if.uj.edu.pl/ZINHAC`

Trac [90] is an open source, web-based project management and bug-tracking tool for software development projects. Among the users of Trac is HepForge (development environment for high energy physics software development projects), UBS bank and NASA's Jet Propulsion Laboratory. The screen-print of the ZINHAC Trac website is shown in Fig. 1.7. Trac also provides an interface to Subversion SVN [91] which is a version-control system widely used by open source community. SVN is also used by ZINHAC for the management of changes to the source code and input files of the program. The ZINHAC input files are written in XML (Extensible Markup Language). XML [92] is a textual data format which design goals emphasize simplicity and generality. Although the XML's design focuses on documents, it is widely used for the representation of arbitrary data structures, for example in web services. ZINHAC includes two XML input files. The first, `ParticleDataBase.xml`, contains only information about the particles (particle charge, mass, PDG code, etc.) and the second one, `InputData.xml`, contains all other necessary information needed for the event generation (coupling constants, mathematical constants, flags and switches of the generator, etc.). The ZINHAC program hes been designed and modeled in Unified Modeling Language (UML) [93] using VisualParadigm [94]

[14] Doxygen [89] is a tool for writing software reference documentation.

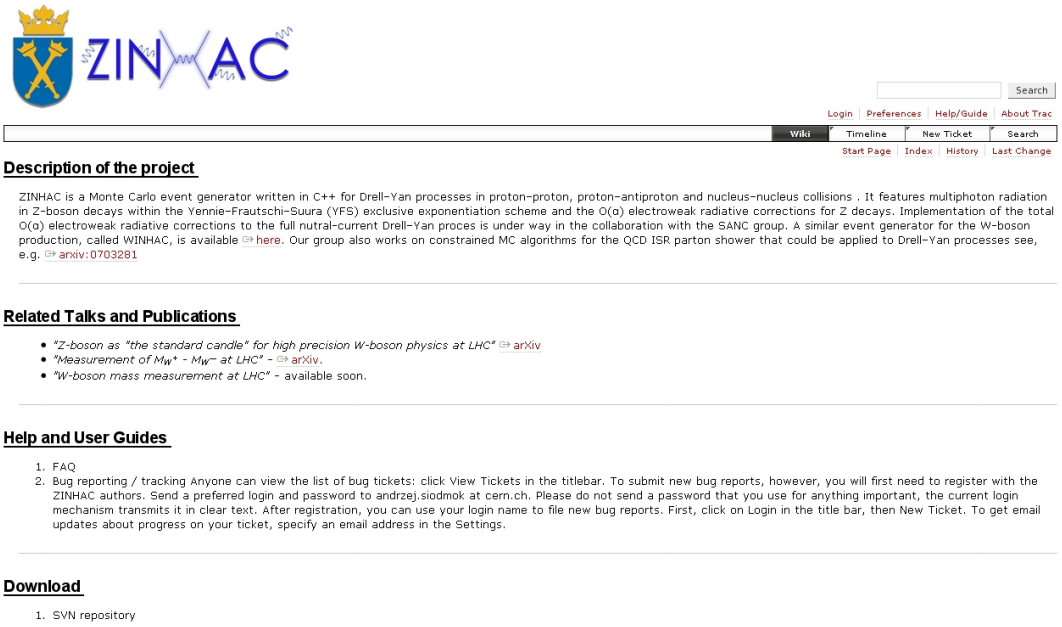

Figure 1.7: The ZINHAC Trac website.

and Eclipse [95] software development environment. The very simplified version of the ZINHAC UML model is presented in Fig. 1.8. Each part of ZINHAC is implemented as a C++ class[15] that contains the implementation of the presented in the previous section Monte Carlo algorithm.

For reading of the input files is responsible the `Reader` base class, which must be inherited. In such a way we keep flexibilty of different ways of reading input files. Currently in ZINHAC, `Reader` is inherited by the `XercescReader` class which uses the Xerces-C++ XML parser [96]. The Xerces-C++ parser makes it easy for ZINHAC to read and write XML data, however, as mentioned above, we keep the possibility of using other ways to read input files. The actual generation of each event is the responsibility of the so-called `Manager` class, see Fig. 1.8. The `Manager` class has pointers to all objects relevant for the event generation, starting from `InitializationHandler`, which is responsible for the initialization of each part of the ZINHAC program, and ending at the `AnalysisHandler`, which aim is to perform physics analysis of the event and book histograms. The `Manager` class manages the generation of the event via subsequent evolution of the event which is passed through the so-called

[15]Except for the electroweak corrections which are incorporated from the SANC library written in Fortran.

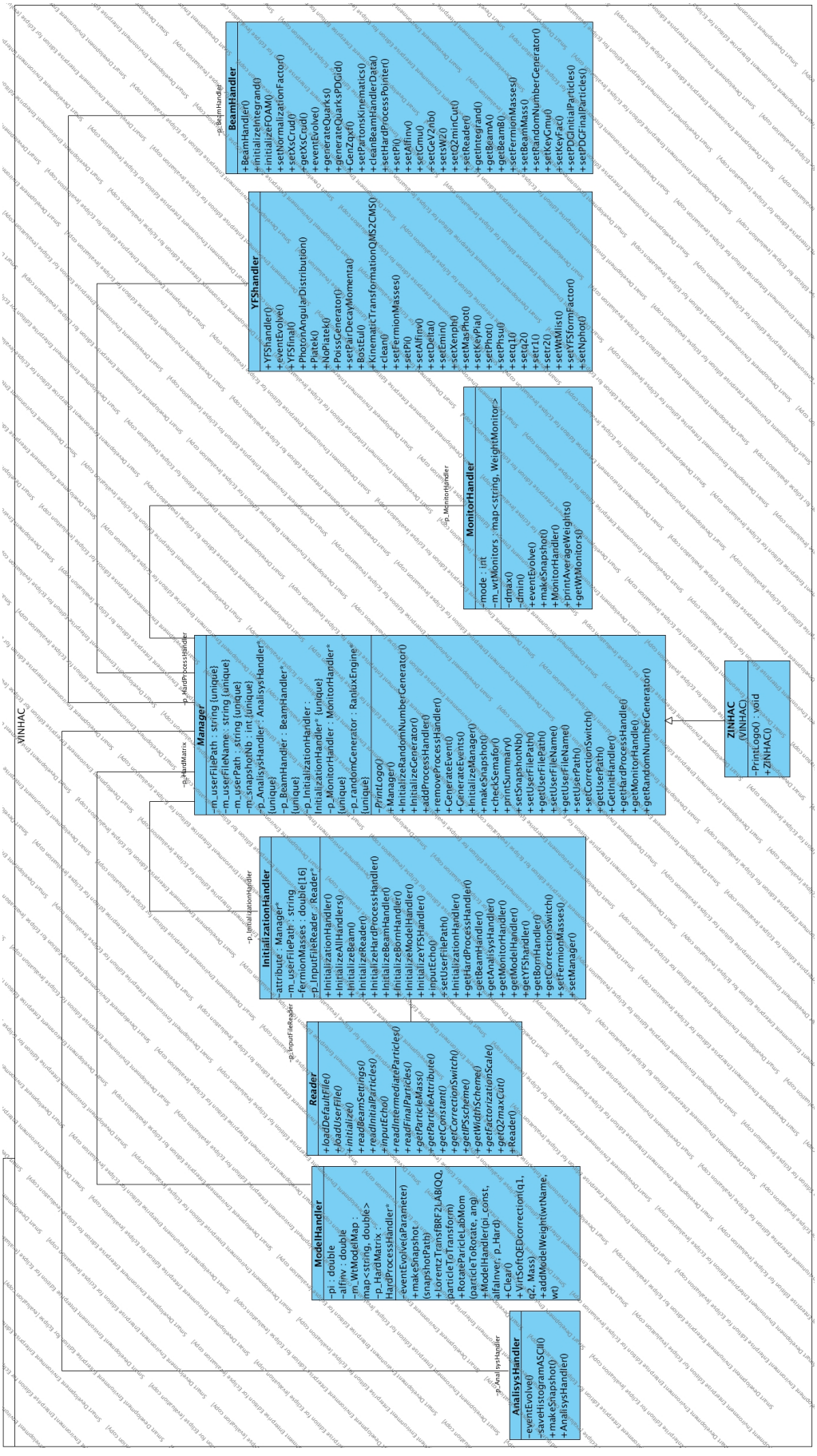

Figure 1.8: The ZINHAC simplified UML scheme.

`ProcessHandlers`. `ProcessHandler` is a base class which contains the virtual method `eventEvolve()` and does not implement any event evolution itself. This must be done by inheriting classes which provide an implementation of a specific event evolution. The `YFSHandler`, for example, inherits from the `ProcessHandler` and implements the ZINHAC YFS multiphoton radiation by overriding the virtual `eventEvolve()` member function. This allows the implementations of different event evolutions to live side-by-side and to be easily exchanged. The most important `ProcessHandlers` in ZINHAC are:

1. `BeamHandler` – is responsible for generating of the initial-state quarks flavours and kinematics, as well as beam remnants.

2. `YFSHandler` – generates the multiphoton radiation, if switched on in the input file, and sets the final-state particles kinematics.

3. `ModelHandler` – is responsible for the calculation of the model weights.

4. `AnalysisHandler` – performs the physics analysis and books histograms.

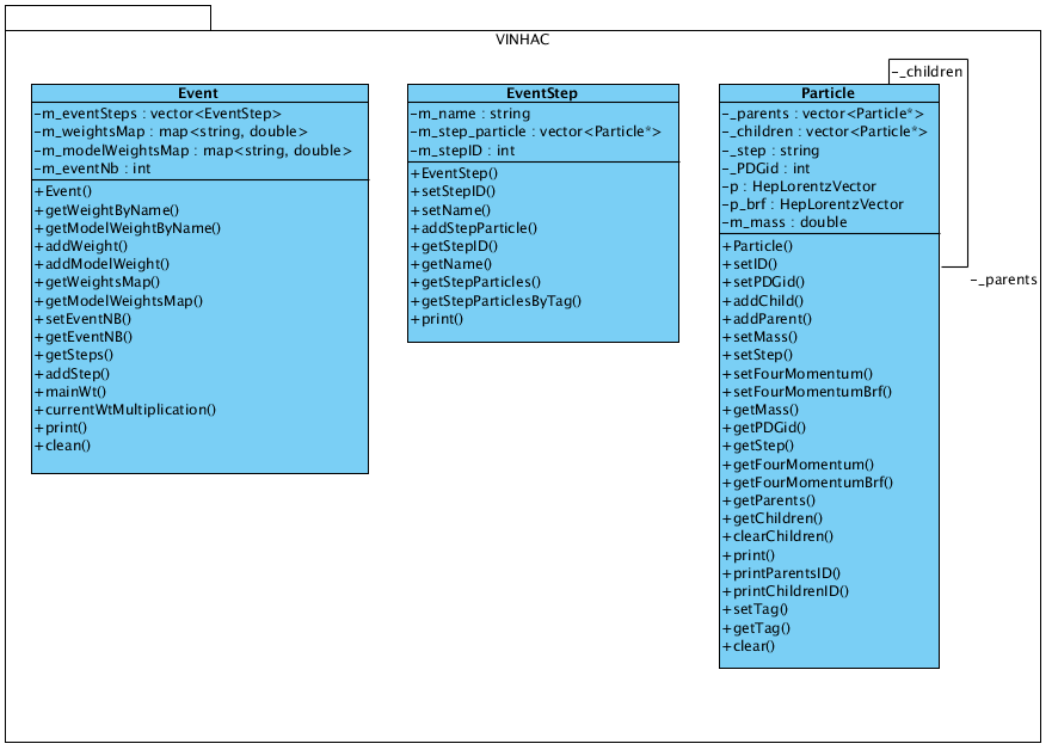

Figure 1.9: The UML scheme of the `Event`, `EventStep` and `Particle` classes.

All `ProcessHandlers` take as input the reference to the `Event` object and modify it. The fully-generated event has to pass through all `ProcessHandlers` in the correct order. The `Event` class contains an STL vector of smaller objects called `EventSteps`, see Fig 1.9. Each `EventStep` is associated with the step of the event evolution (performed by a given `ProcessHandler`) and keeps all the information about all particles available at the end of the evolution step, including modifications made by `ProcessHandler`. The structure of the `EventStep` class allows to keep all the information described in Subsection 1.5.6. This "step" structure of the `Event` class allows the user to easily trace the evolution of the event performed by each `ProcessHandler` as well as analyze the final form of the event given in the last step.

1.7 Numerical tests

We have performed several numerical tests of the MC event generator ZINHAC, which implements the calculations presented in the previous sections. In this section we discuss some of the results. First, we present some parton-level tests of the ZINHAC Monte Carlo event generator and then we show the results of its comparison at hadron-level with the SANC program.

1.7.1 Parton-level tests

We have performed several numerical tests of the MC event generator ZINHAC aimed at checking the correctness of the implemented matrix elements as well as the corresponding MC algorithm.

(a) Setup

In this part of the numerical tests we considered the following process:

$$u + \bar{u} \longrightarrow Z \longrightarrow l + \bar{l}, \tag{1.135}$$

where $l = e, \mu, \tau$. All the results below, unless stated otherwise, have been obtained for the following input parameters:

$$\begin{aligned}
m_e &= 0.51099892 \text{ MeV}, & m_\mu &= 0.105658369 \text{ GeV}, \quad m_\tau = 1.77699 \text{ GeV}, \\
m_u &= 0.0 \text{ GeV}, & & \\
M_Z &= 91.1876 \text{ GeV}, & \Gamma_Z &= 2.4924 \text{ GeV}, \\
M_W &= 80.37399 \text{ GeV}, & \Gamma_W &= 2.0836 \text{ GeV}, \\
\alpha &= 1/137.03599911, & \alpha_s(M_Z^2) &= 0.1176, \quad s_W^2 = 1 - \frac{M_W^2}{M_Z^2}, \\
E_{CM} &= \sqrt{s} = 90 \text{ GeV}, & G_\mu &= 1.16637 \times 10^{-5} \text{ GeV}^{-2}.
\end{aligned} \tag{1.136}$$

In order to cross-check the matrix elements presented here, we have implemented in our MC program the matrix elements of Ref. [43], which in the following we shall call B&K. These latter matrix elements were obtained in the small-fermion-mass approximation $m_f \ll M_Z$; their precision is therefore of $\mathcal{O}(m_f^2/M_Z^2)$. Since our spin amplitudes are obtained for massive fermions, we performed the comparisons of these matrix elements for massless initial and final particles. For both the Born-level and $\mathcal{O}(\alpha)$ matrix elements, we reached an agreement at the level of $\sim 10^{-14}$ for the relative difference.

Then, we performed several tests to check the MC algorithm of the program ZINHAC. An important test of the algorithm for MC integration and event generation according to Eq. (1.8) is to reproduce fixed-order calculations. The strict Born-level cross section can be obtained from Eq. (1.8) by truncating the perturbation series in α at the lowest-order term, which amounts to

$$\sigma_0^{tot} = \int \frac{d^3q_1}{q_1^0} \frac{d^3q_2}{q_2^0} \, \rho_0^{(0)} \, e^{-Y} \, . \tag{1.137}$$

Within the multiphoton MC algorithm, this means calculating an appropriate weight if the photon number $n = 0$ and setting it to zero if $n > 0$. The Born-level total cross section can be easily calculated analytically. In the small-fermion-mass approximation and in the fixed-width scheme it reads

$$\sigma_0^{tot} = \frac{e^4 s}{36\pi} \frac{(v_{Zu\bar{u}}^2 + a_{Zu\bar{u}}^2)(v_{Zl\bar{l}}^2 + a_{Zl\bar{l}}^2)}{(s - M_W^2)^2 + M_W^2 \Gamma_W^2}. \tag{1.138}$$

In Table 1.2 we compare the results for the total Born cross section for the massive e, μ and τ in the final state and massless initial state u quark, obtained from the analytical formula of Eq. (1.138) with those calculated with the MC

Calculation	σ_0^{tot} [nb]		
	e	μ	τ
Analytical	0.3665193	0.3665193	0.3665193
ZINHAC-Born	0.3665192 (3)	0.3665171 (3)	0.3659573 (3)
ZINHAC-YFS ($n = 0$)	0.36650 (4)	0.36648 (3)	0.36596 (1)

Table 1.2: The results of MC program ZINHAC for the total Born-level cross section and YFS exponentiation with $n = 0$ photons compared with the analytical calculation in the small-fermion-mass approximation. The numbers in parentheses are statistical errors for the last digits.

program the ZINHAC, both at the Born-level and for the YFS exponentiation with $n = 0$ photons. We see a very good agreement between these three calculations for e. This it is what we expected because the precision of the analytical small-lepton-mass approximation $m_l \ll M_Z$ for electrons gives $\mathcal{O}(10^{-10})$. For τ both ZINHAC's results agree very well within the statistical errors but they differ from analytical results by $\sim 0.1\%$, which can be explained by the τ-mass effects (they are not negligible as in the case of e or even μ).

In a similar way, the first-order cross section can be obtained from Eq. (1.8) by truncating the perturbative series at $\mathcal{O}(\alpha)$, i.e.

$$\sigma_1^{tot} = \int \frac{d^3q_1}{q_1^0}\frac{d^3q_2}{q_2^0}\,\delta^{(4)}(p_1+p_2-q_1-q_2)\,\bar{\beta}_0^{(0)}\left[1+\delta_{\rm QED}^{(1)}+Y\right] + \int \frac{d^3q_1}{q_1^0}\frac{d^3q_2}{q_2^0}\frac{d^3k}{k^0}\,\delta^{(4)}(p_1+p_2-q_1-q_2-k)\left[\bar{\beta}_1^{(1)}+\tilde{S}\bar{\beta}_0^{(0)}\right]\theta(k^0-E_{min})\,, \tag{1.139}$$

where the first term on the r.h.s. corresponds to the Born plus virtual and real-soft-photon contribution and the second one to the real-hard-photon contribution. In practice, this means that the first term is evaluated within the multiphoton algorithm only for $n = 0$, the second only for $n = 1$, otherwise the appropriate MC weights are set to zero. In Table 1.3 we show the results from the program ZINHAC for the pure $\mathcal{O}(\alpha)$ QED correction to the total cross section. As can be seen, we have reached a very good agreement with the analytical calculations, see e.g. Ref. [43].

In Table 1.4 we compare the results for the $\mathcal{O}(\alpha)$ hard-photon correction as a function of the lower photon-energy cut-off k_0, i.e.

$$\delta_1^h(k_0) = \frac{1}{\sigma_1^{tot}}\int_{k_0} dE_\gamma\,\frac{d\sigma_1}{E_\gamma}\times 100\%\,, \tag{1.140}$$

Calculation	$\delta_1 = \sigma_1^{tot}/\sigma_0^{tot} - 1$		
	e	μ	τ
Analytical	1.75×10^{-3}	1.75×10^{-3}	1.75×10^{-3}
ZINHAC	$1.9(2) \times 10^{-3}$	$1.7(1) \times 10^{-3}$	$1.9(3) \times 10^{-3}$

Table 1.3: The results for the $\mathcal{O}(\alpha)$ QED correction to the total cross section from the MC program ZINHAC. The numbers in parentheses are statistical errors for the last digits.

$2k_0/E_{CM}$	e		μ	
	ZINHAC	B&K	ZINHAC	B&K
0.01	41.04 (6)	41.1	21.93 (7)	22.0
0.05	24.18 (4)	24.2	12.85 (5)	12.9
0.10	17.27 (3)	17.3	9.13 (4)	9.1
0.15	13.45 (2)	13.5	7.08 (3)	7.1
0.20	10.87 (2)	10.9	5.70 (3)	5.7
0.30	7.50 (2)	7.5	3.89 (2)	3.9
0.40	5.34 (1)	5.4	2.74 (2)	2.8
0.50	3.82 (1)	3.8	1.94 (2)	2.0
0.60	2.67 (1)	2.7	1.34 (1)	1.4
0.70	1.79 (1)	1.8	0.88 (1)	0.9
0.80	1.07 (1)	1.1	0.52 (1)	0.5
0.90	0.485 (3)	0.4	0.227 (5)	0.2

Table 1.4: The fraction of events (in %) with a photon energy greater than k_0 at $\mathcal{O}(1)$ from the MC program ZINHAC and from the MC program of Berends & Kleiss [43] (denoted as B&K) for $E_{CM} = 90\,\text{GeV}$. The numbers in parentheses are statistical errors for the last digits.

for the centre-of-mass energy $E_{CM} = 90\,\text{GeV}$, obtained from the program ZINHAC and from the B&K MC program [43]. First of all we see that there is more radiation from the electrons than from the muons which we expected. Morover, assuming that the errors from B&K MC program, which were not specified in Ref. [43], are of the order of the last significant digit, we see that the both programs agree very well within the statistical errors.

Calculation	e	μ	τ
$\delta_{exp} = \frac{(\sigma^{tot}_{\rm YFS} - \sigma^{tot}_1)}{\sigma^{tot}_0}$	$-3.0\,(5) \times 10^{-4}$	$-1.1\,(2) \times 10^{-4}$	$-3.6\,(9) \times 10^{-4}$

Table 1.5: The results for the fixed-$\mathcal{O}(\alpha)$ and the YFS-exponentiated total cross section from the MC program ZINHAC. The numbers in parentheses are statistical errors for the last digits.

As the above fixed-order results from ZINHAC have been obtained in the framework of the YFS-type multiphoton algorithm, they make us strongly confident in the correctness of the corresponding MC algorithm.

In Table 1.5 we give the results for the higher order corrections, beyond $\mathcal{O}(\alpha)$ to the total cross-section, as given in Eq. (1.8). The YFS-exponentiation corrections beyond $\mathcal{O}(\alpha)$ are $\sim 10^{-4}$, i.e. of the expected size of higher-order corrections. In Table 1.6 we present similar results to those shown in the

$2k_0/E_{CM}$	e		μ	
	$\max_i\{k_i^0\}$	$\sum_i k_i^0$	$\max_i\{k_i^0\}$	$\sum_i k_i^0$
0.01	33.43 (3)	34.02 (4)	19.62 (1)	19.83 (1)
0.05	21.26 (3)	21.92 (3)	11.99 (1)	12.21 (1)
0.10	15.64 (2)	16.30 (2)	8.65 (1)	8.86 (1)
0.15	12.35 (2)	13.00 (2)	6.75 (1)	6.96 (1)
0.20	10.08 (2)	10.69 (2)	5.46 (1)	5.65 (1)
0.30	7.01 (1)	7.56 (1)	3.75 (1)	3.91 (1)
0.40	5.02 (1)	5.49 (1)	2.65 (1)	2.79 (1)
0.50	3.59 (1)	4.00 (1)	1.88 (1)	1.99 (1)
0.60	2.52 (1)	2.87 (1)	1.30 (1)	1.40 (1)
0.70	1.69 (1)	1.98 (1)	0.86 (1)	0.93 (1)
0.80	1.02 (1)	1.24 (1)	0.50 (1)	0.56 (1)
0.90	0.46 (3)	0.63 (1)	0.22 (1)	0.26 (1)

Table 1.6: The fractions of events (in %) with sum of energies of all the photons greater than k_0 (denoted by $\sum_i\{k_i^0\}$) and at least one photon with energy greater than k_0 (denoted by $\max_i\{k_i^0\}$) from the MC program ZINHAC with the YFS-exponentiation for $E_{CM} = 90\,\text{GeV}$. The numbers in parentheses are statistical errors for the last digits.

Table 1.4 but this time obtained from ZINHAC with the YFS-exponentiation. The results corespond to two types of lower photon-energy cuts: $\max_i\{k_i^0\} \geqslant k_0$ and $\sum_i k_i^0 \geqslant k_0$. As we expected, the fractions of the corss-section with the sum of energies are always higher than the once with at least one photon with energy greater than k_0. Moreover, these results are in agreement with the results for the pure $\mathcal{O}(\alpha)$ QED correction presented in Table 1.4. For low values of $2k_0/E_{CM}$ we expect to see the strongest multiphoton corrections, and indeed for the $2k_0/E_{CM}$ valuse between $0.01-0.20$, we see that the fractions of cross-section in the case of pure $\mathcal{O}(\alpha)$ correction are significantly higher than in the case of YFS-exponentiation. From the value $2k_0/E_{CM} = 0.30$ and higher we see that in the case of the pure $\mathcal{O}(\alpha)$ corrections the fractions are in-between of the two types cuts used in the case of YFS-exponentiation. This is also what we expect, because for hard photons the multiphoton effects should not play an important role. In this case the cut on $max\{k_i\}$ for multiphoton radiation should give the results close to the once at $\mathcal{O}(\alpha)$, and this is what we observe in tables 1.4 and 1.6.

All this is a very similar to the QCD parton-shower corrections which we shall discuss in details in Chapter 2. The strongest effect in the parton shower, which is based on the multiple soft and/or collinear emissions, is at low scales and it gives no significant corrections at high scales, see Fig. 2.1.

All these tests make us strongly confident in the correctness of the constructed YFS MC algorithm and the corresponding matrix elements at the parton-level. Therefore, the last thing which we have to do is to ensure ourself that it also works at the hadron-level. This is the main subject of the next subsection.

1.7.2 Hadron-level tests – comparisons with SANC

In this part of the numerical tests we present hadron-level results of the tuned comparisons of the ZINHAC MC generator and the SANC program [72, 73, 74]. SANC is a Monte Carlo integrator base on the VEGAS [97]. It includes the stand-alone packages for calculation of the EW NLO corrections for the neutral and charged current Drell–Yan processes which are used by the WINHAC and ZINHAC MC generators.

Setup

For the numerical comparisons we considered the neutral current Drell–Yan-like process for the proton-proton collisions at the nominal LHC energy, $\sqrt{s} = 14$ TeV:

$$p + \bar{p} \longrightarrow Z + \gamma^* \longrightarrow l + \bar{l}, \tag{1.141}$$

where $l = e, \mu$.

Input parameters

All the results below, unless stated otherwise, have been obtained for the following input parameters[16]:

$$\begin{aligned}
G_\mu = 1.16637 \times 10^{-5}\ \text{GeV}^{-2}, \qquad & \alpha = 1/137.03599911, \quad \alpha_s(M_Z^2) = 0.1176, \\
M_Z = 91.1876\ \text{GeV}, \qquad & \Gamma_Z = 2.4924\ \text{GeV}, \\
M_W = 80.37399\ \text{GeV}, \qquad & \Gamma_W = 2.0836\ \text{GeV}, \\
M_H = 115\ \text{GeV}, & \\
m_e = 0.51099892\ \text{MeV}, \qquad & m_\mu = 0.105658369\ \text{GeV}, \\
m_\tau = 1.77699\ \text{GeV}, & \\
m_u = 0.06983\ \text{GeV}, \qquad & m_c = 1.2\ \text{GeV}, \quad m_t = 174\ \text{GeV}, \\
m_d = 0.06984\ \text{GeV}, \qquad & m_s = 0.15\ \text{GeV}, \quad m_b = 4.6\ \text{GeV}, \\
|V_{ud}| = 0.975, \qquad & |V_{us}| = 0.222, \\
|V_{cd}| = 0.222, \qquad & |V_{cs}| = 0.975, \\
|V_{cb}| = |V_{ts}| = |V_{ub}| = |V_{td}| = |V_{tb}| = 0. &
\end{aligned} \tag{1.142}$$

The results are presented in the fixed-width scheme, both in the $\alpha(0)$ and G_μ one-loop parametrization schemes. The quark masses are set to zero in the matrix element and in the kinematics. To compute the hadronic cross section we use the CTEQ6.1m set of parton density functions [99] and take the renormalization scale, μ_r, and the QED and QCD factorization scales, μ_{QED} and μ_{QCD}, to be $\mu_r^2 = \mu_{\text{QED}}^2 = \mu_{\text{QCD}}^2 = M_Z^2$.

Cuts

We impose only detector acceptance cuts on the leptons transverse momenta and the charged lepton pseudorapidity (η_ℓ):

$$p_{T,l} > 10\ \text{GeV}, \qquad |\eta_\ell| < 3.0, \qquad M_{l^+l^-} > 20\ \text{GeV}, \qquad \ell = e,\ \mu. \tag{1.143}$$

[16] The same parameters were used in the Ref. [98] page 5.

Z boson observables

We consider eight different observables which let us compare not only the total inclusive cross section but also various differential distributions.

- σ_Z: the total inclusive cross section of for the NC Drell–Yan process.

- $\frac{d\sigma}{dM_{l^+l^-}}$: invariant mass distribution of the final-state lepton-pair,

$$M_{l^+l^-} = \sqrt{(p_{l^+} + p_{l^-})^2}. \tag{1.144}$$

- $\frac{d\sigma}{d|y_{l^+l^-}|}$: rapidity distribution of the final-state lepton-pair,

$$y_{l^+l^-} = \frac{1}{2} \ln \frac{P^0_{l^+l^-} + P^3_{l^+l^-}}{P^0_{l^+l^-} - P^3_{l^+l^-}}, \qquad P_{l^+l^-} = p_{l^+} + p_{l^-}. \tag{1.145}$$

- $\frac{d\sigma}{dp_T^{l^+}}$: transverse lepton pluse momentum distribution,

$$p_T^{l^+} = \sqrt{(p^1_{l^+})^2 + (p^2_{l^+})^2}. \tag{1.146}$$

- $\frac{d\sigma}{dp_T^{l^-}}$: transverse lepton minus momentum distribution,

$$p_T^{l^-} = \sqrt{(p^1_{l^-})^2 + (p^2_{l^-})^2}. \tag{1.147}$$

- $\frac{d\sigma}{d|\eta_{l^+}|}$: lepton pluse pseudorapidity distribution,

$$\eta_{l^+} = -\ln \tan \frac{\theta_{l^+}}{2}, \tag{1.148}$$

  where θ_{l^+} is the polar angle of l^+ in the ılab frame.

- $\frac{d\sigma}{d|\eta_{l^-}|}$: lepton minus pseudorapidity distribution,

$$\eta_{l^-} = -\ln \tan \frac{\theta_{l^-}}{2}, \tag{1.149}$$

  where θ_{l^-} is the polar angle of l^- in the *lab* frame.

- A_{FB}: forward-backward asymmetry as a function of $M_{l^+l^-}$,

  $A_{\rm FB}$ is usually defined by

$$A_{\rm FB} = \frac{F-B}{F+B}\,, \tag{1.150}$$

  where

$$F = \int_0^1 \frac{d\sigma}{d\cos\theta^*}\, d\cos\theta^*, \qquad B = \int_{-1}^0 \frac{d\sigma}{d\cos\theta^*}\, d\cos\theta^*. \tag{1.151}$$

  Here, $\cos\theta^*$ is given by

$$\cos\theta^* = \frac{|P^3_{l^+l^-}|}{P^3_{l^+l^-}} \frac{2}{M_{l^+l^-}\sqrt{M^2_{l^+l^-}+(P^T_{l^+l^-})^2}} \left[p^+_{l^-}p^-_{l^+} - p^-_{l^-}p^+_{l^+}\right], \tag{1.152}$$

  with

$$(P^T_{l^+l^-})^2 = (P^1_{l^+l^-})^2 + (P^2_{l^+l^-})^2 \quad \text{and} \quad p^\pm = \frac{1}{\sqrt{2}}\left(p^0 \pm p^3\right). \tag{1.153}$$

Acceptances

For each observable we provide "BARE" results, i.e. without smearing and recombination of final-state particles four-momenta (only lepton separation cuts are applied).

1.7.3 Results

In this section we present the numerical results of the tuned comparisons between `SANC` and `ZINHAC` at the Born level (LO). In Table 1.7 we show the comparisons of the inclusive cross sections (in pb) within the acceptance cuts. The Born cross sections from SANC and ZINHAC agree well within statistical errors in the case of electrons. In the case of muons we see a small difference in the total cross sections which can be attributed to different treatment of the final-state lepton kinematics in the two programs: in ZINHAC the finite lepton masses are fully taken into account while in SANC the massless approximation for leptons is applied. This is also the reason why in the case of SANC the results for muons are the same (within statistical errors) as the ones for electrons, where the finite-mass effects are completely negligible.

In Figs. 1.10–1.16 the distributions are shown for all seven observables under consideration, both for the μ and e final-states in the scheme $\alpha(0)$. The lower

LHC, $pp \to Z + \gamma \to e^+e^- + X$		
	α-scheme	G_μ-scheme
SANC	1331.847(2)	—
ZINHAC	1331.843(6)	1432.287(7)
LHC, $pp \to Z + \gamma \to \mu^+\mu^- + X$		
	α-scheme	G_μ-scheme
SANC	1331.843(3)	—
ZINHAC	1331.781(6)	1432.245(7)

Table 1.7: The tuned comparisons of the LO predictions for σ_Z from SANC and ZINHAC for the "BARE" Cuts. The statistical errors of the Monte Carlo integration are given in parentheses.

parts of the figures shows the relative deviation $\Delta = (\mathrm{Z}-\mathrm{S})/\mathrm{Z}$ between the two calculations (Z for ZINHAC, S for SANC). All the presented above distributions agree very well – within the per-mil (M_{ll}, $p_T^{l^\pm}$) or even sub-permil level (y_{ll}, $\eta_{l^\pm}$). This make us strongly confident in the correctness of the implementation of the hadron-level part in ZINHAC. Particularly important and strong test of the kinematic construction and hadron-level implementation is the presented below comparison of the forward-backward asymmetry distribution as a function of $M_{l^+l^-}$. The both programs give a consistent description of this observable.

The tuned comparisons of the SANC and ZINHAC programs including the $\mathcal{O}(\alpha)$ QED corrections (NLO) are in progress and will be presented in the separate publication in the near future [16].

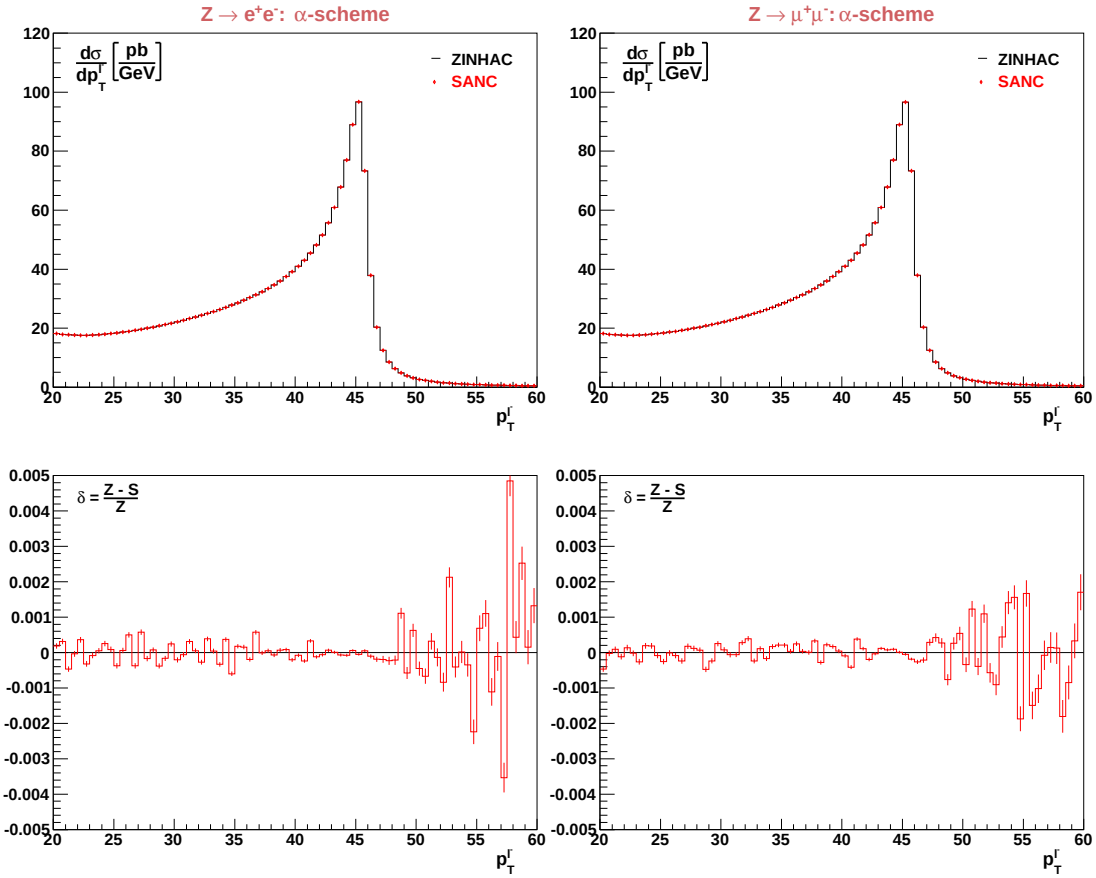

Figure 1.10: The Born distributions of $p_T^{l^-}$ from SANC (red diamonds) and ZINHAC (solid lines) for electrons and muons in final state and their relative deviations $\delta = \frac{\mathrm{Z-S}}{\mathrm{Z}}$.

1.8 Summary and outlook

In this part of the thesis we have presented a new member of the Krakow YFS Monte Carlo event generator family called ZINHAC. ZINHAC is the dedicated Monte Carlo event generator for precision description of the neutral-current Drell–Yan process, i.e. Z/γ^* production with leptonic decays in hadronic collisions. ZINHAC features multiphoton radiation within the Yennie–Frautschi–Suura exclusive exponentiation scheme with $\mathcal{O}(\alpha)$ electroweak corrections and is able to generate weighted as well as unweighted (weight = 1) events.

In order to construct ZINHAC, we first performed the calculations of the YFS exponentiation in the leptonic Z-boson[17] decays. We have provided the

[17] All our calculations include virtual photon γ^* and the full interference between γ^* and Z in the Drell–Yan-like process, but for the convenience we shall refer in the following to this process as to Z-boson production.

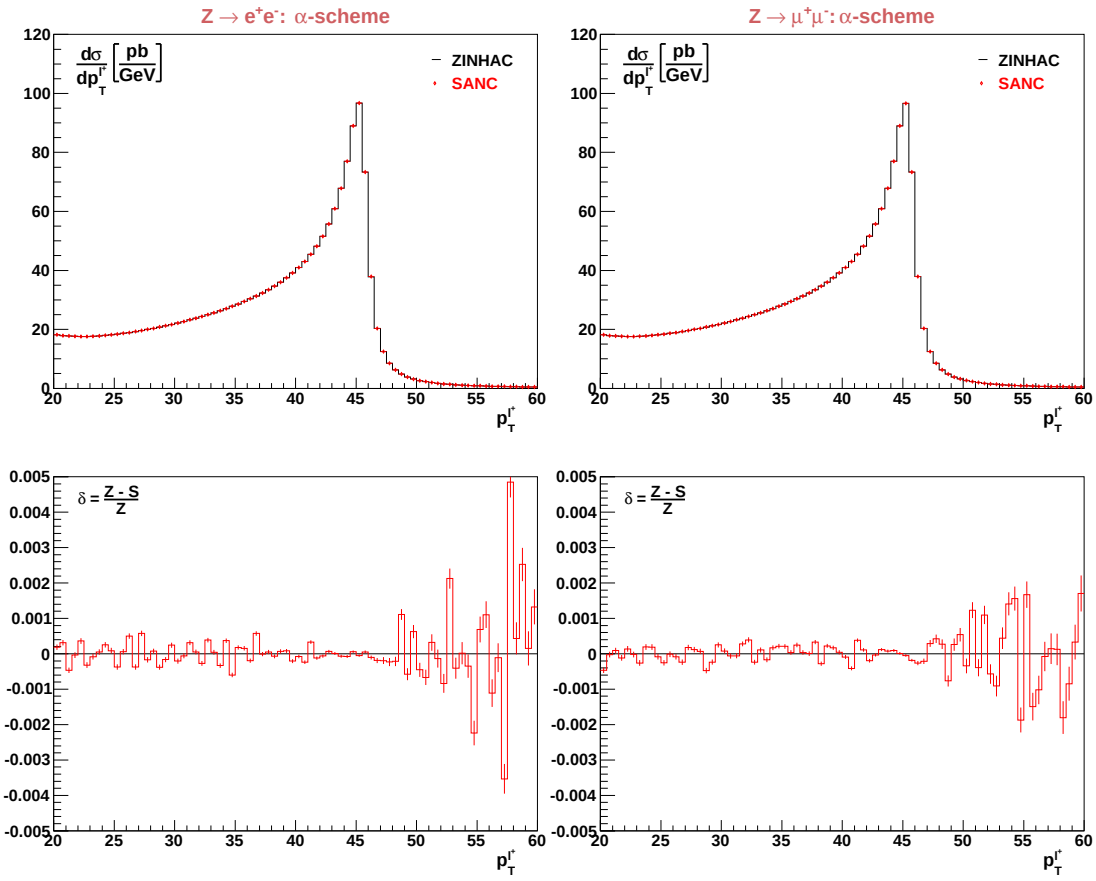

Figure 1.11: The Born distributions of $p_T^{l^+}$ from `SANC` (red diamonds) and `ZINHAC` (solid lines) for electrons and muons in final state and their relative deviations $\delta = \frac{\mathrm{Z-S}}{\mathrm{Z}}$.

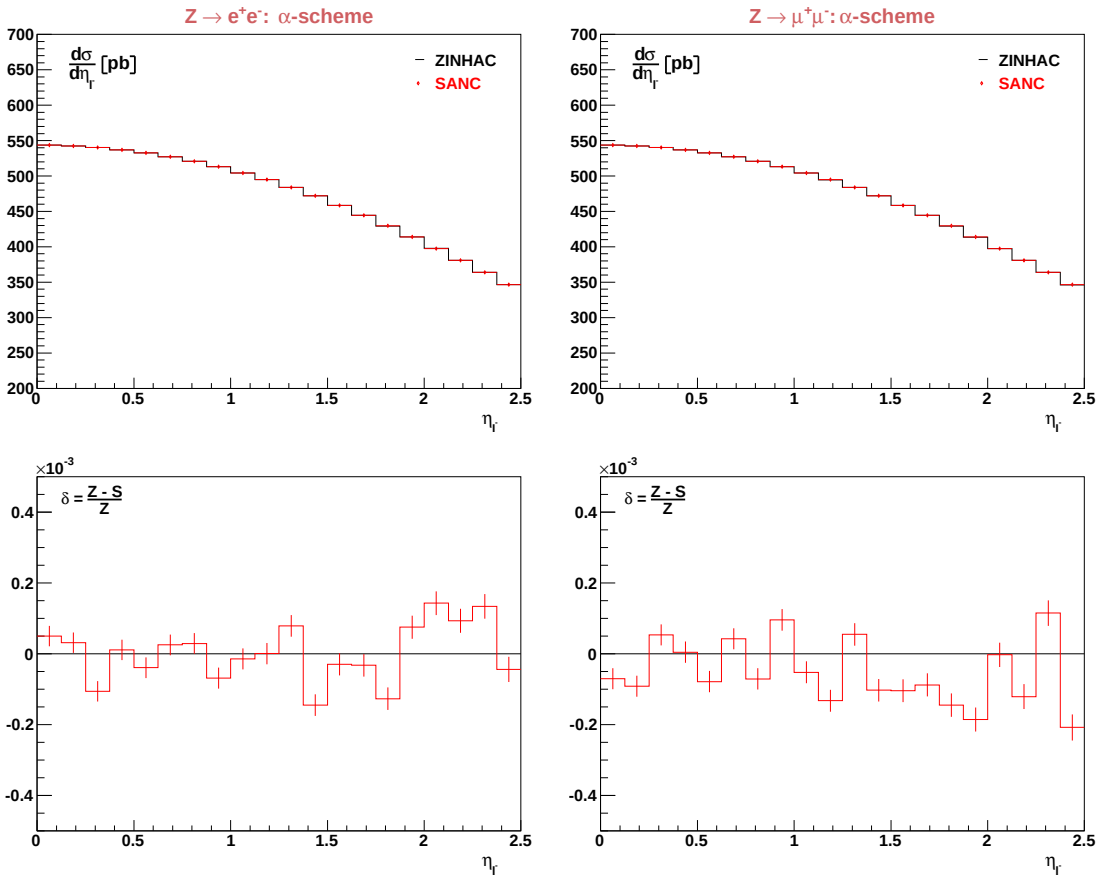

Figure 1.12: The Born distributions of η_{l^-} from SANC (red diamonds) and ZINHAC (solid lines) for electrons and muons in final state and their relative deviations $\delta = \frac{Z-S}{Z}$.

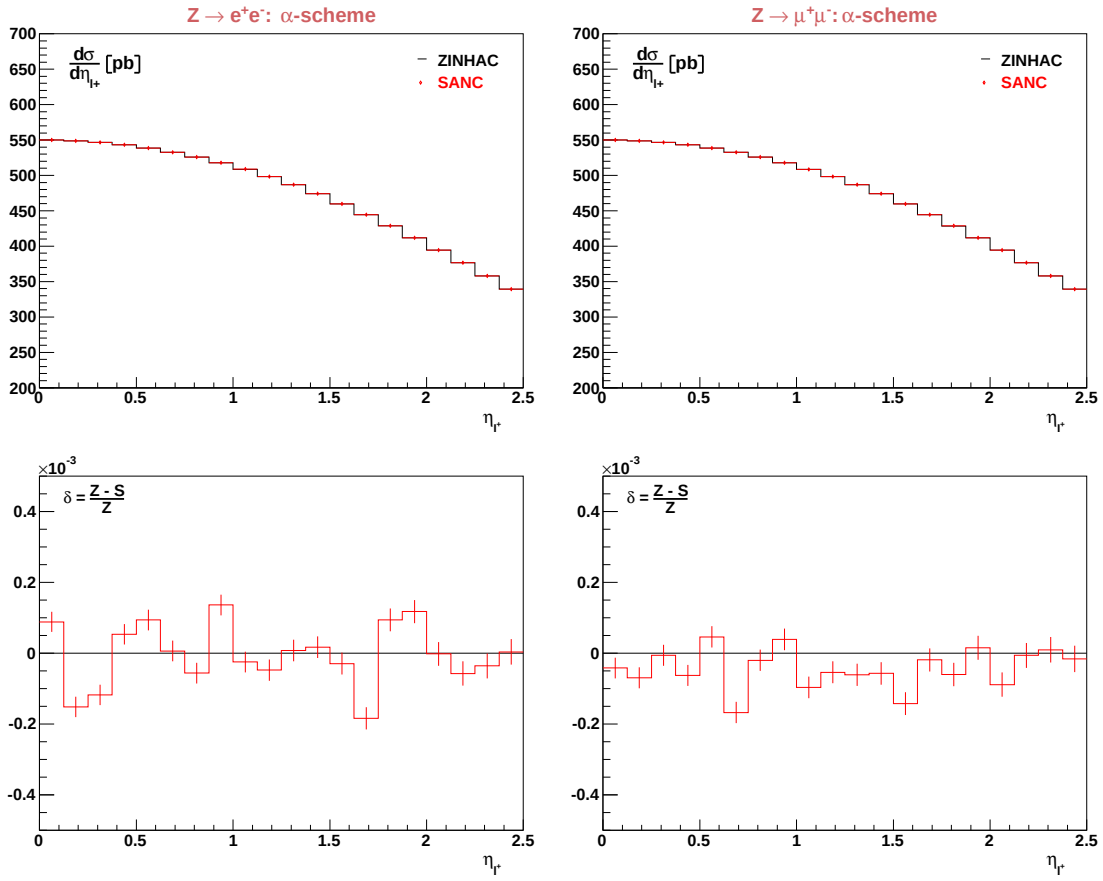

Figure 1.13: The Born distributions of η_{l^+} from `SANC` (red diamonds) and `ZINHAC` (solid lines) for electrons and muons in final state and their relative deviations $\delta = \frac{\mathrm{Z-S}}{\mathrm{Z}}$.

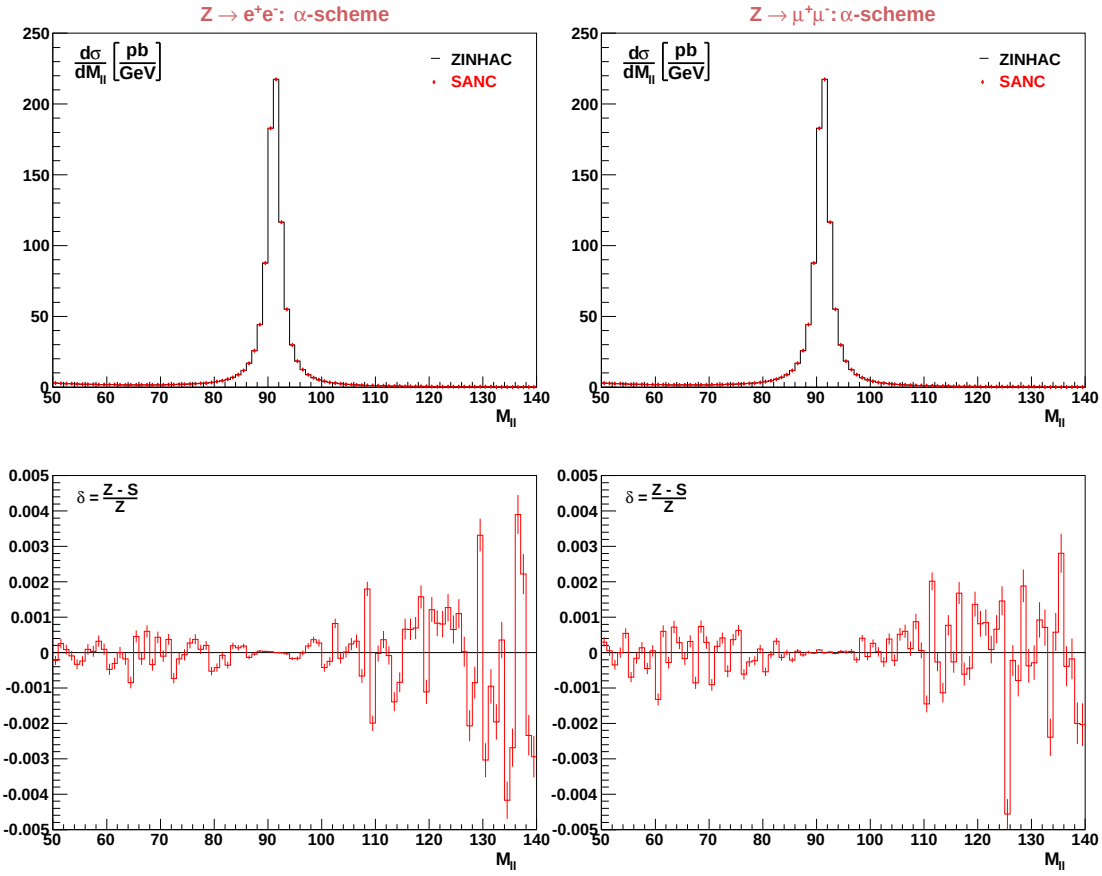

Figure 1.14: The Born distributions of M_{ll} from `SANC` (red diamonds) and `ZINHAC` (solid lines) for electrons and muons in final state and their relative deviations $\delta = \frac{Z-S}{Z}$.

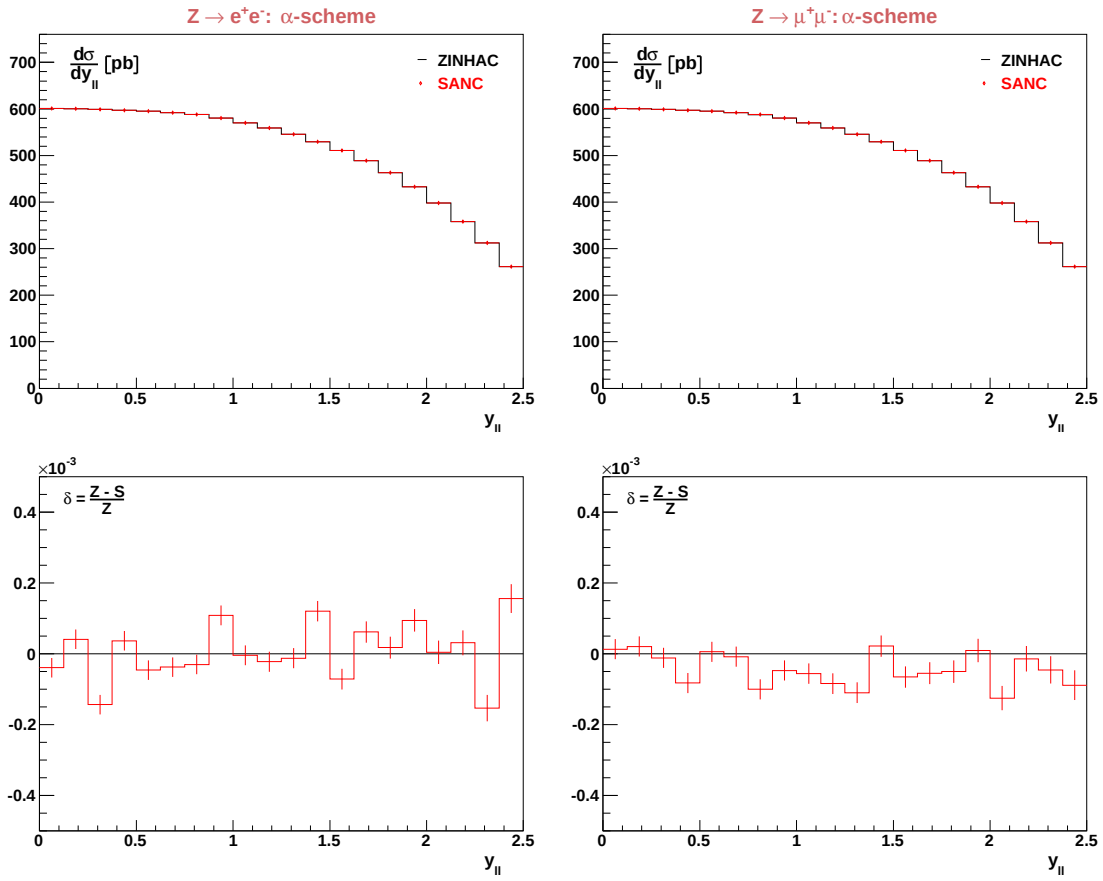

Figure 1.15: The Born distributions of y_{ll} from `SANC` (red diamonds) and `ZINHAC` (solid lines) for electrons and muons in final state and their relative deviations $\delta = \frac{\mathrm{Z-S}}{\mathrm{Z}}$.

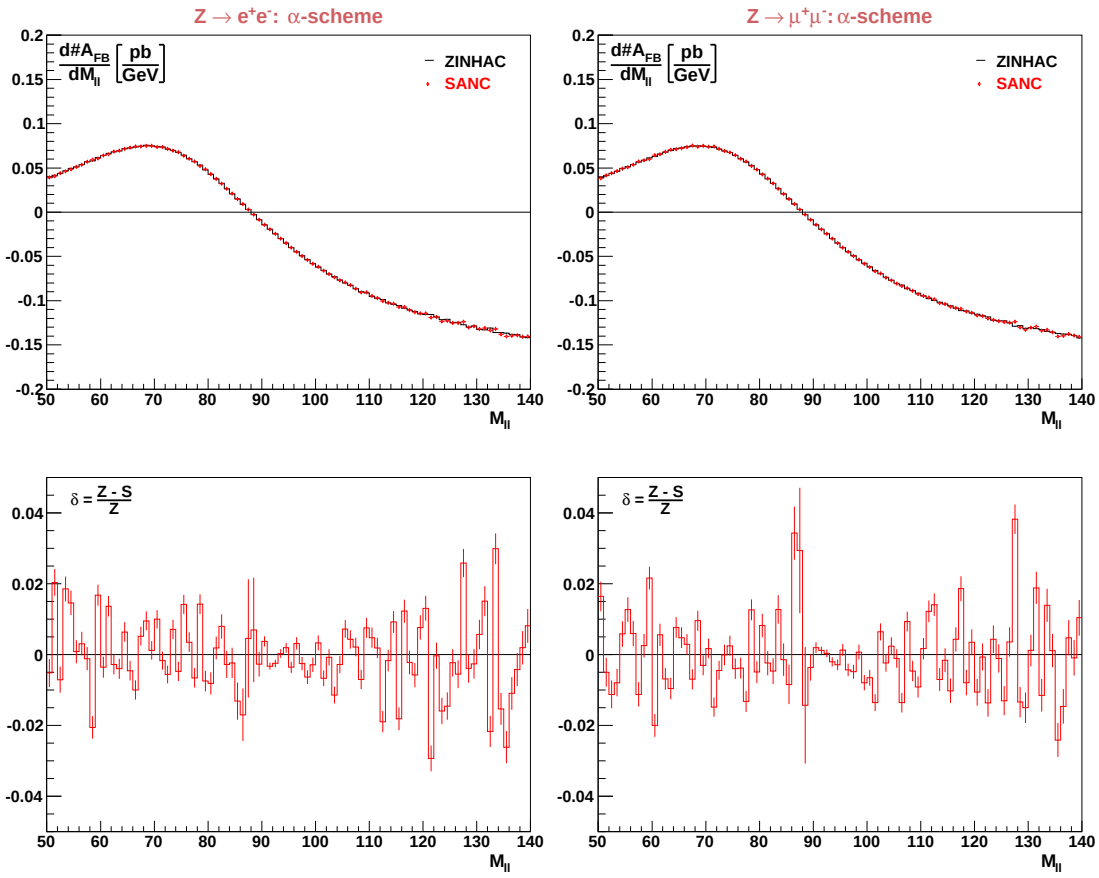

Figure 1.16: The Born distributions of A_{FB} from SANC (red diamonds) and ZINHAC (solid lines) for electrons and muons in final state and their relative deviations $\delta = \frac{\mathrm{Z-S}}{\mathrm{Z}}$.

fully massive spin amplitudes for the single Z-boson production and decay, including the single-real-photon radiation in both Z decay and production, the latter is needed for the inclusion of the initial-final state interface effects. Spin amplitudes allow for studies of the spin-dependent effects in the neutral-current Drell-Yan process. For example, ZINHAC is able to provide separate generations of processes with pure-transversely or pure-longitudinally polarized Z-bosons at the Born level.

All this has been implemented in the Monte Carlo event generator ZINHAC. For this purpose, an efficient multiphoton Monte Carlo algorithm has been developed. The parton-level process is convoluted with the parton distribution functions (PDFs) provided by the LHAPDF package [100, 101]. This package includes a large set of recent PDF parametrisations by several groups.

The ZINHAC Monte Carlo generator has been implemented using a modern computer program development techniques, including C++, SVN, XML,

Doxygen, VisualParadigm, cmake and Trac. This makes ZINHAC easy to maintain (C++, SVN, cmake) and provide a very good feedback to the future users (Doxygen documentation, Trac ticket system, etc.).

Finally, we have performed several tests of the ZINHAC. The spin amplitudes have been cross-checked with the independent analytical representations of the appropriate matrix elements and they have been found to be in very good numerical agreement. We have also performed several numerical tests of the implemented MC algorithm, both at the parton and hadron level. The presented results make us strongly confident in the correctness of the constructed YFS MC algorithm and its implementation into the ZINHAC MC program. Numerically, the YFS-exponentiation corrections beyond the fixed $\mathcal{O}(\alpha)$ calculations are at the level of $\sim 10^4$ for the total cross section, which is the result of the KLN-theorem. However, for some distributions they can be much more significant, for example they are very important for the precision measurement of the $\sin^2\theta_{\mathrm{W}}$ and W-bosons mass, see Chapter 3 for more details.

In the future we plan to implement also the QED interferences between the initial and final-state radiation and the $\mathcal{O}(\alpha)$ weak corrections for the full process. This can be achieved by using the method described in the Subsection 3.2.5. We would like also to perform additional tests, including comparisons of the higher order corrections at the hadron-level with the SANC MC integrator. Then we would like to use ZINHAC for the studies of the influence of the QED and the weak corrections on the measurements of the Standard Model parameters at the LHC and, finally, for the data analysis of the LHC experiments.

Chapter 2

A model of non-perturbative gluon emission in an initial state parton shower

Abstract

The transverse momentum of electroweak bosons in the Drell-Yan process is an important quantity for the experimental program at the LHC. In this Chapter we consider a model of transverse momentum distribution in which non-perturbative smearing takes place throughout the perturbative evolution, by a simple modification to an initial state parton shower algorithm. This new model gives a good description of this quantity for the data taken in previous experiments over a wide range of CM energy. The model's prediction for the transverse momentum distribution of the Z-bosons for the LHC is presented and compared with other approaches.

This chapter is based on the following publications [102], [103].

2.1 Introduction

In this chapter we will concentrate on one particular property of the produced W and Z bosons[1], namely their transverse momentum distribution. This is interesting from the QCD point of view as, sweeping across the distribution, one has regions dominated by hard perturbative emission, multiple soft and/or collinear, but still perturbative, emission, and truly non-perturbative confinement effects, see Fig. 2.1. It is also an important quantity for the experimental

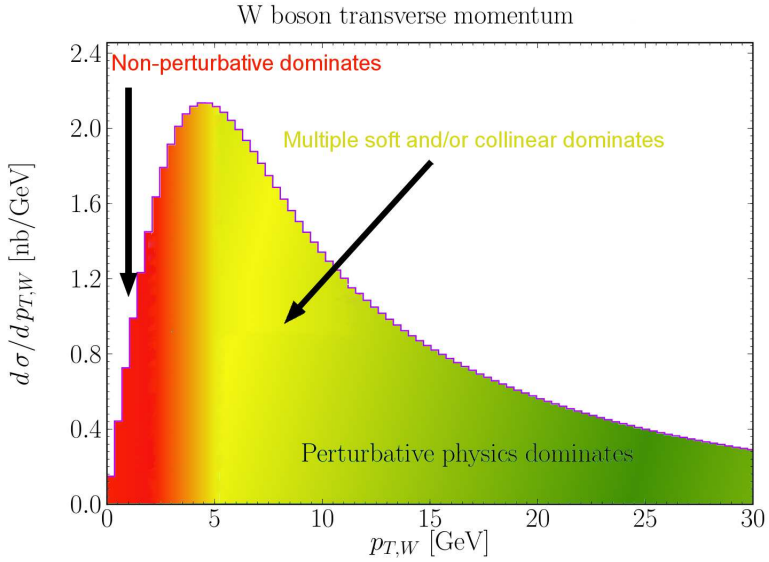

Figure 2.1: The W boson transverse momentum distribution. Colours illustrate the parts of the distribution dominated by non-perturbative confinement effects (red – low p_T), multiple soft and/or collinear approximation (yellow – the middle part of the distribution) and perturbative physics (green – hight p_T).

programme, because the W reconstruction efficiency is transverse momentum dependent, having a direct effect on the ultimate precision of the W mass measurement (see Chapter 3 for details) as well as helping to understand the signature for the Higgs boson production at either the Tevatron or the LHC [104]. Although the experiments measure the Z transverse momentum distribution and use this to infer that of the W, the extent to which the effects are non-universal limits the ultimate accuracy of the measurement, unless elaborate

[1]We are also interested in virtual photons with invariant masses well below that of the Z, particularly for tuning and validating our model. All our calculations include properly the full interference between γ^* and Z, but with an eye on the ultimate application at the LHC, we continue to refer in this introduction to Zs.

tricks as proposed in Ref. [105] are used. Thus, a deeper theoretical understanding and more reliable models are certainly needed.

The two approaches to predicting the transverse momentum distribution are analytical resummation [106, 107, 108, 109, 110, 111, 67] and parton shower (PS) algorithms [7, 112, 113] (there have also been attempts to combine the two approaches [114]). We will focus on the latter, but will draw a few comparisons with the former later on. The parton shower approach starts from the tree-level matrix element, usually supplemented by 'matrix element corrections' [115, 116, 113, 117, 118, 119] that use higher-order tree-level matrix elements to describe emission at scales of the order of the W or Z boson mass and higher[2]. These give a significant tail of events with very high transverse momenta. The hard events are then evolved down to low scales by using the backward evolution parton shower approach [7].

2.1.1 Parton Showers

The parton shower evolution is necessary for a good description of observables, such as, the transverse momentum of electroweak bosons in hadronic collisions which is discussed in this Chapter. This is because there are kinematic regions where higher-order terms in the perturbative expansion are enhanced[3], therefore, have to be included in the calculations. Unfortunately, the complete perturbative calculations have been typically performed at the leading order (LO) in QCD. Next-to-leading order (NLO) calculations are available for many processes and even one further order in α_s, NNLO calculations are available in some special cases [122]. Due to the roughly factorial growth in complexity one cannot expect much higher orders to be computed soon. On the other hand the parton shower algorithm instead of aiming for a precise prediction to some fixed order in perturbation theory give an approximate description in which such enhanced terms are taken in to account to all orders. The source of these enhanced terms are collinear and soft singularities in QCD which have similar origin to the IR singularities in the QED which were discussed in Section 1.1. Parton shower algorithms give an approximate description of these effects to

[2] We do not go into their details, but use the implementation of [120] throughout this paper.

[3] These enhancements due to collinear and soft singularities can be easily seen for example by the examination of the behaviour of the cross section of $e^+e \to 3$ *partons* when two of the parton momenta become collinear or one parton momentum becomes soft, see for example Ref. [121].

all orders, by working in the collinear limit and to the leading-logarithmic accuracy. The short description of the parton shower in this sections is based on Refs. [123, 124].

(a) Single branching

The collinear enhancements are associated with a parton branching. Such a single branching of parton a into partons $b + c$ is depicted in Fig. 2.2. The

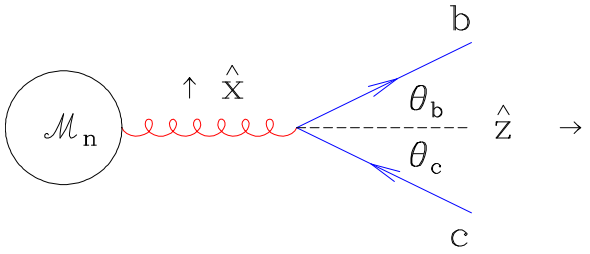

Figure 2.2: Timelike branching.

blob represents the rest of the diagram. That means that a is an outgoing parton with $p_a^2 \equiv t > 0$, which is called *timelike* branching. The branching of an incoming parton is called *spacelike* branching, due to the negative virtuality ($t < 0$) of the parton there. The opening angle is $\theta = \theta_b + \theta_c$. With the energy fractions

$$z = \frac{E_b}{E_a} = 1 - \frac{E_c}{E_a}, \tag{2.1}$$

t is given, in the the collinear limit, by[4]

$$t = 2E_bE_c(q - \cos\theta) = z(1-z)E_a^2\theta^2. \tag{2.2}$$

θ can be expressed in terms of θ_b or θ_c as $\theta = \frac{\theta_b}{1-z} = \frac{\theta_c}{z}$. The different possible branchings are $g \to gg$, $g \to q\bar{q}$ and $q \to qg$, where g denotes gluon and q quark. Using the small angle approximation one finds that the matrix element squared for these $n+1$ particle processes can be expressed in terms of the n particle matrix element as

$$|\mathcal{M}_{n+1}|^2 \sim \frac{4g_{coup}^2}{t}\hat{P}_{ba}(z)|\mathcal{M}_n|^2, \tag{2.3}$$

where g_{coup} is the coupling constant which determines the strength of the interaction between coloured quanta. The additional factors $\hat{P}_{ba}$ are the so-called

[4] assuming that $p_b^2, p_c^2 \ll p_a^2$

unregularised, massless splitting functions related to the Altarelli–Parisi kernels see for example Chapter 4 of Ref. [123]. For the three possible splittings, they are given by

$$\begin{aligned}\hat{P}_{gg}(z) &= 3\left[\frac{1-z}{z}+\frac{z}{1-z}+z(1-z)\right],\\ \hat{P}_{pg}(z) &= \frac{1}{2}[z^2+(1-z)^2],\\ \hat{P}_{gg}(z) &= \frac{4}{3}\frac{1+z^2}{1-z}.\end{aligned} \tag{2.4}$$

The differential cross section can be expressed using the splitting functions, as long as the dependence on the azimuthal angle ϕ of the branched parton is integrated out,

$$d\sigma_{n+1} = d\sigma_n \frac{dt}{t} dz \frac{\alpha_s}{2\pi}\hat{P}_{ab}(z). \tag{2.5}$$

One finds that exactly the same formula also describes spacelike branchings. This universality of hierarchical emissions is known as factorisation of collinear singularities.

(b) Multiple branching

The aim of a parton shower algorithm is now to simulate according to Eq. (2.5) the ensemble effects of multiple parton branchings. Introducing the cut-off scale $Q_0^2 \equiv t_0$ imposes a resolution parameter, such that branchings that are softer or more collinear[5] than that are not distinguishable from no branching at all, i.e. *unresolvable*. By invoking unitarity (requiring the sum of branching plus nobranching probabilities to be one), the cancellation between the divergent parts of the splitting functions and the corresponding loop diagrams is implicitly handled. Let us consider only one type of branching, for example multiple gluon radiation from spacelike quark, see Fig. 2.3. A incoming quark from the hadron A, initially with a low virtuality mass-squared $-t_0$ and carrying a fraction x_0 of the hadron's momentum, moves to more virtual masses and lower momentum fractions by successive small-angle emission. Eventualy it participates in a hard scattering process at a scale Q^2. The cross section for the hard scattering process will depend on the scale Q^2 and on the momentum fraction distribution of the parton $f(x, Q^2)$. The integral equation for $f(x, t)$

[5] The boundaries of the z integration will also depend on t to regularise the divergences in $\hat{P}_{ba}(z)$ at $z = 1$ by $z < 1 - \varepsilon(t)$.

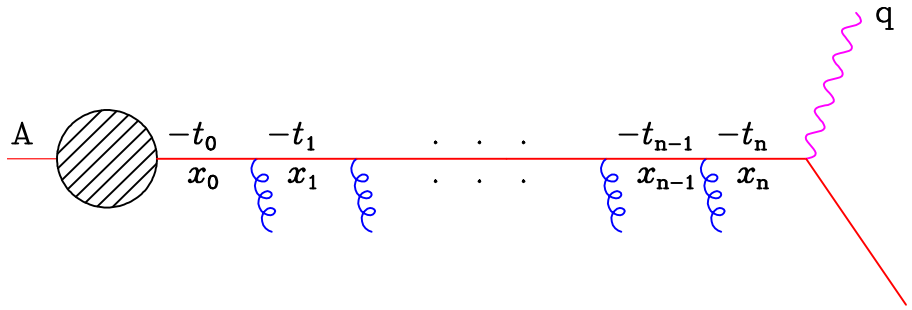

Figure 2.3: Multi-gluon branching processes for the initial-state branching in deep inelastic scattering.

in therms of the initial parton distribution $f(x,t_0)$ can be written as follows:

$$f(x,t) = \Delta(t) f(x,t_0) + \int_{t_0}^{t} \frac{dt'}{t'} \frac{\Delta(t)}{\Delta(t')} \int \frac{dz}{z} \frac{\alpha_s}{2\pi} \hat{P}(z) f(x/z,t). \tag{2.6}$$

where $\Delta(t)$ is so called the Sudakov form factor [125], $\Delta(t)$,

$$\Delta(t) \equiv \exp\left[- \int_{t_0}^{t} \frac{dt'}{t'} \int dz \frac{\alpha_s}{2\pi} \hat{P}(z) \right]. \tag{2.7}$$

The Sudakov form factor has a simple physical interpretation, it gives the probability for a parton i to evolve from t_0 to t without any *resolvable* emission. Therefore, Eq. (2.6) can be read in the following way, the first term on the right-hand side of the equation is the contribution from *branching paths* that do not branch between scales t_0 and t. The second term is the contribution from all *paths* which have their last branching at the scale t'. The factor $\Delta(t)/\Delta(t')$ represents the probability of evolving from t' to t without branching. The generalization of Eq. (2.7) to take into account of several types of partons is straightforward. Each parton species i has its own form factor $\Delta_i(t)$, which describes its probability of evolving from t_0 to t without branching. Since the branching probability has to be summed over all possible $i \to j$, we have

$$\Delta_i(t) \equiv \exp\left[- \sum_j \int_{t_0}^{t} \frac{dt'}{t'} \int dz \frac{\alpha_s}{2\pi} \hat{P}_{ij}(z) \right], \tag{2.8}$$

where $\hat{P}_{ij}(z)$ is the unregularised $i \to j$ spliting function.

Now, we need to find a Monte Carlo prescription how to generate the values for the virtual mass scale t and momentum fraction x according to Eq. (2.6) for a single evolution step, say $(t_1,x_1) \to (t_2,x_2)$. The variable t_2 will have the correct probability distribution, if the equation

$$\frac{\Delta(t_2)}{\Delta(t_1)} = r \tag{2.9}$$

is solved for t_2, with r being a uniformly distributed random number, $r \in [0,1]$. If the value t_2 is higher then the hard subprocess scale Q^2, this means that no further branching occurs (*stopping rule*). Otherwise, we have to generate the value of the momentum fraction $z = \frac{x_2}{x_1}$ for the next branching, with a probability distribution proportional to $(\alpha_s/2\pi)P(z)$ where $P(z)$ is the appropriate spliting function. We can do this by solving the equation

$$\int_{\varepsilon}^{x_2/x_1} dz \frac{\alpha_s}{2\pi} P(z) = r' \int_{\varepsilon}^{1-\varepsilon} dz \frac{\alpha_s}{2\pi} P(z) \tag{2.10}$$

where r' represents another random number in the interval $[0,1]$ and ε is the IR cut-off for resolvable branching. The algorithm is then recursively applied to each of the products of this branching till the moment when *stopping rule* is reached. The values of (t_i, x_i) generated by successive application of the algorithm define the virtual masses and momentum fractions of the exchanged quark, from which momenta of the emitted gluons can be computed. The azmiuthal angles of their emission are generated from the uniform distribution in the range $[0, 2\pi]$.

The evolution described above generates what is known as *forward* evolution. The evolution of spacelike partons (*backward* evolution) must take into account, that these partons are extracted from the incoming hadrons. This can be consistently done, by modifying Eq. (2.9) in the following way

$$\frac{f_i(x,t_1)\Delta_i(t_2)}{f_i(x,t_2)\Delta_i(t_1)} = r \tag{2.11}$$

where parton i evolves backwards from (t_2, x) to (t_1, x). The remaining variables to generate are the momentum fraction z and azimuthal angle ϕ. When averaging over ϕ, a simple uniform distribution $\phi \in [0, 2\pi]$ can be chosen. In the timelike case z was distributed according to $\frac{\alpha_s}{2\pi} P_i(z)$, whereas in the spacelike case $(t', x') \to (t, x)$ according to $\frac{\alpha_s}{2\pi} \frac{P_i(z)}{z} f_i(x'/z, t)$.

(c) Coherent branching

Such an algorithm of multiple branchings treats all leading collinear logarithms, arising from the $\frac{dt}{t}$ term, correctly. However, there are also important soft logarithms, from $\frac{dz}{z}$ terms, for gluon emissions. After averaging over azimuthal angle, their interference is completely destructive. It has been shown [112, 126, 127, 128, 129, 130, 131, 132, 133, 134] that whenever soft gluon emissions are considered, branchings that are not angular ordered do not give

any leading logarithmic contributions. A major success of the original HERWIG program was its treatment of soft gluon interference effects, in particular the phenomenon of colour coherence, via the angular ordering of emissions in the parton shower. Herwig++ simulates parton showers using the coherent branching algorithm of [113], which generalises that used in the original HERWIG program [112, 135, 136]. The new algorithm which we use in our studies retains angular ordering as a central feature and improves on its predecessor in a number of ways, the most notable of these being:

- a covariant formulation of the showering algorithm, which is invariant under boosts along the jet axis;
- the treatment of heavy quark fragmentation through the use of mass-dependent splitting functions [137] and kinematics, providing a complete description of the so-called dead-cone region.

For more details on the parton shower evolution, see for example Refs. [123, 124].

2.1.2 'Intrinsic' transverse momentum

Recoil from the gluons emitted[6] during this evolution builds up a transverse momentum for the W or Z. The evolution terminates at some scale of the order of the confinement or a typical hadron mass scale. However, the confinement effects, described for example as the Fermi motion of partons within the hadron, mean that the partons initiating the shower should have a non-perturbative transverse momentum distribution, often described as their 'intrinsic' transverse momentum, which is also transferred to the W or Z by the recoil [107].

Analysis of higher order corrections shows that the scale of the running coupling used in this evolution should be of the order of the transverse momentum of the emission [138,139], and once this is done, one must introduce an infrared cutoff in the transverse momentum that is active during every step of the evolution. That is, the probability of each backward step in the evolution variable, even at large values of that variable, is logarithmically dependent on the cutoff. In Ref. [140], authors advocated the view that conventional infrared

[6] Together with other backward-evolution steps, such as an incoming sea quark being evolved back to an incoming gluon by emitting a corresponding antiquark.

cutoff scales on perturbative emission (in that case on the transverse momenta used to describe the minijet production in an underlying event model) should be thought of as infrared *matching* scales, with a non-perturbative model of emission below the cutoff supplementing the usual perturbative one above. In this paper we propose such a model for the backward evolution in which an additional non-perturbative component at low transverse momentum provides additional smearing at each step of the evolution.

2.1.3 Motivation

In order to fit existing data, as we have mentioned above the conventional backward evolution parton shower approach needs to be supplemented by the so-called intrinsic (or 'primordial') transverse momentum k_T distribution of partons initiating the shower. The physical motivation behind this additional non-perturbative ingredient is the Fermi motion of partons within a hadron. Therefore, its average value per parton can be estimated, based solely on the proton size and uncertainty principle to be of the order of 0.3–0.5 GeV. But the values extracted from data are, first of all, too large and, secondly, grow with collision energy, which cannot be explained by the Fermi motion. For example, in Herwig++ its value grows from $k_T = 0.9$ GeV, which is needed to describe the data taken at the energy $\sqrt{S} = 62$ GeV (the experiment R209), to 2.1 GeV which, is needed at the Tevatron energies ($\sqrt{S} = 1800$ GeV). This motivated us to propose a model for backward evolution in which an additional non-perturbative component at low transverse momentum provides additional smearing at each step of the evolution. By construction, we expect more non-perturbative smearing for longer parton shower evolution ladder which might cure the problem of dependence on the centre-of-mass energy as well as on the size of the needed intrinsic smearing, which in our studies is kept, according to the Fermi motion argumentation, fixed at 0.4 GeV. Therefore, in this chapter we ask the question whether, with this additional source of the non-perturbative transverse momentum, a truly intrinsic transverse momentum distribution for the initial partons, that does not depend on the collision energy or type, is sufficient. In Fig. 2.4 we show the comparison of the Z–boson transverse momentum spectrum at the Tevatron Run I with the CDF data [141]. The left panel shows that such a description is possible up to large transverse momenta. The high transverse momentum region is, however, dominated by contributions from hard gluon emissions. These will not be the focus of this paper. In

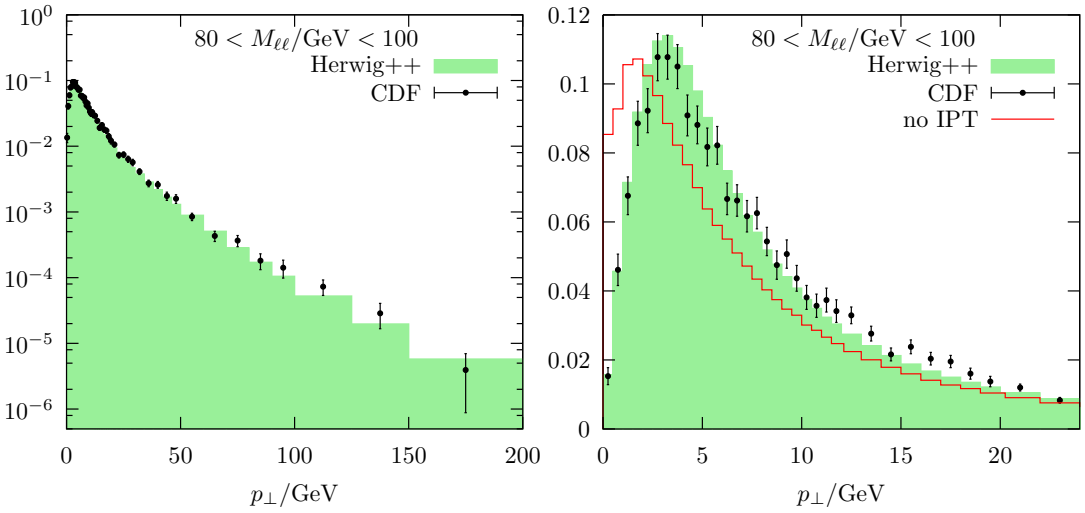

Figure 2.4: The transverse momentum distribution of the Z bosons at the Tevatron energies compared to the CDF data, up to large transverse momenta (left) and only for the small $p_\perp$ region (right). The line denoted "no IPT" is from Herwig++ with intrinsic transverse momentum off.

general, the large transverse momentum region will not be affected by soft, non–perturbative emissions.

In the right panel of Fig. 2.4 we see only the small transverse momentum region. The Herwig++ result is shown with the intrinsic $p_\perp = 2.1\,\text{GeV}$ from the Gaussian smearing [120], which is the default value at Tevatron energies. To show the importance of this effect, we also plot the result with the intrinsic $p_\perp$ set to zero. Clearly, this non–perturbative Gaussian smearing only affects the region of small transverse momenta. At the large boson $p_\perp$, the recoil against the hard, perturbative gluon radiation dominates the spectrum.

We also compared to the D0 data [142] and found a similar agreement. However, the CDF data has a finer binning and is therefore more suitable for our comparison.

2.2 Description of the model

The implementation of transverse momentum generation, in which non-perturbative smearing takes place throughout the perturbative evolution, was achieved by a simple modification to an initial-state parton shower algorithm. The model was implemented in the framework of Herwig++, in which the Sudakov form factor for the backward evolution from some scale $\tilde{q}_{\max}$ down to

$\tilde{q}$ takes the form

$$\Delta(\tilde{q}; p_{\perp_{\max}}, p_{\perp_0}) = \exp\left\{ - \int_{\tilde{q}^2}^{\tilde{q}^2_{\max}} \frac{d\tilde{q}'^2}{\tilde{q}'^2} \int_{z_0}^{z_1} dz \frac{\alpha_s(p_\perp)}{2\pi} \frac{x' f_b(x', \tilde{q}'^2)}{x f_a(x, \tilde{q}'^2)} P_{ba}(z, \tilde{q}'^2) \right\}, \tag{2.12}$$

with $x' = x/z$, for further details cf. Ref. [113].

The argument of the strong coupling α_s in Eq. (2.12) is the transverse momentum $p_\perp$ of an emission[7]. The cut-off scale represented by $p_{\perp_0}$ is needed to avoid divergence (the Landau pole) of the strong coupling. Below the cut-off scale α_s is equal to zero and, consequently, the derivative of the Sudakov form factor is equal to zero, which translates to zero probability of the gluon emission below $p_{\perp_0}$. Therefore, the two arguments of the Sudakov form factor, $p_{\perp_{\max}}$ and $p_{\perp_0}$, are not the evolution variables but only explicitly specify the available phase-space of the emission.

In order to populate the phase-space below $p_{\perp_0}$ by additional non–perturbative emissions, we introduce the additional Sudakov form factor Δ_{NP}, such that

$$\Delta(\tilde{q}; p_{\perp_{\max}}, 0) = \Delta_{\text{pert}}(\tilde{q}; p_{\perp_{\max}}, p_{\perp_0}) \Delta_{\text{NP}}(\tilde{q}; p_{\perp_0}, 0) \tag{2.13}$$

We achieve this by extending $\alpha_s(p_\perp)$ into the non-perturbative region using the following model

$$\alpha_s(p_\perp) = \begin{cases} \varphi(p_\perp), & p_\perp < p_{\perp_0}, \\ \alpha_s^{(\text{pert})}(p_\perp), & p_\perp \geq p_{\perp_0}. \end{cases} \tag{2.14}$$

In this way, the kinematics and phase space of each non–perturbative emission are exactly as in the perturbative case. We only modify their probabilities in the region of small transverse momenta. In Fig. 2.2 we show how the phase space expressed in terms of parton shower variables $\tilde{q}$ and z is populated by gluons without (top plot) and with our non-perturbative model (bottom plot). The two lines (solid and dashed) on each plot denote the lines along which $p_\perp$has a constant value[8] (isolines). The solid line is the isoline with $p_\perp = 0$ GeV and the dashed line with $p_\perp = 1$ GeV. In general, isolines with higher $p_\perp$ are situated closer to the left-top corner of the plot. We can clearly see that, as we wanted, our model introduced additional soft radiation in the region

[7] In Herwig++, the argument of α_s is a slightly simplified expression, equal to the transverse momentum to the required accuracy, but not exactly. We have tested the implementation of our model with this simplified expression and the exact expression for transverse momentum, and found very similar results. We therefore use the default expression.

[8] The value of $p_\perp$ is completely determined by the $\tilde{q}$ and z.

between $0 < p_\perp < 1$. We can also observe that there is a remaining small part of the phase space which is not available for the gluon emission. This is because we have to keep the cut-off on the parton shower variables $\tilde{q}$ – in the case of Fig. 2.2 it was set to 1 GeV. This small remaining non-populated area is the reasons for us to keep a small value of the intrinsic smearing in our studies.

In order to explore the possibility of a reasonable description of experimental data, we have studied in a greater detail two simple choices of the non–perturbative function $\varphi(p_\perp)$:

(a) "*flat*": the flat continuation of $\alpha_S(p_\perp < p_{\perp_0})$ with a constant value $\varphi_0 = \varphi(0)$,

$$\alpha_S(p_\perp < p_{\perp_0}) = \varphi_0 \ . \tag{2.15}$$

(b) "*quadratic*": a quadratic interpolation between the two values $\alpha_S(p_{\perp_0})$ and $\varphi(0)$.

$$\alpha_S(p_\perp < p_{\perp_0}) = \varphi_0 + [\alpha_S(p_{\perp_0}) - \varphi_0]\frac{p_\perp^2}{p_{\perp_0}^2} \ . \tag{2.16}$$

In both cases our model is determined by two free parameters: $p_{\perp_0}$ and φ_0.

We have concentrated our study on the small transverse momentum region of vector boson production. Therefore, the only modification of the Herwig++ code that had to be made was the introduction of the two non–perturbative parameters to $\alpha_S(p_\perp)$. In fact, as we implemented it, this would also affect the final-state radiation but our observable is not sensitive to effects in the final state. Details of the final state effects will be discussed in Section 2.5.3.

We would like to emphasize that we want to keep this model as simple as possible in order to explore the possibility of a reasonable description of the data. Therefore, the shape of α_S in the non–perturbative region is only a crude guess. A further study of the details of the shape would go beyond the scope of this work.

2.3 Parton-level results

To simulate fully exclusive events, Monte Carlo event generators, such as Herwig++, use a hadronization model, which is assumed to be universal across different types of collisions and different processes within them. Therefore for our final results, presented in Sections 2.4 and 2.6, we will combine our model for non-perturbative gluon emission with the standard Herwig++ model for

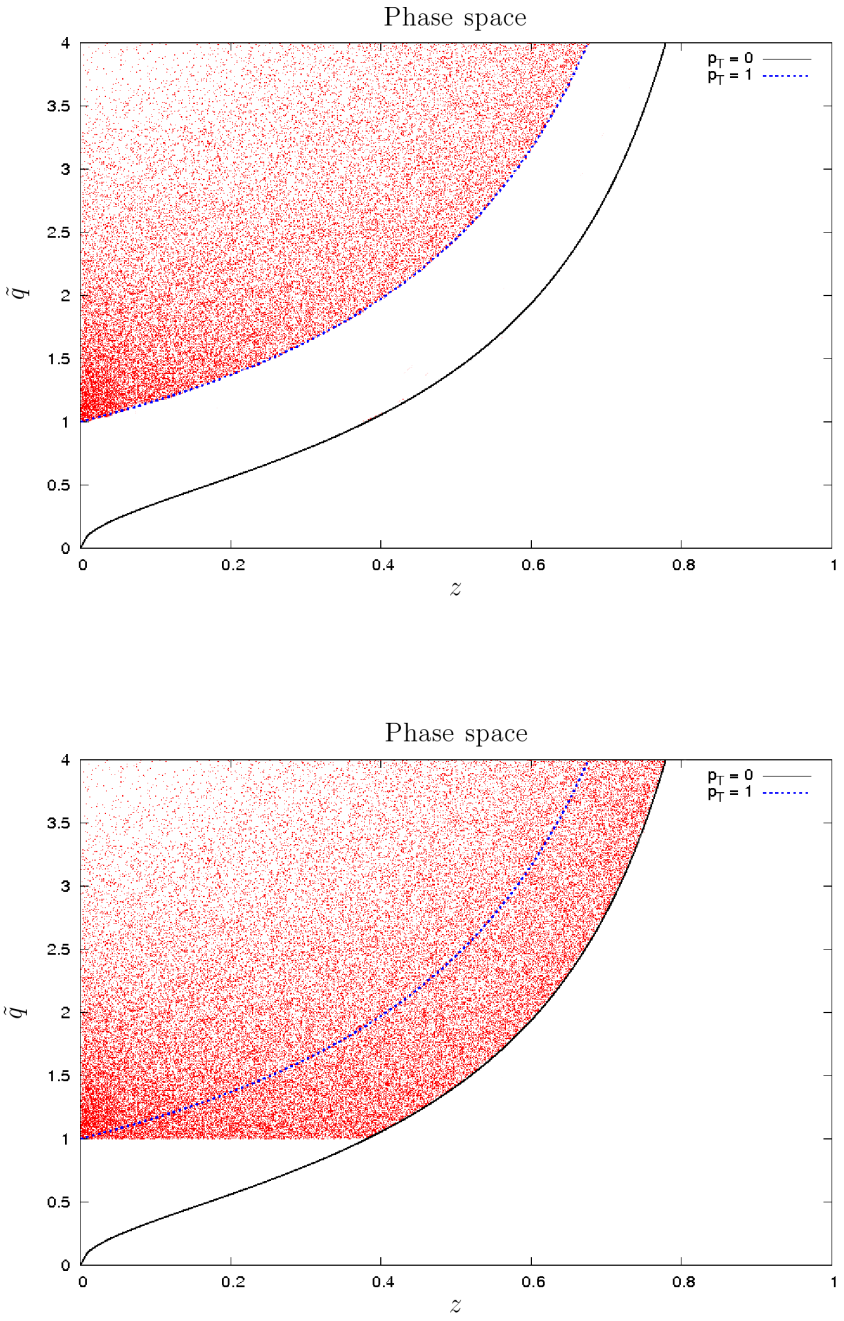

Figure 2.5: Available phase space for the gluon emission without (top plot) and with our non-perturbative model (bottom plot) expressed in terms of the parton shower variables $\tilde{q}$ and z.

the termination of the shower using non-perturbative effective parton masses tuned to e^+e^- data, so that the corresponding hadronization model can be used. However, if we are only interested in the W or Z transverse momentum distribution, we do not need to hadronize the final state: we can terminate the simulation at the end of the parton shower. We can therefore make a purely parton-level study with all light-quark and gluon effective masses and cut-offs set to zero[9] with our model for the low-scale α_S as the only non-perturbative input.

The first observation that we can make with our model is that we can easily find the parameter values that describe the existing Tevatron data. However, the main focus of our work is on the understanding of the dependence of the non–perturbative effects on the typical centre-of-mass (CM) energy of the system or even of the collider. We therefore consider two more data sets. The first is Fermilab E605 [143] fixed target p–Cu data, taken at the 38.8 GeV CM energy. We only take the data with an invariant mass in the range $11.5 < M/\text{GeV} < 13.5$ as this goes out to the highest transverse momentum. The other data we consider were taken in p–p collisions at $\sqrt{S} = 62\,\text{GeV}$ at the CERN ISR experiment R209 [144]. There are more data available but all at even lower CM energies. Our main interest is in finding a reasonable extrapolation to the LHC energies that is still compatible with the early data.

We have run Herwig++ with varying non–perturbative parameters φ_0 and $p_{\perp_0}$ for the two forms of α_S in (2.15) and (2.16). After an initial broader scan, we focussed on the region of φ_0 between 0 and 1 and $p_{\perp_0}$ between 0.5 GeV and 1.0 GeV. Each parameter set was run for the three different experimental setups we consider. For each resulting histogram we have computed the total χ^2/bin in order to quantify its agreement or disagreement with the data. We took the data errors to be at least 5% as we did not want to bias towards exceptionally good data points. Furthermore, we ignored an additional systematic error of the two fixed-target data sets which is quoted to be around 5–10%. Fig. 2.6 shows the χ^2 values we obtain for the "quadratic" model compared to the three considered data sets. The basic features are the same. In each case we find

[9] For technical reasons, it is not possible to set them exactly to zero. However, we have confirmed that if they are small enough, their precise values become irrelevant. For this study we actually set the quark masses and the δ parameter to 1 MeV, so that the non-perturbative mass that cuts off the parton shower, called Q_g in the Herwig++ manual, is given by the so called cParameter. For the cParameter we ran with values in the range 10 MeV to 100 MeV and found very little effect. We therefore use 100 MeV for our main results.

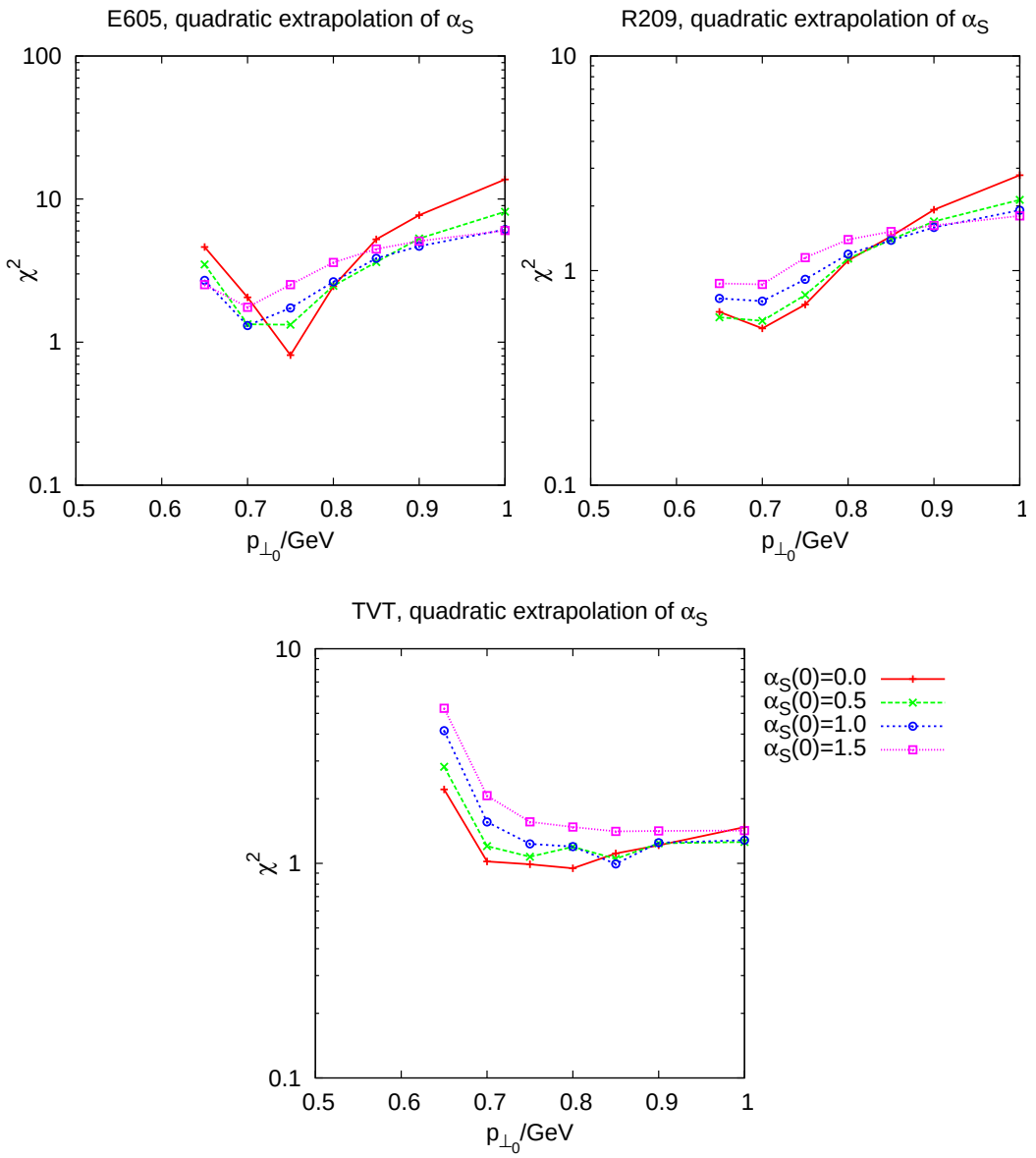

Figure 2.6: The parton-level results for χ^2 values for the quadratic non–perturbative model compared to E605, R209 and Tevatron data as a function of the NP parameter $p_{\perp_0}$. The different lines are for different values of $\varphi_0 = \alpha_S(0)$.

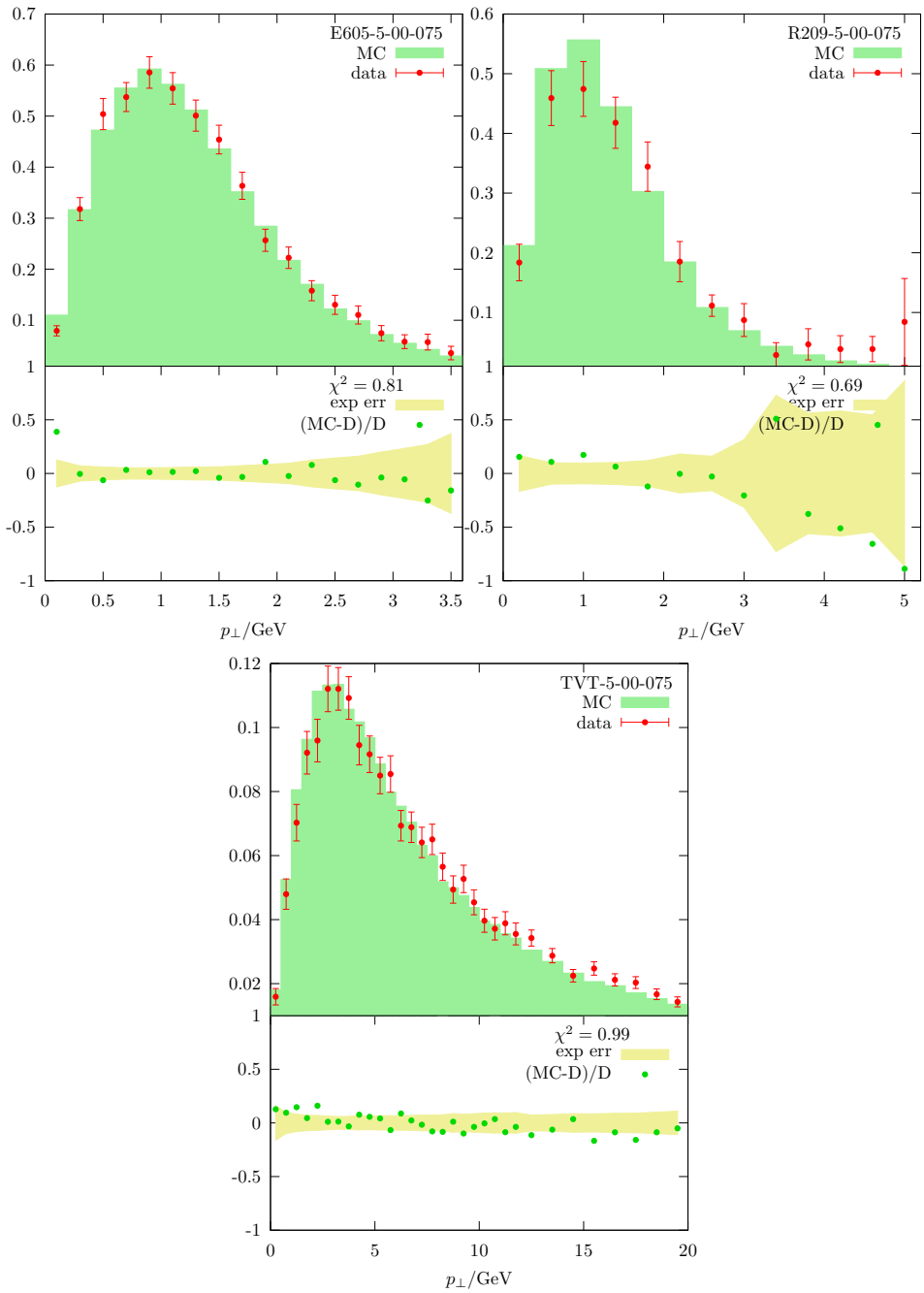

Figure 2.7: The comparisons of the parton level results from the non–perturbative model with data from the E605 (top left), R209 (top right) and CDF (bottom). The Monte Carlo results are from our parameter set with $\varphi_0 = 0.0, p_{\perp_0} = 0.75\,\text{GeV}$. Each panel includes two plots. The upper plot compares MC to the data directly, whereas the lower plot shows the ratio (MC-Data)/Data against the relative data error.

clear minima within the given $p_{\perp_0}$ range. In going from one experiment to another we find the more or less sharp minima. The minimum in Fig. 2.6 for Tevatron is not as clear as in the cases of the other two experiments. The best and most stable situation for all experiments is found for $\alpha_S(0) = 0.0$ and $p_{\perp_0} = 0.75\,\text{GeV}$. In Fig. 2.8 we show the non–perturbative region of our α_S parametrisation. We have inspected all distributions directly as well, and found a consistency with this choice. For this optimal choice over the energy range from 38.8 GeV to 1.8 TeV we show the resulting low $p_\perp$ distributions in Fig. 2.7. We should stress that the used parameter set may not be the optimal choice for each experiment or CM energy but rather the best compromise between the three experiments. As the fixed target data do not even include the systematic errors quoted, we have deliberately put a bit more emphasis on the Tevatron result. Ultimately, our goal will be to extrapolate our results further to the LHC energies, and we believe that for this purpose we have made the right choice of the parameters.

2.4 Hadron-level results

As we have mentioned earlier, the results of the previous section are not suitable for the full event simulation, because the masslessness of the light quarks and gluons is not consistent with the hadronization model used in Herwig++. Therefore, in this section we perform the same comparison with data but with the effective parton masses returned to their default values, tuned to e^+e^- annihilation data. Performing an initial scan over parameter space we find that we need to consider a much wider range of values than in the massless case. We can get a good description of the data from each experiment, but there is more tension between the three experiments leading to a larger total χ^2 value. In this case, the best and most stable situation was found for $\alpha_s(0) = 4$ and $p_{\perp_0} = 2.5\,\text{GeV}$, giving the χ^2/dof value per of 0.74 for CDF, 0.88 for R209, and a little bit worse, 3.1 for E605. This is not bad because, as was mentioned before, the fixed target data in our analysis do not even include the systematic errors quoted to be around 5–10%. We show the results in Fig. 2.10. Although the overall description of the data is somewhat worse with the non-perturbative parton masses, it is acceptable, and we prefer to maintain Herwig++'s description of final states, so we keep this as our default model for the remainder of the study.

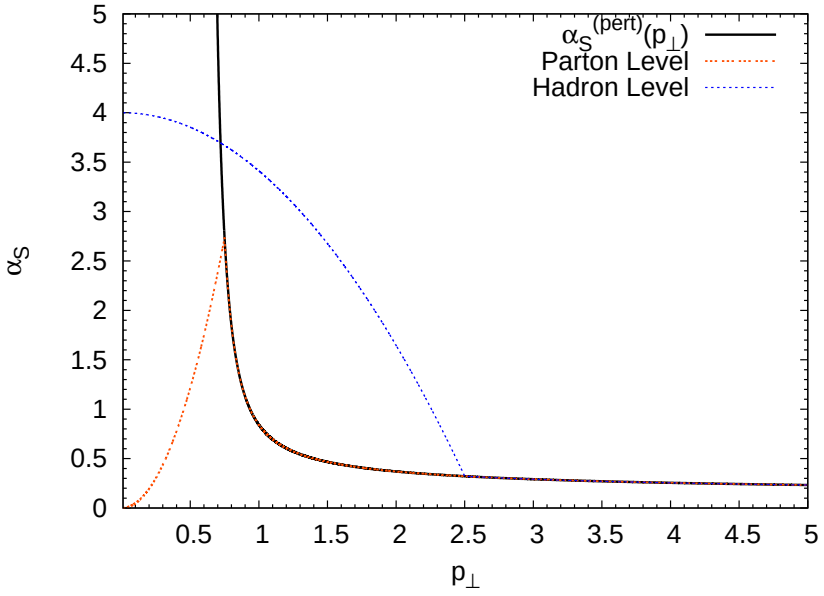

Figure 2.8: The optimal choice: "*quadratic*" interpolation with $\alpha_S(0) = 0$ and $p_{\perp_0} = 0.75\,\text{GeV}$ is shown. For comparison, we also show the purely perturbative α_S (LO) and our best fit for the hadron level results.

2.5 Remarks

Before we present our prediction for the LHC and comparison with other approaches let us make few remarks.

2.5.1 Dependence of the results on the intrinsic momentum $k_\perp$

We have checked how the results depend on the intrinsic momentum $k_\perp$ by varying its value with $\delta k_{\perp_\pm} = \pm 0.1$ GeV around our fixed value $k_\perp = 0.4$ GeV, which is in the range permitted by the Fermi motion. We have repeated the fitting procedure and observed that for both intrinsic momenta, $k_{\perp_\pm} = k_\perp + \delta k_{\perp_\pm}$, we are able to find a pair of parameters for which our model gives equally good description of data sets as for the central value of $k_\perp = 0.4$ GeV. Moreover, we have observed that the value of the $\alpha_s(0)$ parameter for all studied intrinsic momenta remains the same but the $p_{\perp_0}$ value is shifted for a bigger intrinsic momentum to a higher scale and for a smaller one to a lower scale. Therefore, by changing the intrinsic momentum from 0.4 to 0.5 GeV we can obtain exactly the same best model's parameters set as in [102][10] and the

[10] In this thesis we present some new results of the model which have been obtained after important improvements of the Herwig++'s parton shower, released with the version 2.3.1

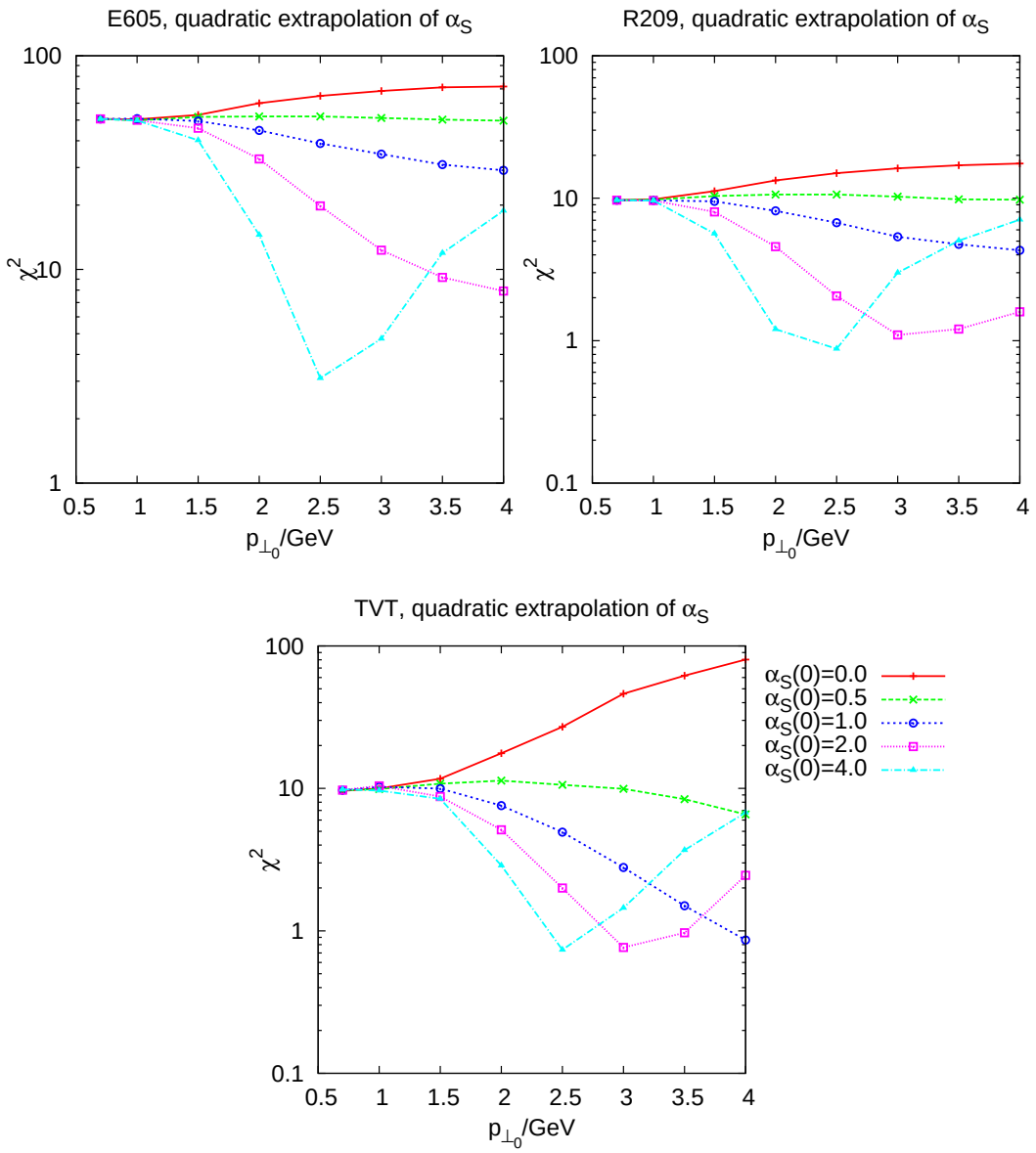

Figure 2.9: The hadron-level results for χ^2 values for the quadratic non–perturbative model compared to the E605, R209 and Tevatron data as a function of the NP parameter $p_{\perp_0}$. The different lines are for different values of $\varphi_0 = \alpha_S(0)$.

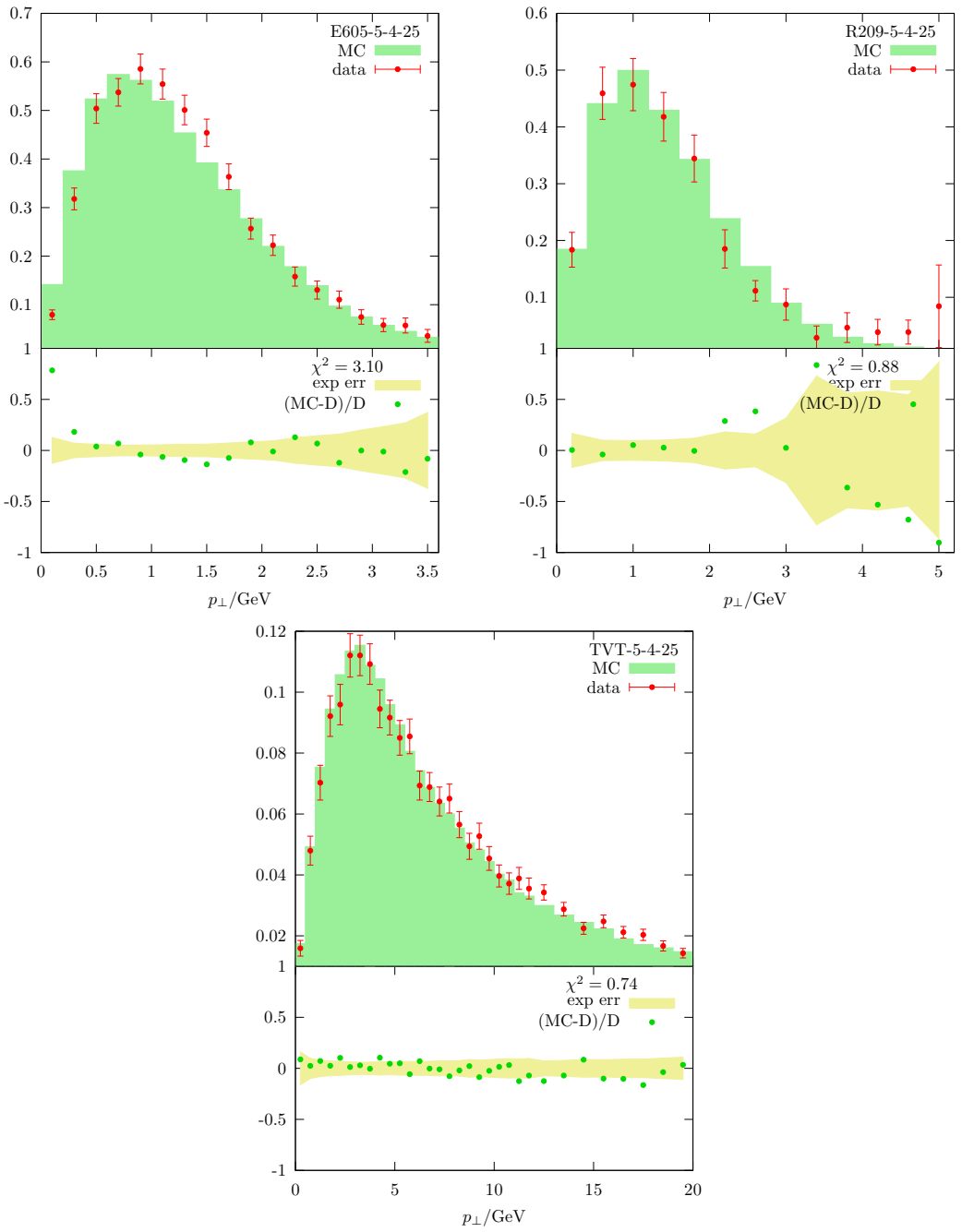

Figure 2.10: Comparison of the hadron level results from the non–perturbative model with data from E605 (top left), R209 (top right) and CDF (bottom) at the Tevatron (TVT). The Monte Carlo results are from our parameter set with $\varphi_0 = 2.5, p_{\perp_0} = 4.0\,\text{GeV}$. Each panel includes two plots. The upper plot compares MC to data directly, whereas the lower plot shows the ratio (MC-Data)/Data against the relative data error.

same shape of α_s as presented in Figure 4 of [102], which is discussed below.

2.5.2 Comparison of our parametrisation of α_s with other approaches

It is interesting to compare our α_s parametrisation with other approaches to modelling of non-perturbative corrections to inclusive observables with a modified coupling in the soft region, see for example Refs. [145,146,147]. Ref. [145] finds an average value of the coupling over the range from 0 to 2 GeV of about 0.5, while Ref. [146] argues that the effective coupling should vanish at $p_\perp \to 0$. For our best-fit parametrisation at the parton level for $k_\perp = 0.5$ (the shape of α_S is the same as in Fig. 4 of Ref. [102]), the average value of the coupling over the range from 0 to 2 GeV is around 0.7. Considering that their fits to data typically use the NLO calculations, while we have used the leading-log parton shower, this could be considered the good agreement. In case of the hadron level our best-fit α_S parametrization is very different from those of Refs. [145,146,147] – it is much larger in the non-perturbative region. This is not surprising since our coupling is now 'fighting against' the emission distribution that is already falling as $p_\perp \to 0$ relative to the perturbative one.

2.5.3 Non-perturbative final-state radiation

As briefly discussed in Introduction, we want to stress that the approach of adding the non–perturbative soft-gluon radiation to the parton shower should be connected to the non–perturbative input that the parton shower is linked to in the initial state. We think of this radiation as originating from long–range correlations within the coloured initial state.

We have checked the effect of the same model for the final-state radiation. We find a dramatic increase in the amount of soft radiation when we compare event shapes, simulated with our new model for soft emissions, to the LEP data, which are described well by the default parton-shower model. Using the default hadronization model, we observe a dramatic softening of the event shapes, leading to a poor description of data. However, the default hadronization model produces a considerable amount of transverse momentum smearing during cluster splitting and decay, and is tuned to data together with

of the program. The main change in the program was a fix for a wrongly applied PDF veto in the parton shower $\bar{q} \to \bar{q}\, g$ splittings which, by construction of our model, could have influenced on results presented in the first publication introducing the model, see [102].

the parton-shower model that does not include the non-perturbative smearing. Therefore, to turn on this smearing, without modifying or, at least, retuning the hadronization model, must lead to a significant amount of double-counting. It is an interesting question, which we reserve for future works, whether a good fit can be obtained with our model?

The last remark is that using our model as the only non-perturbative ingredient in the simulation, i.e. removing the non-perturbative constituent parton masses that usually cut off the parton shower in Herwig++, gives a somewhat better description of the data. This lays open the speculation that perhaps, in some way, the two approaches could be combined. One could, for example, use our model for the initial-state radiation, and the usual model, tuned to describe the final states of e^+e^- annihilation, for the final-state radiation.

2.6 LHC results and comparisons with other approaches

2.6.1 Z boson transverse momentum

At the end of this chapter we would like to compare the results for a transverse momentum distribution of the Z-boson at the LHC energies using our non-perturbative gluon emission model and two other approaches: ResBos [148] and the Gaussian intrinsic $k_\perp$ extrapolation. But first let us compare our prediction at the parton level, marked as the filled histogram in Fig. 2.11, and at the hadron level, the dot–dashed blue line. Both histograms, as expected, give a consistent extrapolation. The result from ResBos in Fig. 2.11 (the solid black line) shows a slightly different behaviour from our prediction. We predict a slightly more prominent peak and a stronger suppression towards larger transverse momenta. The same trend is already visible when comparing both approaches to the Tevatron data, although both are compatible with the data within the given error band, see Fig. 2.12. Both computations match the data well at large transverse momenta as they rely on the same hard matrix element contribution for the single hard-gluon emission. We want to stress the remarkable feature that we both predict the same peak position with these two different models, which is very important from the experimental point of view. This feature is quite understandable, as both models are built on the same footing: extra emissions of soft gluons. The comparisons of ResBos to

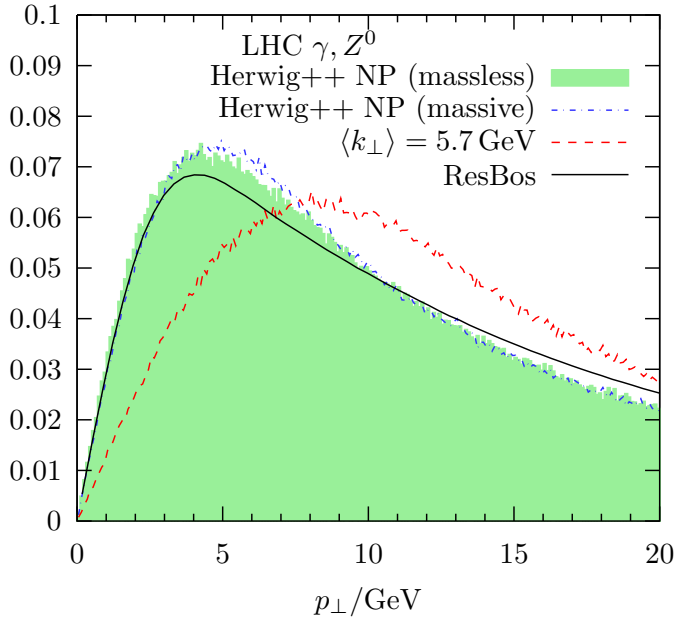

Figure 2.11: The vector boson $p_\perp$ distribution at the LHC. Our model is compared to the extrapolation of Gaussian intrinsic $k_\perp$ to LHC energies and the result from ResBos.

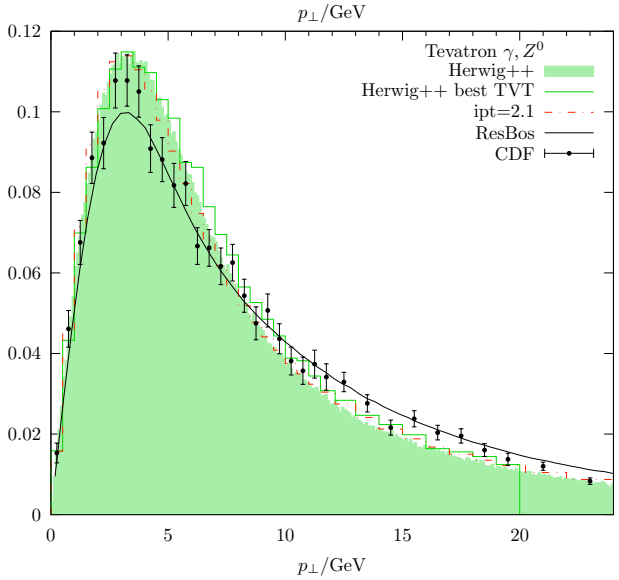

Figure 2.12: The comparisons of the Z vector boson $p_\perp$ distribution obtained from the non–perturbative model (filled green), ResBos (solid black) and the Gaussian intrinsic $k_\perp$ fit (dashed red) with the CDF data at the Tevatron.

data from experiments at various energies, including the experiments E605 and R209, were done in [149].

Furthermore the dashed red line in Fig. 2.11 is the Herwig++ result where only intrinsic $\langle k_\perp \rangle = 5.7\,\text{GeV}$ was used, as recommended in [150,10]. This large value stems from the extrapolation of lower-energy data, with the assumption that the average $k_\perp$ depends linearly on $\ln(M/\sqrt{S})$. The peak is seen to lie at a considerably higher value of transverse momentum. It would clearly be of interest to have experimental data to distinguish these two models of the non–perturbative transverse momentum.

2.7 Herwig++ parameter settings

The study has been done with Herwig++ 2.3.1. We ran with the default matrix element for the γ, Z production with only initial state parton showers. We left final state parton showers and hadronic decays switched off as they were irrelevant for this study. The following parameters in the release 2.3.1 are important to switch off the final-state parton shower and to adjust the intrinsic $p_\perp$:

```
cd /Herwig/Shower
set SplittingGenerator:FSR No
set Evolver:IntrinsicPtGaussian 0.4*GeV
```

Our preferred result, as shown in Fig. 2.10, was obtained by setting

```
set AlphaQCD:NPAlphaS 5
set AlphaQCD:Qmin 2.5*GeV
set AlphaQCD:AlphaMaxNP 4
```

Here, "`AlphaQCD:NPAlphaS 5`" selects the quadratic non–perturbative model. The flat model corresponds to setting this parameter to `6`.
`AlphaQCD:Qmin` sets the value of $p_{\perp_0}$ and `AlphaQCD:AlphaMaxNP` directly sets the value $\alpha_S(0)$. As obtaining the results for the parton level with very small masses and cutoffs was very CPU intensive, we have also modified the code in order to leave out the time-like showers from partons radiated in the initial-state shower.

2.8 Conclusions

Aiming for a universal model of the non–perturbative soft gluon radiation we have achieved a good description of the experiment data at three different energies. We have considered the model based on the soft-gluon radiation, much like the resummation procedure in ResBos [148], to have a more meaningful physics input than simply extrapolating the Gaussian smearing of the primordial transverse momentum. Let us sum up by citing the opinion of B. R. Webber about the model from his CERN Academic Training Lecture [151] given at CERN on 21 Feb 2008, the video is available from CERN website http://cdsweb.cern.ch/record/1082256 (see 67th minute of the video):

The question from a person from audience:

"I have a question on this intrinsic p_T. In principle, for example the p_T distribution of the Z-boson we will be able to measure very precisely."

B. R. Webber:

"Right."

The person from audience:

"Now you said, there is a theory problem. There is something like phenomenological intrinsic p_T which needs to be added, but it is a several GeV and it looks not just to be non-perturbative, what is the strategy in order to better understand this?"

B. R. Webber:

"Well. I think in my mind the most interesting theoretical development has been the recent model for that, I mean it is still phenomenological but seems very reasonable to me and that is a model of [102] (...)"

which is the model described in this chapter.

Of course, if this model is universal, it should make good predictions for other processes, such as the jet and photon production. We plan to study these processes in a more detail in the future.

We have also found that using our model as the only non-perturbative ingredient in the simulation, i.e. removing the non-perturbative constituent parton masses that usually cut off the parton shower in Herwig++, gives a somewhat better description of the data. This lays open the speculation that perhaps, in

some way, the two approaches could be combined, using our model for initial-state radiation, and the usual model, tuned to describe the final states of e^+e^- annihilation, for final-state radiation. However we leave considerations of this combination to our future works.

Chapter 3

W-mass measurement at the LHC

Abstract

In this chapter we focus our attention on the measurement of the W-boson mass. This is one of the most important Standard Model measurements at the LHC. In the first part of the chapter we discuss the systematical effects which are the largest and, as a consequence, the most important for the W-mass measurement at the Tevatron hadron collider experiments. We propose a novel method of the W-mass measurement. It is robust with respect to these systematic measurement and modeling error sources. In the second part we investigate whether this method can reduce the present uncertainty of M_W at the LHC. An emphasis is put on effects that are not important at the Tevatron but may play an important role at the LHC. The result of this investigation shows that several important sources of errors have been neglected in all the previous analyses performed by the LHC experimental Collaborations (ATLAS and CMS). For the very first time the precision of the W-boson mass is evaluated in the presence of these effects. This evaluation shows that in order to reach a desired precision of the W-boson mass at the LHC, novel measurement strategies must be developed. At the end of this chapter we provide two examples of such strategies.

This chapter is based on the following works: [5, 13, 105, 152, 153, 154].

3.1 Introduction

One of the major goals of the experimental programme at the LHC is to improve the precision of the Electroweak Standard Model (SM) parameters, in particular the mass of the W-boson. Given the precise measurements of the

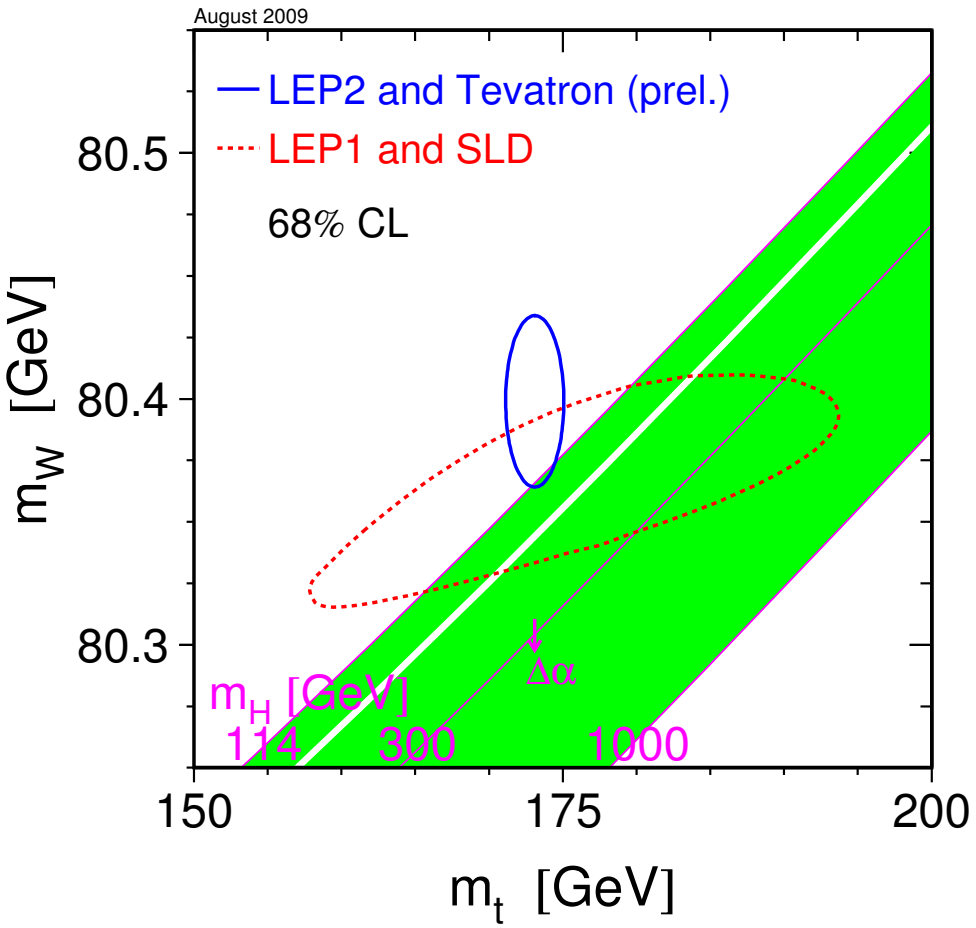

Figure 3.1: The plot from Ref. [155]. The comparison of the indirect constraints on M_W and m_t based on LEP/SLD data (dashed contour) and the direct measurements from the LEP2/Tevatron experiments (solid contour). In both cases the 68% CL contours are plotted. Also shown is the SM relationship for the masses as a function of the Higgs mass in the region favoured by theory (< 1000 GeV) and allowed by direct searches (114 GeV to 170 GeV and > 180 GeV). The arrow labelled $\Delta\alpha$ shows the variation of this relation if $\alpha(M_Z^2)$ is changed by plus/minus one standard deviation. This variation gives an additional uncertainty to the SM band shown in the figure.

Fermi constant $G_F = 1.166367(5) \times 10^{-5}$ GeV^{-2} [156], the electromagnetic coupling constant α and the Z-boson mass $M_Z = 91.1876 \pm 0.0021$ GeV [156],

a precision measurement of the W mass, which is known to a much worse accuracy: $M_W = 80.399 \pm 0.023$ GeV [156], plays a central role, as it allows for both testing the Standard Model – by confronting predictions of the W and top quark masses [157] with measurements [158, 159], as well as putting limits on the SM Higgs boson mass [160]. The W-boson mass is given by

$$M_W = \sqrt{\frac{\pi\alpha}{\sqrt{2}G_F}} \frac{1}{\sin\Theta_W \sqrt{1-\Delta_R}}. \tag{3.1}$$

At the lowest order the radiative correction Δ_R is equal to zero. At higher orders of the perturbation theory Δ_R depends upon the masses of the particles in the W self-energy diagrams. That is why, in the context of the SM, the precise measurements of the top quark mass and the W mass provide a constraint on the unobserved Higgs boson mass. The recent results of such a constraint are shown in Fig. 3.1, taken from Ref. [155]. Of course, Δ_R could also be modified by the radiative corrections involving masses of heavy Beyond-Standard-Model particles [161]. Therefore, the precise measurement of M_W provides also constraints on new physics, see Fig. 3.2 (this plot is taken from Ref. [162]) for more information about the current status of such studies.

At the Large Electron-Positron Collider LEP2 the W-mass has been measured to be 80.376 ± 33 MeV [160], while at the hadron collider Tevatron, both experiments CDF and D0 have measured the W-mass respectively to be:

$$M_W = 80.413 \pm 0.034(\text{stat}) \pm 0.034(\text{sys}) \text{ GeV (CDF)}, \tag{3.2}$$

$$M_W = 80.401 \pm 0.021(\text{stat}) \pm 0.038(\text{sys}) \text{ GeV (D}\emptyset\text{)}. \tag{3.3}$$

Combining the above two Tevatron measurements gives [163]:

$$M_W = 80.420 \pm 0.031 \text{ GeV (Tevatron)}, \tag{3.4}$$

which is more precise than the combined LEP2 measurement. The current world-average value of M_W is [163]

$$M_W = 80.399 \pm 0.023 \text{ GeV (World average)}. \tag{3.5}$$

Although a precision of the W mass that matches the precision of the Z-boson mass (± 2 MeV) is experimentally not within a reach at the LHC, a much better precision than available at present is desirable to make the most use out of the relation between the W mass and the Fermi constant G_F given by Eq. (3.1). Therefore, in this chapter we examine the upper limit on the precison of the

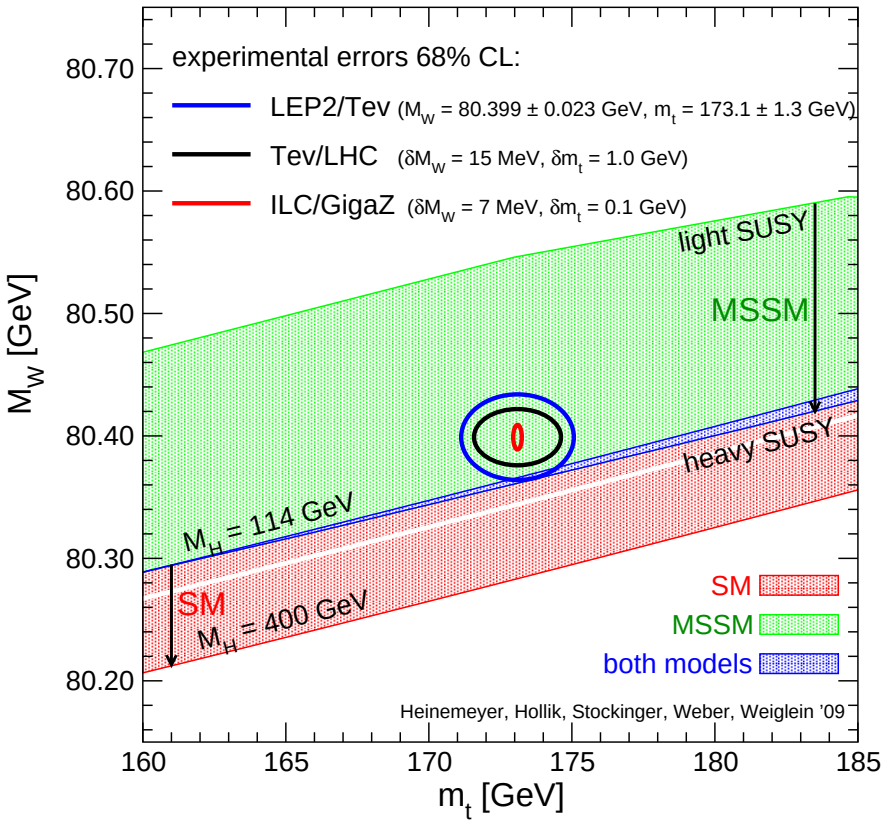

Figure 3.2: Predictions for M_W in the MSSM and the SM as a function of m_t in comparison with the present experimental results for M_W and m_t and the prospective accuracies (using the current central values) at the Tevatron/LHC and at the ILC. The allowed region in the MSSM, corresponding to the light-shaded (green) and dark-shaded (blue) bands, results from varying the SUSY parameters independently of each other in a random parameter scan. The allowed region in the SM, corresponding to the medium-shaded (red) and dark-shaded (blue) bands, results from varying the mass of the SM Higgs boson from $M_H = 114$ GeV to $M_H = 400$ GeV.

W-boson mass measurement at the LHC. This examination is divided into two main stages. In the first stage, we will consider the systematical effects which are the largest and, as a consequence, the most important for the W-mass measurement at hadron collider experiments performed at the Tevatron. We will show, step-by-step, a construction of a novel method of the W-mass measurement at the LHC which is robust with respect to these systematic measurement and modeling error sources. We call it the "Z candle" method because it optimizes the use of the Z-boson, which properties are measured to the high-level precicion, as *"the standard reference candle"* for the W-mass

measurement. Coping with reduction of the most important systematic errors from the previous hadron experiments is, of course, a mandatory step for the precision measurement of W-boson mass at the LHC. However, the question that remains to be addressed is whether dealing with these effects is enough to make this measurement competitive or whether one will be faced with new kinds of problems that are not important at the Tevatron. This question is addressed in the second part of the chapter called "LHC specific effects". In order to answer this question we first look in more detail at the differences in the production and decay of W^+, W^- and Z bosons in hadronic collisions. Next, we discuss how these differences are reflected in the relationship between W and Z boson observables at the Tevatron and at the LHC. We trace the principal differences between the Tevatron and the LHC, identify the effects which are specific to the LHC $p\,p$ collision scheme and evaluate their impact on the M_W measurement biases at the LHC. This is the first time that the precision of the W-boson mass is evaluated in the presence of these effects. We reveal that several important sources of errors have been neglected in the previous analyses performed by both ATLAS [6] and CMS [14] Collaborations, resulting in too an optimistic, of $\mathcal{O}(10)$ MeV, assessment of the expected measurement precision of the W-boson mass. We argue that in order to reach the desired precision target, claimed by both the ATLAS [6] and CMS [14] Collaborations, novel LHC-specific measurement strategies must be developed. At the end of this chapter two examples of such strategies are discussed. In the first one we circumvent the LHC specific precision 'brick-walls' by proposing the dedicated LHC runs with deuterium or helium ion beams. The second, alternative strategy includes a dedicated fixed target "LHC-support" experiment with a high-intensity muon beam. At the end of the chapter we summarize our studies.

3.2 Basic information and definitions

In this section we provide the basic information and definitions needed by subsequent sections. First, we specify the event selection rules and define the observables. Next, we describe the tools used in our studies. Finally, at the end of the section, we present the analysis method used in this chapter. All the technical aspects of the analysis discussed here were also presented in the publications devoted to the measurement of $M_{W^+} - M_{W^-}$, see Refs. [13, 164].

Throughout this chapter, we assume that the intrinsic M_{W^+} and M_{W^-}

masses are equal[1].

3.2.1 Event selection and basic observables

In our studies we consider the charged and neutral current Drell–Yan processes, *i.e.* the single W-boson and Z-boson production with leptonic decays:

$$\begin{aligned} p+p\ (p+\bar{p},\ d+d) &\longrightarrow W^{\pm}+X \longrightarrow l^{\pm}+\overset{(-)}{\nu}_l+X\,, \\ p+p\ (p+\bar{p},\ d+d) &\longrightarrow Z+\gamma \longrightarrow l^{+}+l^{-}+X\,, \end{aligned} \tag{3.6}$$

where p denotes the proton, d–deuteron and $l = e,\, \mu$. The nucleon–nucleon centre-of-mass energy, $\sqrt{s}$, is assumed to be 14 TeV for the $p\,p$ and $p\,\bar{p}$ collisions and 7 TeV/nucleon for the $d\,d$ collisions. The studies reported in this chapter have been performed for the one-year-long low-luminosity LHC run allowing to collect the integrated luminosity of $10\,\mathrm{fb}^{-1}$. By the time of reaching such a luminosity, the leptonic decays of $\mathcal{O}(10^8)$ W and $\mathcal{O}(10^7)$ Z bosons will be recorded at the LHC.

The extraction of the W-mass is made by studying the electronic and muonic decays of W and Z boson, namely $W \to l\,\nu_l$ and $Z \to l^{+}l^{-}$, where $l = e,\, \mu$. The choice of leptonic decays is motivated by the fact the dijet QCD-background is by several orders of magnitude higher than the $W \to q\,\bar{q}'$ and $Z \to q\,\bar{q}$ signals. The leptonic decays provide processes with large cross sections and ensure the absence of the QCD effects in the final state. The decays of electroweak bosons into the τ channel is not considered because τ decays predominantly into hadrons (huge background), while its leptonic decays involve two neutrinos (not detected).

Basic observables. The commonly chosen kinematical variables for the above processes are the charged lepton transverse momentum $p_{T,l}$ (or equivalently $\rho_l = 1/p_{T,l}$) and the pseudorapidity η_l, defined as

$$p_{T,l} = \sqrt{p_{x,l}^2 + p_{y,l}^2}\,, \tag{3.7}$$

$$\rho_l = \frac{1}{p_{T,l}}\,, \tag{3.8}$$

$$\eta_l = -\ln\tan(\theta_l/2)\,, \tag{3.9}$$

[1] The best experimental support of this assumption stems from a comparison of the measured μ^+ and μ^- lifetimes [156], which translates into an equality of M_{W^+} and M_{W^-} masses at the 1.6 MeV level.

where θ_l is the polar angle of the outgoing charged lepton in the laboratory frame. The general features of the pseudorapidity distribution $d\sigma/d\eta_l$ and the

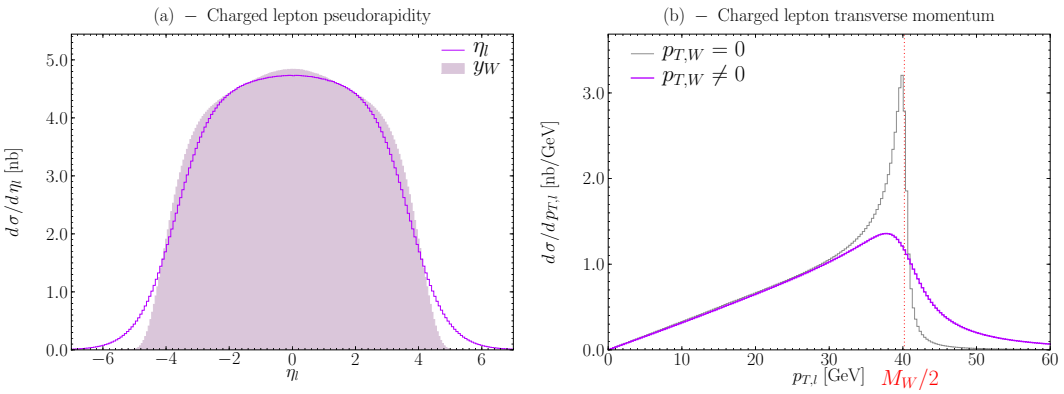

Figure 3.3: The plots from Ref. [164]. General features of the charged lepton pseudorapidity (a) and transverse momentum (b) in the Drell–Yan process. In the case of $p_{T,l}$ both LO and improved LO are shown.

transverse momentum distribution $d\sigma/dp_{T,l}$ for the charge lepton originating from W-decay in the Drell–Yan process are presented in Fig. 3.3 (plots taken from [164]). As we can see from Fig. 3.3 (a) the main pattern of the η_l distribution resembles the one of the W rapidity distribution $d\sigma/dy_W$, where

$$y_W \equiv \frac{1}{2}\ln\left(\frac{E_W + p_{z,W}}{E_W - p_{z,W}}\right). \tag{3.10}$$

In the Fig. 3.3 (b) we can see the transverse momentum distribution $d\sigma/dp_{T,l}$ for the two cases. First, when $p_{T,W} = 0$ – in this case a Jacobian peak around $\approx M_W/2$ is visible and the measurement of $p_{T,l}$ distribution allows to deduce the value of M_W. However, this case is not realistic, as we have already discussed in detail in Chapter 2. Because of the non-perturbative effects and higher-order corrections, the transverse momentum distribution of the W-boson is highly nontrivial. In this case, as we can see from Fig. 3.3 (b), the transverse momentum of W smears the sharpness of the Jacobian peak. This means that the extraction, from the bare $p_{T,l}$ distribution, of M_W implies a refined Monte Carlo modelling of the $p_{T,W}$. A model of the perturbative and non-perturbative effects in the electroweak bosons transverse momenta was presented in Chapter 2.

Just for completness we mention here two alternative methods to measure the mass of the W boson. The first one uses the transverse momentum distribution of the neutrino, which is similar to the transverse momentum of the

charged lepton. However, p_{T,ν_l} can only be derived from the measurement of the missing transverse energy given by the energy decomposition in the calorimeters. This leads to the larger systematic errors on M_W when using the $\not{p}_{T,\nu}$ distribution. The second method is based on the measurement of the transverse mass, defined as follows

$$\begin{aligned} m_{T,l\,\nu_l} &\equiv \sqrt{(p_{T,l}+p_{T,\nu_l})^2-(\vec{p}_{T,l}+\vec{p}_{T,\nu_l})^2}, \\ &= \sqrt{2\,p_l\,p_{\nu_l}\,(1-\cos\phi_{l\nu_l})}. \end{aligned} \tag{3.11}$$

The discussions in this chapter can be, to a large extent, applied to the determination of the W mass from $m_{T,l\,\nu_l}$ spectra. The determination of $m_{T,l\,\nu_l}$, however, involves the reconstruction of the neutrino transverse momentum as the missing transverse momentum. The systematic error of this measurement is too large to be useful for the measurement of the W mass at the 10 MeV level, therefore is not considered in our studies.

3.2.2 Tools

All the results discussed below have been obtained using the Born-level Drell–Yan processes implemented in WINHAC (see Section 1.1 for more details on the generator). The parton-level process is convoluted with the parton distribution functions (PDFs) provided by the LHAPDF package [101] which includes a large set of recent PDF parametrisations by several groups. WINHAC is also interfaced with the Pythia 6.4 [9] MC event generator in order to provide the QCD/QED initial-state parton shower as well as hadronisation. WINHAC, in addition to the charged-current Drell–Yan process, includes the neutral-current Drell–Yan process (with $\gamma + Z$ bosons in the intermediate state) but only at the Born level. Therefore, for a more precise description of the latter process, including the full set of the QED/EW radiative corrections, a dedicated MC event generator, called ZINHAC [15], has been developed and presented in detail in Chapter 1. We plan to use these twin MC generators for precision studies/analyses of the Drell–Yan processes at the LHC.

For the presented study the version 1.23 of WINHAC has been used. It is equivalent to the recent version 1.31 [53] for all the aspects addressed in this chapter.

3.2.3 The detector model

The methods presented in this chapter are suited for the two general-pourpose LHC experiments: CMS and ATLAS. For both experiments the high-precision measurements of the W-boson production observables will be based on samples of at least 10^8 recorded W-boson production events, therefore a full detector simulation of a comparable sample of Monte Carlo events for presented studies is both unrealistic and unnecessary. Therefore, instead of the full detector simulation we use the average response functions of the ATLAS tracker to charged particles as specified in Refs. [165, 166, 167, 168]. The inner detector performances in p_T, θ and ϕ are parametrised using Gaussian functions (cf. Ref. [165] § 3.3.1.6) with, the σ-parameters:

$$\sigma_{1/p_T} = 3.6 \times 10^{-4} \oplus \frac{1.3 \times 10^{-2}}{p_T^{(\mathrm{true})} \sqrt{\sin\theta^{(\mathrm{true})}}} \quad [\mathrm{GeV}^{-1}], \tag{3.12}$$

$$\sigma_{\mathrm{cotan}\,\theta} = 0.7 \times 10^{-3} \oplus \frac{2.0 \times 10^{-3}}{p_T^{(\mathrm{true})} \sin^{3/2}\theta^{(\mathrm{true})}}, \tag{3.13}$$

$$\sigma_{\phi} = 0.075 \times 10^{-3} \oplus \frac{1.8 \times 10^{-3}}{p_T^{(\mathrm{true})} \sqrt{\sin\theta^{(\mathrm{true})}}} \quad [\mathrm{rad}], \tag{3.14}$$

where $p_T^{(\mathrm{true})}$ are in GeV and (true) superscript means that kinematics is considered at the generator level. In the future, the response functions of the LHC detectors will be determined *in situ* from the measurements of the decay products of the known narrow resonances. The ATLAS detector response functions are used here merely for the initial estimate of the size of the systematic measurement effects. Charged track are measured in the ATLAS detector within the pseudorapidity range of

$$-2.5 \leq \eta_l \leq 2.5. \tag{3.15}$$

We therefore restrict our studies to a lepton tracks measured within these pseudorapidity limits.

3.2.4 The analysis method

Below we present technical aspects of the analysis method used in the evaluation of the achievable precision of the measurement of the W-boson mass. In order to evaluate the impact of the systematic uncertainties on the extracted values of M_W we use the *likelihood analysis* of the distributions for the

pseudo-data ($\mathcal{PD}$) event-samples and those for the *mass-template* ($\mathcal{MT}$) event-samples. Each of the $\mathcal{PD}$ samples represents a given systematic bias ξ in the detector response or in the theoretical modeling of W-boson production processes, implemented respectively in the event-simulation or event-generation process. We have already discussed an example of the theoretical modeling bias source caused by the non-perturbative effects (Chapter 2) which affects the measured distribution of the lepton transverse momentum. This and the other systematic effects will be discussed in Sections 3.3 and 3.5. Here we concentrate only on technical aspects.

Each of the $\mathcal{MT}$ samples was generated by assuming a specific M_W value. The $\mathcal{MT}$ samples were simulated using the unbiased detector response and fixed values of all the parameters used in the modeling of the W-boson production and decays, except for the W-boson mass. The likelihood analysis, explained below in more detail, allows us: (1) to find out which of the systematic measurement and modeling errors could be falsely absorbed into the measured value of the W-boson masses and (2) to evaluate quantitatively the corresponding measurement biases.

(a) Likelihood analysis

Let us consider, as an example, the impact of a systematic effect ξ on the bias in the measured value of the W mass determined from the likelihood analysis of the $d\sigma/dp_{T,l}$ distributions.

The simulation of the pseudo-data event sample, $\mathcal{PD}$, representing a given systematic bias ξ, is carried out for a fixed value of the mass $M_W^{\rm ref}$. Subsequently, a set of the $2k+1$ unbiased (*i.e.* $\xi = 0$) template data samples, $\mathcal{MT}$, is simulated. Each sample n of the $\mathcal{MT}$ set corresponds to a given value of $M_W^{(n)} = M_W^{\rm ref} + \delta M_W^{(n)}$, $n = -k, \ldots, k$. The likelihood between the binned $d\sigma/dp_{T,l}$ distributions for the $n^{\rm th}$ $\mathcal{MT}$ sample and the ξ-dependent $\mathcal{PD}$ sample is quantified in terms of the χ^2 value:

$$\chi^2(p_{T,l};\, \xi, n) \,=\, \sum_i \frac{(d\sigma_{i;\,\xi} - d\sigma_{i;\,\xi=0,n})^2}{\Delta d\sigma^2_{i;\,\xi} + \Delta d\sigma^2_{i;\,\xi=0,n}}, \tag{3.16}$$

where $d\sigma_i$ is the content of the $i^{\rm th}$ bin of the $d\sigma/dp_{T,l}$ histogram and $\Delta d\sigma_i$ is the corresponding statistical error. The results presented in this chapter have been obtained using a bin size equal to σ of the anticipated measurement resolution of the track curvature [167]. The $\chi^2(p_{T,l};\, \xi, n)$ dependence

upon $\delta M_W^{(n)}$ is fitted by a second order polynomial. The position of the minimum, $M_W(\xi)_{min}$, of the fitted function determines the systematic mass shift $\Delta M_W(\xi) = M_W(\xi)_{min} - M_W^{\text{ref}}$ due to the systematic effect ξ. As an illustration of this procedure one example is shown in Fig. 3.4, taken from Ref. [164] (p. 139). In order to see the difference between the $d\sigma/dp_{T,l}$ distributions, the mass templates were generated with $\pm 500\,\text{MeV}$. Note that these plots were made for unbiased (*i.e.* $\xi = 0$) pseudodata $\mathcal{PD}$, therefore as expected the parabola fit is centered at $M_{W^+}^{\mathcal{PD}} - M_W^{\text{ref}} = 0$, more precisely $M_{W^+}^{\mathcal{PD}} - M_W^{\text{ref}} = (-1.4 \pm 2.7)\,\text{MeV}$ with $\chi^2_{\text{min}}/\text{dof} = 0.86, (\text{dof} = 100)$. It shows that no systematic biases are introduced by the proposed analysis method and determines the size of the statistical errors. If the systematic effect under study

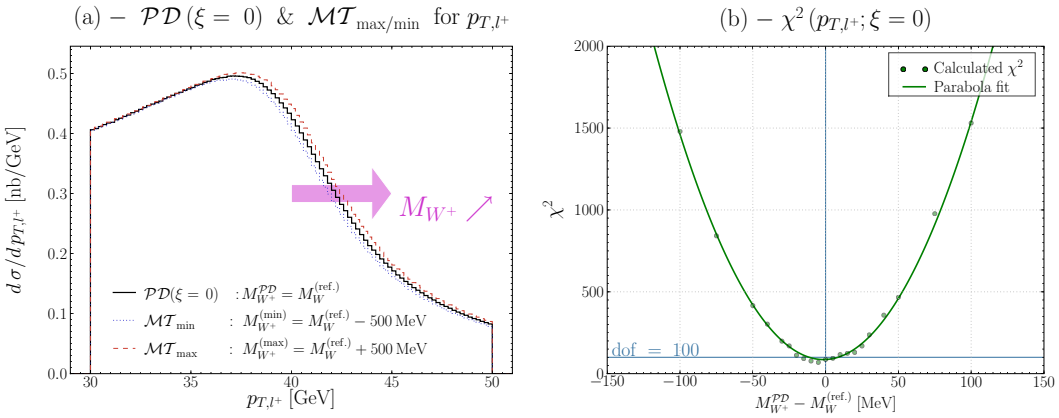

Figure 3.4: Distributions of the transverse momentum of the positively charged lepton for the three values of $\delta M = -500$, 0, $+500\,\text{MeV}$ with respect to $80.403\,\text{GeV}$ (a) and the χ^2 dependence for each $\{\mathcal{PD}, \mathcal{MT}\}$ couple (points) and their associated polynomial fit (line) in function of $\Delta_{(+,-)}$ (b). Figure from Ref. [164] (p. 139).

can be fully absorbed into a shifted value of M_W, then the expectation value of χ^2_{min}/dof, where $\text{dof} = \sum_i$, is close to 1. The position of the minimum of the parabola fit will be shifted from the central value $M_{W^+}^{\mathcal{PD}} - M_W^{\text{ref}} = 0$ by some value $\Delta M_W(\xi)$ which estimates size of the mass shift caused by the effect ξ, see for example Fig. 3.6. The error of the estimated value of the mass shift, $\delta\ (\Delta M_W(\xi))$, can be determined from the condition $\chi^2(M_W(\xi)_{min} + \delta\ (\Delta M_W(\xi))) = \chi^2_{\text{min}} + 1$. Of course, not all the systematic and modeling effects can be absorbed into a variation of a single parameter, even if the likelihood is estimated in a narrow bin-range, purposely chosen to have the highest sensitivity to the mass parameters. In such a case the value of $\chi^2_{\text{min}}/\text{dof}$ can be substantially different from 1 and, consequently, $\delta\ (\Delta M_W(\xi))$ looses its statistical meaning. This

can partially be recovered by introducing supplementary degrees of freedom However, even in such a case the estimated value of δ ($\Delta M_W(\xi)$) will remain dependent upon the number of the $\mathcal{MT}$ samples, $2k+1$, their M_W spacing in the vicinity of the minimum and the functional form of the fit. Varying these parameters in our analysis procedure in a ξ-dependent manner would explode the PC farm CPU time and, therefore, it was abandoned in our studies. Instead, we have calibrated the propagation of statistical bin-by-bin errors into the δ ($\Delta M_W(\xi)$) error and checked the biases of all the aspects of the above method using the statistically independent "$\mathcal{PD}$-calibration samples" in which, instead of varying the ξ effects, we have varied the values of M_W. More details on this calibration method can be found in Ref. [13].

3.2.5 Event generation and simulation

The results presented below have been obtained using the dedicated processor farm, CCALI in Lyon [169]. We have generated several large samples of events, for the Z-boson $\mathcal{O}(10^7)$ and W-bosons $\mathcal{O}(10^8)$ production events which correspond to one year of the low-luminosity LHC run. Every pseudo-data/sample batch has been generated using a different seed for the random number generation to avoid any events redundancies. These events have been generated for the mass samples starting from $M_W^{\rm PDG}$ [156] with the mass shifts shown in Table 3.2.5. In addition, several samples of events corresponding to the measurement and modeling biases ξ has been simulated. The list of studied effects is presented in the next section.

3.3 Tevatron effects

In this section we consider the systematic effects which were dominant in the measurements made by the two Tevatron's experiments: CDF [170, 171, 172] and D0 [173]. Those effects are listed below:

- **Energy scale (ES).** The energy scale is the most important source of error at the Tevatron and should be the one as well at the LHC. This bias arises from the misalignment of the different tracker cells which, in turn, affects the reconstruction of the charged lepton track ρ_l like:

$$\rho_l^{(\rm rec.)} = \rho_l^{(\rm smr.)}\,(1+\varepsilon_l), \tag{3.17}$$

No.	$\delta M_W > 0$	$\delta M_W < 0$
1	+5 MeV	−5 MeV
2	+10 MeV	−10 MeV
3	+15 MeV	−15 MeV
4	+20 MeV	−20 MeV
5	+25 MeV	−25 MeV
6	+30 MeV	−30 MeV
7	+40 MeV	−40 MeV
8	+50 MeV	−50 MeV
9	+75 MeV	−75 MeV
10	+100 MeV	−100 MeV
11	+200 MeV	−200 MeV

Table 3.1: The list of positive and negative mass shifts for which $\mathcal{MT}$ samples have been generated.

where $\rho_l^{(\mathrm{rec.})}$ is the reconstructed curvature, $\rho_l^{(\mathrm{smr.})}$ – the particle true curvature smeared by the detector resolution, and ε_l – a constant accounting for the energy scale bias for the charged lepton l. The biases which are charge independent (the same for l^+ and l^-) have been chosen with values

$$\varepsilon_{l^+} = +\varepsilon_{l^-} = \pm 0.5\%,\ \pm 0.05\%, \tag{3.18}$$

where the first value is the precision achieved at the Tevatron.

- **Energy resolution factor (ERF).** The finite resolution of measuring the lepton track parameters may lead to biases in the measured value of M_W. We model the possible biases introduced by the ambiguity in the assumed size of the σ_{1/p_T} (Eq. 3.12) and $\sigma_{\mathrm{cotan}\,\theta}$ (Eq. 3.13) smearing by decreasing or increasing the widths of their Gaussian distributions by the factor ERF = 0.7, 1.0, 1.3.

On top of the apparatus effects, we consider the following theoretical biases, which are important for the Tevatron's experiments:

- **PDFs errors.** In order to assess the relevance of uncertainties arising from the parton distribution functions we follow the standard procedure

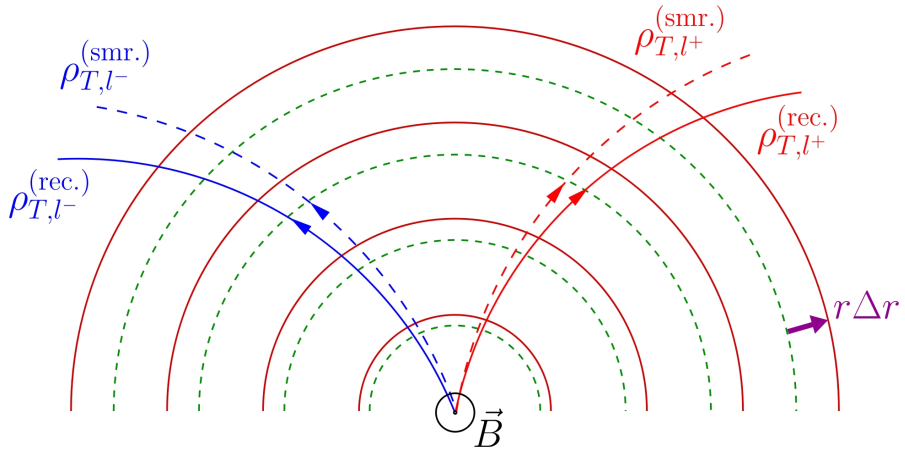

Figure 3.5: Consequences of the radial expansion distortion on the positively and negatively charged particles reconstructed tracks. Tracks of the same curvature, *i.e.* $\rho_{T,l^+}^{(\mathrm{smr.})} = \rho_{T,l^-}^{(\mathrm{smr.})}$, are considered. Figure from Ref. [164] (p. 61).

described in Ref. [174]. It allows us to determine a global PDF error by studying the pseudodata samples with minimum and maximum weights $\mathrm{PDF}_{\mathrm{max/min}} = \mathrm{PDF}_{\mathrm{cen}} \pm \delta\mathrm{PDF}$, where $\mathrm{PDF}_{\mathrm{cen}}$ is the central value from the PDF's set. All calculations have been performed with the CTEQ6m PDF sets.

- W **and** Z **transverse momenta** are driven by the strong interaction effects (see Chapter 2). They are difficult to predict because of the interplay between the leading and higher-twist perturbative effects [45] as well as the non-perturbative effects [102]. The influence of the uncertainties in modelling the transverse momenta of the W and Z bosons were investigated by changing the partonic intrinsic transverse momentum distribution modeled by Pythia Gaussian scheme [9]. In this scheme the primordial k_T distribution inside hadron is given by $\exp\left(-{k_T}^2/\sigma_{k_T}^2\right) k_T dk_T$ and has only one free parameter, namely the width of the distribution σ_{k_T}. For the LHC experiments the width of the distribution is estimated to be $\sim 4\,\mathrm{GeV}$. In our studies we were changing it by the following values: $\Delta\sigma_{k_T} = \{\pm 4, \pm 2, \pm 1\}\,\mathrm{GeV}$. Such a shift of partonic intrinsic transverse momentum is transferred in a wide-enough range to the W/Z transverse momentum distribution change.

- W**-boson width.** The uncertainty in Γ_W can translate to a significant systematic bias on M_W. This effect have been estimated by chang-

ing width of the boson to the values in the range of the error from PDG 2008 [156].

The possible improvement of the W-width measurements at the LHC will be presented in a forthcoming paper [175].

- **Photon radiation.** The QED radiation in the final-state decreases the value of $p_{T,l}$ because of the lepton four-momentum loss to the emitted photons. This effect is of high importance for the precision measurements of M_W. Since such effectes for the W bosons are included in WINHAC and for the Z boson have been recently implemented in ZINHAC, we plan to study their influence on the precision the W-mass measurement in the near future. As long as radiation processes are neglected, the electron and muon track reconstruction quality remains the same. In the following, leptons will have the meaning of either electrons or muons.

- **Backgrounds.** In the present studies we do not investigate the contribution of the QCD background to the selected samples of the W and Z boson events. Earlier studies [172] (see Fig. 46) and [4] have shown that the QCD background contamination is small and its uncertainty will have a negligible effect on the final measurement precision.

This ends the list of the most dominant systematic effects in measurements performed by the Tevatron's experiments.

3.4 The methods

In this section we evaluate the measurement strategy which was proposed in [105]. One of the key ideas of this strategy is an attempt to factorize the electroweak and the strong interaction effects as much as possible. The latter, not precisely known from the theoretical point of view, are proposed to be determined using the dedicated procedure based solely on the data. Contrary to the QCD effects, the electroweak corrections in the neutral and charged Drell–Yan process are controlled using the dedicated Monte Carlo generators, such as WINHAC and ZINHAC.

The ratio between the characteristic scale of the p_{T} spectrum of decay leptons, which is at the 40 GeV level, and the desired W-mass precision, which is at the 10 MeV level, amounts to a factor of 4000. Since the W mass is

largely derived from the characteristics of the Jacobian peak, it is intuitively clear that unusually precise understanding of the shape of the p_{T} spectrum is mandatory. Such a precision can be reached only by relating the p_{T} spectra for the W-boson decays to the corresponding ones for the Z-bosons. This is the second key idea of this method, i.e. to use of the Z-boson as a *"standard candle"* for the W-mass measurement.

3.4.1 The "standard method"

The starting point and the first step in our procedure is to use the simplest possible method. This method uses the standard setup of the LHC and the standard observable for extracting the W mass, namely the transverse momentum[2] of the charge lepton $p_{T,l}$ originating from the W-boson. Therefore, we shall refer to this method as to the "standard method". The domain for the χ^2 computation is restricted to the range

$$30\,\mathrm{GeV} < p_{T,l} < 50\,\mathrm{GeV}, \tag{3.19}$$

which is most sensitive to the mass of the W-boson, see for example Fig. 3.4. The likelihood analyses described in Subsection 3.2.4(a) show that in the case of the "standard method" all considered systematic effects ξ give huge uncertainties to M_W. The smallest distortion is caused by the ES systematic effect for its smaller value $\varepsilon_l = \pm 0.05\%$ and gives ~ 30 MeV shift of the W mass ($\chi^2/\mathrm{dof} = 1.2$, $\mathrm{dof} = 100$) which is much bigger than its statistical errors[3] ~ 5 MeV. The χ^2-plots for the ES effects for all the methods presented in this section will be shown later in Fig. 3.6. It is worth to add that for some of these effects the "standard method" gives a large value of χ^2 which means that the effect cannot be absorbed into variation of a single parameter and their values are only indicative.

3.4.2 The "standard Z-candle method"

The "standard method" requires a very precise control of the systematic errors to make the W-mass measurement competitive at the LHC. Therefore, in order to reduce the influence of the systematic effects, we will introduce

[2] In our studies we use $\rho_l = 1/p_{T,l}$ instead of the transverse momentum $p_{T,l}$, – the reason for that will be explained later in this section.

[3] For one year of a low-luminosity LHC run which means the integrated luminosity of $10\,\mathrm{fb}^{-1}$.

the Z-boson as a "standard candle" for the W-mass measurement. We expect that this procedure can improve the precision of the W-mass measurement because the Z-boson's parameters have been much more precisely measured than the corresponding W-boson's onces, and some of the considered effects affect both boson's observables in a similar way. Therefore, we expect that some of the effects will cancel. The main difference between Z and W boson events is such that in the case of Z-boson both leptons momenta can be directly measured while in the case of W-boson only the charged lepton can be detected[4]. Therefore, in order to preserve democracy in both the W and Z samples, we apply the dedicated triggering and data-selection scheme to minimize the uncertainty in the relative efficiency and the acceptance corrections for the Z and W boson samples of events. This scheme consists of using the inclusive charged-lepton Level-1 trigger followed by the Z/W-symmetric cut in the reconstructed lepton-track curvature ρ_l in the high-level trigger and in the off-line event selection phases. This is achieved by searching for a second, same flavour but opposite charge lepton in the selected bunch crossings. If such a track is found to point to the same vertex, it is removed from the charged-track sample and the event is flagged as the Z-boson event. The missing transverse momentum measurement is then identical for the W and the Z-boson samples. The corresponding choice for a observable which will be used to determine M_W is a ratio of the charged lepton track curvature radius ρ_l:

$$R_{WZ} = \frac{d\sigma/d\rho_l^W}{d\sigma/d\rho_l^Z}. \tag{3.20}$$

The main improvement is for the PDF systematic effects which are reduced from a few hundred MeV to $\sim 18 \pm 6$ MeV. It also makes a change in the case of ES systematic effects which are reduced by $\sim 30\%$, i.e. to the value $\sim 22 \pm 6$ MeV for the $\varepsilon_l = \pm 0.05\%$, and to the value $\sim 220 \pm 6$ MeV for the $\varepsilon_l = \pm 0.5\%$, see Fig. 3.6. This result confirms the result of the analysis presented in ATLAS [6]: using this method the charge-average scale of the lepton momentum must be known to the precision better than 0.02% for the W-boson mass to be measured with the precision better than 10 MeV. As was demonstrated in Ref. [6], such a detector-fiducial-volume-average precision can be achieved for an integrated luminosity of $10\,\mathrm{fb}^{-1}$ using the Z-peak method,

[4]The neutrino four-momentum can be reconstructed only indirectly, by using the reconstructed momenta of all the particles produced in the collision of the beam particles, which, in our opinion, is not suited for high-precision measurements.

regardless of the functional form of the momentum-dependent biases. However, still the errors due to all considered effects are bigger (especially RF and $\Delta\sigma_{k_T}$) than the statistical errors. Therefore, this method must be improved in order to further reduce the influence of these effects.

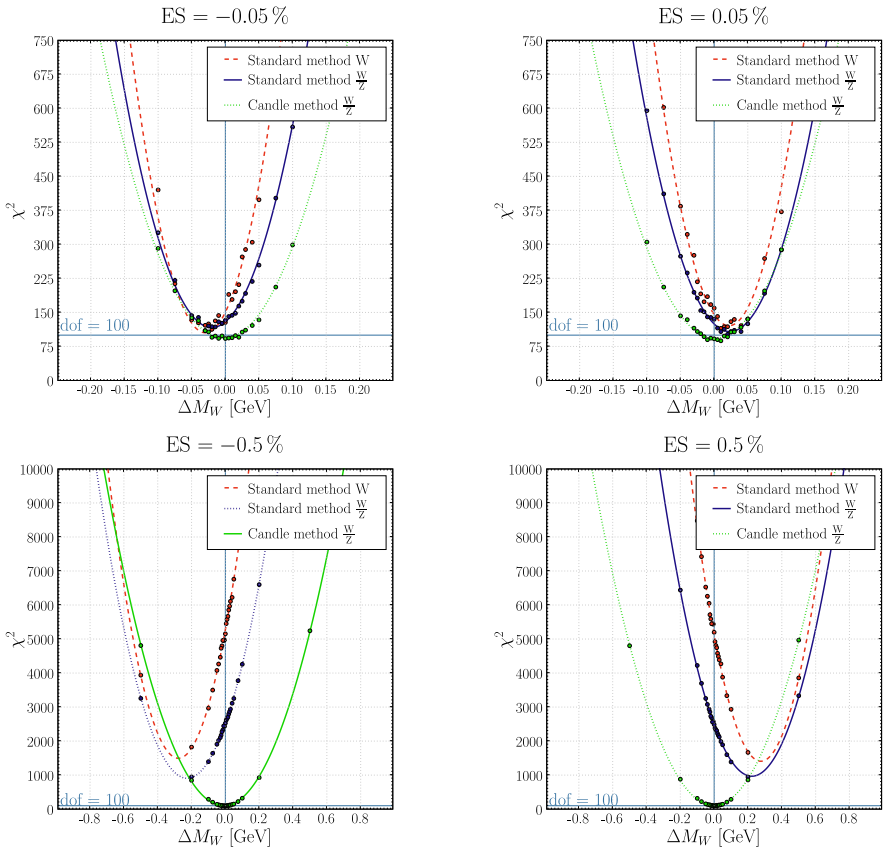

Figure 3.6: The χ^2 results for the energy scale (ES) systematic effects for three methods: the "standard method" (denoted on plots by "Standard method W"), the "standard Z-candle" (denoted by "Standard method $\frac{W}{Z}$") and the "improved Z-candle" (denoted by "Candle method $\frac{W}{Z}$").

3.4.3 The "improved Z-candle method"

In the previous step we have seen that indeed some of the considered systematic effects affect the $d\sigma/d\rho_l^W$ and $d\sigma/d\rho_l^Z$ observables in the similar way and, as a consequence, their impact on M_W error can be reduced. However, there are still differences between the distributions which lead to the visible and different distortions of the bosons observables. Therefore, in this section we will introduce a new method: the "improved Z-candle method". In this method

we put both bosons, as much as possible, on the same footing. This is done by the following procedure:

- We propose to collect data at the two CM-energies: $\sqrt{s_1}$ and $\sqrt{s_2} = \frac{M_Z}{M_W} \times \sqrt{s_1}$. These two settings allow to keep the momentum fractions of the partons producing the Z and W bosons equal if the W-boson sample is collected at the CM-energy $\sqrt{s_1}$ and the Z-boson sample at the CM-energy $\sqrt{s_2}$. $\sqrt{s_2}$ in our studies is set to the nominal LHC energy, i.e. $\sqrt{s_2} = 14$ TeV.

- We propose to rescale the solenoid current while running at the two CM-energies $\sqrt{s_1}$ and $\sqrt{s_2}$ by the factor $i_2/i_1 = M_Z/M_W$ to equalize (up to the effects of the QCD/QED radiative corrections) the distribution of the curvature radius ρ_l for charged leptons originating from the decays of the Z and W bosons.

The W and Z boson events are then selected by demanding the presence of the charged lepton with the track curvature radius ρ_l satisfying the following conditions:

$$\rho_{l_1}(s,i) \;\leq\; \rho_l^B(s,i) \;\leq\; \rho_{l_2}(s,i), \tag{3.21}$$

here B stands for the W or Z boson, $\rho_{l_k}(s,i) = \frac{i(s)}{i(s_2)} \, \frac{1}{p_{T,k}(s)}$, where $k = 1, 2$ and

$$\begin{aligned} p_{T,1}(s_2) = 50\,\text{GeV}, \qquad & p_{T,2}(s_2) = 20\,\text{GeV}, \quad p_{T,k}(s_1) = p_{T,k}(s_2)\frac{M_W}{M_Z}, \\ i(s_2) = i_2, \qquad & i(s_1) = i_2\,\frac{M_W}{M_Z}, \end{aligned} \tag{3.22}$$

and the pseudorapidity η_l within the range:

$$-\,2.5 \leq\; \eta_l \;\leq 2.5\,. \tag{3.23}$$

For the event sample with two charged leptons (Z candidates) we first randomly choose one of the two leptons and select an event only if this lepton satisfies the same selection criteria as specified above. Note that by specifying the selection condition in terms of the radius of the track curvature rather than in terms of the transverse momentum and by rescaling the solenoid current and CM-energy we achieve almost symmetric selection of the W-boson and Z-boson events[5].

[5]The remaining residual asymmetry reflects the differences in the transverse momentum of the Z and W bosons and in the angular distributions of the charged leptons.

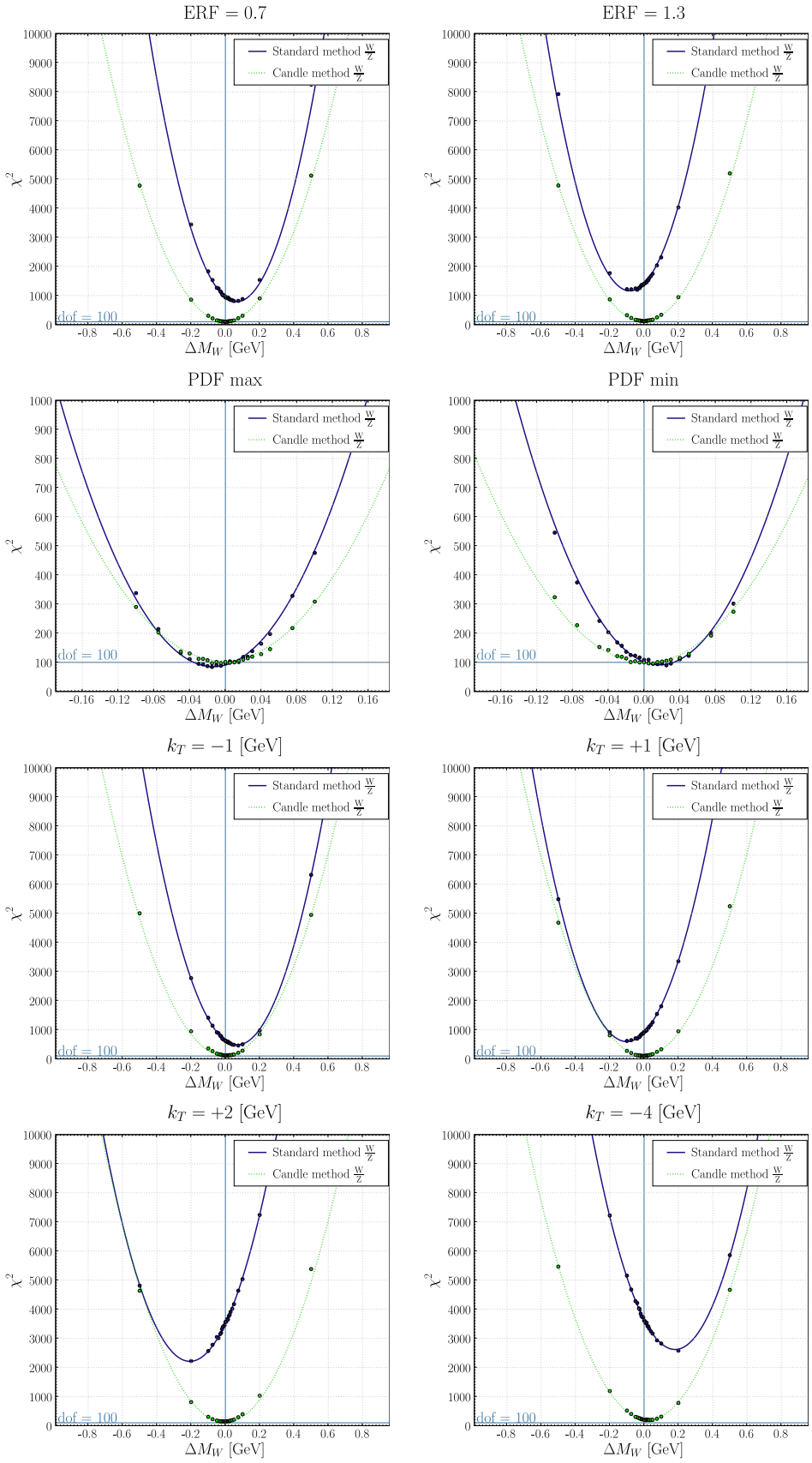

Figure 3.7: The χ^2 results for ERF, PDF and intrinsic p_T systematic effects for two methods: the "standard Z-candle" (denoted by "Standard method $\frac{W}{Z}$") and the "improved Z-candle" (denoted by "Candle method $\frac{W}{Z}$").

We introduce the following new observable

$$R^c_{WZ} = \frac{d\sigma/d\rho^W_l(s_1, i_1)}{d\sigma/d\rho^Z_l(s_2, i_2)}. \tag{3.24}$$

In Table 3.2 we present the results (the W mass shifts, their statistical errors and their χ^2 values) for all considered in this section systematic effects, both for the "standard Z-candle" and "improved Z-candle" methods. The same results can be seen in the series of plots in Figure 3.7. We can see the striking improvement of all the results in the case of the "improved Z-candle" method – this procedure reduces the impact of the almost all effects on the M_W precision (except for the $\Delta\sigma_{k_T}$) to the level of the statistical error.

		R_{WZ}		R^c_{WZ}	
	Syst. ξ	ΔM_W [MeV]	$\chi^2_{\min}$/dof	ΔM_W [MeV]	$\chi^2_{\min}$/dof
Cent. Exp.	$\xi = 0$	2.1 ± 5.7	0.9	-0.0 ± 7.2	1.0
ES [%]	-0.05 %	-20.2 ± 5.7	1.2	-2.0 ± 7.2	0.9
	$+0.05$ %	23.3 ± 5.7	1.1	1.2 ± 7.2	0.9
	-0.50 %	-224.5 ± 5.6	9.3	-4.5 ± 7.1	1.0
	$+0.50$ %	227.4 ± 5.7	9.1	2.1 ± 7.2	1.0
ERF	0.7	-83.4 ± 5.7	5.9	1.9 ± 7.2	1.0
	1.3	104.0 ± 5.7	9.5	4.0 ± 7.2	1.3
PDF	Max	12.2 ± 5.7	0.9	4.0 ± 7.2	1.0
	Min	-18.2 ± 5.7	1.0	-4.5 ± 7.2	1.0
$\Delta\sigma_{k_T}$ [GeV]	-2	-149.8 ± 5.6	18.1	-18.9 ± 7.2	1.2
	-1	-72.0 ± 5.7	4.7	-7.8 ± 7.2	1.2
	$+1$	97.7 ± 5.7	6.1	8.1 ± 7.2	1.1
	$+2$	204.4 ± 5.7	22.4	12.7 ± 7.2	1.4

Table 3.2: The systematic errors for the "standard Z-candle"(R_{WZ}) and "improved Z-candle" (R^c_{WZ}) methods.

In particular, we observe that the sensitivity of the W-boson mass to the charge-averaged scale uncertainty is reduced by a factor of ~ 100. This is easy to understand by noticing that (leaving aside the polarization, flavour-dependent and QCD-scale effects) the leptons from decays of Z and W bosons will give rise to the same topology of reconstructed space points. One has to admit that this method brings a burden of the necessity of the detector re-calibration and re-alignment for the reduced energy runs. But this extra burden exist only for a perfectly stable detector. In reality its calibration must be optimized in shorter time intervals with respect to those devoted to running at the different CM-energies. The net gain, as far as the measurement of the

W mass is concerned, is obvious and the decrease of luminosity collected at the highest achievable CM-energy is statistically insignificant.

3.4.4 The fourth step – the C_{QCD} factor.

The change of partonic intrinsic momentum distribution, governed by the Gaussian smearing parameter σ_{k_T}, which is the last remaining effect exceeding the statistical error, has been introduced in order to investigate the influence of QCD uncertainties. From the QCD point of view, one of the differences between the Z and W bosons is the difference in their masses (scales). We propose to remove this remaining asymmetry by correcting the R^c_{WZ} observable by the C_{QCD} factor. This factor is extracted from the data rather than modeled.

We propose to select the samples of events containing a pair of opposite charge and same flavour leptons and to measure the ratio of the integrated lepton pair production rates

$$C_{\mathrm{QCD}} = \frac{\int_{M_Z-3\Gamma_Z}^{M_Z+3\Gamma_Z} N_{l^+l^-}(s_2, i(s_2), M_{l^+l^-})\, dM_{l^+l^-}}{\int_{M_W-3\Gamma_W}^{M_W+3\Gamma_W} f_{\mathrm{BW}}(s_{l^+l^-}; M_W, \Gamma_W)\, w_{\mathrm{EW}}\, N_{l^+l^-}(s_1, i(s_1), M_{l^+l^-})\, dM_{l^+l^-}} \tag{3.25}$$

as a function of ρ_l and as a function of η_l of the randomly chosen lepton, l^+ or l^-. The rates $N_{l^+l^-}$ in the above formula are integrated over the invariant-mass $M_{l^+l^-}$ of the lepton pairs in the ranges $(M_Z - 3\Gamma_Z, M_Z + 3\Gamma_Z)$ and $(M_W - 3\Gamma_W, M_W + 3\Gamma_W)$, correspondingly. Each event having a reconstructed invariant-mass in the latter region is weighted by the Breit–Wigner function[6]

$$f_{\mathrm{BW}}(s_{l^+l^-}; M_W, \Gamma_W) = \frac{1}{\pi}\, \frac{M_W\Gamma_W}{(s_{l^+l^-} - M_W^2)^2 + M_W^2\Gamma_W^2}\,, \tag{3.26}$$

where $s_{l^+l^-} = (M_{l^+l^-})^2$, and by the QCD-independent normalization factor w_{EW}. This factor is defined such that the integral of the weighted lepton invariant-mass spectrum in the region of $(M_W - 3\Gamma_W, M_W + 3\Gamma_W)$ is equal to the cross section of a Z-like boson having the mass and the width of the W-boson[7]. The lepton-pair production events used in the determination of $C_{\mathrm{QCD}}(\rho_l, \eta_l)$ must be triggered and selected on the basis of the presence of

[6] This formula corresponds to the so-called fixed-width scheme, however it can also be applied to the running-width scheme, in which case both M_W and Γ_W have to be divided by the factor $\sqrt{1 + (\Gamma_W/M_W)^2}$.

[7] The weighting procedure takes care of the asymmetries of the angular distributions of the leptons produced in the region of the Z-peak and in the region outside the Z-peak.

		R^c_{WZ}	$R^c_{WZ} + C_{QCD}$
	Systematic ξ	ΔM_W [MeV]	ΔM_W [MeV]
$\Delta\sigma_{k_T}$	+2	12.7	4.6
	+1	8.1	−0.3
	−1	−7.8	−3.3
	−4	−26.6	−8.5

Table 3.3: The W-mass shifts corresponding to the $\Delta\sigma_{k_T}$ systematic effect for the "Z-candle" and "Z-candle + C_{QCD}" methods.

two same-flavour, opposite-charge lepton candidates. Each of the leptons must satisfy the kinematical selection criteria specified in the previous step. This requirement, stronger than the corresponding one for the Z-boson sample of events discussed in the previous step, is necessary to reduce the background to the inclusive lepton samples in the lepton-pair invariant-mass region outside the Z-peak. Table 3.3 shows that this procedure is able to decrease significantly the influence of the $\Delta\sigma_{k_T}$ effect on the W-mass measurement.

3.4.5 Summary

As we have demonstrated (Tables 3.2 and 3.3), the final measurement method proposed in this section is capable to reduce the influence of all the considered so far systematic effects on the measured W-boson mass uncertainty below its statistical error. Note that these studies have been preformed for one year of the low-luminosity LHC run, therefore for higher luminosity or/and longer time of collecting data these results should be even better.

As we have mentioned in the introduction, dealing with the most important systematic errors from the previous and current hadron experiments, is of course, a mandatory step for the precision measurement of M_W at the LHC. However, the question which remains to be answered is whether this is sufficient for the LHC measurement, or whether one will be faced with new kinds of problems which were not important at the Tevatron but become apparent at the LHC. This question is addressed in the next section.

3.5 LHC specific effects

In this section we discuss the biases which are of negligible importance at the Tevatron but become dominant at the LHC. These sources of errors have been neglected in the ATLAS [6] and CMS [14] analyses, resulting in too an optimistic assessment of the expected measurement precision of the W-boson mass. The common origin of those new sources are:

- the net excess of quarks over antiquarks in $p\,p$ collisions,
- the flavour dependence of the quarks momentum distributions (PDFs),
- the increase of the collider energy.

In this section we discuss in some details the differences in the production and decay of W^+, W^- and Z bosons in hadronic collisions. We show how these differences are reflected in the relationship between W and Z boson observables at the Tevatron and at the LHC. We trace the principal differences between the Tevatron and the LHC, identify the effects which are specific to the LHC $p\,p$ collision scheme and evaluate their impact on the M_W measurement biases at the LHC. For the first time the precision of the W-boson mass is evaluated taking into account these effects. We argue that the present precision of M_W cannot be improved at the LHC unless a dedicated "precision-support measurement programme" is persued. Two examples of such a programme are proposed at the end of this section. The first one involves colliding at the LHC, for a fraction of time, light iscoscalar ion beams – for example of the deuterium or helium nuclei. The core of the second one is a dedicated muon scattering experiment with proton and deuteron targets.

3.5.1 Production and decay of W and Z bosons

At the begining of this subsection we will assume that the masses of the W and Z bosons are equal[8]. The rationale behind it is to simplify our discussion by factorizing the electroweak and QCD effects and by considering only the former. In the subsequent sections we will restore the canonical mass values and consider the QCD effects.

[8] We have already seen that the methods developed in Section 3.4 allow us to suppress, to some extent, the effects caused by the difference in the electroweak-bosons masses.

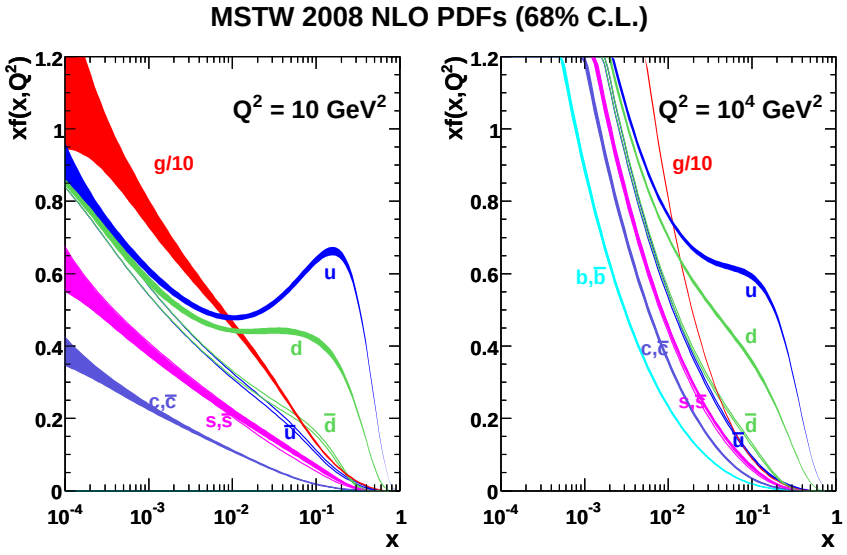

Figure 3.8: MSTW 2008 NLO PDFs at $Q^2 = 10$ GeV^2 and $Q^2 = 10^4$ GeV^2. The plot taken from Ref. [176].

(a) Production

Let us start the discussion on the differences in the production of electroweak bosons from recalling that quite different quark–antiquark pairs contribute predominantly to the production of W^+, W^- and Z, see Table 3.4. As a

W^+	$u\bar{d} + u\bar{s} + u\bar{b} + c\bar{d} + c\bar{s} + \cdots$
W^-	$d\bar{u} + d\bar{c} + s\bar{u} + s\bar{c} + \cdots$
Z	$u\bar{u} + d\bar{d} + s\bar{s} + c\bar{c} + b\bar{b} + \cdots$

Table 3.4: Quark–antiquark pairs that contribute to the W^+, W^- and Z production.

consequence, in the production mechanisms of W^+, W^- and Z, the following differences need to be carefully assessed:

(i) differences in the respective partonic distribution functions, see Fig. 3.8,

(ii) differences in the respective EW quark coupling constants,

(iii) differences in the respective transverse momenta k_{T} distribution of annihilating quarks in W and Z production.

Because the W mass is determined from the p_{T} spectrum of decay leptons, our interest focuses on the direction *perpendicular* to the beam. For the following three reasons they are mutually different:

- the correlation of the Bjorken-x of the participating quarks and anti-quarks with their k_{T} (small x is correlated with large k_{T}), see Fig. 3.11[9],
- the dependence of k_{T} on the quark type (heavier quarks have larger k_{T}, on average),
- the types of quarks that participate according to their EW coupling constants and to the values of the CKM matrix elements.

These differences in the production of W^+, W^- and Z propagate through leptonic-decay characteristic into differences of the charged-lepton momenta spectra.

(b) Decay

With respect to the W^+, W^- and Z spin directions, the angular distributions of decay leptons are different according to the $V-A$ and $V+A$ amplitudes in the boson-lepton coupling. In the $W^{\pm}$-rest frame, the pure $V-A$ coupling leads to the following angular distribution of the charged-lepton emission amplitude:

$$w(\theta) \propto 1 \pm \cos\theta \ , \tag{3.27}$$

where θ denotes the angle between the directions of the W-spin vector and the charged-lepton emission. In the Z-rest frame, the quark-charge-specific mixture of $V-A$ and $V+A$ leads to the angular distribution of the corresponding emission amplitude:

$$w(\theta) \propto 1 + \gamma \cos\theta \ , \tag{3.28}$$

where $|\gamma| < 1$.

The charged-lepton emission asymmetries are modified by the Lorenz boost from the boson rest frame into the laboratory frame. As can be expected, an important contribution to the differences in the p_{T} distribution of charged leptons from W^+, W^- and Z decays that are observable in the laboratory frame comes from the interference between transverse and longitudinal boson polarization amplitudes. Finally, since the charged leptons with the pseudorapidity

[9] This effect will be discussed in more details in Section 3.5.2(b).

$|\eta| > 2.5$ can hardly be measured in both ATLAS and CMS detectors, a limited pseudorapidity range impacts on the charged-lepton p_{T} distribution.

Altogether, the different polarizations of W^+, W^- and Z, in conjunction with the different angular distributions of charged-lepton emission, and in conjunction with their different p_{T} spectra, lead to the question whether the differences of the p_{T} spectra of decay leptons from W^+, W^- and Z can be sufficiently well understood to achieve the desired precicion of the W-boson mass measurement at the LHC.

Following the above discussion on the differences between the production and decay of electroweak bosons, we can now discuss how the important differences of W^+, W^- and Z production in the $p\,p$ collisions at the LHC and in the $p\,\bar{p}$ collisions at the Tevatron come into play. The goal of this discussion is to identify the LHC-specific effects, which are of no significant importance for the Tevatron measurements, but will limit the measurement precision of the W-boson mass at the LHC.

3.5.2 W and Z bosons at $p\,p$ and $p\,\bar{p}$ colliders

(a) Charge and polarization effects

The Tevatron case.

In the $p\,\bar{p}$ collisions, there is a small forward–backward asymmetry in the production of charged leptons, at the polar angles θ and $\pi - \theta$, for Z-boson decays and a large asymmetry for W-boson decays – in both cases positively charged leptons are produced preferentially along the incoming proton direction. However, the rates and the momentum spectra of positive leptons from W^+ at the polar angle θ are exactly the same as the rates of negative leptons from W^- at the polar angle $\pi - \theta$, see plots on the left-hand side of Fig. 3.9. The same holds when integrated over the same range of θ and $\pi - \theta$, respectively. Since for any θ-symmetric cuts the rates and distributions of positive and negative leptons are the same, a common analysis of leptons with positive and negative charge is justified at the Tevatron.

The common analysis of charged leptons from the W^+ and W^- decays is equivalent to the W decay with equal $V - A$ and $V + A$ amplitudes, which is parity-conserving and resembles closely (because of the Nature's choice of the electroweak mixing angle $\sin^2\theta_W$, close to 1/4) the nearly parity-conserving Z decay amplitude. There is thus a fortunate cancellation of polarization effects

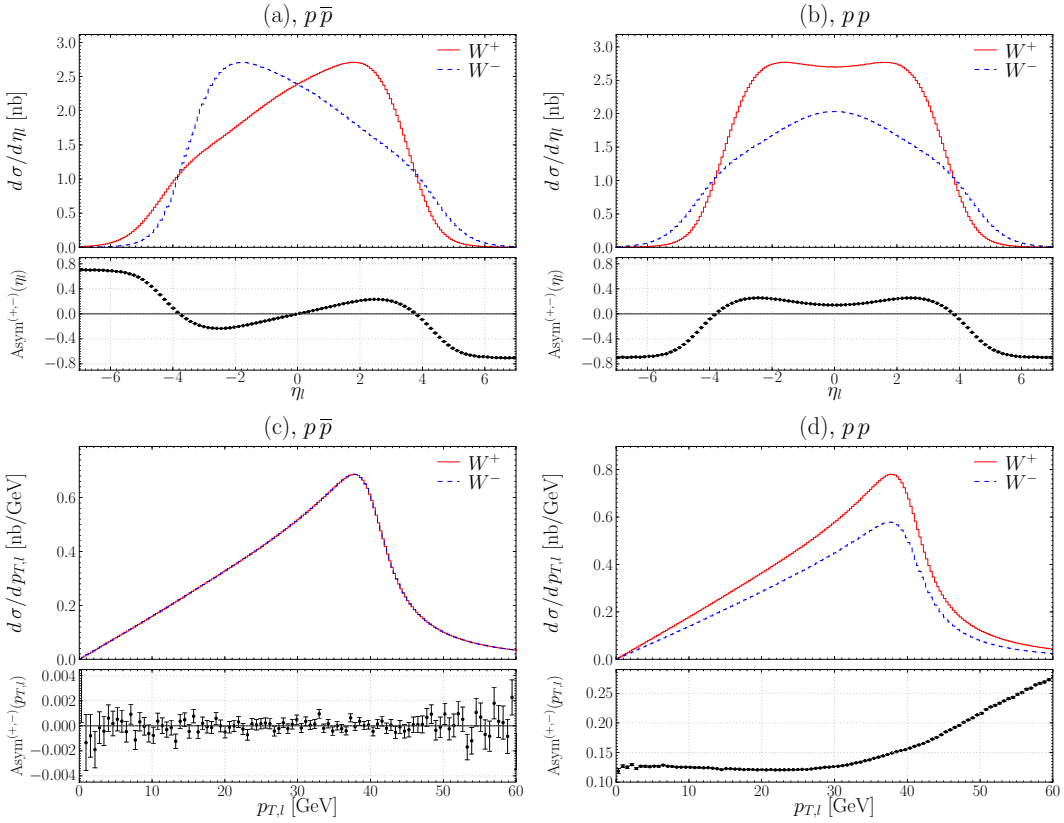

Figure 3.9: The pseudorapidity η_l and transverse momentum $p_{T,l}$ distributions for charged leptons produced in W-boson decays for the $p\bar{p}$ (a,b) and pp (c,d) collisions, see Ref. [13] for details.

when calibrating, without regard to the charge sign, charged lepton spectra from the W decays with lepton spectra from the Z decays – for the charge blind analysis. Let us note that for the equal proportion of the W^+ and W^- bosons and in the presence of the full overall symmetry of the quark and antiquark PDFs, the relations of the Z and W boson rapidities and the lepton pseudorapidities are similar, and boiling down predominantly to smearing effects.

The LHC case.

In the pp collisions at the LHC, there is, for each electroweak boson, an inherent symmetry in the forward–backward production of both the positively and the negatively charged leptons: at the polar angles θ and $\pi - \theta$ the rates and the momentum spectra are identical. However, the rates and the momentum spectra are different between W^+, W^- (see plots on the right-hand side

of Fig. 3.9) as well as for Z. First of all, we note the difference in the rates and the momentum spectra of charged leptons from the W^+ and W^- decays, which *a priori* renders a common analysis of leptons with positive and negative particularly difficult. Because of the preponderance of W^+ over W^- in the pp collisions, none of the cancellations is at work. This opens the LHC 'Pandora box' containing several important effects that have been circumvented at the Tevatron but must be understood at the LHC. We note that the relative proportion of W^+ over W^- will depend both upon the choice of the lepton angular acceptance region and upon the asymmetry in the PDFs of the up and down-type quarks.

The first consequence of the LHC asymmetry in the W^+ and W^- production is that the calibration procedure of the lepton transverse momentum scale, which has been developed at the Tevatron [172], cannot be applied at the LHC. To be more specific, the charge-average calibration using the 'Z-peak' position method, applicable both in the Tevatron and in the LHC case, can no longer be supplemented by an unbiased lepton-charge dependent calibration. Note that at the LHC, contrary to the Tevatron, the p_{T} distributions of positive and negative leptons coming from the W decays are no longer identical. If one would ignore this effect and calibrate the relative momentum scale for positive and negative leptons by adjusting the peak positions of their respective p_{T} distributions, then the M_W would be biased by $\sim 240\,\mathrm{MeV}$ for the central $|\eta_l| < 0.3$ region, rising to $\sim 2000\,\mathrm{MeV}$ for the forward $3.5 < |\eta_l| < 4.5$ region. These LHC-specific calibration biases, absent at the Tevatron, must be controlled at the LHC with a high precision by introducing the LHC-dedicated calibration method.

(b) Valence quarks

If only the sea quarks were involved in the production of W's in pp collisions, the symmetry in the production of W^+ and W^- would not be broken and the LHC measurement of the W-boson mass could follow the path chartered by the Tevatron experiments. In practice, the symmetry is broken by valence quarks, more specifically by the difference of the $u^{(\mathrm{v})}$ and $d^{(\mathrm{v})}$ PDFs of the proton, see Fig. 3.8. In Fig. 3.10 we show the distributions of the transverse momentum, $p_{T,l}$, of the leptons coming (a) from the W^+ decays and (b) from the W^- decays for the two following cases: (1) the W-bosons are produced only by the sea quarks and antiquarks and (2) the W-bosons are produced

by all the quarks and antiquarks of the colliding protons. The positions of the Jacobian peaks are determined using the second-order polynomial fit in the range $37\,\text{GeV} < p_{T,l} < 52\,\text{GeV}$. Such a fit can be considered as a rough estimate of the size of the LHC-specific effects induced by the valence quarks. We find that by including the processes of the W-boson production by the valence quarks, one generates a shift in the M_{W^+} value by 360 MeV and in the M_{W^-} value by -50 MeV with respect to the sea-only driven production. At the Tevatron these biases are of no relevance.

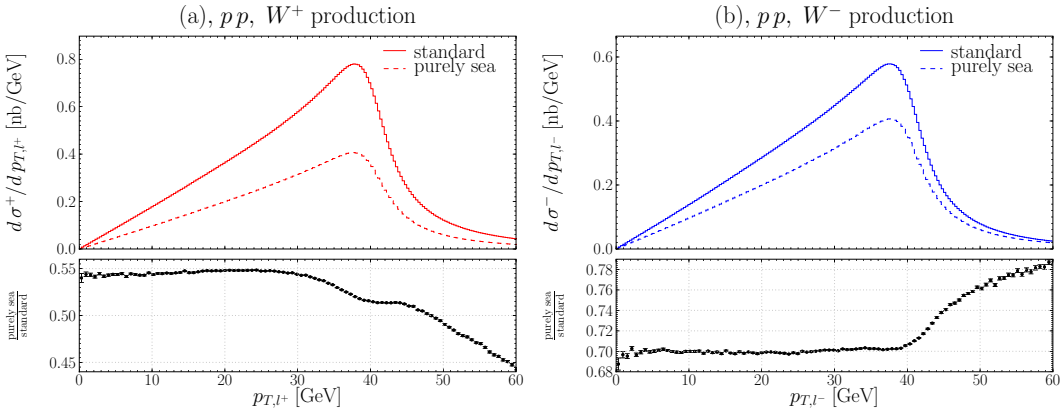

Figure 3.10: The polarization effects in the $p_{T,l}$ distributions for the W^+ (left plot) and W^- (right plot) production at the LHC.

The dominant source of the observed shifts are the charge-dependent W-boson polarization effects which are generated by the presence of the valence quarks ($u^{(\text{v})}$ and $d^{(\text{v})}$). The polarization effects alone could not, however, explain the magnitude of the observed biases, in particular their large charge-asymmetry. Clearly, other effects must come into play. It turns out that they originate from the shape difference of the up-type and down-type quark PDFs, coming predominantly from the asymmetry in the $u^{(\text{v})}$ and $d^{(\text{v})}$ PDFs. This asymmetry is reflected in the transverse momentum spectra of leptons through the correlation of the Bjorken-x's of the quarks and antiquarks forming the W-bosons with their k_{T}'s. In order to understand the subtle interplay of the above two effects we have factorized out the polarization effects and analyzed the flavour decomposition of the transverse momentum spectra of the W and Z-bosons, rather than the spectra of their decay products. In the plot on the left hand side of Fig. 3.11 we show the ratio of the k_{T} distribution of the $\bar{u}$-antiquark participating in the production of the W^--boson to the corresponding distri-

bution for the Z-boson. The integrals of both distributions are normalized to the same value. We observe a harder k_{T} spectrum for the Z formation process than for the W^- formation process as expected from the relative difference of the hardness scale ($M_Z > M_W$). In the plot on the right hand side of Fig. 3.11 we show the same ratio for equal masses of W and Z bosons. Note that for the $p\bar{p}$ collision such a ratio is independent of k_{T} and equal to 1. Surprisingly, the large asymmetry remains for the pp collisions. Its origin is explained in the following. The $\bar{u}$ partners to produce Z and W-bosons are, respectively,

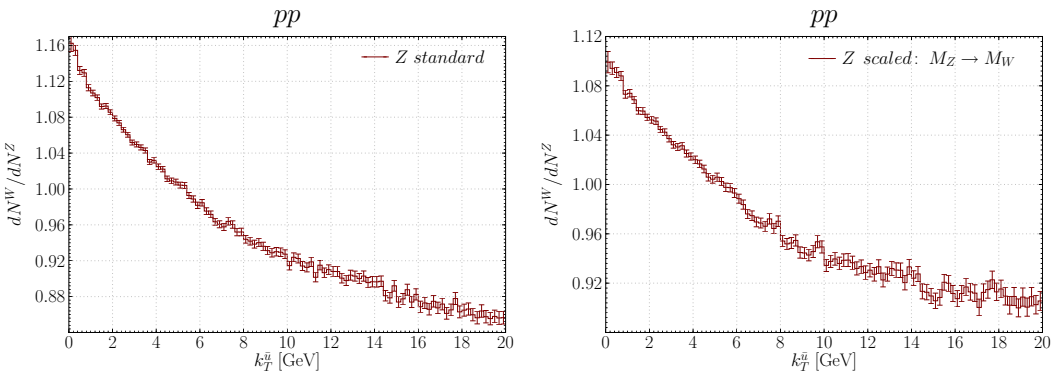

Figure 3.11: The ratio of k_{T} distribution of $\bar{u}$-quarks taking part in producing W and Z bosons.

the u and d-quarks[10]. Because of large momentum asymmetry of the valence $u^{(\mathrm{v})}$ and $d^{(\mathrm{v})}$ quarks, the average Bjorken-x of the $\bar{u}$ quark forming the Z-boson is smaller than the average Bjorken-x of the $\bar{d}$ quark forming the W^--boson. This leads to a harder k_{T} spectrum of the $\bar{u}$ quark forming the Z-boson with respect to that for the W^--boson. The above effect turns out to be larger than the QCD scale effect between M_W and M_Z (!) and it is present only for the $p\,p$ collider. A similar analysis has been performed for each quark and antiquark flavour. In each case significant asymmetries in the k_{T} distributions of quarks (antiquarks) forming the Z, W^+ and W^- bosons have been observed. The key point here is not only the presence of such asymmetries but the fact that they cannot be circumvented by taking the sums of isospin mirrored processes (relevant for the charge-blind analysis).

So far we have focussed our discussion on the effects generated by the quarks

[10]For simplicity of arguments, we discuss here only the Cabibbo-allowed processes of the W-boson formation. The sub-leading Cabibbo-suppressed effects are included in the presented plots but are of no significant relevance for the current discussion.

of the first flavour family. In the following we will discuss the contribution of the second and of the third family of quarks to the W and Z boson production processes. Their contribution, of residual importance at the Tevatron, becomes significant at the LHC – complicating further the relationship between the W and Z boson production processes.

(c) The second and the third quarks family effects

At the Tevatron energies, the Z-bosons are produced predominantly by the u, d and s quarks, see Fig. 3.12 (only $\sim 3\%$ of the Z-bosons are produced by the c and b quarks, see Table 3.5). Similarly, the W-bosons are produced predominantly by the u and d quarks (annihilations involving the c and s quarks contribute to the total cross section at the $\sim 7\%$ level). Altogether, the systematic error of the W mass at the Tevatron due to uncertainties in the heavy-quark sector is negligible in comparison with the statistical error. The contribution

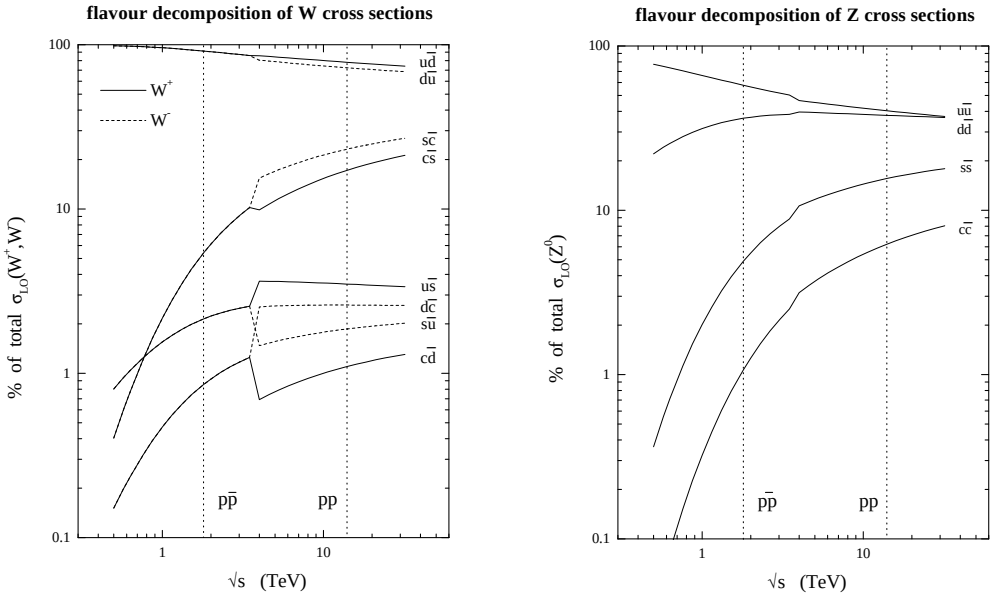

Figure 3.12: Parton decomposition of the W^+, W^- (plot on the left) and Z (plot on the right) total cross sections in $p\bar{p}$ and pp collisions. Individual contributions are shown as a percentage of the total cross section in each case. The plot taken from Ref. [177].

of the second and third quark family to the W and Z production cross section increases sizeably at the LHC energies. The probabilities that the W^+ (W^-)-

boson is formed from the charm (anti-charm) quark are $\sim 21\%$ ($\sim 28\%$). The probability that the Z-boson is formed in the annihilation of the c and b quarks rises to $\sim 15\%$. They can no longer be disregarded. There are two essential

	W^+					W^-				
Subprocesses	$u\bar{d}$	$u\bar{s}$	$c\bar{d}$	$c\bar{s}$	$c\bar{b}$	$d\bar{u}$	$s\bar{u}$	$d\bar{c}$	$s\bar{c}$	$b\bar{c}$
Tevatron II	90	2	1	7	0	90	2	1	7	0
LHC	74	4	1	21	0	67	2	3	28	0

	Z				
Subprocesses	$u\bar{u}$	$d\bar{d}$	$s\bar{s}$	$c\bar{c}$	$b\bar{b}$
Tevatron II	57	35	5	2	1
LHC	36	34	15	9	6

Table 3.5: The results from Ref. [178] showing partial contributions $\sigma_{q\bar{q}'}/\sigma_{tot}$ of quark–antiquark annihilation subprocesses to the total Born cross sections in $W^{\pm}$ and Z boson production at the Tevatron and LHC (in percent).

reasons why the presence of the second and third family quarks introduces the biases to the relationship between the transverse momentum distribution of the leptons coming from the W and Z decays and, as a consequence, the biases in the unfolded M_W value. The first and the most important one is related to the flavour asymmetries of the Bjorken-x and k_{T} distributions of both the quarks and antiquarks. These asymmetries are of nonperturbative origin and must be constrained experimentally. They influence the lepton transverse momentum spectra through the transverse momentum spectra of the parent bosons which, in turn, are driven by the Bjorken-x and k_{T} spectra participating quarks (antiquarks) and their correlations[11]. These correlations are different for the light (u, d, s) quarks, for the c-quark and for the b-quark. The second reason is the large gap in the masses of the quarks in the third family. As a consequence the b quarks do not participate in formation of the W-bosons, see Fig. 3.12, while they participate in the formation of the Z-bosons. Since the Z-boson serves as a calibration template for the W-boson, the broadening of the $p_{T,l}$ distribution due to the contribution of the b-quark annihilation processes must be taken into account.

[11] The presence of the quarks of the second and third families modifies also the polarization of the produced bosons. These polarization effects are Cabibbo suppressed. They are taken into account throughout this paper but, in order to simplify the discussion, omitted in this section.

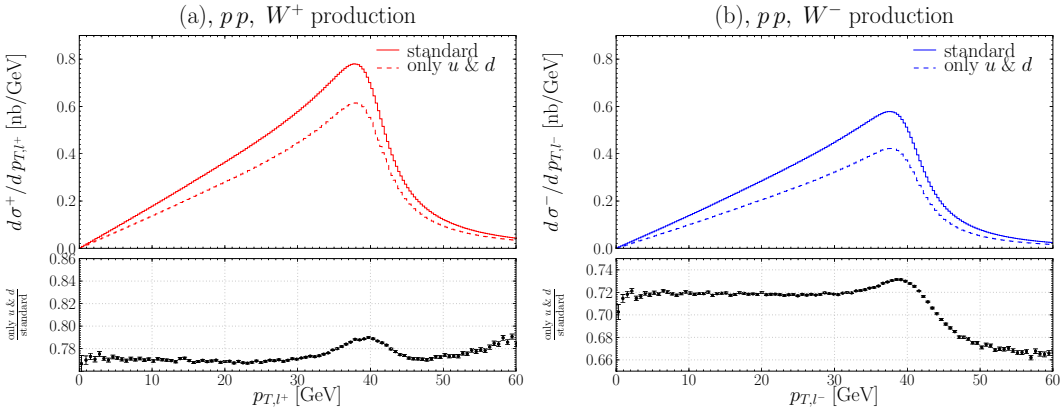

Figure 3.13: The effects of the second quark family in the $p_{T,l}$ distributions for the W^+ and W^- production at the LHC.

In Fig. 3.13 we show the shapes of the distributions of the transverse momentum, $p_{T,l}$, of the leptons coming (a) from the W^+ decays and (b) from the W^- decays, for the following two cases: (1) the W-bosons produced only by the first-family quarks and antiquarks, and (2) the W-bosons produced by all the quarks and antiquarks. The positions of Jacobian peaks are determined using the second order polynomial fit in the range $37\,\text{GeV} < p_{T,l} < 52\,\text{GeV}$. Such a fit can be considered as a rough estimate of the size of the LHC-specific effects induced by the second-family quarks. We find that by including the processes of production of the W-bosons by the second-family quarks one generates a shift in the M_{W^+} value by $-140\,\text{MeV}$ and in the M_{W^-} value by $-120\,\text{MeV}$. These biases must be understood at the LHC to the precision better than $\sim 10\%$ in order to measure the W-boson mass to the precision of 10 MeV. At the Tevatron the corresponding biases are smaller by approximately the factor ~ 5 and do not contribute significantly to the overall measurement error of the W mass.

3.6 A biased W mass

The goal of the analysis presented above was to explain the basic reasons why the measurement strategy which is justified for the $p\bar{p}$ collisions at the Tevatron cannot *a priori* be used as the template for the $p\,p$ collisions at the LHC. The assessment of the impact of the uncertainties in the longitudinal and in the transverse polarization amplitudes of the W^+, W^- and Z bosons

and in their interferences on the $p_{\rm T}$ spectra of decay leptons has been missed in all the studies made so far. We note as well that not a single LHC-physics study has made so far a difference between charged leptons coming from the W^+ and W^- decays. In addition, even if the effects of the heavy quarks on the $p_{\rm T}$ spectra of decay leptons have been discussed, the detailed assessment of the flavour-dependent effects has been largely missing in the previous studies. As a consequence, unrealistically small errors were reported for the W mass measurement at the LHC.

Below we evaluate the uncertainties caused by these "new" effects and show that their effect is not only significant but also dominant in the case of the W-mass measurement at the LHC. For technical reasons, not M_{W^+} and M_{W^-} are separately determined but, equivalently, the average $(M_{W^+} + M_{W^-})/2$ and difference $(M_{W^+} - M_{W^-})$ of the bosons masses. Since in $p\,p$ collisions the spectra of positive and negative leptons are to be analyzed separately, it is natural to make the same distinction also for the leptons from Z decay. Along this line of reasoning, 'Z^+' and 'Z^-' lepton p_T spectra are considered, in analogy to 'W^+' and 'W^-' lepton p_T spectra.

3.6.1 Uncertainties in the parton distribution functions

In the studies of the sensitivity of the M_W measurement precision to the modeling uncertainties of the PDFs discussed in the previous section we have used the CTEQ6.1 PDF set [179] as the standard template distributions. The uncertainties in the PDFs are conventionally propagated to the measurement errors of the physics observables by varying the PDF sets chosen in the event generation process. Alternatively, the uncertainties of the QCD-fit parameters of a given PDF set are propagated by re-weighting the generated events with "min" and "max" weights, $\mathrm{PDF}_{\rm max/min} = \mathrm{PDF}_{\rm cen} \pm \delta\mathrm{PDF}$, where $\mathrm{PDF}_{\rm cen}$ are the central-value distributions of a given PDF set and δPDF is computed according to the method described in Ref. [174] – this method was used in the Section 3.4. However, in our view the above methods largely underestimate the influence of the PDFs uncertainty on the measurement precision of the W-boson mass. The current understanding of the parton density functions is summarized in Fig. 3.8 which shows the MSTW-2008 set [176]. It is advocated and widely believed that the proton PDFs are precise enough not to pose a limitation for the LHC data analysis. For example, the $u^{(\rm v)}$ and $d^{(\rm v)}$ PDF are claimed to be precise to 2% [176]. But for example, from Fig. 3.14 we clearly

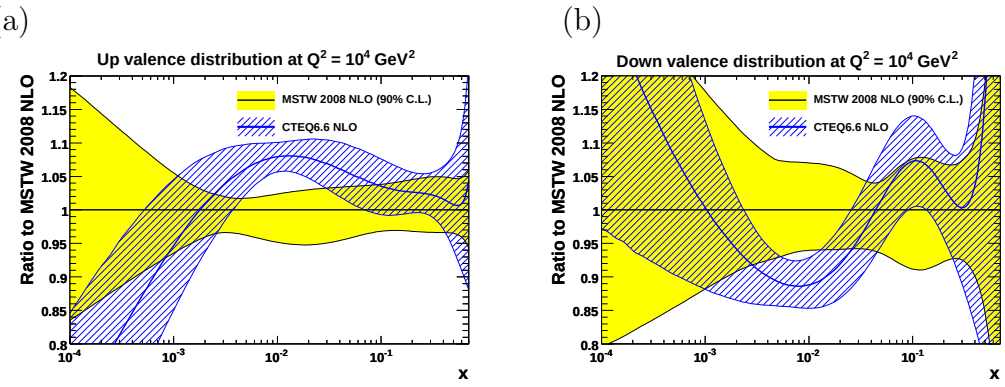

Figure 3.14: MSTW 2008 NLO PDFs compared to CTEQ6.6 NLO PDFs. The plot taken from Ref. [176].

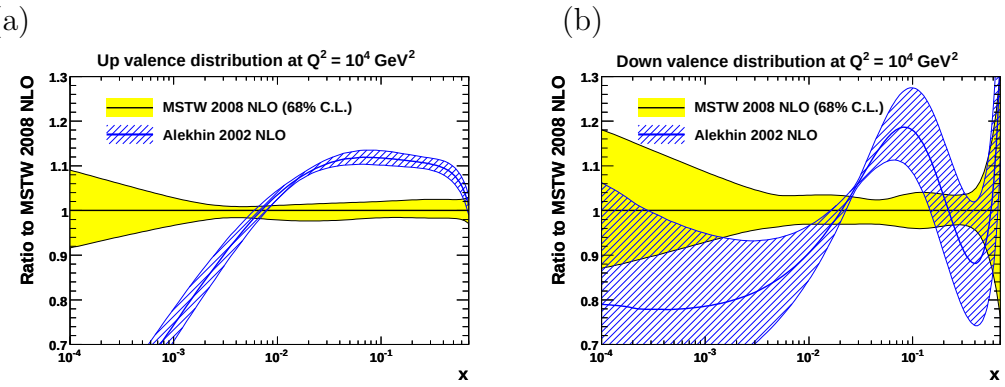

Figure 3.15: MSTW 2008 NLO PDFs compared to Alekhin NLO PDFs. The plot taken from Ref. [176].

see that CTEQ6.6 NLO [180] and MSTW 2008 NLO [176] proton $u^{(v)}$ and $d^{(v)}$ PDFs differ by much more than 2%, although they stem largely from the same input data. The difference between the MSTW 2008 NLO PDFs and Alekhin NLO PDFs is even more striking, see Fig. 3.15. Therefore, a 5% error of the PDFs of the u and d quarks appears more realistic. Another problem for the use of the current proton PDFs in the analysis of W and Z production and decay at the LHC arises from 'compensating' PDF changes: a change of the PDF of one quark can be compensated by a change of the PDF of the other quark of the same family that leaves the Z rapidity distribution nearly invariant, and hence escapes detection[12].

[12] The condition of invariance of the Z rapidity distribution, and hence invisibility even in high-statistics data samples, is decisive: if the measured Z rapidity distribution looked

Therefore, in the studies presented in this section the following two ways of modeling the uncertainty in the $u^{(v)} - d^{(v)}$ distribution have been assumed:

$$u^{(v)}_{max/min} = u^{(v)} \pm 0.05\, u^{(v)}, \qquad d^{(v)}_{min/max} = d^{(v)} \mp 0.05\, u^{(v)}, \tag{3.29}$$

and

$$u^{(v)}_{max/min} = u^{(v)} \pm 0.02\, u^{(v)}, \qquad d^{(v)}_{min/max} = d^{(v)} \mp 0.08\, d^{(v)}. \tag{3.30}$$

The first one preserves the sum of the distributions of the the u and d quarks and is constrained, to a good precision, by the measured singlet structure function in neutrino and antineutrino deep-inelastic scattering (DIS) off isoscalar nuclei. At the LHC the sum of the distributions will be constrained by the rapidity distribution of the Z-bosons[13]. The second one assures the correct propagation of the measurement errors of the sum of the charge-square-weighted distributions of the u and d quarks, constrained by the high-precision charged-lepton-beam DIS data, to the uncertainty of the individual distributions.

While the sums of the distributions are well controlled by the existing and future data, their mutually compensating shifts are not. The only experimental constraints on such shifts come from (1) the measurements of the ratio of the cross sections for deep-inelastic scattering of charged leptons on proton and deuteron targets and (2) the measurements of the ratio of the neutrino–proton to antineutrino–proton DIS cross sections. They determine the present uncertainty range of the $u^{(v)} - d^{(v)}$ asymmetry.

The present experimental uncertainty of the PDF of the c quark is at the 10% level[14], see Fig. 3.16. Therefore, we have assumed the following way of modeling the uncertainty in the $s - c$ distribution:

$$s_{max/min} = s \pm \gamma\, c, \qquad c_{min/max} = c \mp \gamma\, c, \tag{3.31}$$

with $\gamma = \{0.2, 0.1\}$. As in the case of the $u^{(v)} - d^{(v)}$ asymmetry, we have assumed that the sum of the distribution of the s and c quarks will be controlled to a very good precision by the Z-boson rapidity distribution. Therefore, we

differently than expected from the current proton PDFs, an appropriate change of the proton PDFs would be unavoidable.

[13]Note that the precise compensation of the correlated shifts in the observed rapidity distribution of the Z-bosons require the equality in the coupling of the u and d quarks to the Z-boson and the symmetry of the $\bar{u}$ and $\bar{d}$ sea. Neglecting these small effects has no significant effect on the results presented in this section.

[14] Theoretical calculations of heavy-quark PDFs from the gluon PDF are claimed to have a smaller error margin.

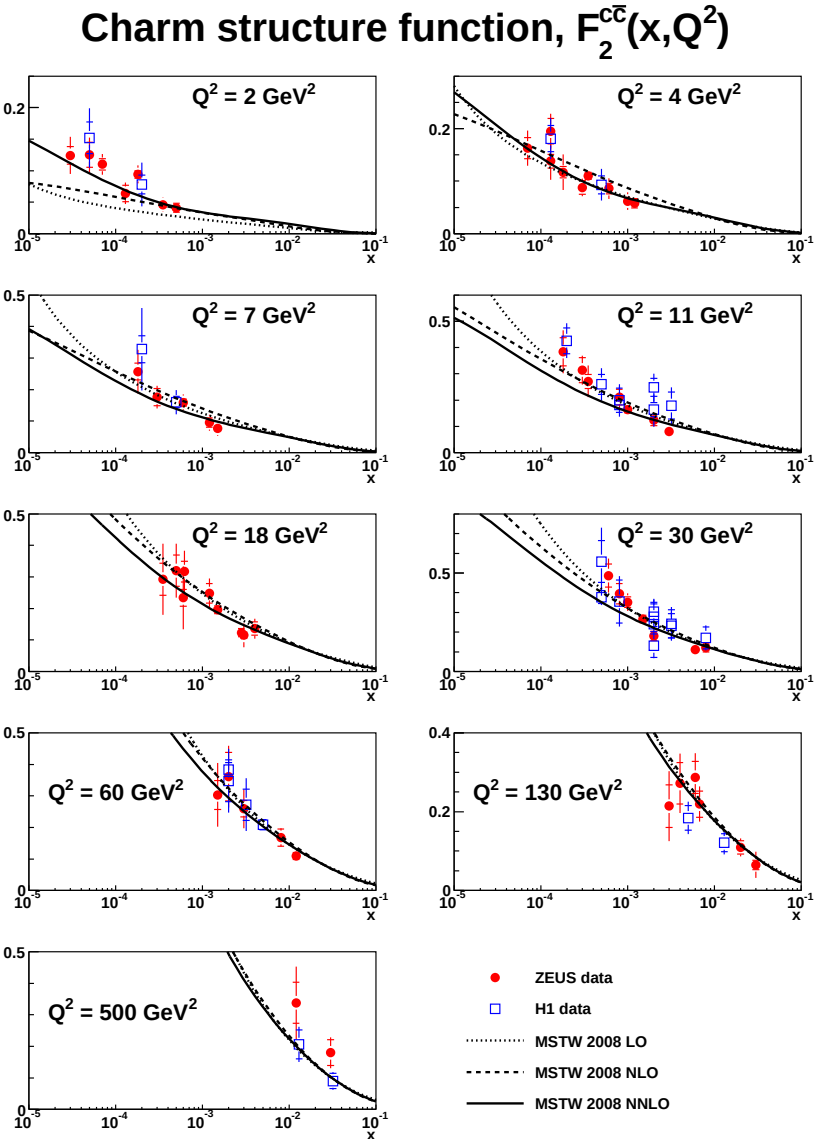

Figure 3.16: The charm structure function, $F_2^{c\bar{c}}(x, Q^2)$, compared to data from H1 and ZEUS. The plot taken from Ref. [176].

have introduced only unconstrained, mutually compensating modifications of the s and c quark distributions[15].

Finally, the present experimental uncertainty of the PDF of the b quark is at the 20% level, see Fig. 3.17. Therefore, the uncertainty in the b distributions is modeled by using the following ansatz:

$$b_{\mathrm{max/min}} = b \pm \kappa b \tag{3.32}$$

with $\kappa = \{0.4, 0.2, 0.1\}$.

The impact of these uncertainties in the missing input in the parton distribution distributions on the measurement precision of the W mass has been evaluated by the consecutive simulations of the measurement procedure for all the partonic distributions defined in this section. The simulation results have been quantified using the likelihood analysis methods, described in detail in Section 3.2.4(a). The observable used for average mass in the likelihood analysis is the one defined in the framework of the "improved Z-candle" method, the results for difference $(M_{W^+} - M_{W^-})$ of the bosons masses are taken from Ref. [13,164]. The systematic shifts of the measured values of M_W induced by the $u^{(\mathrm{v})} - d^{(\mathrm{v})}$, $s - c$ and b biases are presented in Tables 3.6, 3.7 and 3.8, respectively. Evidently, with the present precision of the PDFs, which cannot be improved by the LHC data, there is no way to improve the precision of the W-boson mass. Moreover, it will be impossible to approach the precision reached at the Tevatron. We stress again that these effects are a direct consequence of the pp rather than $p\bar{p}$ collision scheme of the LHC.

3.6.2 Momentum calibration

At the Tevatron, the determination of the W-boson mass is almost independent of the relative biases in the calibration scale of the positive versus negative leptons. At the LHC, the excess of the positive over negative leptons and the differences of their transverse momentum spectra are reflected in the sensitivity of the measured M_W to the relative momentum scales of positive and negative leptons. Therefore, we have to consider in addition to the charge independent systematic biases in the momentum scale calibration (discussed in Section 3.4,

[15] As in the case of the first quark family, the s and c quarks couple to the Z-boson with slightly different strength. The resulting effect will play no important role in the presented analysis. Similarly, the effect of the initial asymmetry of the s and c quark distributions is ignored here.

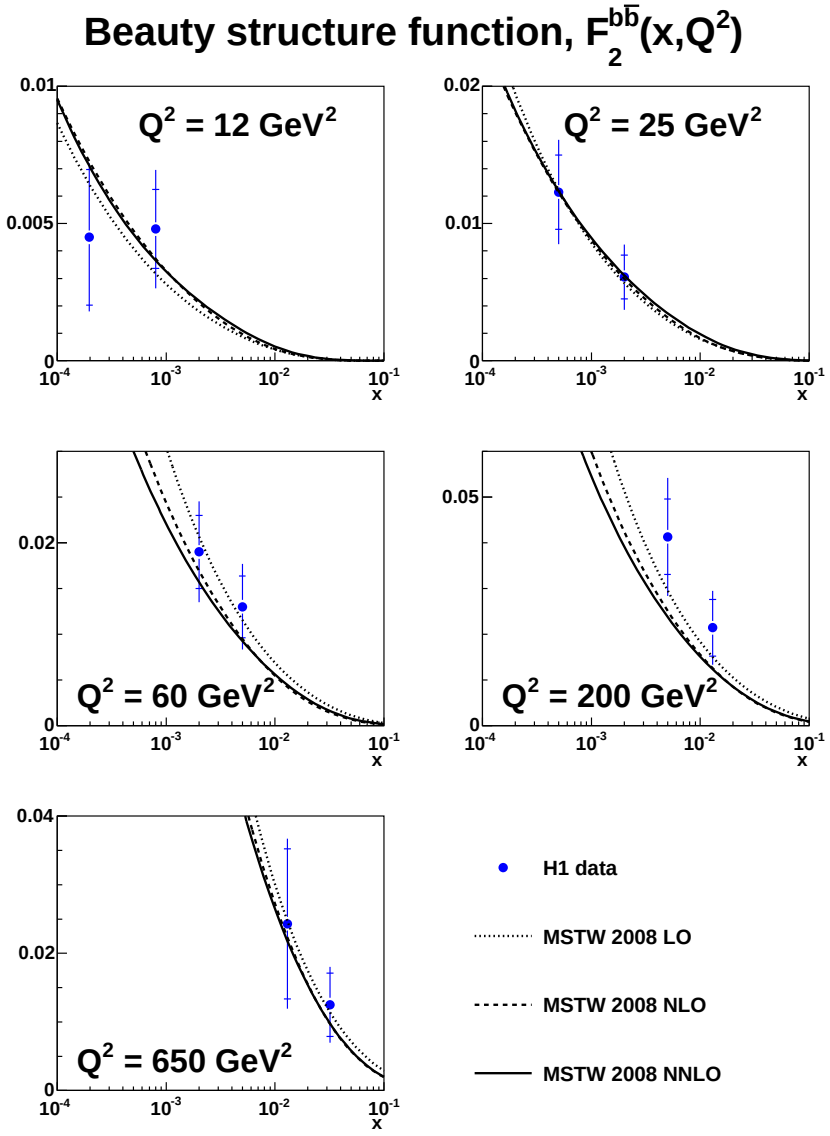

Figure 3.17: Predictions for the beauty structure function, $F_2^{b\bar{b}}(x, Q^2)$, compared to data from H1. The plot taken from Ref. [176].

		ΔM[MeV]	$\Delta(M_{W^+} - M_{W^-})$[MeV]
	Systematic ξ	pp: $\lvert\eta_l\rvert < 2.5$	pp: $\lvert\eta_l\rvert < 2.5$
$u^{(\mathrm{v})}$, $d^{(\mathrm{v})}$	$u^{(\mathrm{v})}_{\mathrm{max}} = 1.05\, u^{(\mathrm{v})}$ $d^{(\mathrm{v})}_{\mathrm{min}} = d^{(\mathrm{v})} - .05\, u^{(\mathrm{v})}$	-79	115
	$u^{(\mathrm{v})}_{\mathrm{min}} = 0.95\, u^{(\mathrm{v})}$ $d^{(\mathrm{v})}_{\mathrm{max}} = d^{(\mathrm{v})} + .05\, u^{(\mathrm{v})}$	64	-139
	$u^{(\mathrm{v})}_{\mathrm{max}} = 1.02\, u^{(\mathrm{v})}$ $d^{(\mathrm{v})}_{\mathrm{min}} = 0.92\, d^{(\mathrm{v})}$	-48	84
	$u^{(\mathrm{v})}_{\mathrm{min}} = 0.98\, u^{(\mathrm{v})}$ $d^{(\mathrm{v})}_{\mathrm{max}} = 1.08\, d^{(\mathrm{v})}$	32	-89

Table 3.6: Systematic shifts of M_W induced by the valence-quarks biases discussed in the text.

		ΔM[MeV]	$\Delta(M_{W^+} - M_{W^-})$[MeV]
	Systematic ξ	pp: $\lvert\eta_l\rvert < 2.5$	pp: $\lvert\eta_l\rvert < 2.5$
s, c	$c_{\mathrm{min}} = 0.8\, c$ $s_{\mathrm{max}} = s + 0.2\, c$	-257	39
	$c_{\mathrm{max}} = 1.2\, c$ $s_{\mathrm{min}} = s - 0.2\, c$	237	-29
	$c_{\mathrm{min}} = 0.9\, c$ $s_{\mathrm{max}} = s + 0.1\, c$	-148	17
	$c_{\mathrm{max}} = 1.1\, c$ $s_{\mathrm{min}} = s - 0.1\, c$	111	-11

Table 3.7: Systematic shifts of M_W induced by the s and c quarks biases discussed in the text.

		ΔM[MeV]
	Systematic ξ	pp : $\lvert\eta_l\rvert < 2.5$
Cent. Exp.	$\xi = 0$	-6.1 ± 7.4
b	$b_{\max} = 1.4\,b$	-77
	$b_{\min} = 0.6\,b$	56
	$b_{\max} = 1.2\,b$	-42
	$b_{\min} = 0.8\,b$	39
	$b_{\max} = 1.1\,b$	-13
	$b_{\min} = 0.9\,b$	12

Table 3.8: Systematic shifts of M_W induced by the b-quark biases discussed in the text. The shifts for the value $\xi = 0$ correspond to a bias-free pseudo-sample of events; their errors illustrate the statistical precision of the likelihood method for the integrated luminosity of $10\,\text{fb}^{-1}$.

		ΔM [MeV]	
	Systematic ξ	R_{WZ}	R^c_{WZ}
Cent. Exp.	$\xi = 0$	-1 ± 6	0 ± 7
ES [%]	$\varepsilon_{l^+} = -\varepsilon_{l^-} = +0.05\,\%$	5.3	0
	$\varepsilon_{l^+} = -\varepsilon_{l^-} = -0.05\,\%$	-0.3	-8
	$\varepsilon_{l^+} = -\varepsilon_{l^-} = +0.50\,\%$	39.5	22
	$\varepsilon_{l^+} = -\varepsilon_{l^-} = -0.50\,\%$	-19	-31

Table 3.9: Systematic shifts of M_W induced by the charge-dependent energy-scale biases discussed in the text for the "standard candle" (R_{WZ}) and "Z-candle" (R^c_{WZ}) observables. The shifts for the value $\xi = 0$ correspond to a bias free pseudo-sample of events. Their errors illustrate the statistical precision of the likelihood method for the integrated luminosity of 10 fb^{-1}.

see Eq. 3.18) the lepton charge-dependent systematic biases in the scale calibration factors[16]. We studied the influence of the following scale biases of the reconstructed momenta of positive and negative leptons:

$$\varepsilon_{l^+} = -\varepsilon_{l^-} = \pm 0.5\%, \pm 0.05\%. \tag{3.33}$$

The impact of the above bias on the W-mass measurement was not studied in Ref. [6]. The result of our studies, presented in Table 3.9, is that the relative scale-factor calibration biases of the positive and the negative lepton samples must be controlled to the precision better than 0.2% for the W-boson mass to be measured with the precision better than 10 MeV. As expected, the sensitivity of the W-boson mass to the lepton-charge asymmetric momentum-scale bias is the same for the methods based upon the "standard Z-candle" (R_{WZ}) and "improved Z-candle" (R^c_{WZ}) observables, see Table 3.9. Even if the sensitivity to the lepton-charge dependent effects is by a factor of 10 smaller than the lepton-charge independent effects (see Table 3.2), their experimental control at the LHC is a big challenge. This is because the Z-peak position is invariant with respect to the charge-asymmetric momentum biases.

A method for the precise relative calibration of the momentum scale for the positive and negative leptons has been proposed in the papers Refs. [13, 164]. We recall here that the calibration precision needed to measure $M_{W^+} - M_{W^-}$ must be by the factor of 10 higher than the one needed to measure M_W under the assumption that the masses of the positive and negative W-bosons are equal (for equal measurement errors). The "Double Asymmetry" method proposed in Refs. [13, 164] is based upon a dedicated measurement procedure with two running periods characterized by a reversed polarity of the central tracker solenoid. Such a method could also be used for the M_W measurement, providing the requisite calibration precision. However, a sufficient calibration precision for the M_W measurement can be delivered by a complementary method which we propose below. This method uses the l^+l^- event samples and optimizes the choice of the M_{ll} region where the differences of the transverse momentum distributions of positive and negative leptons are minimized. By definition, in the optimal "calibration region" the forward–backward asymmetry of leptons coming from the $u\bar{u}$ and $d\bar{d}$ annihilations, reflecting the excess of quarks over antiquarks in the proton beams, averages out to zero. The

[16] For detailed discussion of the tracker deformation modes giving rise to the miscalibration of the transverse momentum scales see our analysis presented in Refs. [13, 164].

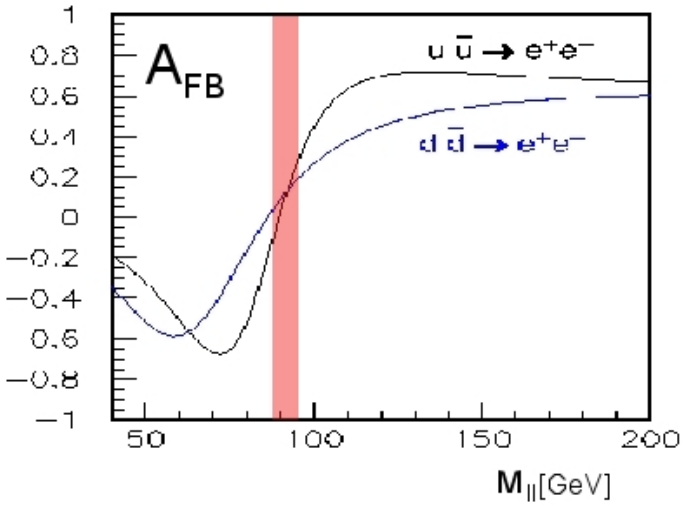

Figure 3.18: The forward–backward asymmetry (A_{FB}) as a function of the centre of mass energy in the neutral current Drell–Yan process – the plot taken from Ref. [181].

first lucky coincidence is that, for the actual value of $\sin^2\theta_W$, this region lies in the vicinity of the Z-boson mass peak marked in Fig. 3.18, such that the statistical precision of the method could be maximized. The second lucky coincidence is that the sensitivity of the calibration method to the assumed value of the $\sin^2\theta_W$ is sufficiently weak to assure the factorization of the calibration procedure aiming at the precision of 0.2% from the procedure of precise determination of $\sin^2\theta_W$ at the LHC.

In Fig. 3.19 we show the $\mathrm{Asym}_Z^{(+,-)}()$ distribution in the $-2.5 < \eta_l < 2.5$ region. We observe that the choice of the statistically optimal narrow mass region centered at the M_Z value is sufficient to reduce the asymmetries in the transverse momentum distribution for the positive and negative leptons to the requisite level of 0.2%. This sample of events could thus be used to calibrate the relative momentum scale for positive and negative leptons to the same precision. An improvement of the calibration precision by a factor of 20 – necessary for the measurement of the $M_{W^+} - M_{W^-}$ to a comparable precision as M_W – is no longer independent of the assumed form of the $u^{(v)}$ and $d^{(v)}$ distributions. It would involve as well the necessity of simultaneous determination of the $\sin^2\theta_W$ value. We have thus demonstrated that the calibration of the momentum scale for the positive and negative leptons can be made with the sufficient precision to keep the corresponding M_W bias below 10 MeV.

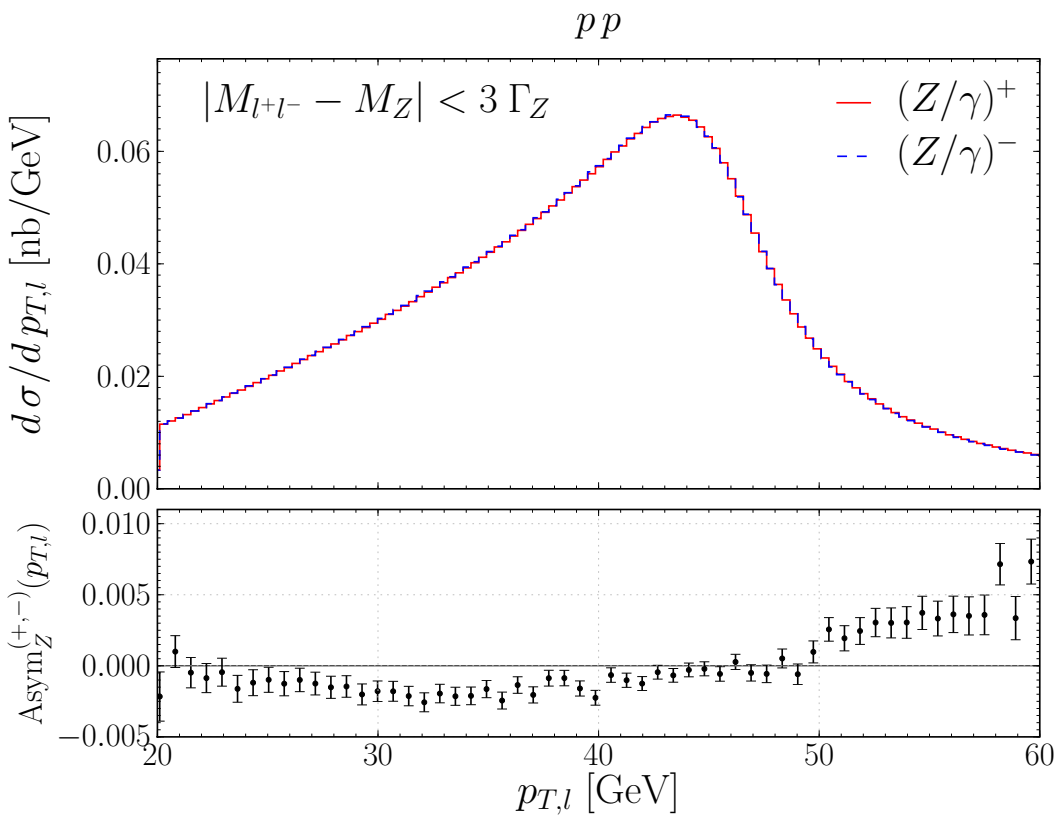

Figure 3.19: The $\mathrm{Asym}_Z^{(+,-)}()$ distribution as a function of $p_{T,l}$ at the LHC.

3.7 The way forward

3.7.1 Isoscalar beams

The LHC collider programme context

The difficulty of relating the W-boson observables to the Z-boson ones, inherent to the $p\,p$-collision scheme, can be largely avoided by running the isoscalar beams at the LHC. The unique capacity of the LHC collider to run the ion collisions, if exploited, could put the LHC collider back into the EW measurement precision competition. The complementarity of the $p\,p$ and the isoscalar-ion collision modes is similar to that of the collisions of neutrino and antineutrino beams with proton and iron (or calcium) targets.

It has to be stressed that colliding one of the low atomic number isoscalar beams at the LHC, optimally the deuterium (or He_4) ions, even if technically feasible, is not foreseen in the present LHC plans and has never been dis-

cussed. This section can thus be considered as building the case for running the isoscalar light-ion beams in the advanced phase of the LHC operation.

If the LHC can deliver the luminosity which scales as $L_{AA} = L_{pp}/A^2$ (A being the mass number of a given ion) for the light isoscalar ion beams, then the event rates containing the high-p_T signatures will be similar for the proton and for the light-ion collisions.

(a) $d\,d$ collisions

The deuteron beams restore the isospin symmetry for the quarks of the first family. In addition, the spin density matrices for the W and Z bosons produced by the first quark-family are almost the same, especially if the effect of the difference of the masses of the Z and W bosons are circumvented by using the measurement procedure explained in Subsection 3.4.4. Therefore, if one could neglect the contribution of quarks coming from the second and third families, the isospin symmetry at the LHC would play the same role as the matter–antimatter symmetry at the Tevatron. Namely, it would result in a quasi model-independent relationship between the "charge-blind" W and the Z boson observables. However, in the realistic studies one has to consider all the quark families. Let us assume that: $s(x) = \bar{s}(x)$, $c(x) = \bar{c}(x)$ and $b(x) = \bar{b}(x)$. In that case we can propose to reduce (control) the sensitivity of the unfolding of M_W to the uncertainty in the b-quark distribution by analyzing the "improved Z-candle" observable in the restricted region of the lepton pseudorapidity: $2 < |\eta_l| < 2.5$. Since the sensitivity of this variable to the b-quark distribution enters only via the Z-boson observables and since the contribution of the $b\bar{b}$ annihilations to the Z-bosons is reduced in this kinematical region, we expect a significant reduction of the sensitivity of the unfolded M_W value to the exact form of the b-quark distribution. We have simulated the full unfolding procedure by changing the distribution of the b-quark within 40% of its template value and found that the biases in the unfolded M_W values were reduced from the values shown in Table 3.8 to the negligibly small values, compatible with the statistical errors representing the integrated luminosity of $50\,\mathrm{fb}^{-1}$.

Once this PDF is eliminated, the unfolding of the remaining PDFs using the LHC deuteron collision data is straightforward. Its main precision limitation comes from the statistical error of the $\mathrm{Asym}_W^{(+,-)}()$ observable measuring directly, for the dd collisions, the $s(x) - c(x)$ distribution [13,164]. In Fig. 3.20

we show the statistical unfolding precision of the $s - c$ distribution for the integrated $d\,d$ luminosity of $25\,\text{fb}^{-1}$ (equivalent to the nucleon–nucleon luminosity of $100\,\text{fb}^{-1}$). The compensating differences of the input distribution of $\pm 10\%$ are easily detectable at this collected luminosity, even if the initial charge asymmetry is small[17]. However, reducing this uncertainty to the level sufficient to determine the W-boson mass to the precision better than 10 MeV requires collecting 10 times more luminosity. In Table 3.10 we show the ex-

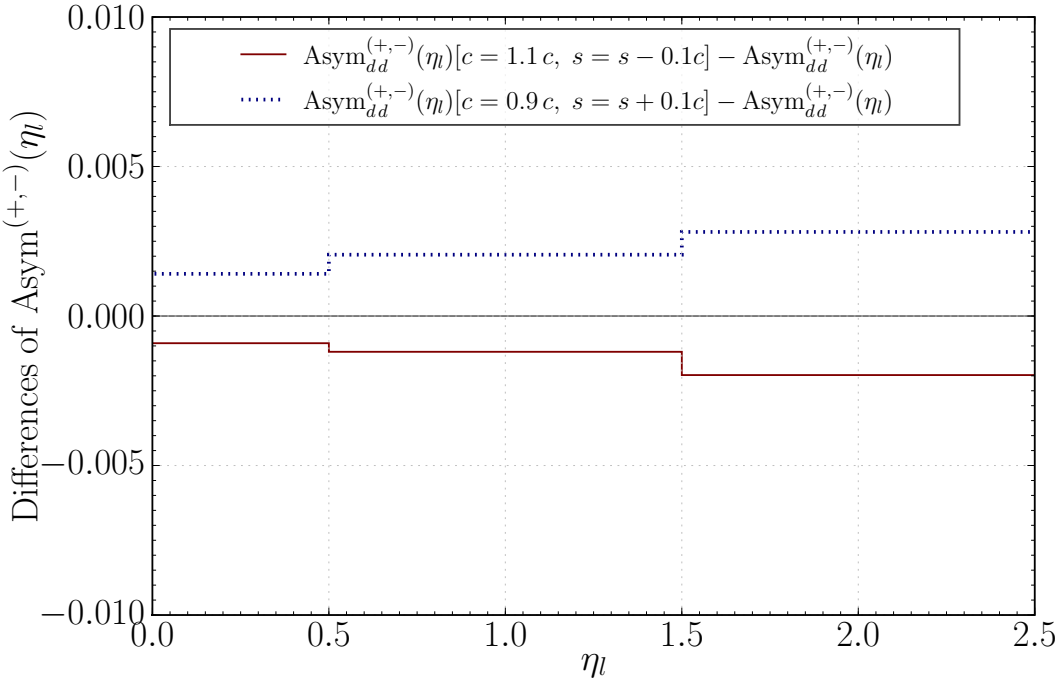

Figure 3.20: Unfolding of $s - c$ in $d\,d$ runs.

pected reduction of biases in the measured value of M_W by replacing the $p\,p$ collision scheme by the $d\,d$ collision scheme. Note that the remaining isospin asymmetry of the u and d quark reflects the effect of different electric charges of the u and d quarks. This residual asymmetry is irrelevant as long as the LHC precision target stays at the level of 10 MeV. We thus demonstrate that by using the deuteron beams one can restore the favourable "Tevatron-like" environment for the measurement of the W-mass. For the $d\,d$ collision scheme the LHC data alone is able to constrain both the W-mass and the relevant

[17]The $s - c$ contribution to the charge asymmetry of the W-boson is proportional to the value of $\sin^2\theta_C$, where θ_C is the Cabibbo angle.

Systematic ξ	Expected precision [%]	ΔM [MeV]
"$u^{(v)} - d^{(v)}$"	0.2	< 5
"$s - c$" $\mathcal{L}_{int} = 2.5 fb^{-1}$	2	25
"$s - c$" $\mathcal{L}_{int} = 25 fb^{-1}$	0.7	8
"b"	40	< 10

Table 3.10: The expected biases of the measurement of M_W for the $d\,d$ collisions at the LHC due to remaining uncertainties of the PDFs. The quark–antiquark symmetry for s, c and b quark distribution is assumed in the unfolding procedure.

partonic distributions. It has to be stressed, however, that the exact quark–antiquark symmetry for s, c and b quarks, inherent to the presented unfolding method, cannot be verified experimentally and has to be taken for granted. In the subsequent section we discuss an alternative, complementary method for reducing the space of the LHC-unconstrained PDFs .

3.7.2 $p\,p$ and $d\,d$ collisions

An alternative method could use both the $d\,d$ collision runs and the $p\,p$ runs taken at a half of the energy of the deuteron beam as the basic data-taking configuration for the W-mass measurement. In such a scheme only two assumptions are needed to fully constrain the unfolding procedure of the PDFs: $c(x) = \bar{c}(x)$ and $b(x) = \bar{b}(x)$. These assumptions have never been put in doubt. The equality is exact if the c and b quarks have purely bosonic (gluonic and photonic) origin.

The combined $p\,p$ and $d\,d$ data could then provide the fully model-independent determination of the W-mass at the LHC. However, even in such a scheme some problems exist and need to be handled or circumvented, see Ref. [153, 182, 183].

3.7.3 Solving LHC problems with LHC-auxiliary measurement programme

The proposed way to solve the LHC-specific problem by colliding isoscalar beams is elegant, technically feasible, but not realistic in the foreseeable future. The other option is to try to reduce the present uncertainty of the

"missing input" to the LHC analysis in a dedicated "LHC-precision-support" measurement programme. It must be stressed right away that we will not consider here a new round of the PDF measurements but the ways of obtaining the experimental information that can directly be incorporated into the LHC-specific EW-sector measurement procedures with minimized extrapolation uncertainties. This problem is highly nontrivial, as one has to combine the measurements made by different experiments, using different beams, at different collision energies and the correspondingly different x and Q^2 scales.

The analysis presented in Section 3.6.1 has shown that the present precision of understanding of the flavour-nonsinglet PDFs is insufficient to improve the precision of the measurement of the W-boson mass at the LHC, even if we circumvent most of the QCD extrapolation uncertainties using the dedicated measurement procedures. The important question now is whether the presently running experimental programme in high energy physics will be able to deliver eventually the requisite measurements with the sufficient precision or whether new experimental initiatives are indispensable.

Analysis of present experimental programme.
The HERA DIS programme came to the end. The final analysis of the full inclusive DIS data collected by the H1 and ZEUS collaborations and corresponding to the integrated luminosity of $250\,\mathrm{pb}^{-1}$ has just been published. The published uncertainty of the $u^{(\mathrm{v})}$, $d^{(\mathrm{v})}$, s and c quark distributions is compatible (larger) as compared to the uncertainty assumed in the analysis presented in this chapter. It has to be stressed that the statistical accuracy of the HERA data for the electron and positron scattering charged-current processes is by far too low to provide the LHC-precision-programme-adequate accuracy for the flavour dependent separation of the quark and the antiquark densities. Moreover, the proton collision neutral-current data are largely insensitive to the relative movements of the u, d and s quark densities.

The final H1 and ZEUS combined data on DIS–associated heavy-flavour production has not been published yet. It is, however, highly improbable that this data will allow to pin down experimentally the relative densities of the charm and bottom quarks with respect to the corresponding light quarks to the level of $\mathcal{O}(1\%)$. We are thus bound to conclude that the final HERA data cannot put the LHC precision programme back in competition with the Tevatron one. They may be of some help in constraining the following flavour

singlet combination of partonic densities: $4/9\,[u(x)+\bar{u}(x)+c(x)+\bar{c}(x)]+1/9\,\left[d(x)+\bar{d}(x)+s(x)+\bar{s}(x)\right]$ in the small-x region. However, it will remain to be proven that the extrapolation of the above combination of partonic densities from the HERA Q^2 region to the M_W^2 region can be fully controlled by the perturbative QCD – the DGLAP evolution scheme leading to a $\mathcal{O}(2\%)$ extrapolation uncertainty [184] cannot be *a priori* taken for granted in the very low-x region.

The Thomas Jefferson National Accelerator Facility (TJNAF, Newport News, USA) DIS programme will provide a very detailed and precise insight into the large-x structure of protons. These data are, however, of no direct relevance to the LHC programme because the LHC W and Z production data will be insensitive to the quark structure of protons at such a large x values.

The data which certainly could be of help in pinning down the missing input for the LHC programme are the Tevatron W and Z boson production data. If the Tevatron reaches the integrated luminosity of $10\,\mathrm{fb}^{-1}$ before its shut-down, then of the order of 10^7 W-boson production events and 10^6 Z-boson production events will be available to provide important constraints of the missing PDF densities.

The measurement of the lepton-charge asymmetry will certainly provide a very high precision, $\mathcal{O}(1\%)$, constraint of the ratio of the u and the d quark densities. It has to be stressed, however, that the Tevatron W^-/W^+-boson production data cannot, alone, constrain the d/u ratio but only the double ratio $[d(x_1)/u(x_1)]\,/\,[d(x_2)/u(x_2)]$, where $M_W = s x_1 x_2$ and x_1 (x_2) are respectively the fractional momenta carried by the faster (slower) parton. In order to constrain u/d, a supplementary experimental measurement must be provided by the LHC (or other complementary data covering, at least partially, the requisite x_1 or x_2 kinematical region). The Tevatron data are unable to control separately the ratios for the valence and for the sea quarks – a necessary condition to understand the W-boson polarization effects (of no importance for the Tevatron measurements as long as the Z template is used for the W events, but of high importance at the LHC).

The large statistics data on the forward–backward asymmetry of charged leptons from the Z-boson decays at the Tevatron will provide some constraint on the of sum of the $u^{(\mathrm{v})}$ and $d^{(\mathrm{v})}$ quarks but will not provide a sufficiently precise constraint on each of the distribution separately[18]. A very important

[18]The statistical precision of the forward–backward asymmetry data outside the Z-boson

constraint will come from the precision measurement of the Z-boson rapidity distribution, provided that it could be incorporated into the LHC measurement strategy in a way which minimizes the impact of the uncertainty in the absolute normalization of the measured distribution and the uncertainties in the relative energy-dependent effects in the interpretation of this ratio in terms of partonic densities.

The key question which we will address now is: will the Tevatron data alone provide the missing input with a sufficient precision? As demonstrated in Refs. [153,185,154], the unconstrained degree of freedom remains. Therefore, the combined analysis of the LHC and Tevatron data must be complemented by a dedicated DIS scattering experiment, optimized to serve as a provider of high-precision missing input-data for the M_W measurement. The Letter Of Intent (LOI) for such an LHC-programme-dedicated experiment at the SPS was submitted in September 2009 to the SPSC and the LHCC [185].

3.8 Conclusions and outlook

In this chapter we have focused our attention on the measurement of the W-boson mass, the most important Standard Model measurements to be made at the LHC.

We have presented a novel method for the W-mass measurement at the LHC. This method is robust with respect to the systematic measurement and modeling error sources which were found to be dominant for the W-boson mass measurements at the Tevatron. We have shown that already for one year running of the LHC at the low-luminosity this method removes the sensitivity of the W-mass to these effectes.

Then we have identified and pointed out the principal differences of the measurement for the Tevatron's $p\bar{p}$ and for the LHC's pp collision scheme. We have explained how those differences lead to the LHC-specific error sources which are not relevant in the case of the Tevatron but will play an extremely important role in the case of the LHC. Even if the W-boson measurement has already been intensively discussed over the last decade, the impact of these LHC-specific effects on the precision of the W-mass was overlooked in the previous ATLAS and CMS analyses. We have evaluated the uncertainties caused by the LHC-specific effects and have shown that their effect is dominant for

mass peak will be too low.

the W-mass measurement at the LHC. Therefore, it will be impossible to reach the precision of the order of 10 MeV, sugested by the ATLAS and CMS analyses, unless an additional experimental support is provided. It will be even difficult to approach the precicion reached at the Tevatron. Therefore, we have proposed two measurement programmes allowing to put back the LHC SM parameters measurement program into the precision competition: (1) colliding the deuteron beams at the LHC and (2) improving the precision of the LHC-external missing-input information in a dedicated "LHC-precision-support" programme. Both programmes have complementary merits and shortcomings. Both are capable to measure the W-boson mass with the precision better than 10 MeV. Running of deuteron beams at the LHC is very elegant solution but it is highly unlikely, at least in the initial phase of the collider operation. The "LHC-precision-support" programme must be based on a correlated LHC and Tevatron measurement scheme. This is a necessary but not sufficient condition of its success. The core of such a programme is a dedicated precision experiment to measure the proton–neutron asymmetry in DIS collisions of leptons with the proton and deuterium targets. It must use the TJNAF programme to understand the deuteron nuclear effects.

Acknowledgements

In the first place, I would like to thank my supervisors, Wiesław Płaczek for so long and outstanding supervision, and Mieczysław Witold Krasny for teaching me secrets of experimental physics. Without their continuous support and infinite patience during the period of my PhD this work would never be possible. Their enthusiasm and readiness to discuss, which I consider simply invaluable, allowed me to gain or improve understanding of various aspect of High Energy Particle physics both from the theoretical and experimental point of view. Our common work led to the results documented in the Chapter 1 (W. Płaczek) and 3 (M.W. Krasny and W. Płaczek) of this thesis. I am also grateful to Wiesław Płaczek for careful reading of the manuscript and for many valuable remarks.

I am likewise obliged to my other collaborators, Stefan Gieseke and Mike Seymour, with whom I have obtained the results reported on in Chapters 2, and last but not least, Florent Fayette for his excellent work on the precision measurements of the Standard Model parameters at the LHC, reported in Chapter 3. I wish also to thank Fred Olness, Pavel Nadolsky for sharing the estimations of the p_T spectrum of the Z boson expected in the pp collisions at the LHC and A. Arbuzov, D. Bardin, S. Bondarenko and L. Kalinovskaya from SANC group for sharing the SANC results needed in Chapter 1.

Over the years of my PhD I took part in many enriching discussions with David Grellscheid, Manuel Bähr, Andreas van Hameren, Stanisław Jadach, Aleksander Kusina, Leif Lönnblad, Oluseyi Latunda-Dada, Peter Richardson, Sebastian Sapeta, Torbjörn Sjöstrand, Magdalena Sławińska, Maciej Skrzypek, Elżbieta Richter-Wąs, Zbigniew Wąs, Bryan Webber and many members of the MCnet Collaboration.

I wish also to thank the Theory Group at the Institute of Physics at Jagiellonian University for providing me nice and comfortable environment to work and study. Part of the work which constitutes this thesis was obtained dur-

ing my stay at the LPNHE laboratory in Paris and at the Durham University. I acknowledge the hospitality of these institutions and invaluable help from Philippe Schwemling with solving the administration issues during my one-year stay in Paris. I feel gratitude to the members of the CERN Theory Group for their hospitality at the time of my one-year stay at CERN. I wish to thank Mike Seymour for his supervision during this period. I acknowledge the support of the Marie Curie Early Stage Research Training Fellowship of the European Communitys Sixth Framework Programme under contract number (MEST-CT-2005-020238), which made the stay at CERN possible.

This research has been supported also by HEPTOOLS (No. MRTN-CT-2006-035505) and MCnet (No. MRTN-CT-2006-035606) European Union funded Marie Curie Research Training Networks, the Polish Ministry of Science and Higher Education (MNiSW) grant No. N N202 175435 and by the program of the French–Polish cooperation between the IN2P3 and COPIN No. 05-116.

And last but not the least I would like to thank my family for all.

Appendix

A.1 YFS infrared functions

The YFS infrared functions (see Section 1.3) are defined by:

$$\begin{aligned} Y_\Omega(p_1,p_2) &\equiv 2\alpha\tilde{B}(\Omega,p_1,p_2) + 2\alpha\Re B(p_1,p_2) \\ &\equiv -2\alpha\,\frac{1}{8\pi^2}\int\frac{d^3k}{k^0}\Theta(\Omega;k)\left(\frac{p_1}{kp_1}-\frac{p_2}{kp_2}\right)^2 \\ &\quad + 2\alpha\Re\int\frac{d^4k}{k^2}\frac{i}{(2\pi)^3}\left(\frac{2p_1+k}{2kp_1+k^2}-\frac{2p_2-k}{2kp_2-k^2}\right)^2,. \end{aligned} \tag{A.1}$$

In this appendix we present the explicit and general form, from Refs. [77] and [48], for both the virtual IR function $\Re B(s,p_1,p_2)$ and the real IR function $\tilde{B}(p_1,p_2;E_{min})$ for both s and t channels.

A.1.1 Virtual photon IR function for s-channel

The YFS form factor in the s-channel is needed in ZINHAC for the final-state radiation. The virtual photon YFS IR function for this channel $\Re B(s,p_1,p_2)$ for any two charged particles with the four-momenta p_1,p_2 and the masses m_1,m_2 reads

$$\begin{aligned} 2\alpha\Re B(s,p_1,p_2) = \frac{\alpha}{\pi}\Bigg\{ &\left(\frac{1}{\rho}\ln\frac{\mu(1+\rho)}{m_1m_2}-1\right)\ln\frac{m_\gamma^2}{m_1m_2} + \frac{\mu\rho}{s}\ln\frac{\mu(1+\rho)}{m_1m_2} \\ &+ \frac{m_1^2-m_2^2}{2s}\ln\frac{m_1}{m_2} + \frac{1}{\rho}\Bigg[\pi^2 - \frac{1}{2}\ln\frac{\mu(1+\rho)}{m_1^2}\ln\frac{\mu(1+\rho)}{m_2^2} - \frac{1}{2}\ln^2\frac{m_1^2+\mu(1+\rho)}{m_2^2+\mu(1+\rho)} \\ &- \mathrm{Li}_2\left(\frac{2\mu\rho}{m_1^2+\mu(1+\rho)}\right) - \mathrm{Li}_2\left(\frac{2\mu\rho}{m_2^2+\mu(1+\rho)}\right)\Bigg] - 1\Bigg\}, \end{aligned} \tag{A.2}$$

where

$$\begin{aligned} &\mu = p_1p_2, \quad s = 2\mu + m_1^2 + m_2^2, \\ &\rho = \sqrt{1-\left(\frac{m_1m_2}{\mu}\right)^2}, \end{aligned} \tag{A.3}$$

and m_γ is the mentioned above fictitious photon mass used to regularize the IR singularity.

A.1.2 Virtual photon IR function for t and u channels

The t and u channel virtual photon YFS IR function $\Re B(p_1, p_2)$ is needed in ZINHAC in order to include interferences between the final and initial states. For two charged particles with the four-momenta p_1, p_2 and the masses m_1, m_2, where $m_1 > m_2$, this function, according to Ref. [48], in the case of $t, u \neq 0$ reads

$$2\alpha\Re B(p_1,p_2;m_\gamma) = \frac{\alpha}{\pi}\left\{[\,\nu A(p_1,p_2)-1\,]\,\ln\frac{m_\gamma^2}{m_1m_2}+\frac{1}{2}A_1(p_1,p_2)-\nu A_3(p_1,p_2)\right\}, \tag{A.4}$$

$$\begin{aligned}
A(p_1,p_2) &= \frac{1}{\lambda}\ln\frac{\lambda+\nu}{m_1m_2},\\
A_1(p_1,p_2) &= \frac{m_1^2-m_2^2}{t}\ln\frac{m_1}{m_2}-\frac{2\lambda^2}{t}\,A(p_1,p_2)-2,\\
A_3(p_1,p_2) &= A(p_1,p_2)\,\ln\frac{2\lambda}{m_1m_2}+\frac{1}{\lambda}\left[\frac{1}{4}\left(\ln\frac{\lambda+\nu}{m_1^2}+2\ln\left|\frac{\lambda-\nu+m_1^2}{t}\right|\right)\ln\frac{\lambda+\nu}{m_1^2}\right.\\
&\quad+\frac{1}{4}\left(\ln\frac{\lambda+\nu}{m_2^2}-2\ln\left|\frac{\lambda+\nu-m_2^2}{m_2^2}\right|\right)\ln\frac{\lambda+\nu}{m_2^2}\\
&\quad\left.+\frac{1}{2}\ln|\eta|\ln(1+\eta)-\frac{1}{2}\ln|\zeta|\ln(1+\zeta)+\Re\mathrm{Li}_2(-\eta)-\Re\mathrm{Li}_2(-\zeta)\right],
\end{aligned}$$

$$\nu = p_1p_2, \quad \lambda=\sqrt{(\nu-m_1m_2)(\nu+m_1m_2)}, \quad p_1^2=m_1^2,\ p_2^2=m_2^2,\ m_1>m_2\,,$$
$$t=m_1^2+m_2^2-2\nu, \quad \eta=\frac{m_2^2t}{2\lambda(2\lambda+\nu-m_2^2)}, \qquad \zeta=\frac{\lambda+\nu}{m_2^2}\,\eta\,.$$

A.1.3 Real photon IR function

The YFS IR function $\tilde{B}$ corresponding to the emission of real photons with energy $k^0 \leq E_{min}$ in a process involving any two charged particles with the four-momenta p_1, p_2 and the masses m_1, m_2 can be expressed as

$$\begin{aligned}
2\alpha\tilde{B}(p_1,p_2;E_{min}) = \frac{\alpha}{\pi}\left\{\left(\frac{1}{\rho}\ln\frac{\mu(1+\rho)}{m_1m_2}-1\right)\ln\frac{4E_{min}^2}{m_\gamma^2}+\frac{1}{2\beta_1}\ln\frac{1+\beta_1}{1-\beta_1}\right.\\
\left.+\frac{1}{2\beta_2}\ln\frac{1+\beta_2}{1-\beta_2}+\mu A_4(p_1,p_2)\right\},
\end{aligned} \tag{A.5}$$

where $\beta_i = \sqrt{1 - m_i^2/E_i^2}$, and μ and ρ are defined in Eq. (A.3). The most complex part of the above expression is the function $A_4(p_1, p_2)$. It can be expressed in terms of logarithms and dilogarithms

$$A_4(p_1,p_2) = \frac{1}{\sqrt{(Q^2+\omega^2)(Q^2+\delta^2)}}\Big\{ \ln\frac{\sqrt{\Delta^2+Q^2}-\Delta}{\sqrt{\Delta^2+Q^2}+\Delta}\left[X_{23}^{14}(\eta_1) - X_{23}^{14}(\eta_0)\right] + Y(\eta_1) - Y(\eta_0)\Big\}, \tag{A.6}$$

where

$$\begin{aligned} X_{kl}^{ij}(\eta) &= \ln\left|\frac{(\eta-y_i)(\eta-y_j)}{(\eta-y_k)(\eta-y_l)}\right|, \\ Y(\eta) &= Z_{14}(\eta) + Z_{21}(\eta) + Z_{32}(\eta) - Z_{34}(\eta) + \frac{1}{2}X_{34}^{12}(\eta)X_{14}^{23}(\eta), \\ Z_{ij}(\eta) &= 2\Re\mathrm{Li}_2\left(\frac{y_j-y_i}{\eta-y_i}\right) + \frac{1}{2}\ln^2\left|\frac{\eta-y_i}{\eta-y_j}\right|, \end{aligned} \tag{A.7}$$

and

$$\begin{aligned} \eta_0 &= \sqrt{E_2^2-m_2^2}, \qquad \eta_1 = \sqrt{E_1^2-m_1^2} + \sqrt{\Delta^2+Q^2}, \\ y_{1,2} &= \frac{1}{2}\left[\sqrt{\Delta^2+Q^2} - \Omega + \frac{\omega\delta \pm \sqrt{(Q^2+\omega^2)(Q^2+\delta^2)}}{\sqrt{\Delta^2+Q^2}+\Delta}\right], \\ y_{3,4} &= \frac{1}{2}\left[\sqrt{\Delta^2+Q^2} + \Omega + \frac{\omega\delta \pm \sqrt{(Q^2+\omega^2)(Q^2+\delta^2)}}{\sqrt{\Delta^2+Q^2}-\Delta}\right], \end{aligned} \tag{A.8}$$

where we used the following notation

$$\begin{aligned} \Delta &= E_1 - E_2, \quad \Omega = E_1 + E_2, \\ \delta &= m_1 - m_2, \quad \omega = m_1 + m_2, \\ Q^2 &= -(p_1-p_2)^2. \end{aligned} \tag{A.9}$$

The only approximation used in deriving the above formulae is that $m_\gamma \ll E_{min}$.

One can easily check that the dependence of the above functions on the IR regulator m_γ, as was mentioned in Section 1.3, cancels out in the sum $2\alpha\Re B + 2\alpha\tilde{B}$, which is used to construct the YFS form factor.

A.2 Chiral reprezentation of γ matrices

In the Section 1.4 we used the chiral reprezentation of γ matrices,

$$\gamma^\mu = \begin{bmatrix} 0 & \sigma_+^\mu \\ \sigma_-^\mu & 0 \end{bmatrix}, \tag{A.10}$$

with

$$\sigma^{\mu}_{\pm} = (1, \pm\vec{\sigma}), \tag{A.11}$$

where $\vec{\sigma}$ denotes the "vector" of Pauli matrices in the standard basis,

$$\vec{\sigma} = \left(\sigma^1, \sigma^2, \sigma^3 \right) = \left[\begin{pmatrix} 0 & 1 \\ 1 & 0 \end{pmatrix}, \begin{pmatrix} 0 & -i \\ i & 0 \end{pmatrix}, \begin{pmatrix} 1 & 0 \\ 0 & -1 \end{pmatrix} \right]. \tag{A.12}$$

The γ^5 matrix in this reprezentation is defined as follows

$$\gamma^5 = i\gamma^0\gamma^1\gamma^2\gamma^3 = \gamma_5, \tag{A.13}$$

which in this representation takes the following form,

$$\gamma^5 = \begin{bmatrix} -1 & 0 \\ 0 & 1 \end{bmatrix}. \tag{A.14}$$

Using the definition (A.10) and (A.13) one can proof the anti-commutation relations for these matrices:

$$\{\gamma^5, \gamma^\mu\} = 0 \tag{A.15}$$

and get square of γ^5 matrix,

$$\gamma_5^2 = 1. \tag{A.16}$$

Let us also define the Levi-Civita symbol, also called the antisymmetric symbol, as fallows:

$$\epsilon^{\mu\nu\rho\sigma} = \begin{cases} +1 & \text{for an even permutation of 0, 1, 2, 3} \\ 0 & \text{if any index is repeated,} \\ -1 & \text{for an odd permutation of 0, 1, 2, 3.} \end{cases} \tag{A.17}$$

which implies: $\epsilon_{0123} = -1$.

$$\epsilon^{\alpha\beta\gamma\delta}\epsilon_{\alpha\beta\gamma\delta} = -24, \tag{A.18}$$

$$\epsilon^{\alpha\beta\gamma\mu}\epsilon_{\alpha\beta\gamma\nu} = -6\delta^{\mu}_{\nu}, \tag{A.19}$$

$$\epsilon^{\alpha\beta\mu\nu}\epsilon_{\alpha\beta\rho\sigma} = -2(\delta^{\mu}_{\rho}\delta^{\nu}_{\sigma} - \delta^{\mu}_{\sigma}\delta^{\nu}_{\rho}). \tag{A.20}$$

A.3 Feynman rules

The Feynman amplitude for a given graph in QED is obtained form the Feynman rules. This appendix collects together the formulae which were used in 1.4.

A.3.1 External lines

This section lists the factors that are associated with the external lines of a Feynman graph for the initial or final particles of an amplitude.

(a) Initial particles

The following factors give the (momentum-space) Feynman rules appropriate to an incoming spin-half and spin-one particle. The arrows on the fermion lines indicate the direction of fermion flow, the dot indicates where the line attaches to an interaction vertex.

spin–half particle:

$u_i(p,\sigma)$

spin–half antiparticle:

$\bar{v}_i(p,\sigma)$

spin-one particle:

$\varepsilon_\mu(p,\sigma)$

(b) Final particles

Feynman rules for a outgoing spin-half and spin-one particle.

spin–half particle:

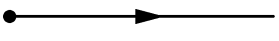

$\bar{u}_i(p,\lambda)$

spin–half antiparticle:

$v_i(p,\sigma)$

spin-one particle:

$\varepsilon^*_\mu(p,\sigma)$

A.3.2 Internal lines (propagators)

The momentum space description for an internal line is given by the propagator for the corresponding particle.

spin–half particle:

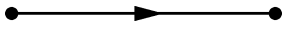

$$\frac{i}{\not{p} - m + i\epsilon} = i\frac{\not{p} + m}{p^2 - m^2 + i\epsilon}$$

photon:

(t'Hoofta–Feynman gauge)

$$\frac{-ig^{\mu\nu}}{k^2 + i\epsilon}$$

massive vector-boson ($W^{\pm}$,Z):

(unitary gauge)

$$\frac{i}{k^2 - M_V^2 + i\epsilon}\Big(- g^{\mu\nu} + \frac{k^\mu k^\nu}{M_V^2}\Big)$$

A.3.3 Vertices

The Feynman Rules that differentiate the standard model from any other theory of interacting spin-one, spin-half particles are those that describe the vertices or interactions of the theory.

$\gamma f\bar{f}$ **vertex:**

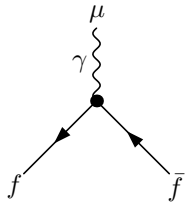

$$= -ieQ_f\gamma^\mu = -ie\gamma^\mu\Big(c_L^{\gamma f\bar{f}}\frac{1-\gamma_5}{2} + c_R^{\gamma f\bar{f}}\frac{1+\gamma_5}{2}\Big)$$

where:

$$c_L^{\gamma f\bar{f}} = Q_f, \quad c_R^{\gamma f\bar{f}} = Q_f \ , \quad \text{for a fermion } f.$$

$Zf\bar{f}$ **vertex:**

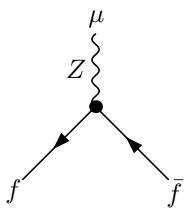

$$= -ie\gamma^\mu\Big(c_L^{Zf\bar{f}}\frac{1-\gamma_5}{2} + c_R^{Zf\bar{f}}\frac{1+\gamma_5}{2}\Big)$$

where:

$$
\begin{aligned}
&c_L^{Zf\bar{f}} = g(-\tfrac{1}{2} + \sin^2\theta_W), \qquad c_R^{Zf\bar{f}} = g\sin^2\theta_W, \qquad \text{for } f = e^-,\ \mu^-.\\
&c_L^{Zf\bar{f}} = g(+\tfrac{1}{2} - \tfrac{2}{3}\sin^2\theta_W), \quad c_R^{Zf\bar{f}} = -\tfrac{2}{3}g\sin^2\theta_W, \quad \text{for } f = u,\ c,\ t.\\
&c_L^{Zf\bar{f}} = g(-\tfrac{1}{2} + \tfrac{1}{3}\sin^2\theta_W), \quad c_R^{Zf\bar{f}} = \tfrac{1}{3}g\sin^2\theta_W, \qquad \text{for } f = d,\ s,\ b.\\
&g = \tfrac{1}{\cos\theta_W \sin\theta_W}.
\end{aligned}
$$

If we denote by t_3 the third component of the weak–isospin and by Q_f the charge of the fermion f then we can write general formuleas for c_L and c_R :

$$
c_L^{Zf\bar{f}} = g(t_3 - Q_f\sin^2\theta_W), \qquad c_R^{Zf\bar{f}} = g(-Q_f\sin^2\theta_W).
$$

The $Bf\bar{f}$ vertex, where $B = Z,\ \gamma$ can also be written in terms of axial and vector coupling constants

$$
-ie\gamma^\mu\left(c_L^{Bf\bar{f}}\frac{1-\gamma_5}{2} + c_R^{Bf\bar{f}}\frac{1+\gamma_5}{2}\right) = -ie\gamma^\mu(v_{Bf\bar{f}} + a_{Bf\bar{f}}\gamma_5). \tag{A.21}
$$

Therefore, we may express axial and vector coupling constants in therms of chiral coupling constats in the following maner

$$
v_{Bf\bar{f}} = \frac{1}{2}(c_R^{Bf\bar{f}} + c_L^{Bf\bar{f}}), \qquad a_{Bf\bar{f}} = \frac{1}{2}(c_R^{Bf\bar{f}} - c_L^{Bf\bar{f}}). \tag{A.22}
$$

A.4 Spin amplitudes

A.4.1 Born Level

The spin amplitude for single Z or γ^* production at the Born level in fermion–antifermion collisions can be obtained in the very similar way to corresponding spin amplitude for single Z or γ^* decay, see Subsection 1.4.2(a):

$$
\begin{aligned}
\mathcal{M}_P^{(0)B} &= \varepsilon_\mu^*(Q,\lambda)\bar{v}(p_2,\sigma_2)(-ie)\gamma^\mu(c_L^{Bq\bar{q}}P_- + c_R^{Bq\bar{q}}P_+)u(p_2,\sigma_2) =\\
&= ie\bar{v}(p_2,\sigma_2)(c_L^{Bq\bar{q}}P_+ + c_R^{Bq\bar{q}}P_-)\not{\varepsilon}_Z^*(Q,\lambda)u(p_2,\sigma_2) =\\
&= -ie\left[c_L^{Bq\bar{q}}v_-^\dagger(p_2,\sigma_2)[\varepsilon^*(Q,\lambda)]^- u_-(p_2,\sigma_2) + c_R^{Bq\bar{q}}v_+^\dagger(p_2,\sigma_2)[\varepsilon^*(Q,\lambda)]^+ u_+(p_2,\sigma_2)\right]\\
&= ie\Big[c_L^{Bq\bar{q}}\sigma_2\omega_{\sigma_2}(p_2)\omega_{-\sigma_1}(p_1)S(p_2,\varepsilon^*,p_1)^-_{-\sigma_2,\sigma_1}\\
&\quad - c_R^{Bq\bar{q}}\sigma_2\omega_{-\sigma_2}(p_2)\omega_{\sigma_1}(p_1)S(p_2,\varepsilon^*,p_1)^+_{-\sigma_2,\sigma_1}\Big]
\end{aligned}
\tag{A.23}
$$

A.4.2 Real hard-photon radiation

(a) Single hard-photon radiation in leptonic Z boson decays

The spin amplitude for single hard-photon radiation in the leptonic Z-boson or γ^* decays $M_D^{(1)B}$ is a sum of two amplitudes – the amplitude for the single

hard-photon radiation from a lepton $M_D^{(1l)B}$ (see the left plot in Fig. 1.4) and the amplitude for the single hard-photon radiation from an antilepton $M_D^{(1\bar{l})B}$ (see, the right plot in Fig. 1.4):

$$M_D^{(1)B} = M_D^{(1l)B} + M_D^{(1\bar{l})B} \tag{A.24}$$

where the amplitude for a single hard-photon radiation from antilepton reads:

$$\begin{aligned}
\mathcal{M}_D^{(1\bar{l})B} =& \frac{ie^2Q_l}{2q_2\cdot k}\bar{u}(q_1,\tau_1)\{c_L^{Bl\bar{l}}P_+ + c_R^{Bl\bar{l}}P_-\}\not{\varepsilon}_Z(Q,\lambda)\big(\not{q}_2+\not{k}-m\big)\not{\varepsilon}^*(k,\kappa)v(q_2,\tau_2)\\
=& \frac{ie^2Q_l}{2q_2\cdot k}\bar{u}(q_1,\tau_1)\{c_L^{Bl\bar{l}}P_+ + c_R^{Bl\bar{l}}P_-\}\not{\varepsilon}_Z(Q,\lambda)\big(\not{k}+2k\cdot q_2\big)\not{\varepsilon}^*(k,\kappa)v(q_2,\tau_2)\\
=& \frac{ie^2Q_l}{2q_2\cdot k}\times\Big[c_L^{Bl\bar{l}}\bar{u}(q_1,\tau_1)_-\big\{[\varepsilon_Z k\varepsilon^*]^- + 2q_2\cdot\varepsilon^*[\varepsilon_Z]^-\big\}v(q_2,\tau_2)_- +\\
&+ c_R^{Bl\bar{l}}\bar{u}(q_1,\tau_1)_+\big\{[\varepsilon_Z k\varepsilon^*]^+ + 2q_2\cdot\varepsilon^*[\varepsilon_Z]^+\big\}v(q_2,\tau_2)_+\Big]\\
=& \frac{-ie^2Q_l}{2q_2\cdot k}\Big[c_L^{Bl\bar{l}}\omega_{-\tau_1}(q_1)\tau_2\omega_{\tau_2}(q_2)\Big\{S(q_1,\varepsilon_Z,k,\varepsilon^*,q_2)^-_{\tau_1,-\tau_2} + 2q_2\cdot\varepsilon^*S(q_1,\varepsilon_Z,q_2)^-_{\tau_1,-\tau_2}\Big\}-\\
&- c_R^{Bl\bar{l}}\omega_{\tau_1}(q_1)\tau_2\omega_{-\tau_2}(q_2)\Big\{S(q_1,\varepsilon_Z,k,\varepsilon^*,q_2)^+_{\tau_1,-\tau_2} + 2q_2\cdot\varepsilon^*S(q_1,\varepsilon_Z,q_2)^+_{\tau_1,-\tau_2}\Big\}\Big]
\end{aligned} \tag{A.25}$$

The amplitude for a single hard-photon radiation from lepton:

$$\begin{aligned}
&\mathcal{M}_D^{(1l)B}(\lambda;\tau_1,\tau_2,\kappa) =\\
&= -ie^2Q_l\bar{u}(q_1,\tau_1)\not{\varepsilon}^*(k,\kappa)\frac{\not{q}_1+\not{k}+m}{2q_1\cdot k}\not{\varepsilon}_Z(Q,\lambda)\{c_L^{Bl\bar{l}}P_- + c_R^{Bl\bar{l}}P_+\}v(q_2,\tau_2)\\
&= \frac{-ie^2Q_l}{2q_1\cdot k}\bar{u}(q_1,\tau_1)\big[\not{\varepsilon}^*\not{k}\not{\varepsilon}_Z + 2q_1\cdot\varepsilon^*\not{\varepsilon}_Z\big]\{c_L^{Bl\bar{l}}P_- + c_R^{Bl\bar{l}}P_+\}v(q_2,\tau_2)\\
&= \frac{-ie^2Q_l}{2q_1\cdot k}\bar{u}(q_1,\tau_1)\{c_L^{Bl\bar{l}}P_+ + c_R^{Bl\bar{l}}P_-\}\big[\not{\varepsilon}^*\not{k}\not{\varepsilon}_Z + 2q_1\cdot\varepsilon^*\not{\varepsilon}_Z\big]v(q_2,\tau_2)\\
&= \frac{-ie^2Q_l}{2q_1\cdot k}\Big[c_L^{Bl\bar{l}}\bar{u}(q_1,\tau_1)_-\big\{[\varepsilon^* k\varepsilon_Z]^- + 2q_1\cdot\varepsilon^*[\varepsilon_Z]^-\big\}v(q_2,\tau_2)_-\\
&\qquad + c_R^{Bl\bar{l}}\bar{u}(q_1,\tau_1)_+\big\{[\varepsilon^* k\varepsilon_Z]^+ + 2q_1\cdot\varepsilon^*[\varepsilon_Z]^+\big\}v(q_2,\tau_2)_+\Big]\\
&= \frac{ie^2Q_l}{2q_1\cdot k}\Big[c_L^{Bl\bar{l}}\omega_{-\tau_1}(q_1)\tau_2\omega_{\tau_2}(q_2)\Big\{S\big(q_1,\varepsilon^*,k,\varepsilon_Z,q_2\big)^-_{\tau_1,-\tau_2} + 2q_1\cdot\varepsilon^*S\big(q_1,\varepsilon_Z,q_2\big)^-_{\tau_1,-\tau_2}\Big\}-\\
&- c_R^{Bl\bar{l}}\omega_{\tau_1}(q_1)\tau_2\omega_{-\tau_2}(q_2)\Big\{S\big(q_1,\varepsilon^*,k,\varepsilon_Z,q_2\big)^+_{\tau_1,-\tau_2} + 2q_1\cdot\varepsilon^*S\big(q_1,\varepsilon_Z,q_2\big)^+_{\tau_1,-\tau_2}\Big\}\Big].
\end{aligned} \tag{A.26}$$

(b) Single hard-photon radiation in quarkonic Z boson production

The spin amplitude for single hard-photon radiation in the quarkonic Z-boson or γ^* production $M_P^{(1)B}$ is a sum of two amplitudes – the amplitude for the single hard-photon radiation from a quark $M_D^{(1q)B}$ (see the left plot in Fig. 1.5) and

the amplitude for the single hard-photon radiation from an antiquark $M_D^{(1\bar{q})B}$ (see the right plot from Fig. 1.5):

$$M_P^{(1)B} = M_P^{(1q)B} + M_P^{(1\bar{q})B}, \tag{A.27}$$

where the amplitude for a single hard-photon radiation from quark reads:

$$\begin{aligned}
\mathcal{M}_P^{Z(1q)} &= \frac{-ie^2Q_q}{2p_1\cdot k}\bar{v}(p_2,\sigma_2)\{c_L^{Bq\bar{q}}P_+ + c_R^{Bq\bar{q}}P_-\}\not{\varepsilon}_Z^*(Q,\lambda)(\not{p}_1 - \not{k} + m)\not{\varepsilon}^*(k,\kappa)u(p_1,\sigma_1)\\
&= \frac{-ie^2Q_q}{2p_1\cdot k}\bar{v}(p_2,\sigma_2)\{c_L^{Bq\bar{q}}P_+ + c_R^{Bq\bar{q}}P_-\}\not{\varepsilon}_Z^*(Q,\lambda)\big[2p_1\varepsilon^*(k,\kappa) - \not{k}\not{\varepsilon}^*(k,\kappa)\big]u(p_1,\sigma_1)\\
&= \frac{-ie^2Q_q}{2p_1\cdot k}\times\Big[c_L^{Bq\bar{q}}\bar{v}(p_2,\sigma_2)_-\Big\{2p_1\varepsilon^*(k,\kappa)[\varepsilon^*(Q,\lambda)]^- - [\varepsilon^*(Q,\lambda),k,\varepsilon^*(k,\kappa)]^-\Big\}u(p_1,\sigma_1)_-\\
&\quad + c_R^{Bq\bar{q}}\bar{v}(p_2,\sigma_2)_+\Big\{2p_1\varepsilon^*(k,\kappa)[\varepsilon^*(Q,\lambda)]^+ - [\varepsilon^*(Q,\lambda),k,\varepsilon^*(k,\kappa)]^+\Big\}u(p_1,\sigma_1)_+\Big]\\
&= \frac{ie^2Q_q}{2p_1\cdot k}\times\Big[c_L^{Bq\bar{q}}(-\sigma_2)\omega_{\sigma_2}(p_2)\omega_{-\sigma_1}(p_1)\Big\{2p_1\varepsilon^*S(p_2,\varepsilon_Z^*,p_1)^-_{-\sigma_2,\sigma_1} - S(p_2,\varepsilon_Z^*,k,\varepsilon^*,p_1)^-_{-\sigma_2,\sigma_1}\Big\}\\
&\quad - c_R^{Bq\bar{q}}(\sigma_2)\omega_{-\sigma_2}(p_2)]\omega_{\sigma_1}(p_1)\Big\{2p_1\varepsilon^*S(p_2,\varepsilon_Z^*,p_1)^+_{-\sigma_2,\sigma_1} - S(p_2,\varepsilon_Z^*,k,\varepsilon^*,p_1)^+_{-\sigma_2,\sigma_1}\Big\}\Big].
\end{aligned} \tag{A.28}$$

The amplitude for a single hard-photon radiation from antiquark reads:

$$\begin{aligned}
\mathcal{M}_P^{Z(1\bar{q})} &= \frac{-ie^2Q_q}{2p_2\cdot k}\bar{v}(p_2,\sigma_2)\not{\varepsilon}^*(k,\kappa)(-\not{p}_2 + \not{k} + m)\not{\varepsilon}_Z^*(Q,\lambda)\{c_L^{Bq\bar{q}}P_- + c_R^{Bq\bar{q}}P_+\}u(p_1,\sigma_1)\\
&= \frac{-ie^2Q_q}{2p_2\cdot k}\bar{v}(p_2,\sigma_2)[\not{\varepsilon}^*(k,\kappa)\not{k} - 2p_2\varepsilon^*(k,\kappa)]\not{\varepsilon}_Z^*(Q,\lambda)\{c_L^{Bq\bar{q}}P_+ + c_R^{Bq\bar{q}}P_-\}u(p_1,\sigma_1)\\
&= \frac{-ie^2Q_q}{2p_2\cdot k}\bar{v}(p_2,\sigma_2)\{c_L^{Bq\bar{q}}P_+ + c_R^{Bq\bar{q}}P_-\}\Big[\not{\varepsilon}^*(k,\kappa)\not{k}\not{\varepsilon}_Z^*(Q,\lambda) - 2p_2\varepsilon^*(k,\kappa)\not{\varepsilon}_Z^*(Q,\lambda)\Big]u(p_1,\sigma_1)\\
&= \frac{ie^2Q_q}{2p_2\cdot k}\times\Big[c_L^{Bq\bar{q}}\bar{v}(p_2,\sigma_2)_-\Big\{2p_2\varepsilon^*(k,\kappa)[\varepsilon_Z^*(Q,\lambda)]^- - [\varepsilon^*(k,\kappa),k,\varepsilon_Z^*(Q,\lambda)]^-\Big\}u(p_1,\sigma_1)_-\\
&\quad + c_R^{Bq\bar{q}}\bar{v}(p_2,\sigma_2)_+\Big\{2p_2\varepsilon^*(k,\kappa)[\varepsilon_Z^*(Q,\lambda)]^+ - [\varepsilon^*(k,\kappa),k,\varepsilon_Z^*(Q,\lambda)]^+\Big\}u(p_1,\sigma_1)_+\Big]\\
&= \frac{-ie^2Q_q}{2p_2\cdot k}\times\Big[c_L^{Bq\bar{q}}\sigma_2\omega_{\sigma_2}(p_2)\omega_{-\sigma_1}(p_1)\Big\{2p_2\varepsilon^*S(p_2,\varepsilon_Z^*,p_1)^-_{-\sigma_2,\sigma_1} - S(p_2,\varepsilon^*,k,\varepsilon_Z^*,p_1)^-_{-\sigma_2,\sigma_1}\Big\}\\
&\quad - c_R^{Bq\bar{q}}(\sigma_2)\omega_{-\sigma_2}(p_2)]\omega_{\sigma_1}(p_1)\Big\{2p_2\varepsilon^*S(p_2,\varepsilon_Z^*,p_1)^+_{-\sigma_2,\sigma_1} - S(p_2,\varepsilon^*,k,\varepsilon_Z^*,p_1)^+_{-\sigma_2,\sigma_1}\Big\}\Big].
\end{aligned} \tag{A.29}$$

A.5 Born level differential cross section in terms of Mandelstam variables

The Born-level differential cross section in the small fermion-mass approximation expressed in terms of Mandelstam variables reads:

$$\begin{aligned}
\rho_0(\hat{s},\phi,\cos\theta) &= \frac{\mathrm{d}\sigma_0}{\mathrm{d}\hat{\Omega}} = \frac{d^2\sigma_0}{d\phi d\cos\theta} = \frac{1}{12}\frac{1}{64\pi^2\hat{s}}\sum_{\text{pol}}|M_{q\bar{q}}^{\text{LO}}|^2 \\
&= \frac{\alpha^2}{12\,\hat{s}^3}\Big\{\, 2\,Q_q^2Q_l^2\,(\hat{t}^2+\hat{u}^2) \\
&\quad + 2\,Q_qQ_l\,\Re\Big[\big[(c_R^{Zq\bar{q}}c_R^{Zl\bar{l}}+c_L^{Zq\bar{q}}c_L^{Zl\bar{l}})\,\hat{u}^2+(c_R^{Zq\bar{q}}c_L^{Zl\bar{l}}+c_L^{Zq\bar{q}}c_R^{Zl\bar{l}})\,\hat{t}^2\big]\,\chi_{Z(\hat{s})}\Big] \\
&\quad + \Big[(|c_R^{Zq\bar{q}}|^2|c_R^{Zl\bar{l}}|^2+|c_L^{Zq\bar{q}}|^2|c_L^{Zl\bar{l}}|^2)\,\hat{u}^2 \\
&\qquad + (|c_R^{Zq\bar{q}}|^2|c_L^{Zl\bar{l}}|^2+|c_L^{Zq\bar{q}}|^2|c_R^{Zl\bar{l}}|^2)\,\hat{t}^2\Big]\,|\chi_{Z(\hat{s})}|^2\Big\}.
\end{aligned} \tag{A.30}$$

The explicit factor $1/12$ in the above equation results from the average over the quark spins and colours, and $\hat{\Omega}$ is the solid angle of the outgoing l^- in the partonic centre-of-mass (CM) frame. In our convenientionthe $+z$ axsis is pointing in the direction of the momentum of the quark q. The Mandelstam variables in the CMS frame take form:

$$\begin{aligned}
\hat{s} &= (p_1+p_2)^2 = 2p_1p_2, \\
\hat{t} &= (p_1-q_1)^2 = -2p_1q_1 = -\frac{\hat{s}}{2}(1-\cos\theta), \\
\hat{u} &= (p_1-q_2)^2 = -2p_1q_2 = -\frac{\hat{s}}{2}(1+\cos\theta).
\end{aligned} \tag{A.31}$$

and $\chi_{Z(\hat{s})} = \hat{s}/Z(\hat{s})$ where $Z(\hat{s})$ is the inverse of the Z-boson propagator defined in the Eq. (1.46).

List of Figures

List of Tables

Bibliography

[1] W. J. Stirling and M. R. Whalley, J. Phys. **G19**, D1 (1993).

[2] The CDF Collaboration, F. Abe *et al.*, Phys. Rev. **D43**, 2070 (1991).

[3] R. Brock *et al.*, Report of the working group on precision measurements, in Proceedings of the workshop QCD and weak boson physics in Run II, Fermilab, 1999, arXiv:hep-ex/0011009.

[4] S. Haywood *et al.*, (1999), arXiv:hep-ph/0003275.

[5] A. Siódmok, F. Dydak, F. Fayette, M. W. Krasny, and W. Płaczek, Measurement of the W-boson mass at the LHC, in preparation, to be submitted to EPJC.

[6] ATLAS, N. Besson, M. Boonekamp, E. Klinkby, T. Petersen, and S. Mehlhase, Eur. Phys. J. **C57**, 627 (2008), arXiv:0805.2093 [hep-ex].

[7] T. Sjostrand, Phys. Lett. **B157**, 321 (1985).

[8] G. Corcella *et al.*, JHEP **01**, 010 (2001), arXiv:hep-ph/0011363.

[9] T. Sjöstrand, S. Mrenna, and P. Skands, JHEP **05**, 026 (2006), arXiv:hep-ph/0603175.

[10] M. Bahr *et al.*, Eur. Phys. J. **C58**, 639 (2008), arXiv:0803.0883 [hep-ph].

[11] T. Sjostrand, S. Mrenna, and P. Z. Skands, Comput. Phys. Commun. **178**, 852 (2008), arXiv:0710.3820 [hep-ph].

[12] T. Gleisberg *et al.*, JHEP **02**, 007 (2009), arXiv:0811.4622 [hep-ph].

[13] F. Fayette, M. W. Krasny, W. Placzek, and A. Siodmok, Measurement of $MW^+ - MW^-$ at LHC, Eur. Phys. J. **C63**, 33 (2009), arXiv:0812.2571 [hep-ph].

[14] CMS Collaboration, V. Buge *et al.*, J. Phys. **G34**, 193 (2007).

[15] A. Siódmok and W. Płaczek, ZINHAC: The Monte Carlo event generator for single Z-boson production with leptonic decays in hadron collisions, in preparation.

[16] D. Bardin *et al.*, Implementation of SANC EW corrections in ZINHAC Monte Carlo generator, in preparation.

[17] A. Siodmok, Spin amplitude formalisms for massive particles in the Drell-Yan process, Acta Phys. Polon. **B37**, 2209 (2006).

[18] http://th-www.if.uj.edu.pl/ZINHAC.

[19] F. Bloch and A. Nordsieck, Phys. Rev. **52**, 54 (1937).

[20] Berestetsky, V.B., Lifshitz, E.M., and Pitaevsky, L.P., *Quantum Electrodynamics* (Pergamon, Oxford, 1982).

[21] Bjorken, J.D. and Drell, S.D., *Relativistic Quantum Mechanics* (McGraw-Hill, New York, 1965).

[22] Smilga, A., *Lectures on Quantum Chromodynamics* (World Scientific, 2001).

[23] D. R. Yennie, S. Frautschi, and H. Suura, Ann. Phys. (NY) **13**, 379 (1961).

[24] Weinberg, S., *The quantum theory of fields* (Cambridge Univ. Press, 2000).

[25] S. Jadach, MPI-PAE/PTh 6/87.

[26] S. Jadach and B. F. L. Ward, Phys. Rev. **D38**, 2897 (1988).

[27] S. Jadach and B. F. L. Ward, Phys. Rev. **D40**, 3582 (1989).

[28] S. Jadach and B. F. L. Ward, Comput. Phys. Commun. **56**, 351 (1990).

[29] S. Jadach and B. F. L. Ward, Phys. Lett. **B274**, 470 (1992).

[30] S. Jadach, B. F. L. Ward, and Z. Was, Comput. Phys. Commun. **66**, 276 (1991).

[31] S. Jadach, B. F. L. Ward, and Z. Was, Comput. Phys. Commun. **79**, 503 (1994).

[32] S. Jadach, B. F. L. Ward, and Z. Was, Comput. Phys. Commun. **124**, 233 (2000), arXiv:hep-ph/9905205.

[33] S. Jadach, E. Richter-Was, B. F. L. Ward, and Z. Was, Comput. Phys. Commun. **70**, 305 (1992).

[34] S. Jadach, W. Placzek, E. Richter-Was, B. F. L. Ward, and Z. Was, Comput. Phys. Commun. **102**, 229 (1997).

[35] S. Jadach, W. Placzek, and B. F. L. Ward, Phys. Lett. **B390**, 298 (1997), arXiv:hep-ph/9608412.

[36] S. Jadach, B. F. L. Ward, and Z. Was, Comput. Phys. Commun. **130**, 260 (2000), arXiv:hep-ph/9912214.

[37] S. Jadach, W. Placzek, M. Skrzypek, B. F. L. Ward, and Z. Was, Comput. Phys. Commun. **140**, 432 (2001), arXiv:hep-ph/0103163.

[38] M. Skrzypek, S. Jadach, W. Placzek, and Z. Was, Comput. Phys. Commun. **94**, 216 (1996).

[39] S. Jadach, W. Placzek, M. Skrzypek, B. F. L. Ward, and Z. Was, Comput. Phys. Commun. **119**, 272 (1999), arXiv:hep-ph/9906277.

[40] S. Jadach, W. Placzek, M. Skrzypek, B. F. L. Ward, and Z. Was, Comput. Phys. Commun. **140**, 475 (2001), arXiv:hep-ph/0104049.

[41] S. Jadach, W. Placzek, and B. F. L. Ward, Phys. Rev. **D56**, 6939 (1997), arXiv:hep-ph/9705430.

[42] B. F. L. Ward, Acta Phys. Polon. **B39**, 1745 (2008), arXiv:0804.1528 [hep-ph].

[43] F. A. Berends and R. Kleiss, Z. Phys. **C27**, 365 (1985).

[44] U. Baur, S. Keller, and D. Wackeroth, Phys. Rev. **D59**, 013002 (1999), arXiv:hep-ph/9807417.

[45] P. M. Nadolsky, AIP Conf. Proc. **753**, 158 (2005), arXiv:hep-ph/0412146.

[46] U. Baur, (2003), arXiv:hep-ph/0304266.

[47] U. Baur and T. Stelzer, Phys. Rev. **D61**, 073007 (2000), arXiv:hep-ph/9910206.

[48] W. Płaczek and S. Jadach, Eur. Phys. J. **C29**, 325 (2003), hep-ph/0302065.

[49] C. M. Carloni Calame, G. Montagna, O. Nicrosini, and M. Treccani, Phys. Rev. **D69**, 037301 (2004), arXiv:hep-ph/0303102.

[50] C. M. Carloni Calame, Phys. Lett. **B520**, 16 (2001), arXiv:hep-ph/0103117.

[51] C. M. Carloni Calame, S. Jadach, G. Montagna, O. Nicrosini, and W. Placzek, Acta Phys. Polon. **B35**, 1643 (2004), arXiv:hep-ph/0402235.

[52] D. Bardin, S. Bondarenko, S. Jadach, L. Kalinovskaya, and W. Placzek, (2008), arXiv:0806.3822 [hep-ph].

[53] W. Płaczek and S. Jadach, WINHAC version 1.30: The Monte Carlo event generator for single W-boson production with leptonic decays in hadron collisions, available from http://cern.ch/placzek/winhac.

[54] W. Placzek, WINHAC - the Monte Carlo event generator for single W-boson production in hadronic collisions, 2009, arXiv:0911.0572 [hep-ph].

[55] http://www.pv.infn.it/~hepcomplex/horace.html.

[56] http://home.thep.lu.se/~torbjorn/Pythia.html.

[57] http://hepwww.rl.ac.uk/theory/seymour/herwig/herwig65.html.

[58] http://projects.hepforge.org/herwig/.

[59] T. Gleisberg *et al.*, JHEP **02**, 056 (2004), arXiv:hep-ph/0311263.

[60] http://projects.hepforge.org/sherpa/dokuwiki/doku.php.

[61] S. Frixione and B. R. Webber, JHEP **06**, 029 (2002), arXiv:hep-ph/0204244.

[62] http://www.hep.phy.cam.ac.uk/theory/webber/MCatNLO/.

[63] B. P. Kersevan and E. Richter-Was, (2004), arXiv:hep-ph/0405247.

[64] http://borut.home.cern.ch/borut/.

[65] Q.-H. Cao and C. P. Yuan, Phys. Rev. Lett. **93**, 042001 (2004), arXiv:hep-ph/0401026.

[66] http://hep.pa.msu.edu/people/cao/ResBos-A.html.

[67] C. Balazs and C. P. Yuan, Phys. Rev. **D56**, 5558 (1997), arXiv:hep-ph/9704258.

[68] http://www.pa.msu.edu/~balazs/ResBos/.

[69] http://ubpheno.physics.buffalo.edu/~dow/wgrad.html.

[70] U. Baur, O. Brein, W. Hollik, C. Schappacher, and D. Wackeroth, Phys. Rev. **D65**, 033007 (2002), arXiv:hep-ph/0108274.

[71] http://ubpheno.physics.buffalo.edu/~dow/.

[72] A. Arbuzov *et al.*, Eur. Phys. J. **C46**, 407 (2006), arXiv:hep-ph/0506110.

[73] A. Arbuzov *et al.*, Eur. Phys. J. **C54**, 451 (2008), arXiv:0711.0625 [hep-ph].

[74] http://sanc.jinr.ru.

[75] J. Alwall *et al.*, Comput. Phys. Commun. **176**, 300 (2007), arXiv:hep-ph/0609017.

[76] U. Baur, S. Keller, and W. K. Sakumoto, Phys. Rev. **D57**, 199 (1998), arXiv:hep-ph/9707301.

[77] S. Jadach, W. Placzek, M. Skrzypek, and B. F. L. Ward, Phys. Rev. **D54**, 5434 (1996), arXiv:hep-ph/9606429.

[78] K. Hagiwara and D. Zeppenfeld, Nucl. Phys. **B274**, 1 (1986).

[79] S. Dittmaier and M. Kramer, Phys. Rev. **D65**, 073007 (2002), arXiv:hep-ph/0109062.

[80] S. Jadach, (1999), arXiv:physics/9906056.

[81] S. Jadach, Comput. Phys. Commun. **152**, 55 (2003), arXiv:physics/0203033.

[82] A. Rimoldi, Nuclear Physics B - Proceedings Supplements **172**, 49 (2007), Proceedings of the 10th Topical Seminar on Innovative Particle and Radiation Detectors, Proceedings of the 10th Topical Seminar on Innovative Particle and Radiation Detectors.

[83] The ATLAS Collaboration, W. Armstrong, W. *et al.*, CERN-LHCC-94-43.

[84] D. Acosta, M. Della Negra, L. Fo, A. Herv, and A. Petrilli, *CMS physics: Technical Design Report* (CERN, Geneva, 2006).

[85] S. Agostinelli *et al.*, Nuclear Instruments and Methods in Physics Research Section A: Accelerators, Spectrometers, Detectors and Associated Equipment **506**, 250 (2003).

[86] S. Jadach, *Comoving Reference Frames For Multi-Bremsstrahlung*, to be submitted to Comput. Phys. Commun.

[87] E. Byckling and K. Kajantie, *Particle kinematics [by] E. Byckling [and] K. Kajantie* (Wiley London, New York,, 1973).

[88] F. James, *Statistical methods in experimental physics* (World Scientific, 2006).

[89] www.doxygen.org.

[90] http://trac.edgewall.org.

[91] http://subversion.apache.org/.

[92] http://www.w3.org/TR/REC-xml/.

[93] http://www.omg.org/spec/UML/2.0/.

[94] http://www.visual-paradigm.com.

[95] http://www.eclipse.org/.

[96] http://xerces.apache.org/xerces-c/.

[97] G. P. Lepage, J. Comput. Phys. **27**, 192 (1978).

[98] C. Buttar *et al.*, (2008), arXiv:0803.0678 [hep-ph].

[99] D. Stump *et al.*, JHEP **10**, 046 (2003), hep-ph/0303013.

[100] Durham University, Parton Distribution Generator available at : http://hepforge.cedar.ac.uk/lhapdf/.

[101] M. R. Whalley, D. Bourilkov, and R. C. Group, (2005), arXiv:hep-ph/0508110.

[102] S. Gieseke, M. H. Seymour, and A. Siódmok, A model of non-perturbative gluon emission in an initial state parton shower, JHEP **06**, 001 (2008), arXiv:0712.1199 [hep-ph].

[103] A. Siodmok, S. Gieseke, and M. H. Seymour, Non-perturbative effects in the transverse momentum distribution of electroweak bosons at the LHC, Acta Phys. Polon. **B40**, 2109 (2009), arXiv:0905.3455 [hep-ph].

[104] C. Balazs, J. Huston, and I. Puljak, Phys. Rev. **D63**, 014021 (2001), arXiv:hep-ph/0002032.

[105] M. W. Krasny, F. Fayette, W. Placzek, and A. Siodmok, Z-boson as 'the standard candle' for high precision W- boson physics at LHC, Eur. Phys. J. **C51**, 607 (2007), arXiv:hep-ph/0702251.

[106] Y. L. Dokshitzer, D. Diakonov, and S. I. Troian, Phys. Lett. **B79**, 269 (1978).

[107] G. Altarelli, G. Parisi, and R. Petronzio, Phys. Lett. **B76**, 356 (1978).

[108] J. C. Collins, D. E. Soper, and G. Sterman, Nucl. Phys. **B250**, 199 (1985).

[109] C. T. H. Davies, B. R. Webber, and W. J. Stirling, Nucl. Phys. **B256**, 413 (1985).

[110] R. K. Ellis, D. A. Ross, and S. Veseli, Nucl. Phys. **B503**, 309 (1997), arXiv:hep-ph/9704239.

[111] R. K. Ellis and S. Veseli, Nucl. Phys. **B511**, 649 (1998), arXiv:hep-ph/9706526.

[112] G. Marchesini and B. R. Webber, Nucl. Phys. **B310**, 461 (1988).

[113] S. Gieseke, P. Stephens, and B. Webber, JHEP **12**, 045 (2003), arXiv:hep-ph/0310083.

[114] S. Mrenna, (1999), arXiv:hep-ph/9902471.

[115] G. Corcella and M. H. Seymour, Phys. Lett. **B442**, 417 (1998), arXiv:hep-ph/9809451.

[116] M. H. Seymour, Comp. Phys. Commun. **90**, 95 (1995), arXiv:hep-ph/9410414.

[117] S. Catani, F. Krauss, R. Kuhn, and B. R. Webber, JHEP **11**, 063 (2001), arXiv:hep-ph/0109231.

[118] M. Bengtsson and T. Sjostrand, Phys. Lett. **B185**, 435 (1987).

[119] G. Miu and T. Sjostrand, Phys. Lett. **B449**, 313 (1999), arXiv:hep-ph/9812455.

[120] O. Latunde-Dada, JHEP **11**, 040 (2007), arXiv:0708.4390 [hep-ph].

[121] D. E. Soper, (1996), arXiv:hep-ph/9702203.

[122] G. Dissertori *et al.*, (2009), arXiv:0910.4283 [hep-ph].

[123] R. K. Ellis, W. J. Stirling, and B. R. Webber, *QCD and collider physics* (Camb. Monogr. Part. Phys. Nucl. Phys. Cosmol., 1996).

[124] M. Bahr, *Jet simulations at hadron colliders*, PhD thesis, Karlsruhe University, 2008.

[125] V. V. Sudakov, Sov. Phys. JETP **3**, 65 (1956).

[126] A. Bassetto, M. Ciafaloni, G. Marchesini, and A. H. Mueller, Nucl. Phys. **B207**, 189 (1982).

[127] A. Bassetto, M. Ciafaloni, and G. Marchesini, Phys. Rept. **100**, 201 (1983).

[128] S. Catani and M. Ciafaloni, Nuclear Physics B **236**, 61 (1984).

[129] M. Ciafaloni, Phys. Lett. **B95**, 113 (1980).

[130] M. Ciafaloni, Lectures given at Summer Workshop on High Energy Physics, Trieste, Italy, Aug 1981.

[131] Y. L. Dokshitzer, V. A. Khoze, and S. I. Troian, Adv. Ser. Direct. High Energy Phys. **5**, 241 (1988).

[132] A. H. Mueller, Phys. Lett. **B104**, 161 (1981).

[133] B. I. Ermolaev and V. S. Fadin, JETP Lett. **33**, 269 (1981).

[134] Y. L. Dokshitzer, V. S. Fadin, and V. A. Khoze, Phys. Lett. **B115**, 242 (1982).

[135] G. Marchesini and B. R. Webber, Nucl. Phys. **B238**, 1 (1984).

[136] B. R. Webber, Nucl. Phys. **B238**, 492 (1984).

[137] S. Catani, S. Dittmaier, and Z. Trocsanyi, Phys. Lett. **B500**, 149 (2001), arXiv:hep-ph/0011222.

[138] D. Amati and G. Veneziano, Phys. Lett. **B83**, 87 (1979).

[139] S. Catani, B. R. Webber, and G. Marchesini, Nucl. Phys. **B349**, 635 (1991).

[140] I. Borozan and M. H. Seymour, JHEP **09**, 015 (2002), arXiv:hep-ph/0207283.

[141] The CDF Collaboration, A. A. Affolder *et al.*, Phys. Rev. Lett. **84**, 845 (2000), arXiv:hep-ex/0001021.

[142] The D0 Collaboration, B. Abbott *et al.*, Phys. Rev. **D61**, 032004 (2000), arXiv:hep-ex/9907009.

[143] G. Moreno *et al.*, Phys. Rev. **D43**, 2815 (1991).

[144] D. Antreasyan *et al.*, Phys. Rev. Lett. **48**, 302 (1982).

[145] Y. L. Dokshitzer and B. R. Webber, Phys. Lett. **B352**, 451 (1995), arXiv:hep-ph/9504219.

[146] Y. L. Dokshitzer, G. Marchesini, and B. R. Webber, Nucl. Phys. **B469**, 93 (1996), arXiv:hep-ph/9512336.

[147] A. Guffanti and G. E. Smye, JHEP **10**, 025 (2000), arXiv:hep-ph/0007190.

[148] S. Berge, P. M. Nadolsky, F. Olness, and C. P. Yuan, Phys. Rev. **D72**, 033015 (2005), arXiv:hep-ph/0410375.

[149] F. Landry, R. Brock, P. M. Nadolsky, and C. P. Yuan, Phys. Rev. **D67**, 073016 (2003), arXiv:hep-ph/0212159.

[150] M. Bahr *et al.*, (2007), arXiv:0711.3137 [hep-ph].

[151] B. R. Webber, Talk on in CERN Main Auditorium **B500**, 67 min (21 Feb 2008), http://cdsweb.cern.ch/record/1082256.

[152] F. Fayette, M. W. Krasny, W. Placzek, and A. Siodmok, Prospect for precision measurements of MW+ -MW- & MW at the LHC: Shortcuts revisited, 2009, arXiv:0909.1443.

[153] M. W. Krasny, F. Dydak, F. Fayette, W. Płaczek, and A. Siódmok, A programme to reduce the uncertainty of Standard Model parameters at the LHC, in preparation, to be submitted to EPJC.

[154] M. W. Krasny, F. Dydak, F. Fayette, W. Płaczek, and A. Siódmok, $\Delta M_W = 10 MeV/c2$ at the LHC: a forlorn hope?, in preparation, to be submitted to Phys. Lett.

[155] The ALEPH Collaboration *et al.*, (2009), arXiv:0911.2604 [hep-ex].

[156] Particle Data Group, C. Amsler *et al.*, Phys. Lett. **B667**, 1 (2008).

[157] The ALEPH Collaboration, Phys. Rept. **427**, 257 (2006), arXiv:hep-ex/0509008.

[158] The D0 Collaboration, S. Abachi *et al.*, Phys. Rev. Lett. **74**, 2632 (1995), arXiv:hep-ex/9503003.

[159] The CDF Collaboration, F. Abe *et al.*, Phys. Rev. Lett. **74**, 2626 (1995), arXiv:hep-ex/9503002.

[160] The ALEPH Collaboration, J. Alcaraz *et al.*, (2006), arXiv:hep-ex/0612034.

[161] S. Heinemeyer, W. Hollik, and G. Weiglein, Phys. Rept. **425**, 265 (2006), arXiv:hep-ph/0412214.

[162] S. Heinemeyer, W. Hollik, D. Stockinger, A. M. Weber, and G. Weiglein, JHEP **08**, 052 (2006), arXiv:hep-ph/0604147.

[163] Tevatron Electroweak Working Group, (2009), arXiv:0908.1374.

[164] F. Fayette, Strategies for precision measurements of the charge asymmetry of the W boson mass at the LHC within the ATLAS experiment, 2009, arXiv:0906.4260 [hep-ex], Ph. D. thesis.

[165] The ATLAS Collaboration, ATLAS: Detector and physics performance technical design report. Volume 1, CERN-LHCC-99-14.

[166] The ATLAS Collaboration, ATLAS detector and physics performance. Technical design report. Vol. 2, CERN-LHCC-99-15.

[167] The ATLAS Collaboration, ATLAS inner detector: Technical design report. Vol. 1, CERN-LHCC-97-16.

[168] The ATLAS Collaboration, ATLAS inner detector: Technical design report. Vol. 2, CERN-LHCC-97-17.

[169] Le centre de calcul de lin2p3/cnrs, http://cc.in2p3.fr/.

[170] The CDF Collaboration, F. Abe *et al.*, Phys. Rev. Lett. **65**, 2243 (1990).

[171] The CDF Collaboration, T. Aaltonen *et al.*, Phys. Rev. Lett. **99**, 151801 (2007), arXiv:0707.0085.

[172] The CDF Collaboration, T. Aaltonen *et al.*, (2007), arXiv:0708.3642 [hep-ex].

[173] The D0 Collaboration, V. M. Abazov *et al.*, Phys. Rev. Lett. **103**, 141801 (2009), arXiv:0908.0766 [hep-ex].

[174] J. Pumplin *et al.*, JHEP **07**, 012 (2002), arXiv:hep-ph/0201195.

[175] K. Rejzner, M. W. Krasny, F. Fayette, W. Płaczek, and A. Siódmok, Measurement of the W-boson width at the LHC, in prepration.

[176] A. D. Martin, W. J. Stirling, R. S. Thorne, and G. Watt, Eur. Phys. J. **C63**, 189 (2009), arXiv:0901.0002 [hep-ph].

[177] A. D. Martin, R. G. Roberts, W. J. Stirling, and R. S. Thorne, Eur. Phys. J. **C14**, 133 (2000), arXiv:hep-ph/9907231.

[178] S. Berge, P. M. Nadolsky, and F. I. Olness, Phys. Rev. **D73**, 013002 (2006), arXiv:hep-ph/0509023.

[179] D. Stump *et al.*, JHEP **10**, 046 (2003), hep-ph/0303013.

[180] P. M. Nadolsky *et al.*, Phys. Rev. **D78**, 013004 (2008), arXiv:0802.0007.

[181] G. Veramendi, Presentation: *"The Measurement of AFB in Electron-Positron Pairs"* available at: http://www-cdf.fnal.gov/physics/ewk/2004/afb/.

[182] M. W. Krasny, J. Chwastowski, and K. Słowikowski, Luminosity measurement method for LHC: The theoretical precision and the experimental challenges, 2006, hep-ex/0610052.

[183] M. W. Krasny, J. Chwastowski, and K. Slowikowski, Nucl. Phys. Proc. Suppl. **179-180**, 245 (2008).

[184] The H1, ZEUS Collaborations, Combined Measurement and QCD Analysis of the Inclusive ep Scattering Cross Sections at HERA, 2009, arXiv:0911.0884 [hep-ex].

[185] F. Dydak, M. W. Krasny, and R. Voss, CERN-SPSC-2009-028/SPC-I-239, CERN-LHCC-2009-014/LHCC-I-017, September 2009.